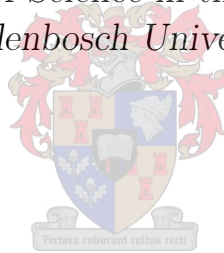


Characterization of the pre-eminent 4- α cluster state candidate in ^{16}O

by

Kevin Ching Wei Li

*Thesis presented in partial fulfilment of the requirements for
the degree of Master of Science in the Faculty of Science at
Stellenbosch University*



Department of Physics,
University of Stellenbosch,
Private Bag X1, Matieland 7602, South Africa.

Supervisors:

Prof P. Papka

Dr R. Neveling

Dr P. Adsley

Department of Physics
University of Stellenbosch

iThemba Laboratory for
Accelerator Based Sciences

Department of Physics
University of Stellenbosch

December 2015

Declaration

By submitting this thesis electronically, I declare that the entirety of the work contained therein is my own, original work, that I am the sole author thereof (save to the extent explicitly otherwise stated), that reproduction and publication thereof by Stellenbosch University will not infringe any third party rights and that I have not previously in its entirety or in part submitted it for obtaining any qualification.

Date:

Copyright © 2015 Stellenbosch University
All rights reserved.

Abstract

Characterization of the pre-eminent 4- α cluster state candidate in ^{16}O

K.C.W. Li

*Department of Physics,
University of Stellenbosch,
Private Bag X1, Matieland 7602, South Africa.*

Thesis: MSc Nuclear Physics

April 2015

The pre-eminent candidate for a Hoyle-analogue state in ^{16}O , which has been previously observed at 15.097(5) MeV and assigned a $J = 0^+$ spin and parity, was investigated. It is postulated that this resonance may exhibit α -cluster structure and in particular, be the manifestation of a Bose Einstein Condensate in nuclear matter.

In this work, the resonance was populated using the $^{16}\text{O}(\alpha, \alpha')$ reaction, which was studied at 0° with an incident beam energy of $E_{lab} = 200$ MeV. The focal plane detector system of the K600 spectrometer was employed to identify excited states of the ^{16}O nucleus whilst a double sided silicon strip detector array enabled the study of the charged particle decay channels.

An R-matrix fitting code was written to extract yields, widths and resonance energies from the excitation energy spectra. Whilst many resonances in the excitation energy range have been analysed, the focus of this thesis was the investigation of α -cluster candidate resonance at $E_x \sim 15.1$ MeV. The observed resonance energies of this resonance, from the singles spectra, α_0 and α_1 decay modes, are 15.076(1) MeV, 15.090(1) MeV and 15.046(3) MeV respectively. The observed widths, extracted from the singles spectrum, α_0 and α_1 decay modes, are 162(4) keV, 164(5) keV and 210(16) keV respectively, which agree well with the literature value of 166(30) keV.

The aforementioned R-matrix fitting code was employed to extract the angular distributions of the α_0 and α_1 decay modes. The angular distribution of the α_1 decay mode, at $E_x \sim 15.1$ MeV in ^{16}O , exhibits isotropy, however the angular distribution of the α_0 decay mode deviates from isotropy in a statistically significant manner.

We therefore refute the nature of the resonance previously observed at 15.097(5) MeV: the spin and parity of the resonance is either not 0^+ , or there is a previously unresolved resonance at $E_x \sim 15.1$ MeV. Either of these hypotheses has major implications for investigations into the structure of the ^{16}O nucleus. If the spin and parity of the resonance is determined to not be 0^+ , this results in the rejection of the primary candidate for a Hoyle-analogue α cluster state in ^{16}O . If there is a previously unidentified resonance in the $E_x \sim 15.1$ MeV excitation energy region, this may explain why the theoretically calculated width, for the aforementioned cluster state at 15.097(5) MeV, is consistently exceeded by the observed widths of the resonance in previous measurements.

Uittreksel

Karakterisering van 'n moontlike 4 α -groep toestand in ^{16}O

K.C.W. Li

*Departement van Fisika,
Universiteit van Stellenbosch,
Privaatsak X1, Matieland 7602, Suid Afrika.*

Tesis: MScIng (Meg)

April 2015

In hierdie studie word die toestand ondersoek wat beskou word as die beste kandidaat vir 'n analoog van die Hoyle toestand in ^{16}O , naamlik die $J^\pi=0^+$ toestand by 15.097(5) MeV. Dit is gepostuleer dat hierdie toestand bestaan uit α -deeltjies in die vorm van die sogenaamde Bose-Einstein kondensaat.

Die toestand is opgewek deur gebruik te maak van die $^{16}\text{O}(\alpha, \alpha')$ reaksie. Hierdie eksperimentele meting is uitgevoer by 'n bundel energie $E_{kin} = 200$ MeV en baie klein verstrooiingshoeke, insluitend 0° . Deur gebruik te maak van die detektors in die fokale vlak van die K600 magnetiese spektrometer kon die opwekkingsenergie van die ^{16}O kern bepaal word. Terselfertyd is die deeltjie verval van die ^{16}O kern bestudeer met behulp van 'n posisie sensitiewe silikon detektor opstelling rondom die teiken.

Sagteware is ontwikkel om R-matriks passings te doen ten einde waardes soos die wydte, energie en opbrengs van verskeie toestande in die opwekkingsenergie-spektrum te verkry. Daar word egter uitsluitlik op die 15.097(5) MeV toestand gefokus in hierdie studie. In die geval van die resultate vir inklusiewe opwekkingsenergie spektrum is gevind dat die gemete energie van die betrokke toestand 15.076(1) MeV is, terwyl die α_0 en α_1 verval modes resultate oplewer van onderskeidelik 15.090(2) MeV en 15.046(3) MeV. Die gemete piekwydtes is onderskeidelik 162(4) keV, 164(5) keV en 210(16) keV, wat in ooreenstemming is met die waarde bekend uit literatuur (166(30) keV).

Bogenoemde sagteware is ook benut om inligting te bekom aangaande die hoek verspreiding van die α_0 en α_1 verval modes van die 15.097(5) MeV toestand. In die geval van die α_1 verval mode is die hoek verspreiding van verval isotroop, in kontras met die resultate van die α_0 verval mode.

Hierdie resultate dui daarop dat die spin en pariteit van die 15.097(5) MeV toestand nie 0^+ is nie, of dat daar 'n ekstra, tot op hede onbekende, toestand rondom $E_x \sim 15.1$ MeV bestaan. Beide hierdie hipotese het verreikende gevolge vir struktuur studies van die ^{16}O kern. Indien dit bewys kan word dat die 15.097(5) MeV toestand inderdaad nie 'n 0^+ toestand is nie moet daar opnuut gesoek word na 'n Hoyle-toestand kandidaat vir ^{16}O . Aan die ander kant sal die bevestiging van die bestaan van 'n nuwe toestand rondom $E_x \sim 15.1$ MeV moontlik kan lig werp op die feit dat die gemete wydte van die toestand soveel groter is as die teoreties voorspelde waarde.

Acknowledgements

I wish to express my thanks in two distinct contexts: academic and personal.

- Thank you to the NRF for financially supporting this research.
- Thank you to the DST for for the NEP UID 86052 grant.
- Thank you to the Stellenbosch University Physics Department.
- Thank you to the accelerator team for providing excellent beam for this experiment.
- Thank you to Patriot Technologies Inc. and Intel who provided financial support, of their own volition, for a new workstation computer (which we have dubbed "JET") without which the computationally intensive R-matrix fits performed for this thesis would have not been possible.
- Thank you to the workshop staff at iThemba LABS who accommodated my infinite "urgent and final" modifications with a smile. In many ways, their willingness to go the extra mile was pivotal for the experiment to run properly. I am thankful to Paul for leaving to France just before the experiment and having the (misguided?) confidence in trusting me to deal with the workshop staff and instigate the many necessary modifications to the completely new setup, just in time for the experiment. It was a stressful learning experience that was valuable and I am glad that the workshop staff now all know my face well. Although I am sometimes greeted with a slight sense of a apprehension - in anticipation of the last minute modification that they suspect me to ambush upon them.
- Thank you to the academic staff at iThemba LABS who indulged my obsession to search their archives for old mechanical drawings of detectors and structures. These excavations have proved fruitful in allowing me to model many important pieces of equipment in GEANT4 and create something that, in the future, may be beneficial for people other than myself.

Personally, I would like to thank my supervisors and teachers: Paul Papka, Retief Neveling, Phil Adsley and Ricky Smit. Everything I have learnt so far about experimental nuclear physics, I attribute to you. The effort you place into young students goes far above the call of academic duty. You make personal sacrifices, whether it be late nights or weekends away from your loved ones, all for the singular passion that we share. Your efforts are beyond the realm of the academic and so to is the gratitude from your students.

Thank you to my parents for their support to study something I love. At the risk of sounding cliché, without my family I would not be here. This is true on multiple levels. Every opportunity that you have given your kids, that you yourself did not have, we see. Thank you.

Finally, I thank my Saviour Jesus Christ. Although it may only be a masters, whatever glory there is to be had, it is Yours.

Dedications

To my family

Contents

Declaration	i
Abstract	ii
Uittreksel	iv
Acknowledgements	vi
Dedications	viii
Contents	ix
List of Figures	xi
List of Tables	xvii
1 Introduction	1
2 Theory	7
2.1 Scattering Theory Formalism	8
2.2 Important Results of R-matrix Theory	14
3 Experimental Apparatus and Technique	17
3.1 The K600 Magnetic Spectrometer	20
3.2 Dispersion Matching	21
3.3 Focal Plane Detector System	23
3.4 The CAKE	42
3.5 Target setup	48
3.6 Electronics and DAQ	50
4 Data Analysis	54
4.1 Particle Identification (PID)	54
4.2 Focal Plane Calibration	57
4.3 The Singles Focal Plane Spectra	61
4.4 Data Sorting of the CAKE	68
4.5 Coincident Decay Particles in the CAKE	76

4.6	Background Subtraction of Coincidence Focal Plane Spectra . . .	82
4.7	Selectivity of Magnetic Substates	83
4.8	R-matrix Analysis	86
5	Results	96
5.1	R-matrix Fits of the Focal Plane Spectra	97
5.2	Branching Ratios of Charged Particle Decay	113
5.3	R-matrix Fits with θ_{SCAT} gates	114
5.4	The difference in resonance energies of the α_0 and α_1 decay modes from ^{16}O	119
5.5	Angular Correlations	122
5.6	Theoretical Calculations: Differential Cross Sections of $^{16}\text{O}(\alpha, \alpha')$ and the Angular Dis- tributions of the Subsequent α_0 Decay Modes.	125
5.7	Angular Distributions of Decay Products from Data	132
6	Conclusion and Outlook	141
6.1	Refuting the 0^+ nature of the previously observed 15.097(5) MeV resonance in ^{16}O	141
6.2	Future R-matrix Analysis	142
6.3	Branching Ratios and Angular Distributions	143
	Appendices	144
A	R-matrix Fits of the Focal Plane Spectra to Extract Angular Distributions	145
	List of References	150

List of Figures

1.1	The average binding energy per nucleon of the lightest alpha-conjugate nuclei	2
1.2	The proton separation energies of light alpha-conjugate nuclei and their respective isotopic chains	3
1.3	The neutron separation energies of light alpha-conjugate nuclei and their respective isotopic chains	3
1.4	Binding energy versus number of nearest neighbour bonds for the light alpha-conjugate nuclei	4
1.5	Schematic representation of possible α -clustered geometric configurations for the six lightest alpha-conjugate nuclei	6
3.1	Schematic top view of the SSC facility at iThemba Labs	17
3.2	The new scattering chamber setup with the CAKE mounted at backward angles	18
3.3	Schematic top view of the K600 magnetic spectrometer configuration for PR226	19
3.4	Schematic top view of the new scattering chamber coupled to the spectrometer via the small angle mode chamber	20
3.5	Schematic representation of an achromatic focus mode	22
3.6	Schematic representation of lateral dispersion matching	22
3.7	Schematic top view of the focal plane detector system	23
3.8	A graphical representation of a vertical drift chamber	24
3.9	Cross-sectional top view of a Vertical Drift Chamber	25
3.10	Schematic side view of the VDC wire planes	26
3.11	Schematic top view of the Vertical Drift Chamber operation	27
3.12	The lookup table for the X1 wire plane.	28
3.13	Drift times and drift distances of valid VDC events in the X1 wire plane	28
3.14	Schematic representation of a V-type wire event	30
3.15	Schematic representation of a Z-type wire event	31
3.16	Schematic representation of a W-type wire event	31
3.17	Spectrum of $Y1_{pos}$ versus $X1_{posC}$	33
3.18	Spectrum of $Y1_{pos}$	34
3.19	Schematic representation of θ_{SCAT}	35

3.20	Spectrum of θ_{SCAT} versus $X1_{posC}$	36
3.21	Spectrum of θ_{SCAT}	36
3.22	Spectra of the raw and valid events per wire plane	37
3.23	Position dependent efficiency for each wire plane	38
3.24	The corrected wire plane positional spectrum of the X1 wire plane .	39
3.25	Images of the paddle detectors	40
3.26	The CAKE	42
3.27	Schematic lattice structure of a p-doped silicon material	43
3.28	Schematic lattice structure of a n-doped silicon material	43
3.29	Schematic diagram of a p-n junction	44
3.30	Schematic diagram of an MMM-type DSSSD detector manufactured by Micron Semiconductor Ltd	45
3.31	Images of the CAKE configuration employed for PR226	46
3.32	The CAKE model within the GEANT4 simulation of the K600 . . .	46
3.33	The GEANT4 simulated solid angle versus average angle of each ring in the CAKE	47
3.34	The target ladder configuration for PR226	49
3.35	Schematic diagram of the CAKE and HAGAR electronics for PR226	51
3.36	Schematic diagram of the focal plane detector system electronics for PR226	53
4.1	Li_2CO_3 PID spectrum: the integrated PMT charge upon paddle 1 versus the TOF, indicating the PID gates	55
4.2	The empty frame PID spectrum: the integrated PMT charge upon paddle 1 versus the TOF, indicating the PID gates	56
4.3	Spectrum of the integrated PMT charges from paddle 1 against those from paddle 2	56
4.4	The mapping of Focal Plane position ($X1_{posC}$) to ejectile momentum	58
4.5	The residual energies of the focal plane momentum calibration . . .	58
4.6	The corrected wire plane position spectrum of the X1 wire plane for the Li_2CO_3 target, indicating the resonances selected for calibration	59
4.7	Excitation energy of the recoil nucleus for the Li_2CO_3 target	60
4.8	Singles background spectra for the Li_2CO_3 target	62
4.9	The raw, total background and background-subtracted singles spectra for the Li_2CO_3 target	62
4.10	Singles background spectra of the empty frame	63
4.11	The raw, total background and background-subtracted singles spectra for the empty frame	64
4.12	Singles background spectra of the Mylar target	64
4.13	The raw, total background and background-subtracted singles spectra for the Mylar target	65
4.14	Singles background spectra of the ^{12}C target	66
4.15	The raw, total background and background-subtracted singles spectra for the ^{12}C target	66

4.16	The background-subtracted spectra for the Li_2CO_3 and ^{12}C targets	67
4.17	The background-subtracted Li_2CO_3 spectrum with the normalised ^{12}C target spectrum removed	67
4.18	^{228}Th source calibration data for all ring and sector channels	68
4.19	Energy spectrum of the ring channels displaying the α decays from a ^{228}Th source.	69
4.20	All possible ring-sector hits in the CAKE without energy agreement required between the detected energies of sector channels (E_{sector}) and ring channels (E_{ring})	70
4.21	Valid hits in the CAKE with energy agreement between the detected energies of sector channels (E_{sector}) and ring channels (E_{ring})	70
4.22	The TDC spectrum of hits in the CAKE	71
4.23	Hit patterns for ring and sector channels of the CAKE, from the ^{228}Th source calibration data	73
4.24	Hit patterns for ring and sector channels of the CAKE, from the Li_2CO_3 target data	73
4.25	^{12}C spectra of the CAKE ring energy versus recoil nucleus excitation energy, identifying the beam halo events.	73
4.26	Typical ring and sector triggering permutations for the CAKE	74
4.27	Channel combination multiplicities of the CAKE	75
4.28	The ring energies of coincident hits in the CAKE, from the Li_2CO_3 target, versus the excitation energy of the recoil nucleus	78
4.29	The ring energies of coincident hits in the CAKE, from the ^{12}C target, versus the excitation energy of the recoil nucleus	78
4.30	Li_2CO_3 spectra of the CAKE ring energy versus recoil nucleus excitation energy, illustrating the different electronic thresholds between the MMM detectors	79
4.31	The ring energies of CAKE hits, from the Li_2CO_3 target, with a gate upon the recoil excitation energy: $14.8 \text{ MeV} < E_{x0} < 15.2 \text{ MeV}$	79
4.32	Li_2CO_3 spectra of the CAKE ring energy versus recoil nucleus excitation energy, illustrating the dependency of target attenuation upon the associated ring channel	80
4.33	The ring energies of CAKE hits, from the Li_2CO_3 target, with a gate upon the recoil excitation energy: $11.32 \text{ MeV} < E_{x0} < 11.72 \text{ MeV}$	81
4.34	The background sources of the coincidence focal plane spectra	82
4.35	Schematic representation of the θ_{SCAT} cuts which allow for selection over different distributions of ejectile scattering angles	83
4.36	The ideal ranges of ejectile scattering angle (θ_{lab} and ϕ_{lab}) covered by the θ_{SCAT}^l gate	84
4.37	The ideal ranges of ejectile scattering angle (θ_{lab} and ϕ_{lab}) covered by the θ_{SCAT}^h gate	84
4.38	The Gaussian smeared ranges of ejectile scattering angle (θ_{lab} and ϕ_{lab}) covered by the θ_{SCAT}^l gate	85

4.39	The Gaussian smeared ranges of ejectile scattering angle (θ_{lab} and ϕ_{lab}) covered by the θ_{SCAT}^h gate	85
4.40	Examples of Gaussian, Lorentzian and Voigt lineshapes	87
4.41	Voigt profiles with R-matrix lineshapes, showing the dependence of the width Γ on the l -value (of decay) dependent penetrability	87
5.1	Complete singles spectrum from the Li_2CO_3 target with an R-matrix fit for resonances in ${}^6,7\text{Li}$, ${}^{12}\text{C}$ and ${}^{16}\text{O}$	98
5.2	Complete singles spectrum from the Li_2CO_3 target with the ${}^{16}\text{O}$ and ${}^{12}\text{C}$ resonances superimposed upon the lithium resonances	98
5.3	Complete singles spectrum from the Li_2CO_3 target with Lorentzian resonance line-shapes which are deconvolved from the fitted Voigt lineshapes	99
5.4	Singles spectrum from the Li_2CO_3 target with an R-matrix fit, displayed over an excitation energy range: $9.0 \text{ MeV} < E_x < 13.5 \text{ MeV}$	99
5.5	Singles spectrum from the Li_2CO_3 target with the ${}^{16}\text{O}$ and ${}^{12}\text{C}$ resonances superimposed upon the lithium resonances, displayed over an excitation energy range: $9.0 \text{ MeV} < E_x < 13.5 \text{ MeV}$	100
5.6	Singles spectrum from the Li_2CO_3 target with Lorentzian resonance line-shapes which are deconvolved from the fitted Voigt lineshapes, displayed over an excitation energy range: $9.0 \text{ MeV} < E_x < 13.5 \text{ MeV}$	100
5.7	Singles spectrum from the Li_2CO_3 target with an R-matrix fit, displayed over an excitation energy range: $12.7 \text{ MeV} < E_x < 15.8 \text{ MeV}$	101
5.8	Singles spectrum from the Li_2CO_3 target with the ${}^{16}\text{O}$ and ${}^{12}\text{C}$ resonances superimposed upon the lithium resonances, displayed over an excitation energy range: $12.7 \text{ MeV} < E_x < 15.8 \text{ MeV}$	101
5.9	Singles spectrum from the Li_2CO_3 target with Lorentzian resonance line-shapes which are deconvolved from the fitted Voigt lineshapes, displayed over an excitation energy range: $12.7 \text{ MeV} < E_x < 15.8 \text{ MeV}$	102
5.10	Singles spectrum from the Li_2CO_3 target with an R-matrix fit, displayed over an excitation energy range: $15.6 \text{ MeV} < E_x < 25.0 \text{ MeV}$	102
5.11	Singles spectrum from the Li_2CO_3 target with the ${}^{16}\text{O}$ and ${}^{12}\text{C}$ resonances superimposed upon the lithium resonances, displayed over an excitation energy range: $15.6 \text{ MeV} < E_x < 25.0 \text{ MeV}$	103
5.12	Singles spectrum from the Li_2CO_3 target with Lorentzian resonance line-shapes which are deconvolved from the fitted Voigt lineshapes, displayed over an excitation energy range: $15.6 \text{ MeV} < E_x < 25.0 \text{ MeV}$	103
5.13	The complete α_0 decay mode spectrum of ${}^{16}\text{O}$ from the Li_2CO_3 target	104
5.14	The α_0 decay mode spectrum of ${}^{16}\text{O}$ from the Li_2CO_3 target, displayed over an excitation energy range: $9.0 \text{ MeV} < E_x < 13.5 \text{ MeV}$	105
5.15	The α_0 decay mode spectrum of ${}^{16}\text{O}$ from the Li_2CO_3 target, displayed over an excitation energy range: $12.7 \text{ MeV} < E_x < 15.8 \text{ MeV}$	105

5.16	The α_0 decay mode spectrum of ^{16}O from the Li_2CO_3 target, displayed over an excitation energy range: $15.6 \text{ MeV} < E_x < 24.0 \text{ MeV}$	106
5.17	The complete α_1 decay mode spectrum of ^{16}O from the Li_2CO_3 target	108
5.18	The α_1 decay mode spectrum of ^{16}O from the Li_2CO_3 target, displayed over an excitation energy range: $13.7 \text{ MeV} < E_x < 16.5 \text{ MeV}$	109
5.19	The α_1 decay mode spectrum of ^{16}O from the Li_2CO_3 target, displayed over an excitation energy range: $16.0 \text{ MeV} < E_x < 21.0 \text{ MeV}$	109
5.20	The α_1 decay mode spectrum of ^{16}O from the Li_2CO_3 target, displayed over an excitation energy range: $20.0 \text{ MeV} < E_x < 25.5 \text{ MeV}$	110
5.21	The complete α_1 decay mode spectrum of ^{16}O from the Li_2CO_3 target	112
5.22	The α_0 decay mode spectrum of ^{16}O , from the Li_2CO_3 target, with the θ_{SCAT}^l gate	114
5.23	The α_0 decay mode spectrum of ^{16}O , from the Li_2CO_3 target, with the θ_{SCAT}^l gate	115
5.24	The α_1 decay mode spectrum of ^{16}O , from the Li_2CO_3 target, with the θ_{SCAT}^l gate	115
5.25	The α_1 decay mode spectrum of ^{16}O , from the Li_2CO_3 target, with the θ_{SCAT}^l gate	116
5.26	The excitation energy of coincident particles in the CAKE versus the excitation energy of the recoil nucleus, focusing on the resonance energies of the α_0 and α_1 decay modes from the 15.097(5) MeV resonance in ^{16}O	119
5.27	The excitation energy spectra highlight the different resonance energies of the α_0 and α_1 decay modes from the 15.097(5) MeV resonance in ^{16}O	120
5.28	Penetrabilities of various decay channels which only in the l -value of decay and the final state of the residual nucleus	121
5.29	The differential cross section, of the ejectile from the $^{16}\text{O}(\alpha, \alpha')$ reaction, for a 15.097 MeV state in ^{16}O with $J^\pi = 0^+$ spin and parity	126
5.30	The angular distribution of the α -particle decay product from the α_0 decay mode of a 15.097(5) MeV state in ^{16}O with $J^\pi = 0^+$ spin and parity	126
5.31	The differential cross section, of the ejectile from the $^{16}\text{O}(\alpha, \alpha')$ reaction, for a 15.097 MeV state in ^{16}O with $J^\pi = 1^-$ spin and parity	127
5.32	The angular distribution of the α -particle decay product from the α_0 decay mode of a 15.097(5) MeV state in ^{16}O with $J^\pi = 1^-$ spin and parity	127
5.33	The differential cross section, of the ejectile from the $^{16}\text{O}(\alpha, \alpha')$ reaction, for a 15.097 MeV state in ^{16}O with $J^\pi = 2^+$ spin and parity	128
5.34	The angular distribution of the α -particle decay product from the α_0 decay mode of a 15.097(5) MeV state in ^{16}O with $J^\pi = 2^+$ spin and parity	128
5.35	The differential cross section, of the ejectile from the $^{16}\text{O}(\alpha, \alpha')$ reaction, for a 15.097 MeV state in ^{16}O with $J^\pi = 3^-$ spin and parity	129

5.36	The angular distribution of the α -particle decay product from the α_0 decay mode of a 15.097(5) MeV state in ^{16}O with $J^\pi = 3^-$ spin and parity	129
5.37	The differential cross section, of the ejectile from the $^{16}\text{O}(\alpha, \alpha')$ reaction, for a 15.097 MeV state in ^{16}O with $J^\pi = 4^+$ spin and parity	130
5.38	The angular distribution of the α -particle decay product from the α_0 decay mode of a 15.097(5) MeV state in ^{16}O with $J^\pi = 4^+$ spin and parity	130
5.39	The differential cross section, of the ejectile from the $^{16}\text{O}(\alpha, \alpha')$ reaction, for a 15.097 MeV state in ^{16}O with $J^\pi = 5^-$ spin and parity	131
5.40	The angular distribution of the α -particle decay product from the α_0 decay mode of a 15.097(5) MeV state in ^{16}O with $J^\pi = 5^-$ spin and parity	131
5.41	The GEANT4 simulated solid angle of the CAKE versus the average angle of each ring	132
5.42	The yield of decay particles from the 12.049(2) MeV 0^+ resonance in ^{16}O , versus the average angle of the associated triggered channel in the CAKE	133
5.43	The angular distribution of decay particles from the 12.049(2) MeV 0^+ resonance in ^{16}O , versus the average angle of the associated triggered channel in the CAKE	133
5.44	The yield of decay particles from the 11.520(4) MeV 2^+ resonance in ^{16}O , versus the average angle of the associated triggered channel in the CAKE	135
5.45	The angular distribution of decay particles from the 11.520(4) MeV 2^+ resonance in ^{16}O , versus the average angle of the associated triggered channel in the CAKE	135
5.46	The yield of decay particles from the 11.520(4) MeV 2^+ resonance in ^{16}O , with the θ_{SCAT}^l gate imposed, versus the average angle of the associated triggered channel in the CAKE	136
5.47	The angular distribution of decay particles from the 11.520(4) MeV 2^+ resonance in ^{16}O , with the θ_{SCAT}^l gate imposed, versus the average angle of the associated triggered channel in the CAKE	136
5.48	The yield of decay particles from the 11.520(4) MeV 2^+ resonance in ^{16}O , with the θ_{SCAT}^h gate imposed, versus the average angle of the associated triggered channel in the CAKE	137
5.49	The angular distribution of decay particles from the 11.520(4) MeV 2^+ resonance in ^{16}O , with the θ_{SCAT}^h gate imposed, versus the average angle of the associated triggered channel in the CAKE	137
5.50	The yield of decay particles from the 15.097(5) MeV 0^+ resonance in ^{16}O , versus the average angle of the associated triggered channel in the CAKE	138

5.51	The angular distribution of decay particles from the 15.097(5) MeV 0^+ resonance in ^{16}O , versus the average angle of the associated triggered channel in the CAKE	138
5.52	The yield of decay particles from the 15.097(5) MeV 0^+ resonance in ^{16}O , versus the average angle of the associated triggered channel in the CAKE	139
5.53	The angular distribution of decay particles from the 15.097(5) MeV 0^+ resonance in ^{16}O , versus the average angle of the associated triggered channel in the CAKE	139
A.1	R-matrix fitted focal plane spectrum of the α_0 decay mode from ^{16}O , with a coincidence condition on ring 3	145
A.2	R-matrix fitted focal plane spectrum of the α_0 decay mode from ^{16}O , with a coincidence condition on ring 7	146
A.3	R-matrix fitted focal plane spectrum of the α_0 decay mode from ^{16}O , with a coincidence condition on ring 11	146
A.4	R-matrix fitted focal plane spectrum of the α_0 decay mode from ^{16}O , with a coincidence condition on ring 15	147
A.5	R-matrix fitted focal plane spectrum of the α_1 decay mode from ^{16}O , with a coincidence condition on ring 3	147
A.6	R-matrix fitted focal plane spectrum of the α_1 decay mode from ^{16}O , with a coincidence condition on ring 7	148
A.7	R-matrix fitted focal plane spectrum of the α_1 decay mode from ^{16}O , with a coincidence condition on ring 11	148
A.8	R-matrix fitted focal plane spectrum of the α_1 decay mode from ^{16}O , with a coincidence condition on ring 15	149

List of Tables

1.1	Previous measurements of the 0_6^+ state in ^{16}O	5
3.1	The operating parameters of the K600 spectrometer for this experiment	21
3.2	Tabulated efficiencies of the VDC wire planes	38
4.1	The energies and spin-parities of the resonances used for momentum calibration of the focal plane	57

4.2	The angular momentum selection rules for $^{16}\text{O}(\alpha, \alpha')$, $^{12}\text{C}(\alpha, \alpha')$, $^7\text{Li}(\alpha, \alpha')$ and $^6\text{Li}(\alpha, \alpha')$	89
4.3	The angular momentum selection rules for the α_0 , α_1 and $p0$ decay modes of ^{16}O	91
4.4	The angular momentum selection rules for the α_0 , α_1 and $p0$ decay modes of ^{12}C	92
4.5	The angular momentum selection rules for the α_0 decay mode of ^7Li	93
4.6	The angular momentum selection rules for the α_0 decay mode of ^6Li	93
5.1	Extracted fit parameters from the singles spectrum fit of $^{16}\text{O}(\alpha, \alpha')$	97
5.2	Extracted fit parameters from the α_0 decay mode of ^{16}O	107
5.3	Extracted fit parameters from the α_0 and $p0$ decay modes of ^{16}O . .	111
5.4	The decay branching ratios of the 12.049(2) MeV 0^+ and 15.097(5) MeV resonances in ^{16}O	113
5.5	Extracted yields from the α_0 and α_1 decay modes of ^{16}O with the θ_{SCAT}^l and θ_{SCAT}^h gates	118
5.6	Tabulated resonance energies, which are equivalent to the location parameters for the Voigt R-matrix lineshapes, of the 15.097(5) MeV resonance in ^{16}O	120
5.7	The display colours for the α_0 and α_1 decay modes for a 15.097 MeV resonance in ^{16}O for $J^\pi = 0^+$ and $J^\pi = 3^-$	121

Chapter 1

Introduction

I want to die a slave to
principles. Not to men.

Emiliano Zapata

Clustering in nuclei is a vibrant and enthralling field within nuclear physics. Recent investigations into the nature of α -clustering have been no stranger to controversy and therein lies the allure. In nature, the manifestation of clustering is prevalent - transcending length scales to appear from the atomic to the cosmic regimes, with examples such as molecular clustering and the aggregation of galaxies with stars.

In the nuclear regime, clustering in light nuclei has garnered much interest as nuclei are expected to exhibit cluster-like properties, such as a dilute density structure, when excited. Alpha particles (${}^4\text{He}$), which are composed of a pair of protons and a pair of neutrons, exhibit a ground state with total momentum and parity of $J^\pi=0^+$. This is well understood by the pairing force which favours the configuration of protons and neutrons such that their wave functions are maximally overlapping, resulting in each pair of protons and neutrons to predominantly occupy their respective 1s orbitals with their spins anti-parallel.

The alpha particle has a higher average binding energy per nucleon (BE/A) of 7.074 MeV with respect to its nearest-neighbour stable nuclei, ${}^3\text{He}$ and ${}^6\text{Li}$, which have BE/A values of 2.573 MeV and 5.332 MeV respectively. This increase in stability stems from the doubly magic nature of ${}^4\text{He}$, which when interpreted in terms of the liquid drop model, can be attributed to the pairing and asymmetry terms. The inherent stability of the ground state of α -particles, evidenced by the high 20.21 MeV energy of the first excited state, further motivates the occurrence of α clustering. It is important to note that in this particular context, the phrase " α clustering" does not necessarily allude to nuclei with preformed α -particle subunits; it more conservatively refers to nuclei with observables that are well-reproduced with models exhibiting such

preformation.

Alpha-conjugate nuclei, nuclei which are exactly composed of α -particle subunits, are of particular interest since they are among the strongest candidates to exhibit α clustering structure. One reason being that alpha-conjugate nuclei typically exhibit high (if not the highest) BE/A s relative to their respective isotopic chains, as shown on Figure 1.1.

Figures 1.2 and 1.3 display proton and neutron separation energies (denoted S_p and S_n respectively) for the lightest alpha-conjugate nuclei and their associated isotopic chains. Whilst it is observed that the S_p energies typically increases with neutron number for these light elements, the addition of a neutron to form an alpha-conjugate nucleus consistently yields the most drastic increase in stability. The sawtooth structure of the S_n energies, when plotted against mass number, arises from neutron pairing. It is observed that an addition of a neutron upon an alpha-conjugate nucleus typically results in a decrease in S_n that is distinctly greater than the general sawtooth trend. The behaviour of the S_p and S_n energies for light nuclei, with respect to mass number, implies that whilst the pairing and symmetry of protons and neutrons are conducive to stability, it is the particular case of alpha-conjugation which is consistently superior in this regard.

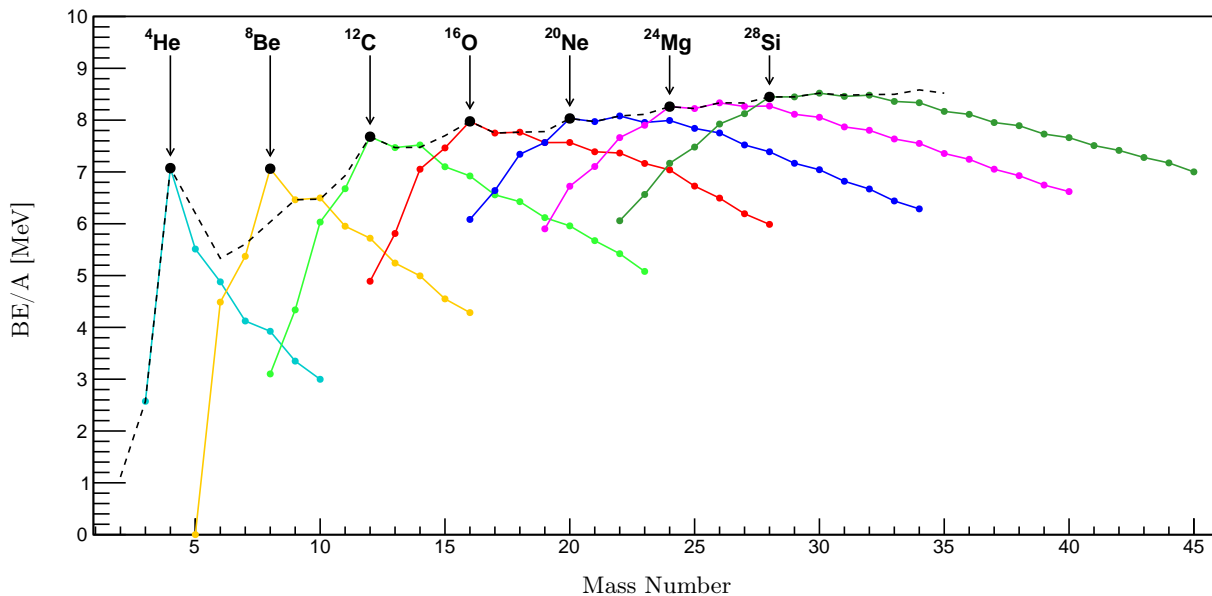


Figure 1.1: The average binding energy per nucleon (BE/A) of the lightest alpha-conjugate nuclei and their respective isotopic chains (represented with coloured data points; the connecting lines are to guide the eye). The dotted black line represents the BE/A for the lightest stable nuclei.

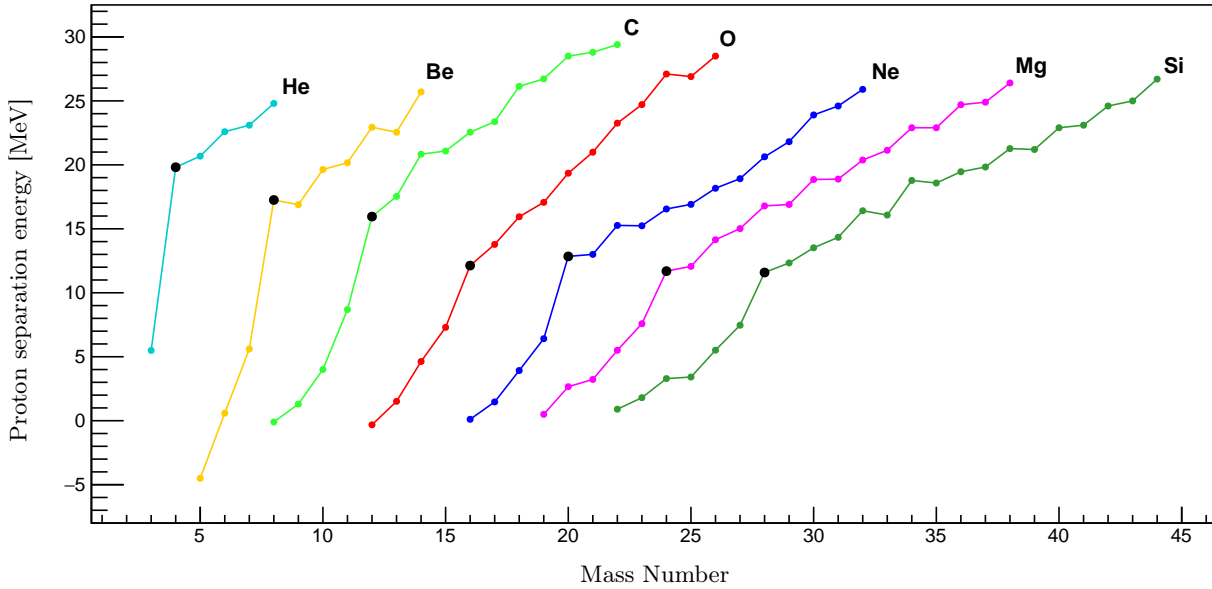


Figure 1.2: The proton separation energies of light alpha-conjugate nuclei and their respective isotopic chains. The black data points highlight the alpha-conjugate nucleus within each isotopic chain.

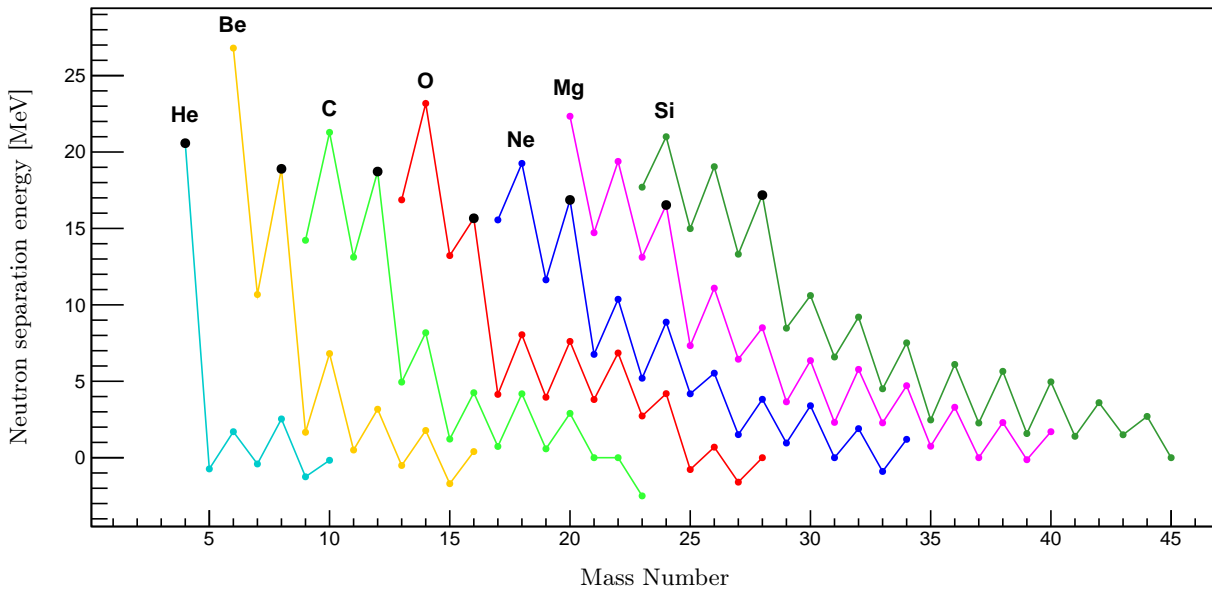


Figure 1.3: The neutron separation energies of light alpha-conjugate nuclei and their respective isotopic chains. The black data points highlight the alpha-conjugate nucleus within each isotopic chain.

Historically, the concept of α clustering in nuclei was pioneered by Hafstad and Teller in 1938 [1]. They observed that under the assumption of preformed α clustering in light alpha-conjugate nuclei, the arrangement of the α -particles can be chosen such that the number of nearest neighbour bonds (N_b) between the α -particles are linearly related to the total binding energy of the nucleus (see Figure 1.4). This assumption is naturally followed by the concept of "molecular" arrangements for these preformed α -particles. Brink and Boeker proposed geometric configurations for light alpha-conjugate nuclei where the N_b values agreed with those introduced by Hafstad and Teller [2], as displayed in Figure 1.5.

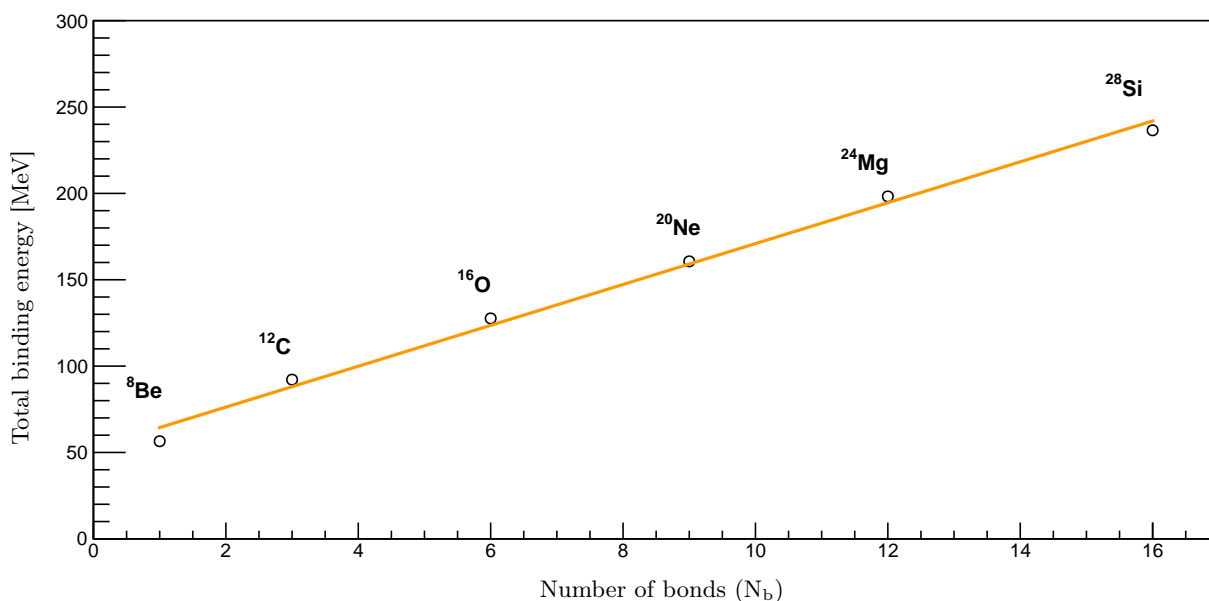


Figure 1.4: Binding energy versus number of nearest neighbour bonds (N_b) for the light alpha-conjugate nuclei, as suggested by Hafstad and Teller, indicating a linear dependency. The corresponding alpha-clustered geometric configurations of these nuclei are shown in Figure 1.5

The Hoyle state (predicted by Fred Hoyle in 1954) is the 0_2^+ state in ^{12}C observed at 7.65 MeV [3] and is regarded as the prototypical alpha-cluster state whose existence is of great import for the nucleosynthesis of ^{12}C within stars. The structure of this state has been thoroughly investigated with experiments [4, 5, 6] and theoretically modelled with both *ab initio* [7, 8] and cluster models [9, 10]. Cluster models, which inherently assume clustering, have been employed extensively to calculate the structures of ^{12}C and in particular, the Hoyle state. Notable theoretical cluster models of ^{12}C are the antisymmetrized molecular dynamics (AMD) [11] and fermionic molecular dynamics (FMD) formalisms [12]. The first *ab initio* calculation of the low-lying states in ^{12}C was performed by E. Epelbaum *et al.* [13]. Another notable formalism with which

^{12}C has been studied is the theory of nuclear energy density functionals (EDFs) by J. Ebran *et al.* [14].

Alpha-clustering is not restricted to alpha-conjugate nuclei however; the definitive case being ^8Be and ^9Be . Whilst ^8Be is invariably unstable, a valence neutron stabilises the ^9Be nucleus which possesses excited states that are interpreted to exhibit a molecular cluster structure of two α -particles with a valence neutron [15].

The manifestation of Bose Einstein Condensate (BEC) states in nuclear matter, in of itself, is a controversial topic in nuclear physics. A BEC state is an exclusively quantum mechanical phenomenon: whereby a system of bosonic particles, which are not constrained by the Pauli exclusion principle, can simultaneously occupy the lowest energy quantum state [16, 17]. A feature of BEC systems is that they often exhibit observables which can be macroscopically measured. The validity of describing a nucleus (which is not a macroscopic system) as a BEC, is consistent with the description of a few Cooper pairs as a manifestation of superconductivity [18].

To assume that the antisymmetrisation between the wavefunctions of the individually fermionic nucleons can be disregarded implicitly assumes that there is sufficient separation between the relevant nucleons. It follows that a dilute and extended nucleus structure is central to the existence of a BEC state in nuclear matter. The root mean square (rms) charge radius of a nucleus therefore elegantly provides an indirect observable with which to verify the occurrence of BEC states. The α -particle, in its aforementioned ground state with $J^\pi=0^+$ spin and parity, is a composite boson. Given the inherent stability of this ground state, α -particles are the natural candidates with which to model nuclear matter with bosonic subunits.

The 15.097(5) MeV 0_6^+ state in ^{16}O , observed above the 4- α threshold of 14.437 MeV, is the pre-eminent candidate for a Hoyle-analogue state. Furthermore, it is postulated to exist as a BEC state. This claim is substantiated by several theoretical predictions which use the OCM (Orthogonality Condition Model) and TSHR (Tohsaki-Horiuchi-Schuck-Röpke) approaches [19, 20].

The data from the previous measurements of the 0_6^+ state in ^{16}O are summarised in Table 1.1. In literature, the currently accepted width of this state is solely acquired from L. Ames [21], whilst the accepted average resonance energy considers all the listed measurements.

Reference	E_R [MeV]	Width [MeV]	Reaction
NPA 180 (1972) 282	15.17(5)	190(30)	$^{12}\text{C}(\alpha, \alpha')$
NPA 294 (1978) 161	15.10(5)	327(100)	$^{15}\text{N}(p, \alpha), ^{15}\text{N}(p, p')$
NPA 305 (1978) 63	15.103(5)	-	$^{14}\text{N}(^3\text{He}, p)$
PRC 25 (1982) 729	15.066(11)	166(30)	$^{12}\text{C}(\alpha, \alpha'), ^{15}\text{N}(\alpha, p)$

Table 1.1: Previous measurements of the 0_6^+ state in ^{16}O .

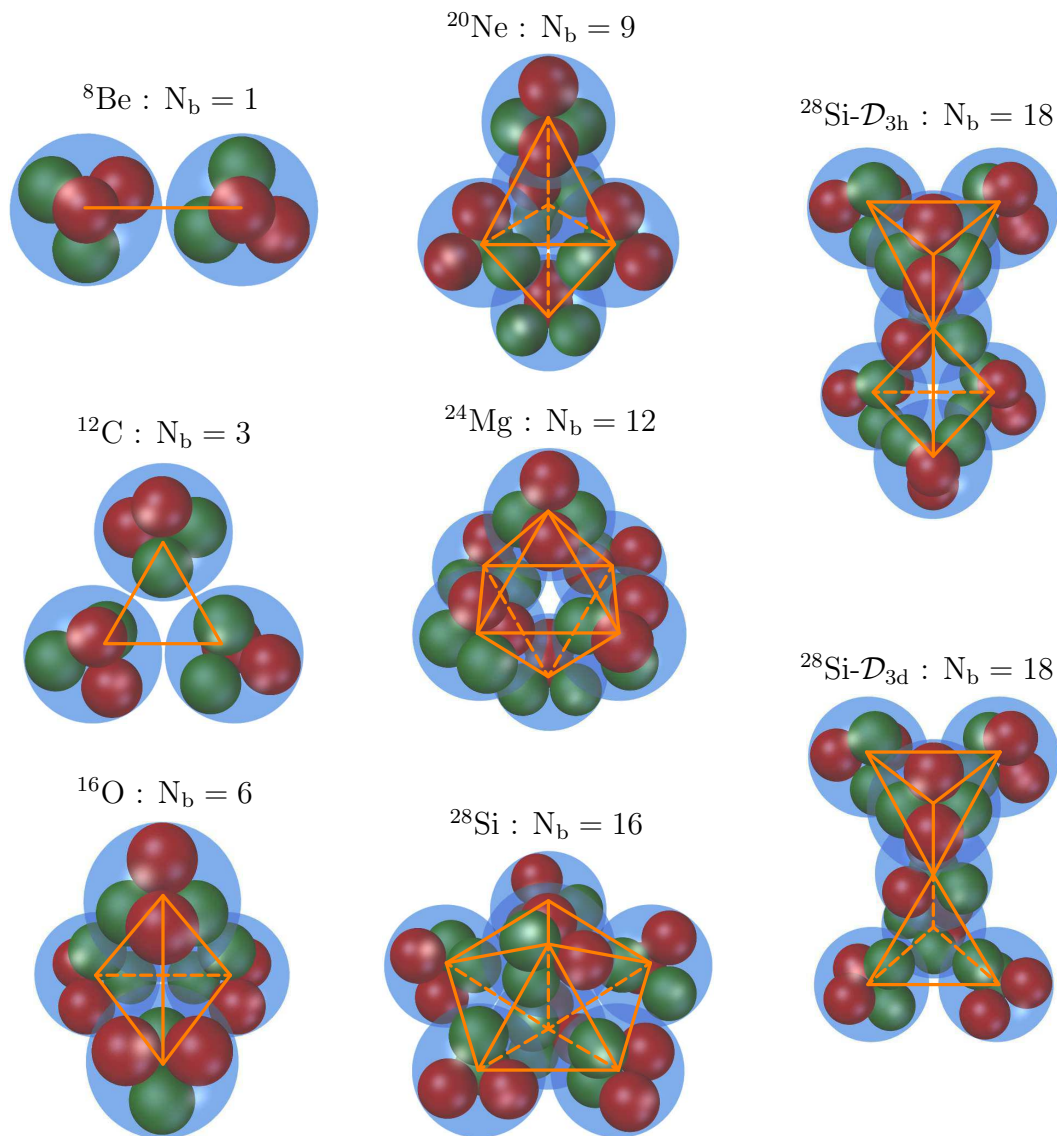


Figure 1.5: Schematic representation of possible α -clustered geometric configurations for the six lightest alpha-conjugate nuclei. The number of nearest neighbour bonds, N_b , for each configuration are displayed. The configurations labelled by ${}^8\text{Be}$, ${}^{12}\text{C}$, ${}^{16}\text{O}$, ${}^{20}\text{Ne}$, ${}^{24}\text{Mg}$ and ${}^{28}\text{Si}$ were predicted Brink and Boeker [2] in 1967, whilst ${}^{28}\text{Si-}\mathcal{D}_{3h}$ and ${}^{28}\text{Si-}\mathcal{D}_{3d}$ label the possible configurations that correspond to values of N_b suggested by Hafstad and Teller [1].

Chapter 2

Theory

And when Alexander saw the
breadth of his domain, he wept,
for there were no more worlds
to conquer

Hans Gruber, *Die Hard*

A prominent formalism used to interpret resonances in nuclei is R-matrix theory, which provides a phenomenological model. This formalism was first introduced by Wigner and Eisenbud in 1947 [22] and is comprehensively described in the seminal paper by Lane and Thomas [23], which lists the fundamental assumptions of the theory as:

- Applicability of non-relativistic quantum mechanics. This is justified by the low kinetic energies of the nucleons within the nucleus with respect to the rest mass energy.
- Absence or unimportance of all processes in which more than two product nuclei are formed. This implies that the theory pertains to the energy range where three-body breakup is energetically inhibited or negligible.
- Absence or unimportance of all processes, creation or destruction. The primary effect of this is to disregard photons in the formalism.
- For any pair of nuclei, there exists a radial separation distance beyond which neither nucleus experiences any potential field from the other. Moreover, the nuclear interaction is negligible beyond this separation distance a .

In this chapter, the fundamentals of non-relativistic scattering theory are pedagogically introduced [24, 25, 26]. This serves as the foundation of R-matrix

theory and defines many of the underlying concepts and mathematical structures. The significant results of R-matrix theory, which are used to interpret the data analysed in this thesis, are then stated without proof.

2.1 Scattering Theory Formalism

The time-independent Schrödinger equation, which describes the relative motion of two particles, is given by

$$\hat{H}\psi(R, \theta, \phi) = [\hat{T} + V - E] \psi(R, \theta, \phi) = 0, \quad (2.1.1)$$

where \hat{H} is the Hamiltonian and E is centre of mass energy. The \hat{z} axis is defined to be aligned with the beam axis so that θ and ϕ denote the polar and azimuthal angles respectively. The kinetic energy operator, \hat{T} , is expressed in spherical coordinates as

$$\begin{aligned} \hat{T} &= -\frac{\hbar^2}{2\mu} \nabla_R^2 \\ &= \frac{\hbar^2}{2\mu} \left[\frac{1}{R^2} \frac{\partial}{\partial R} \left(R^2 \frac{\partial}{\partial R} \right) + \frac{\hat{L}^2}{R^2} \right]. \end{aligned} \quad (2.1.2)$$

where the squared angular momentum operator, \hat{L}^2 , is expressed as

$$\hat{L}^2 = -\hbar^2 \left[\frac{1}{\sin^2 \theta} \frac{\partial^2}{\partial \phi^2} + \frac{1}{\sin \theta} \frac{\partial}{\partial \theta} \left(\sin \theta \frac{\partial}{\partial \theta} \right) \right]. \quad (2.1.3)$$

If we consider the case where neither the target nor the projectile nucleus are polarised, the potential $V = V(R)$ must be spherically symmetric, i.e. corresponding to a central force. The wavefunction of the incoming projection must also be cylindrically symmetric about the beam axis, defined to be \hat{z} , and takes the form of a plane wave e^{ikz} . The axis of quantisation for the angular momentum is chosen to be \hat{z} and the z-component of the angular momentum is given by

$$\hat{L}_z = \frac{\hbar}{i} \frac{\partial}{\partial \phi}. \quad (2.1.4)$$

The incoming plane wave, which is independent of ϕ is therefore an eigenstate of the \hat{L}_z operator with an eigenvalue of $m = 0$.

Given the commutation relations between the components of the \hat{L} operator:

$$[L_x, L_y] = i\hbar L_z, \quad [L_y, L_z] = i\hbar L_x, \quad [L_z, L_x] = i\hbar L_y, \quad (2.1.5)$$

it can be shown that $[\hat{L}^2, \hat{L}] = 0$. Taking $[\hat{L}^2, \hat{L}_y]$ as an example:

$$\begin{aligned}
[\hat{L}^2, \hat{L}_y] &= [\hat{L}_x^2, \hat{L}_y] + [\hat{L}_y^2, \hat{L}_y] + [\hat{L}_z^2, \hat{L}_y] \\
&= \hat{L}_x[\hat{L}_x, \hat{L}_y] + [\hat{L}_x, \hat{L}_y]\hat{L}_x + \hat{L}_z[\hat{L}_z, \hat{L}_y] + [\hat{L}_z^2, \hat{L}_y]\hat{L}_z \\
&= \hat{L}_x(i\hbar L_z) + (i\hbar L_z)\hat{L}_x + \hat{L}_z(-i\hbar L_x) + (-i\hbar L_x)\hat{L}_z \\
&= 0.
\end{aligned} \tag{2.1.6}$$

This is trivially proven for L_x and L_z by cyclicly permuting the x , y , and z indices.

Since the first term of \hat{T} contains no angular dependence and both \hat{L} and \hat{L}^2 possess no radial dependence, it follows that

$$[\hat{H}, \hat{L}] = 0 \tag{2.1.7}$$

and

$$[\hat{H}, \hat{L}^2] = 0. \tag{2.1.8}$$

This implies that angular momentum is conserved and the cylindrical symmetry of the incoming plane wave must be conserved in the outgoing wavefunction. The Schrödinger equation has now been simplified to

$$[\hat{T} + V(R) - E] \psi(R, \theta) = 0, \tag{2.1.9}$$

It is known from scattering theory that for large distances, the wavefunction solutions must take their asymptotic form

$$\psi = \psi^{beam} + \psi^{scat} = A \left[e^{ik_i z} + f(\theta, \phi) \frac{e^{ik_f R}}{R} \right] \tag{2.1.10}$$

where k_i and k_f are the wavenumbers for the ingoing and outgoing relative motions respectively and $f(\theta, \phi)$ is the scattering amplitude.

A consequence of the commutation relations between \hat{H} , L and L^2 is that simultaneous eigenstates exist between these operators. A natural choice of basis is therefore the Legendre polynomials as they are eigenfunctions of both \hat{L} and \hat{L}^2 . They form an orthogonal and complete basis on the interval $0 \geq \theta \geq \pi$, with an associated inner product:

$$\int_0^\pi P_L(\cos \theta) P_{L'}(\cos \theta) \sin \theta d\theta = \frac{2}{2L+1} \delta_{LL'}. \tag{2.1.11}$$

Any continuous and differentiable function $F(\theta)$, defined over the interval $0 \geq \theta \geq \pi$, can therefore be expanded in terms of the Legendre polynomials as:

$$F(\theta) = \sum_L b_L P_L(\cos \theta) \tag{2.1.12}$$

The full wave function, which depends upon the radius R and the polar angle θ can therefore be expanded as

$$\psi(R, \theta) = \sum_{L=0}^{\infty} (2L+1) i^L P_L(\cos \theta) \frac{1}{kR} \chi_L(R) \quad (2.1.13)$$

where the radial and angular dependencies of the wavefunction have been separated. The radial dependency is now contained in the $b_L = b_L(R)$ coefficient given by:

$$b_L(R) = (2L+1) i^L \frac{1}{kR} \chi_L(R) \quad (2.1.14)$$

By substituting partial wave sum in 2.1.13 into 2.1.9, the time-independent Schrödinger equation to be solved is:

$$\left[\hat{T} + V - E \right] \left(\sum_{L=0}^{\infty} (2L+1) i^L P_L(\cos \theta) \frac{1}{kR} \chi_L(R) \right) = 0 \quad (2.1.15)$$

The kinetic energy operator acting on a single term within the partial wave sum yields

$$\begin{aligned} & \hat{T} P_L(\cos \theta) \frac{1}{kR} \chi_L(R) \\ &= \frac{\hbar^2}{2\mu} \left[-\frac{1}{R^2} \frac{\partial}{\partial R} \left(R^2 \frac{\partial}{\partial R} \right) + \frac{\hat{L}^2}{R^2} \right] P_L(\cos \theta) \frac{1}{kR} \chi_L(R) \\ &= \frac{\hbar^2}{2\mu k} P_L(\cos \theta) \left[-\frac{1}{R^2} \frac{\partial}{\partial R} \left(R^2 \frac{\partial}{\partial R} \frac{\chi_L(R)}{R} \right) + \frac{L(L+1)}{R^3} \chi_L(R) \right] \\ &= \frac{\hbar^2}{2\mu k} P_L(\cos \theta) \left[-\frac{1}{R^2} (-\chi'_L(R) + \chi'_L(R) + R\chi''_L(R)) + \frac{L(L+1)}{R^3} \chi_L(R) \right] \\ &= \frac{\hbar^2}{2\mu k R} P_L(\cos \theta) \left[-\frac{d^2}{dR^2} + \frac{L(L+1)}{R^2} \right] \chi_L(R), \end{aligned} \quad (2.1.16)$$

which reduces Equation 2.1.15 to

$$\sum_{L=0}^{\infty} \left[-\frac{\hbar^2}{2\mu} \left(\frac{d^2}{dR^2} - \frac{L(L+1)}{R^2} \right) + V(R) - E \right] \chi_L(R) P_L(\cos \theta) = 0. \quad (2.1.17)$$

Multiplying Equation 2.1.17 by $P_{L'}(\cos \theta)$ and integrating over 0 to π :

$$\begin{aligned}
& \int_0^\pi \sum_{L=0}^{\infty} \left[-\frac{\hbar^2}{2\mu} \left(\frac{d^2}{dR^2} - \frac{L(L+1)}{R^2} \right) + V(R) - E \right] \chi_L(R) P_{L'}(\cos \theta) P_L(\cos \theta) d\theta \\
& = \sum_{L=0}^{\infty} \left[-\frac{\hbar^2}{2\mu} \left(\frac{d^2}{dR^2} - \frac{L(L+1)}{R^2} \right) + V(R) - E \right] \chi_L(R) \frac{2}{2L+1} \delta_{LL'} = 0.
\end{aligned} \tag{2.1.18}$$

It can therefore be concluded that the following equation, known as the partial wave equation, must hold for each $\chi_L(R)$ term of the partial wave expansion:

$$\left[-\frac{\hbar^2}{2\mu} \left(\frac{d^2}{dR^2} - \frac{L(L+1)}{R^2} \right) + V(R) - E \right] \chi_L(R) = 0. \tag{2.1.19}$$

In R-matrix theory, one fundamental assumption is that for any pair of nuclei, there exists a radial separation distance beyond which the nuclear interaction is negligible. The radius $R = a$, which is a chosen parameter, is chosen to be outside this radial separation distance and consequently partitions the system into an internal ($R \leq a$) and an external ($R \geq a$) region.

The partial wave equation, which is a second order differential equation, needs two boundary conditions to specify a particular solution. To match the solutions from the internal and external regions, a number of boundary conditions must be satisfied. The internal and external wavefunction solutions and their respective derivatives must match at this external radius. For the internal wavefunction solution: $\chi(0) = 0$, which ensures that the full wavefunction, shown in Equation 2.1.13, is finite at $R = 0$. For the external wavefunction solution: for $R \gg a$, the wavefunction must take the asymptotic form in Equation 2.1.10.

2.1.1 Radial Solutions for Zero Potential

The partial wave equation to be solved in this external region is given by

$$\left[-\frac{\hbar^2}{2\mu} \left(\frac{d^2}{dR^2} - \frac{L(L+1)}{R^2} \right) - E \right] \chi_L^{ext}(R) = 0. \tag{2.1.20}$$

Typically, a change of variable from R to the dimensionless ρ is used to simplify the equation, where

$$\rho \equiv kR, \tag{2.1.21}$$

which yields

$$\left[\frac{d^2}{d\rho^2} - \frac{L(L+1)}{\rho^2} + 1 \right] \chi_L^{ext}(\rho/k) = 0. \tag{2.1.22}$$

This is a specific case ($\eta = 0$) of the more general Coulomb wave equation

$$\left[\frac{d^2}{d\rho^2} - \frac{L(L+1)}{\rho^2} - \frac{2\eta}{\rho} + 1 \right] \chi_L(\eta, \rho) = 0. \quad (2.1.23)$$

which describes the relative motion of particles under the Coulomb potential. The dimensionless Sommerfeld parameter [27], η , is given by

$$\eta = \frac{Z_1 Z_2 e^2}{\hbar v} = \frac{Z_1 Z_2 e^2}{\hbar} \left(\frac{\mu}{2E} \right)^2, \quad (2.1.24)$$

where Z_1 and Z_2 are the charges of the two decay product nuclei, E is the centre of mass energy, μ is the reduced mass and e denotes the elementary unit of charge. The two prevalent, linearly independent solutions to this second order differential equation are known as the regular and irregular Coulomb wavefunctions [28]. The defining characteristic of the regular Coulomb wave functions, denoted $F(\eta, \rho)$, is

$$F(\eta, 0) = 0, \quad (2.1.25)$$

whereas for the irregular Coulomb wavefunctions

$$G(\eta, 0) \neq 0. \quad (2.1.26)$$

These functions cannot be expressed in terms of elementary functions and are related by the Wronskian

$$G_L(\eta, \rho) \frac{dF_L(\eta, \rho)}{d\rho} - F_L(\eta, \rho) \frac{dG_L(\eta, \rho)}{d\rho} = 1 \quad (2.1.27)$$

Since $F(\eta, \rho)$ and $G(\eta, \rho)$ are linearly independent, the external wavefunction solution $\chi_L(R)$ of the Coulomb wave equation can always be expressed as

$$\chi_L(R) = C_1 G(\eta, \rho) + C_2 F(\eta, \rho) \quad (2.1.28)$$

where C_1 and C_2 are arbitrary constants. The incident plane wave can therefore be expressed in terms of the Coulomb wavefunctions. It has been proven that the plane wave can be expressed purely in terms of the regular Coulomb functions [29]:

$$e^{ikz} = \sum_{L=0}^{\infty} (2L+1) i^L P_L(\cos \theta) \frac{1}{kR} F_L(0, kR), \quad (2.1.29)$$

From $F(\eta, \rho)$ and $G(\eta, \rho)$, two well known linearly independent solutions can be constructed, known as the Coulomb Hankel functions:

$$H_L^\pm(\eta, \rho) = G_L(\eta, \rho) \pm iF_L(\eta, \rho). \quad (2.1.30)$$

Both the plane wave expansion in Equation 2.1.29 and the external wave-function solution can therefore also be equivalently expressed in terms of the Coulomb Hankel Functions:

$$e^{ikz} = \sum_{L=0}^{\infty} (2L+1) i^L P_L(\cos\theta) \frac{1}{kR} \frac{i}{2} [H_L^-(0, kR) - H_L^+(0, kR)] \quad (2.1.31)$$

and

$$\chi_L^{\text{ext}}(R) = A_L [H_L^-(0, kR) - S_L H_L^+(0, kR)], \quad (2.1.32)$$

where A_L and S_L are complex constants and S_L is known as the partial wave S-matrix element.

For $\eta = 0$ and $\rho \gg L$, the regular and irregular Coulomb functions reduce to the following forms:

$$F_L(0, \rho) \sim \sin(\rho - L\pi/2) \quad (2.1.33)$$

and

$$G_L(0, \rho) \sim \cos(\rho - L\pi/2), \quad (2.1.34)$$

which imply that the Coulomb Hankel functions asymptotically reduce to a plane waves

$$H_L^{\pm}(0, \rho) \sim e^{\pm i(\rho - L\pi/2)} = i^{\mp} e^{\pm i\rho} \quad (2.1.35)$$

In this asymptotic limit, the Coulomb Hankel functions $H_L^{\pm}(0, \rho)$ are eigenstates of the radial momentum operator $\hat{p} = \frac{\hbar}{i} \frac{\partial}{\partial R}$ with eigenvalues $\pm \hbar k$. This implies that $H_L^-(0, \rho)$ and $H_L^+(0, \rho)$ represent radially incoming and outgoing waves respectively.

2.1.2 Radial Solutions with a Potential

For radius $R < a$, the nuclear interaction is not negligible, i.e. $V(R) \neq 0$. For pure Coulomb scattering, η is given by Equation 2.1.28. For a general potential, the partial wave equation to be solved in this region is given by Equation 2.1.19. To reiterate, the boundary condition within the internal region is $\chi_L(R=0) = 0$, however $\chi_L'(R=0)$ is unknown. Given some trial radial wavefunction solution $u_L(R)$, the partial wave equation can be expressed as

$$u_L''(R) = \left[\frac{L(L+1)}{R^2} + \frac{2\mu}{\hbar^2} (V(R) - E) \right] u_L(R) \quad (2.1.36)$$

Typically, a numerical integration scheme is employed to solve for $u_L(R)$. The actual radial wavefunction solution $\chi_L(R)$ is related to the trial wavefunction by some complex constant B

$$\chi_L(R) = Bu_L(R). \quad (2.1.37)$$

For $R > a$, the wavefunction must agree with the external form given in Equation 2.1.32. To determine S_L , the internal and external solutions and their respective derivatives are matched at $R = a$. A mathematical object that is convenient for matching derivatives is the inverse logarithmic derivative, known as the R-matrix element:

$$R_L = \frac{1}{a} \frac{\chi_L(a)}{\chi'_L(R)} = \frac{1}{a} \frac{u_L(a)}{u'_L(R)}. \quad (2.1.38)$$

The R-matrix element allows the matching of derivatives with $u_L(R)$ without any knowledge of the complex factor B .

2.2 Important Results of R-matrix Theory

The observed partial width of decay channel i , with the emitted particle carrying angular momentum l , from a recoil nucleus with excitation energy E is given by

$$\Gamma_i = 2\gamma^2 P_l(E), \quad (2.2.1)$$

where $P_l(E)$ is the penetrability of the decay channel, with external radius $R = a$, given by

$$P_l(E) = ka \left| \frac{u_l(\infty)}{u_l(a)} \right|^2. \quad (2.2.2)$$

Given the asymptotic form of the outgoing Coulomb Hankel functions $H_L^\pm(0, \rho)$ in Equation 2.1.35, the penetrability can be alternatively expressed in terms of the regular and irregular Coulomb functions:

$$\begin{aligned} P_l(E) &= ka \left| \frac{e^{ika}}{iF_L(\eta, ka) + G_L(\eta, ka)} \right|^2 \\ \implies P_l(E) &= \frac{ka}{F_l(\eta, ka)^2 + G_l(\eta, ka)^2} \end{aligned} \quad (2.2.3)$$

The penetrability can be interpreted as being analogous to the transmission coefficient in quantum tunnelling. The main differences being that the transmission coefficient is defined as the ratio between the incident and transmitted current densities (denoted J_{inc} and J_{trans} respectively) with respect to some nuclear potential barrier:

$$T = \frac{|J_{trans}|}{|J_{inc}|}, \quad (2.2.4)$$

whereas the R-matrix penetrability is independent of the nuclear interaction as it evaluated with the wavefunction solution for the region $R > a$. Both the penetrability and the transmission coefficient are indicative of the probability of a particle "penetrating through" a potential barrier and are qualitatively similar in energy dependence, i.e. the relative probability of penetration through the barrier increases with the relative energy of the system.

The total width of the resonance Γ , which is a model-independent observable, is given by the sum of the partial widths across all open decay channels:

$$\Gamma = \sum_i \Gamma_i. \quad (2.2.5)$$

The branching ratio of a decay channel can determined from the ratio of the associated partial width and the total width of the resonance:

$$B_i = \Gamma_i/\Gamma. \quad (2.2.6)$$

In time-independent scattering theory, the scattering matrix element S_L is equivalent to a phase shift δ_L :

$$S_L = e^{2i\delta_L}. \quad (2.2.7)$$

In a seminal paper by Wigner [30], the principle of causality is invoked in the derivation of a lower-limit for the energy derivative of this phase shift $\frac{d\delta}{dE}$. Considering the interpretation of the phase shift derivative as a time delay by Eisenbud [31], this lower-limit can be explained as: "the scattered particle cannot leave the scatterer before it arrives". Such a limit corresponds to a weak or uniform potential, giving rise to the extreme case of a radially uniform wavefunction, i.e. $w(R)/R \equiv \text{constant} \implies w(R) \propto R$. Normalisation over the interval $0 \leq R \leq a$:

$$\begin{aligned} \int_0^a \left| \frac{w(R)}{R} \right|^2 R^2 dR &= 1, \\ \implies w(R) &= 3^{1/2} a^{-3/2} R. \end{aligned} \quad (2.2.8)$$

This limiting case directly translates to an upper limit for the reduced width γ_i of a decay channel, known as the Wigner limit:

$$\gamma_W^2 = \frac{\hbar}{2\mu a} |w(a)|^2 = \frac{3\hbar^2}{2\mu a^2}, \quad (2.2.9)$$

The Wigner limit therefore imposes an upper limit upon the observed width of a decay channel. Whilst the Wigner limit is highly dependent upon the chosen

parameter a , it is well-documented that the resulting limit upon the observed width is relatively independent of the chosen radius [32].

For a single-channel R-matrix formalism, it is possible to calculate the single-particle reduced width, given by

$$\gamma_{sp}^2 = \frac{\hbar}{2\mu a} |w_n(a)|^2, \quad (2.2.10)$$

where n labels the pole of the resonance and $w_n(a)$ is the associated solution of the radial wave function. This single-particle reduced width can be interpreted as the limiting case where the resonance is dominated by a single channel.

One can extract reduced widths γ from data and the ratios between these actual reduced widths and those given by the Wigner limit and the single-particle widths are known as the Wigner and single-particle ratios respectively:

$$\theta_W^2 = \frac{\gamma^2}{\gamma_W^2} \quad (2.2.11)$$

$$\theta_{sp}^2 = \frac{\gamma^2}{\gamma_{sp}^2} \quad (2.2.12)$$

Given the width of a resonance, which has an energy dependence that is completely determined by the penetrability, the total lineshape of a resonance is given by

$$N(E) \propto \frac{\Gamma(E)}{[E - E_R - \Delta(E)]^2 + [\Gamma(E)/2]^2}, \quad (2.2.13)$$

where E is the available energy, E_R is the resonance energy and $\Delta(E)$ is given by

$$\Delta(E) = -\gamma^2 [S_l(E) - S_l(E_R)]. \quad (2.2.14)$$

$S(E)$, the shift function, is defined as

$$S(E) = ka \frac{\dot{F}(\eta, \rho)F(\eta, \rho) + \dot{G}(\eta, \rho)G(\eta, \rho)}{F_l(\eta, \rho)^2 + G_l(\eta, \rho)^2}, \quad (2.2.15)$$

where the derivatives, $\dot{F}(\eta, \rho)$ and $\dot{G}(\eta, \rho)$, are with respect to ρ :

$$\dot{F}(\eta, \rho) = \frac{dF(\eta, \rho)}{d\rho}, \quad \dot{G}(\eta, \rho) = \frac{dG(\eta, \rho)}{d\rho}. \quad (2.2.16)$$

Chapter 3

Experimental Apparatus and Technique

They do not know it, but they
are doing it

Karl Marx

The primary purpose of this study is to characterise the decay modes of resonances in ^{16}O . The primary resonance of interest, which has been observed at 15.097(5) MeV, is the pre-eminent candidate for a Hoyle-analogue state. Such an experiment, which was assigned project number PR226 by the iThemba LABS Programme Advisory Committee (PAC) [33], was conducted at the separated-sector cyclotron (SSC) facility of iThemba LABS (see Figure 3.1).

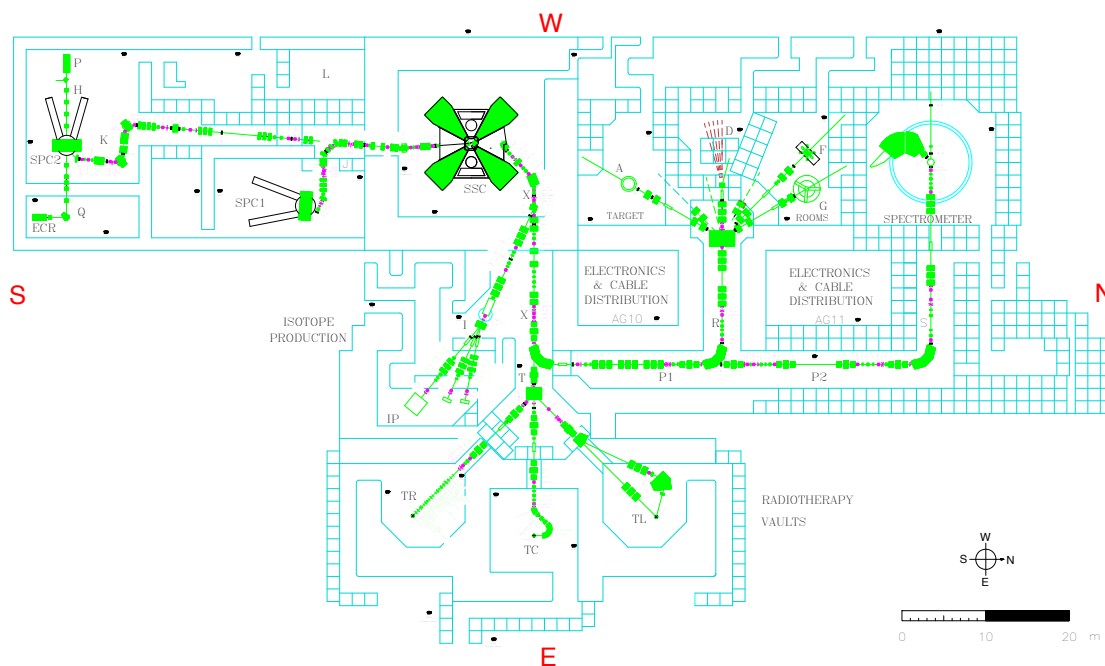


Figure 3.1: Schematic top view of the SSC facility at iThemba Labs.

In this experiment, the $^{16}\text{O}(\alpha, \alpha')$ reaction was studied at 0° with an incident beam energy of 200 MeV. The K600 magnetic spectrometer was used to identify excited states of the ^{16}O nucleus whilst a double sided silicon strip detector (DSSSD) array and a large NaI detector were employed to study the associated charge particle and γ -ray decay modes respectively. Figure 3.2 displays the silicon detector setup, known as the Coincidence Array for K600 experiments (CAKE), which was mounted within a newly developed scattering chamber. The geometry of the pre-existing cylindrically shaped (524 mm in diameter) scattering chamber is not optimised to accommodate ancillary detector systems.

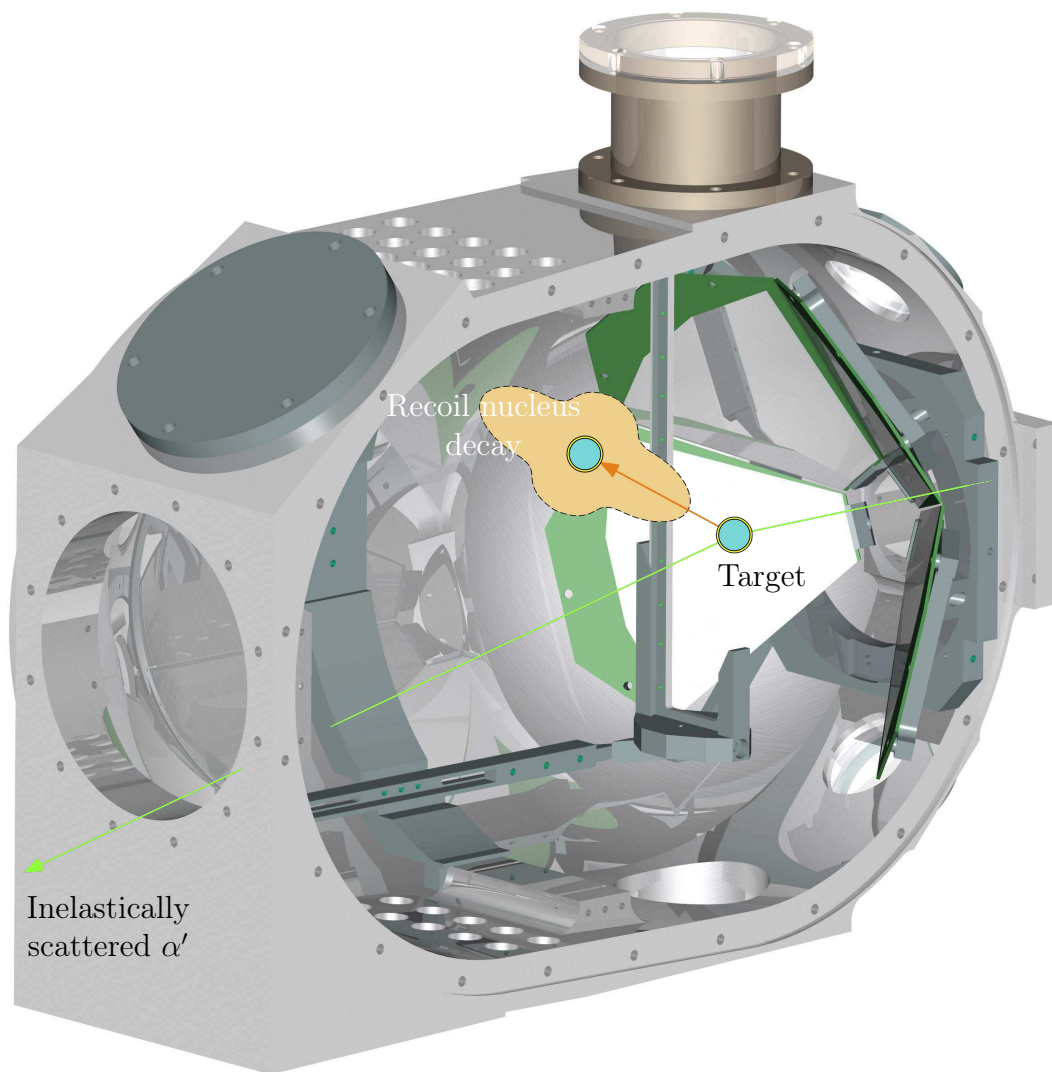


Figure 3.2: The new scattering chamber setup with the CAKE mounted at backward angles. Displayed is a schematic representation of the reaction of interest, accompanied by a subsequent recoil decay with an associated angular correlation.

The K600, which falls within the category of Q2D (two dipole and one quadrupole) spectrometers, was configured for a $\theta_{lab} = 0^\circ$ measurement with a $\pm 2^\circ$ angular acceptance, as shown in Figure 3.3 [34]. The focal plane detector system of the K600 (see Section 3.3) detects inelastically scattered α particles to allow inferences upon the recoil nuclei to be made. The detection of coincident charged decay particles with the CAKE enables the characterisation of resonances through various observables, e.g. branching ratios, angular distributions, widths etc. - ultimately providing insight into the structure of the nucleus. In this chapter, the various detection systems and the associated data acquisition system (DAQ) will be described.

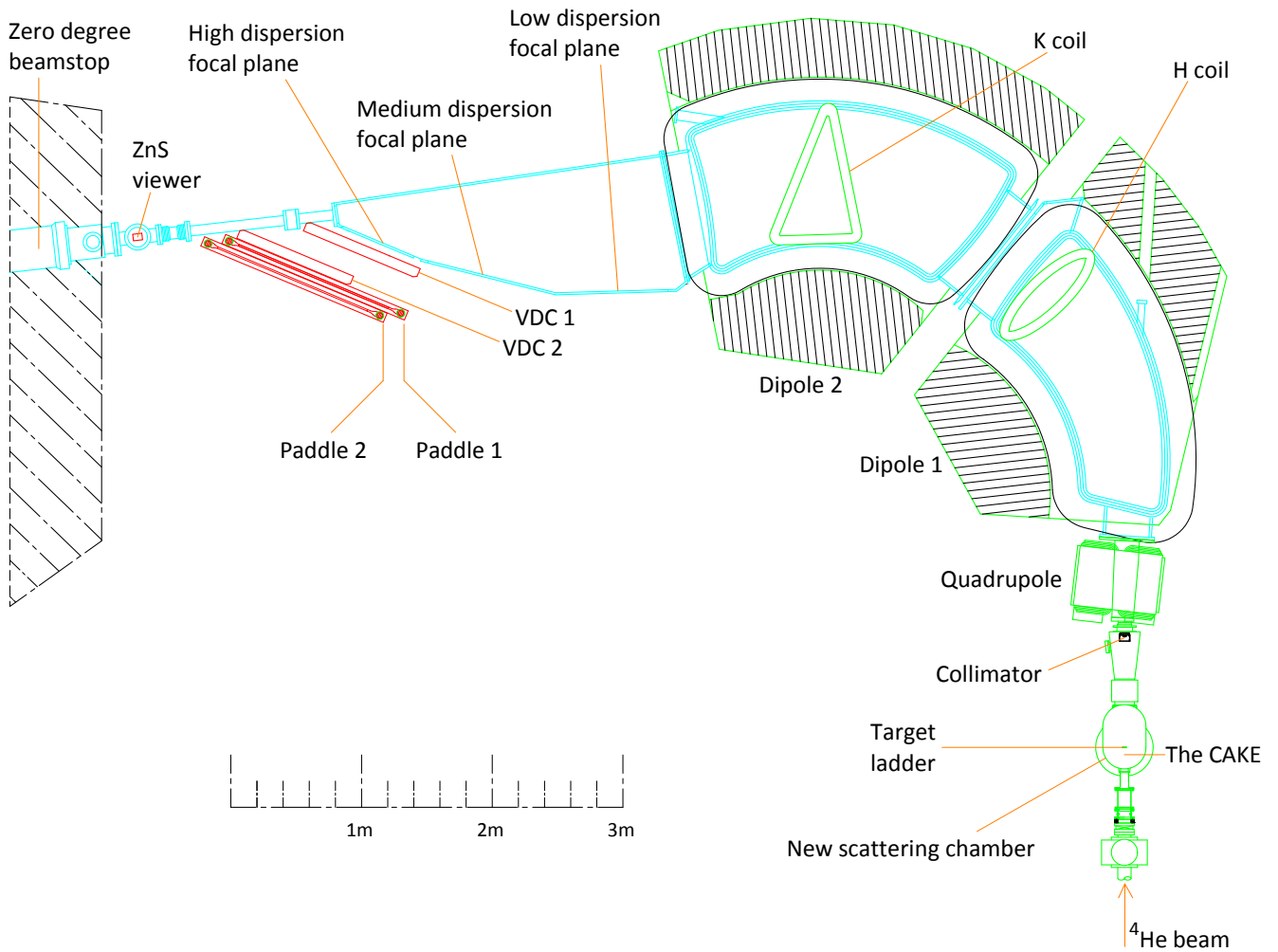


Figure 3.3: Schematic top view of the K600 magnetic spectrometer configured in the 0° mode with the detectors mounted in the high dispersion focal plane.

3.1 The K600 Magnetic Spectrometer

The K600 magnetic spectrometer is primarily composed of the following electromagnets:

- Two dipole magnets: the upstream and downstream dipoles are denoted D1 and D2 respectively. These are the primary bending magnets of the spectrometer.
- A quadrupole magnet: this magnet focuses the accepted ejectiles immediately after collimation (see Figure 3.4). Historically, the quadrupole is rotated off-axis with respect to the beam axis for a now obsolete small angle mode configuration [35].
- The H and K trim coils: in general, the focal plane position is dependent upon the scattering angle of the ejectile. To mitigate this dependency, the H-coil provides a second-order correction within D1 via a dipole and hexapole component. The K-coil provides a first-order correction within D2 via a dipole and quadrupole component. The operating parameters of these coils (see Table 3.1) are calibrated towards the kinematics of a particular mass range of target nuclei, i.e. ^{16}O . A more precise software correction is additionally applied post-experiment to the data (see Section 3.3.10).

These components collectively operate to disperse the flight paths of the ejectiles in terms of their momenta, resulting in different traversal points across the focal plane. These positions upon the focal plane are used to deduce the momenta of the ejectile. Assuming that the scattering reaction is binary and single-step in nature, a given ejectile momentum completely determines both the kinetic and excitation energies of the recoil nucleus of interest. The new scattering chamber was coupled to the internal vacuum chamber of the spectrometer with the small angle mode chamber (see Figure 3.4). The collimator imposed a $\pm 2^\circ$ restriction (centered at 0°) for ejectiles to be accepted to the spectrometer.

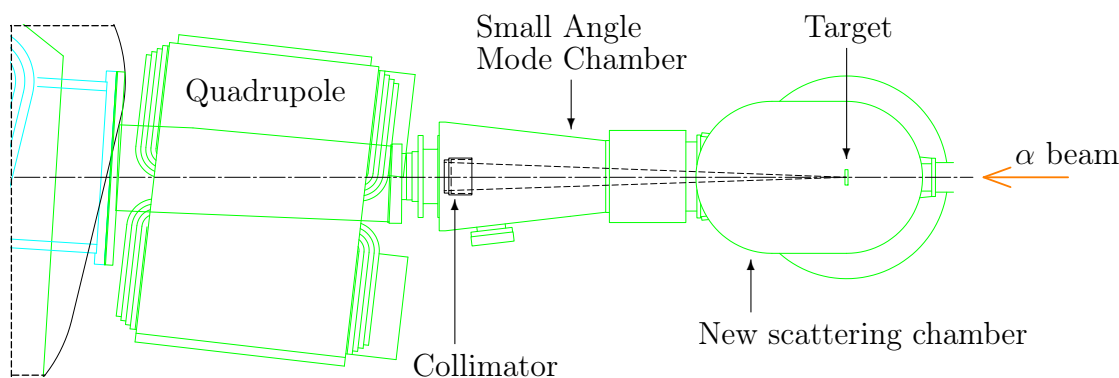


Figure 3.4: Schematic top view of the new scattering chamber coupled to the spectrometer via the small angle mode chamber.

The operating parameters of the K600 magnetic spectrometer are dependent upon the a host of conditions such as:

- the required beam energy,
- the mass and ionisation state of the beam particle,
- the mass of the target nucleus of interest (for kinematic corrections),
- the configuration of the focal plane detector system, i.e. whether it is positioned in the high, medium or low dispersion focal plane.

The field settings were calculated with a programme written at iThemba LABS, named SPEXCIT [36], which utilises a parameterisation of the measured magnetic fields of the K600. The operating parameters for this experiment are summarised in Table 3.1.

	Current [A]	Magnetic Field [T]
Quadrupole	-456.926	—
D1 dipole	415.30	1.0439
H-coil	-2.850	—
D2 dipole	272.65	0.70076
K-coil	2.850	—

Table 3.1: The operating parameters of the K600 spectrometer for this experiment. The magnetic fields for the D1 and D2 dipoles are calculated by SPEXCIT. The magnetic fields produced by the quadrupole, H- and K-coils are less trivial to quantify as they produce inhomogenous magnetic fields of higher order multipolarity.

3.2 Dispersion Matching

Dispersion matching is the process by which the energy resolution of measurements with the magnetic spectrometer can be improved to exceed the energy spread of the initial particle beam [37, 38]. Lateral dispersion matching is achieved with the beam optics of the spectrometer by focusing the different components of the scattered beam (corresponding to different initial beam energies) at the focal plane. This is achieved by spatially separating the trajectories of the beam particles according to momentum such that ejectiles with higher momenta travel a longer distance through the spectrometer (and *vice versa*). Whilst the positional resolution is vastly improved, this form of focusing results in momentum dependence of the ejectile's traversal angle through the focal plane (θ_{fp}). This dependence can be removed by additionally employing angular dispersion matching, allowing for a more accurate reconstruction of the initial scattering angle of the ejectile.

Achromatic Mode

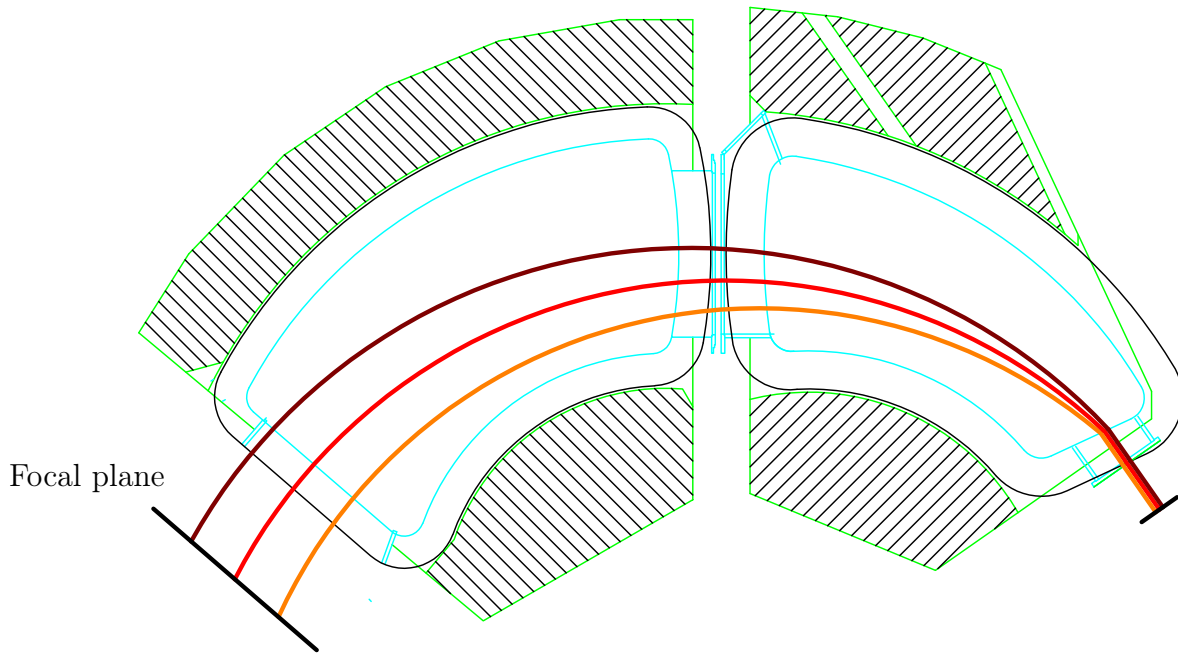


Figure 3.5: Schematic representation of an achromatic focus mode. The momentum distribution of the beam at the target position is independent of position, leading to a kinematic broadening of the focal plane spectrum.

Lateral Dispersion Matching

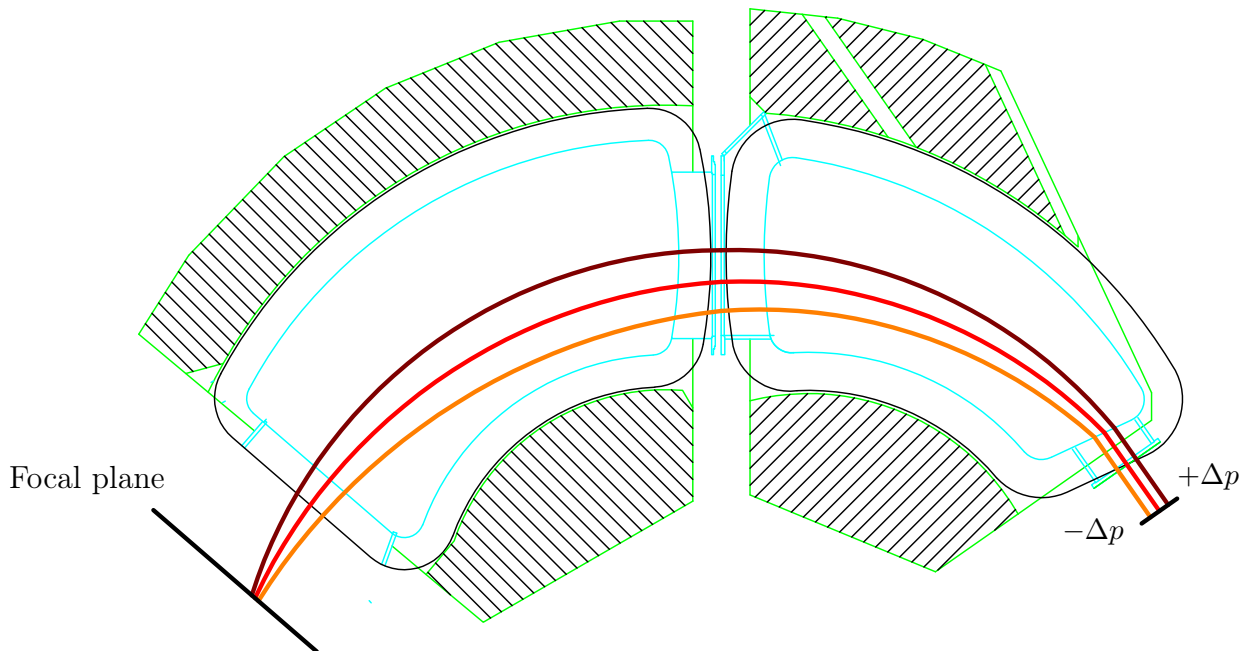


Figure 3.6: Schematic representation of lateral dispersion matching. The beam profile is generated with the lower momentum ($-\Delta p$) and higher momentum ($+\Delta p$) particles upon the inner and outer sides of the bending radius respectively.

3.3 Focal Plane Detector System

The focal plane detector system of the K600 spectrometer (see Figure 3.7) is comprised of two primary components: the Vertical Drift Chambers (VDCs) and the plastic scintillators (colloquially referred to as "paddles"). The purpose of the VDCs is to track ejectile particles traversing the focal plane. The plastic scintillators serve as event triggers whilst also providing particle identification capability.

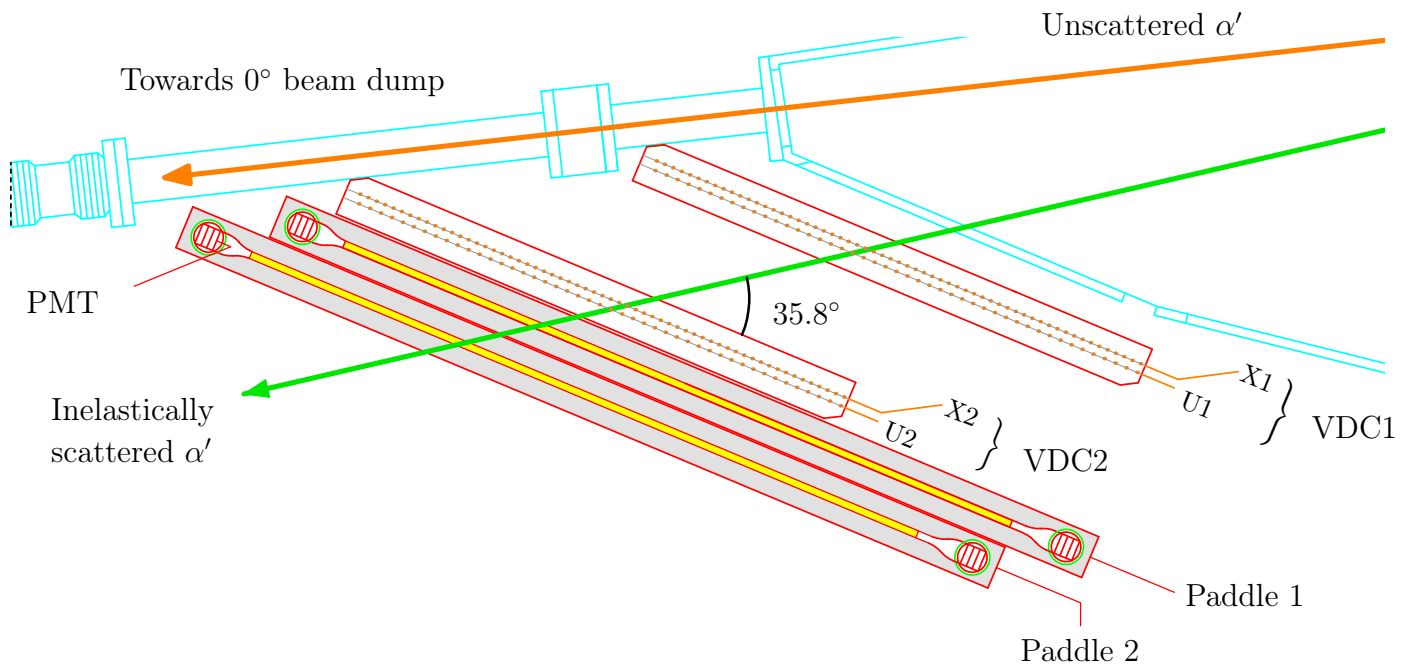


Figure 3.7: Schematic top view of the focal plane detector system. Paddle 1 and paddle 2 were 1/4" and 1/2" thick respectively (see Section 3.3.11). The VDCs were orientated such that the X wire planes were upstream of the inelastically scattered α particles relative to the U wire plane.

3.3.1 Vertical Drift Chambers (VDCs)

The VDCs are gaseous ionisation detectors whose primary purpose is to track ejectiles and consequently infer the excitation energies of the recoil nuclei (see Figure 3.8). For this experiment, the two VDCs were employed in a high dispersion focal plane configuration. Since the dispersion is higher than that of the other focal planes, the distance between the beam pipe and the detector is minimised (in accordance with the physical constraints of the detector geometry). This translates to a detection range of higher energy ejectiles by the VDCs, enabling the observation of lower recoil nuclei excitations. Each

VDC possesses an X and a U wire plane. An X wire plane provides horizontal information of the ejectile whilst a U wire plane provides both horizontal and vertical information. For each triggered event, the triggered TDC (time-to-digital converter) channels from the VDCs are readout. A Kapton exit window is employed upon the exit window of the spectrometer to separate the internal vacuum chamber of the spectrometer from the atmospheric pressure in the vault. The focal plane detector system is mounted directly in the air. The energy losses that occur in both the Kapton window and the air restrict the heaviest detectable ejectiles to light ions such as H and He. Furthermore, the energy losses impose a lower limit upon the detectable energies of the ejectiles.

3.3.1.1 High-voltage Planes

Each VDC is composed of three high-voltage planes that partition the detector into an X and a U wire chamber (see Figure 3.9). The high-voltage (HV) planes are formed from stretched aluminium foil [39]. For the detection of α particles, each HV plane received a potential of approximately -2.95 kV under operation.

3.3.1.2 Mylar Windows

The purpose of the Mylar windows is to isolate the internal VDC wire chambers from the atmosphere. Mylar is a trademarked form of biaxially-oriented polyethylene terephthalate (BoPET) polymer resin with the chemical formula: $C_{10}H_8O_4$. The high structural strength of Mylar allows for thin windows to be employed; this is advantageous in minimising the scattering of traversing ejectiles.



Figure 3.8: A graphical representation of a vertical drift chamber. The wire planes, Mylar planes, high-voltage planes have been omitted.

3.3.1.3 X and U wire planes

The X and U wire planes are accommodated within the wire chambers of the VDCs and their corresponding names are numbered to match their VDC number (e.g. X1 and U1 from VDC1). Each X wire plane is composed of 198 signal wires and 201 guard wires whilst each U wire plane consists of 143 signal and 146 guard wires. The X wires are vertically aligned whilst the U wires are obliquely orientated at 50° relative to the horizontal plane (see Figure 3.10). All signal wires are positioned such that the normal/minimum distance between neighbouring signal wires of a particular wireplane is 4 mm (for both the X and U wire planes). The guard wires are evenly interspersed amongst the signal wires with the addition of two guard wires flanking the ends of each wire plane. All wires are composed of gold plated tungsten with a diameter of $20\ \mu\text{m}$ for signal wires, $50\ \mu\text{m}$ for standard guard wires and $100\ \mu\text{m}$ for all outermost flanking guard wires. All guard wires receive a potential of approximately -500 V whilst the signal wires are connected to the preamplifiers. The electric fields created by the potentials upon the guard wires and high-voltage planes effectively define rectangular cuboidal cells for each signal wire, as illustrated in Figure 3.11. This prevents cross-cell drift of ionised electrons.

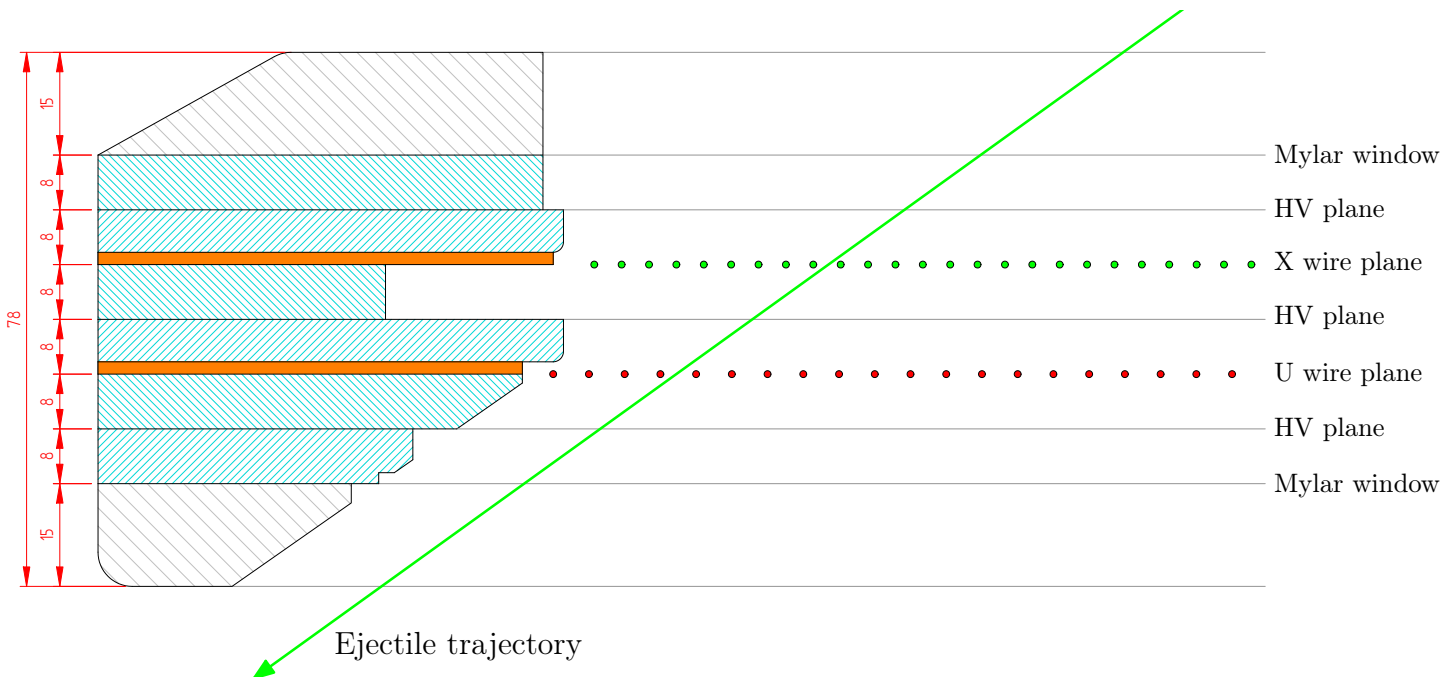


Figure 3.9: Cross-sectional top view of a Vertical Drift Chamber. The VDC components displayed with blue hatching are composed of Stesalam EP107-M950-40: a material with high radiation hardness and low out-gassing properties. The grey hatched components are composed of aluminium. The solid orange regions indicate the printed circuit boards (PCB) upon which the wire planes are mounted. The dimensions displayed are in millimetres.

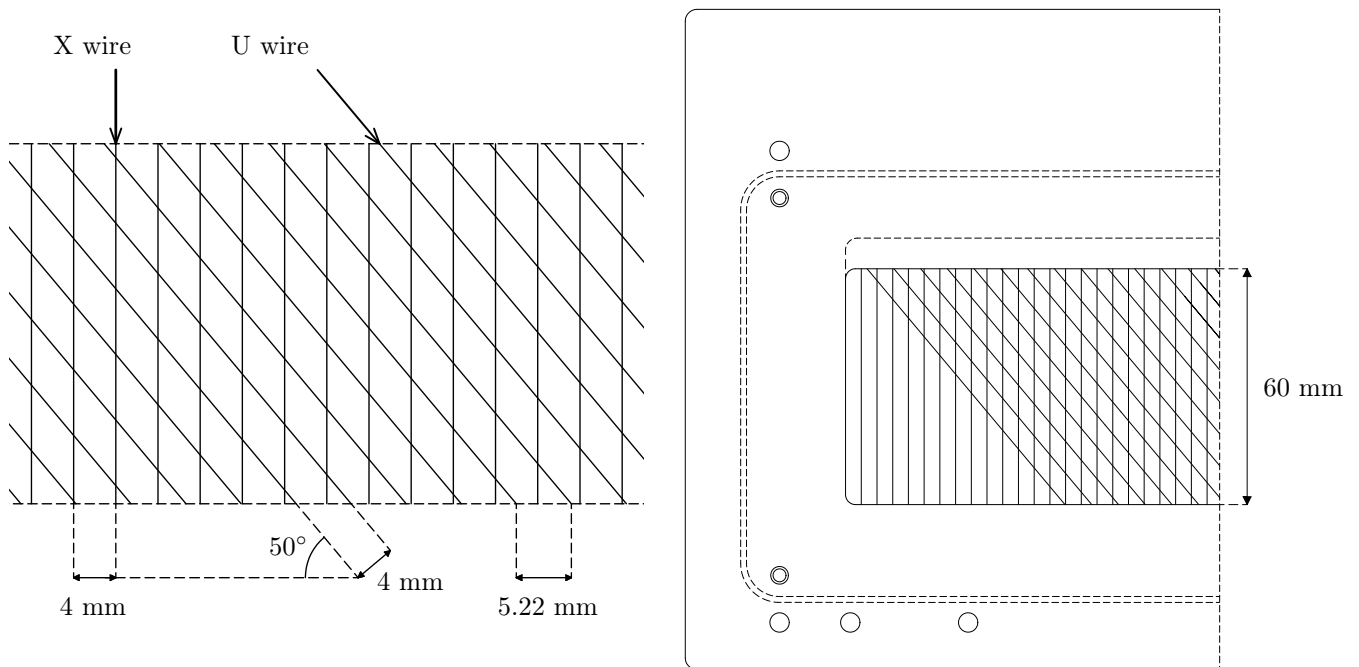


Figure 3.10: Schematic side view of the VDC wire planes (guard wires are excluded for clarity).

3.3.1.4 Gaseous detection medium

During operation of the VDCs, a combination of Ar and CO₂ gas (in a mass ratio of 90% and 10% respectively) is continuously flowed through the detector. This gas mixture is the detection medium and occupies the same cavities within each VDC that house the wire planes.

If a particle traverses this sensitive region, it collides with the Ar atoms and liberate electrons, producing electron-ion pairs. These free electrons then drift towards the signal wires under the influence of the electric field and can initiate avalanches, ultimately inducing electrical signals in the associated signal wires. Within the VDCs, avalanching more readily occurs closer to the wires, where the electric field gradient is strongest. Assuming sufficient ionisation occurs within a particular cell, the signal passes an electronic threshold in the associated preamplifier channel and the amplified signal is then conveyed towards the the TDC in the Data Acquisition system (DAQ). A description of the DAQ is presented in Section 3.6.

The principle obstacle with such a detection method is the fact that the traversing particle's collision may not directly liberate electrons from Ar, but rather excite the atom. The subsequent decay of the excited atoms, primarily through photon emission, poses a threat to positional accuracy as these photons can liberate electrons in other regions of the gaseous medium. These uncorrelated interactions can produce spurious electrical signals, culminating

in poor ejectile track reconstruction. To mitigate these effects, a quenching gas (i.e. CO_2) is added which absorbs the energy of the photons without being ionised; one such mechanism is the excitation of vibrational or rotational states of the quenching gas molecule. The molecules of a quenching gas also have a lower ionisation potential relative to the Ar atoms, allowing electron transfer to the Ar ions through collisions. This has the effect of quenching avalanches.

3.3.2 VDC Operation

Gaseous ionisation primarily occurs under two regimes, namely "ionisation" and "Geiger-Müller". If a sufficiently low potential is applied, the detector is operated under the ionisation regime and there is direct proportionality between the collected charge and the energy deposition within the detection medium. Under the Geiger-Müller regime, which is typified by a relatively high potential, the associated electric field sufficiently accelerates the initially liberated electrons to impinge upon and further liberate bound electrons. The propagation of such successive ionisations through the detection medium leads to a temporary conduction known as a Townsend avalanche. This phenomenon results in the loss of energy deposition information, which is sacrificed in exchange for a large output signal. Avalanching typically occurs close to the wires, where the electric field gradient is strongest

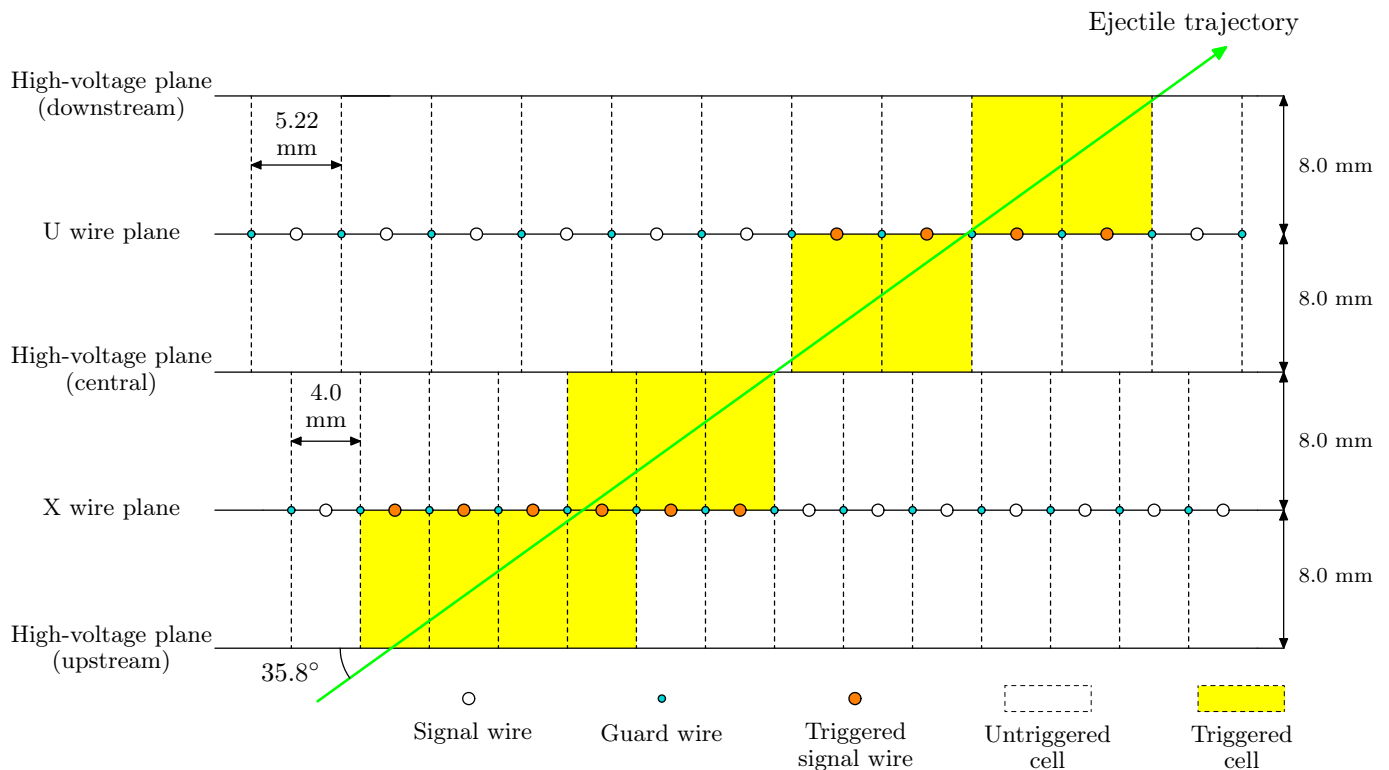


Figure 3.11: Schematic top view of the Vertical Drift Chamber operation.

The aforementioned -2.95 kV potential upon the high-voltage planes of the VDCs, when considered with regards to the separation distance of 8 mm between planes, indicates that the VDCs predominantly operate under the Geiger-Müller regime. The measured quantities are the average drift times of the initially liberated electrons. These drift times are measured relative to the paddle trigger signal. A drift time is used to determine a drift distance: the distance between the average position of ionisation relative to the signal wire of the associated cell. A calibration for each wire plane (see Figure 3.12) is extracted by gating upon a "white spectrum": a structureless region of the focal plane spectrum from in-beam data. In this focal plane region, the particle tracks are uniformly distributed. This provides a one-to-one mapping of drift times to drift distances for a selected domain of drift times. The geometry of the VDCs restrict the maximum possible drift distance to 8mm. After processing the data, one can observe the drift distances of valid VDC events (defined in 3.3.8) which are displayed in Figure 3.13.

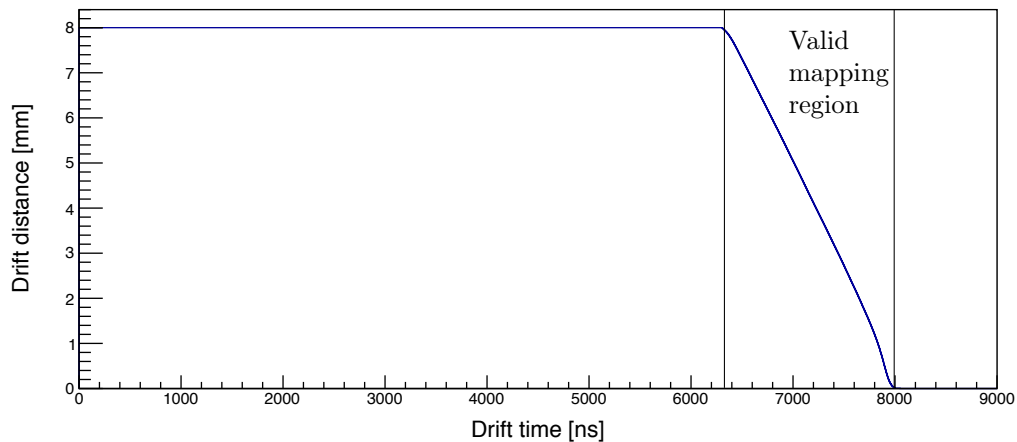


Figure 3.12: The lookup table for the X1 wire plane. Since the drift times are measured with a common stop rather than a common start reference, the shorter the drift time, the longer the drift distance (and *vice versa*).

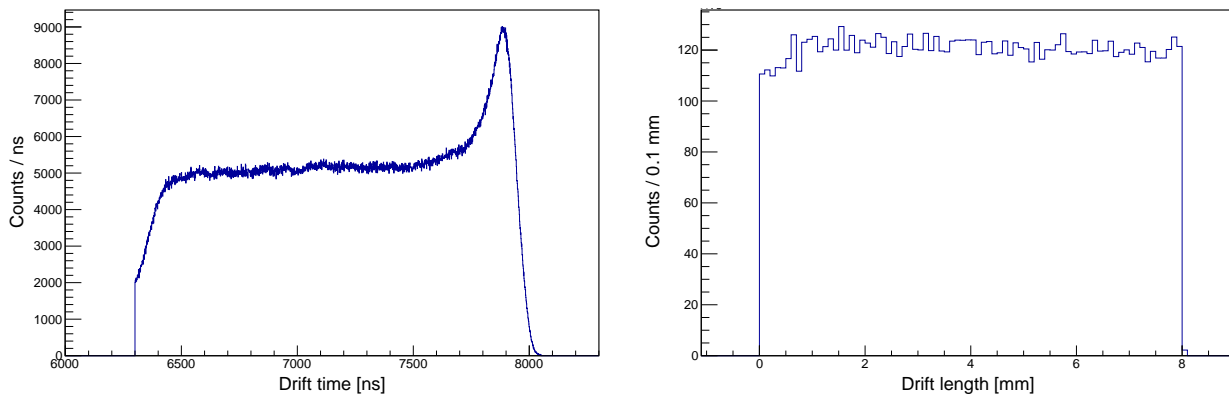


Figure 3.13: The left and right spectra display typical drift times and drift distances respectively for valid VDC events in the X1 wire plane. These events are extracted from a "white spectrum": a structureless region of the focal plane spectrum with uniformly distributed tracks

3.3.3 Wireplane Efficiency

The efficiency for each wireplane, which is to be maximised, is defined as

$$\text{Wireplane Efficiency} = \frac{\text{Number of accepted events}}{\text{Total number of events}}. \quad (3.3.1)$$

The accepted events are those that have passed a list of conditions listed in Section 3.3.8. The aforementioned HV biases for each VDC were chosen to optimise this efficiency for each wireplane. This was performed online with in-beam data before the experiment was commenced.

3.3.4 Raytracing Algorithms

The raytracing algorithm is composed of a myriad of subroutines whose primary purpose is to extract the particle trajectory with the best resolution possible. A secondary, but equally important, objective is to optimise the efficiency for each wire plane, as defined in Equation 3.3.1.

The X wire plane has vertically aligned wires and consequently provides purely horizontal information. The U wire plane possesses obliquely orientated wires, therefore yielding a combination of horizontal and vertical information. Vertical information is obtained by combining information from both the X and U wire planes. The particle of interest's trajectory is extracted from each wire chamber to ultimately calculate the particle's traversal point across each wire plane.

The subroutines of the raytracing algorithm are set out in Subsections 3.3.4.1 to 3.3.4.4 below.

3.3.4.1 Identifying the first, last and shortest drift distance wires

For a particular set of triggered wires upon a wire plane, the outermost wires are identified. The triggered wire channel that possesses the shortest drift distance is then identified for the purposes of exclusion from the raytracing algorithm. When a particle traverses a cell in close proximity to the signal wire, the induced avalanching does not yield a reliable drift distance. Exclusion of the signal wire channel with the shortest drift distance is necessary to prevent impairment of the subsequent raytracing subroutines, resulting in poorer VDC resolution.

3.3.4.2 Identifying and rectifying wires with double hits

For a particular triggered event, it is possible for a signal wire channel to observe multiple hits and to produced two or more drift times. In principle, it is not possible to completely determine which hit is uncorrelated if the drift

times are similar. This algorithm is tailored towards two regimes:

If a channel with multiple hits has a drift distance that exceeds 7.9 mm, the spurious signal/s can be identified with relative ease since the maximum possible drift distance for the geometry of the VDC detector is 8 mm.

If the associated wire was previously identified as an outermost wire (first or last), the relatively larger drift distance is accepted as the correlated signal whilst the other signals are discarded. If the corresponding signal wire is not an outermost wire, a drift distance exceeding 7.9 mm is clearly indicative of an uncorrelated signal and is therefore discarded in favour of the shorter drift distance.

If a channel with multiple hits has no drift distances that exceed 7.9 mm, the rejection of signals is more complex as there is no *a priori* method/property with which can selectively distinguish and reject uncorrelated signals. The current procedure is to discard the shorter drift distance in favour of the larger.

3.3.4.3 Identifying and fixing Z and W wire events

When a particle traverses a wire plane, it triggers a set of signal wires, resulting in a set of associated drift times (or equivalently, drift distances). These exhibit "V" type structure in the channel number versus drift time/distance plot (see Figure 3.14). This structure emerges purely from the geometry of the wire plane structure with respect to the trajectory of the traversing particle.

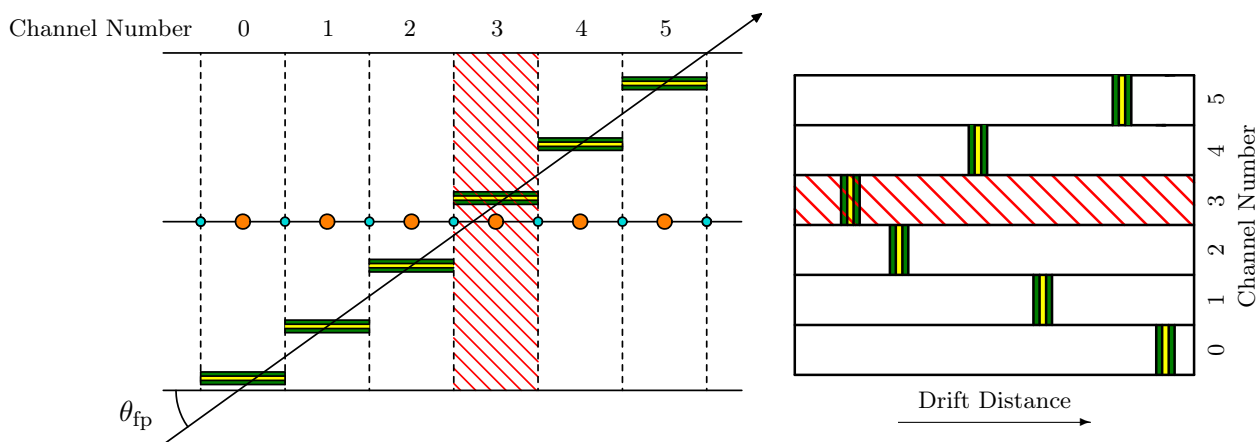


Figure 3.14: Schematic representation of a V-type wire event. The yellow lines indicate the true average distances of a traversing particle within corresponding cells. The green regions illustrate the experimental uncertainty of the drift times/distances.

Experience in the analysis of the VDC data has provided insight in recognising reoccurring artefacts which would typically result in unnecessary event rejection - to the detriment of the wire plane efficiency (see Equation 3.3.1). Two such artefacts have been identified as "Z" and "W" type wire events, whose namesakes are descriptive of their drift time/distance patterns (see Figure 3.15 and 3.16). Two new subroutines to identify and correct these artefacts were recently implemented in the data sorting code. These subroutines remove the uncorrelated triggered wire channels from a Z- or W-type event to recover a V-type event. It is currently hypothesised that the source of these particular spurious signals is purely electronic in nature, i.e. electronic noise. The data analysed for this thesis forms a significant assessment of the updated ray-tracing algorithm. The resulting improvements in efficiency are evidenced in Section 3.3.9 and Table 3.2.

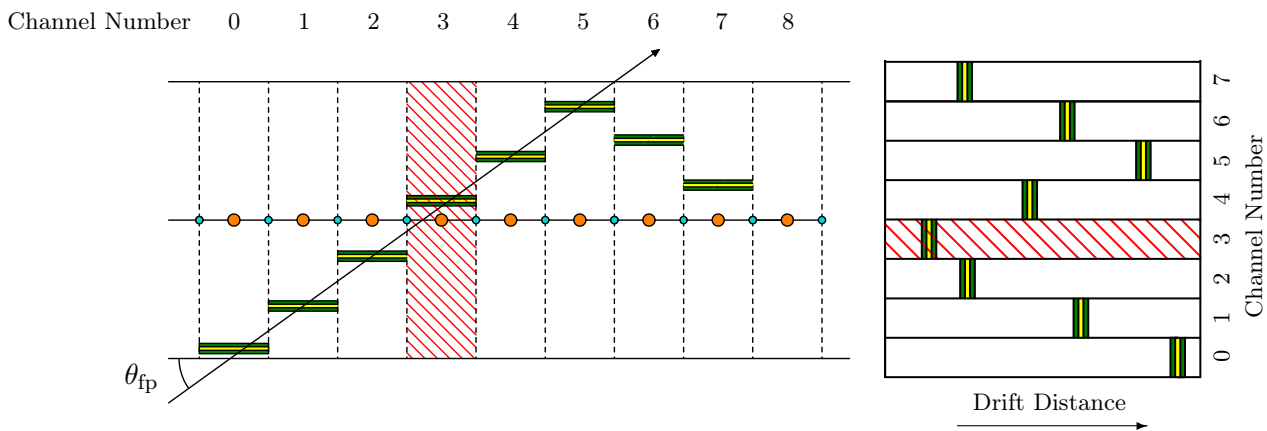


Figure 3.15: Schematic representation of a Z-type wire event. The yellow lines indicate the true average distances of a traversing particle within corresponding cells. The green regions illustrate the experimental uncertainty of the drift times/distances.

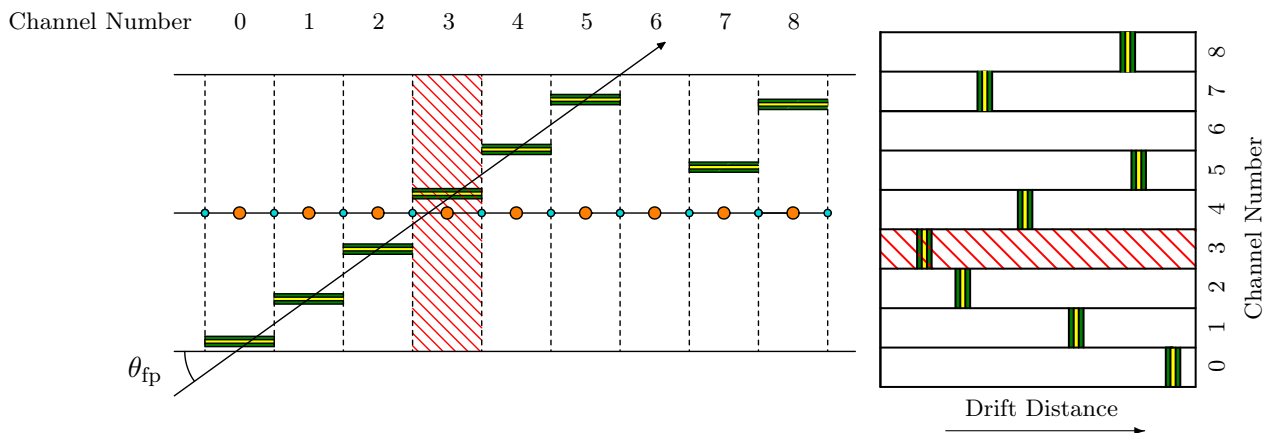


Figure 3.16: Schematic representation of a W-type wire event. The yellow lines indicate the true average distances of a traversing particle within corresponding cells. The green regions illustrate the experimental uncertainty of the drift times/distances.

3.3.4.4 Linear Least-Squares Fit

The projection of the ejectile particle's track upon the plane orthogonal to the signal wires is calculated through a linear least-squares fit. This method assumes that the traversing particle's trajectory is linear within each wire chamber. The ejectile's relatively high energy (approximately 180 MeV for this experiment), when considered with respect to the density of the gaseous detection medium, affords a negligible deviation from its initial trajectory within a wire chamber. For a particular event upon a wire plane with N total triggered wires and d_i associated drift distances, a linear regression is computed. The relevant sum of square differences, involving the drift distances and the wire positions, are denoted by S_{dd} and S_{dx} :

$$S_{dd} = \sum_i^N (d_i - \bar{d})^2 \quad (3.3.2)$$

and

$$S_{dx} = \sum_i^N (d_i - \bar{d})(x_i - \bar{x}), \quad (3.3.3)$$

where \bar{d} and \bar{x} are the average drift distances and signal wire positions respectively for a given set of triggered wire channels. The regression coefficient and offset, denoted by a and b , are given by:

$$a = \frac{S_{dx}}{S_{dd}} \quad (3.3.4)$$

and

$$b = \bar{d} - a\bar{x}. \quad (3.3.5)$$

Ultimately, this enables the calculation of the ejectile's point of traversal across the wire plane, denoted by $X1_{pos}$, $U1_{pos}$, $X2_{pos}$ and $U2_{pos}$ for the various wire planes.

3.3.5 Calculation of θ_{fp}

In principle, the regression coefficient for a wire plane can be converted to the angle between the wire plane and the projection of the ejectile track onto the plane orthogonal to the wires, defined as θ_{fp} (see Figure 3.14):

$$\theta_{fp} = \arctan(a). \quad (3.3.6)$$

A more accurate calculation method for θ_{fp} uses calculated wire plane position from both VDC, i.e. $X1_{pos}$ and $X2_{pos}$. Since the distances between $X1_{pos}$ and

$X2_{pos}$ are far greater than drift distances, θ_{fp} should be more accurate and less contingent upon the inaccuracies of track reconstruction. The preferred expression that is used to calculate θ_{fp} is given by:

$$\theta_{fp} = \arctan\left(\frac{f_0}{X2_{pos} + f_1 - X1_{pos}}\right), \quad (3.3.7)$$

where $f_0 = 515.0$ mm and $f_1 = 285.0$ mm respectively. θ_{fp} is similarly calculated for the U wire planes.

3.3.6 Vertical Position Reconstruction

The U wire planes provide the vertical information of the ejectile's track. The vertical positions of the ejectile's traversal points, across the X1 and X2 wire planes, are denoted $Y1_{pos}$ and $Y2_{pos}$ respectively. The U wires are obliquely orientated at an angle of $\theta_{Uwire} = 50^\circ$ relative to the horizontal plane.

$$Y1_{pos} = -\left(\frac{U1_{pos} \tan(\theta_{Uwire}) - g_0 \sin(\theta_{Uwire})}{\sin(\theta_{Uwire}) \tan(\theta_{fp}) - X1_{posC}}\right) \tan(\theta_{Uwire}) + g_1, \quad (3.3.8)$$

where $g_0 = 16.0$ mm and $g_1 = 26.2$ mm. $Y2_{pos}$ is similarly calculated, however it is not paramount to the analysis as $Y1_{pos}$ exhibits greater resolution. The K600 spectrometer was operated in a Y-focused mode: the quadrupole magnet focused the accepted ejectiles vertically towards the horizontal plane, as shown in Figure 3.17.

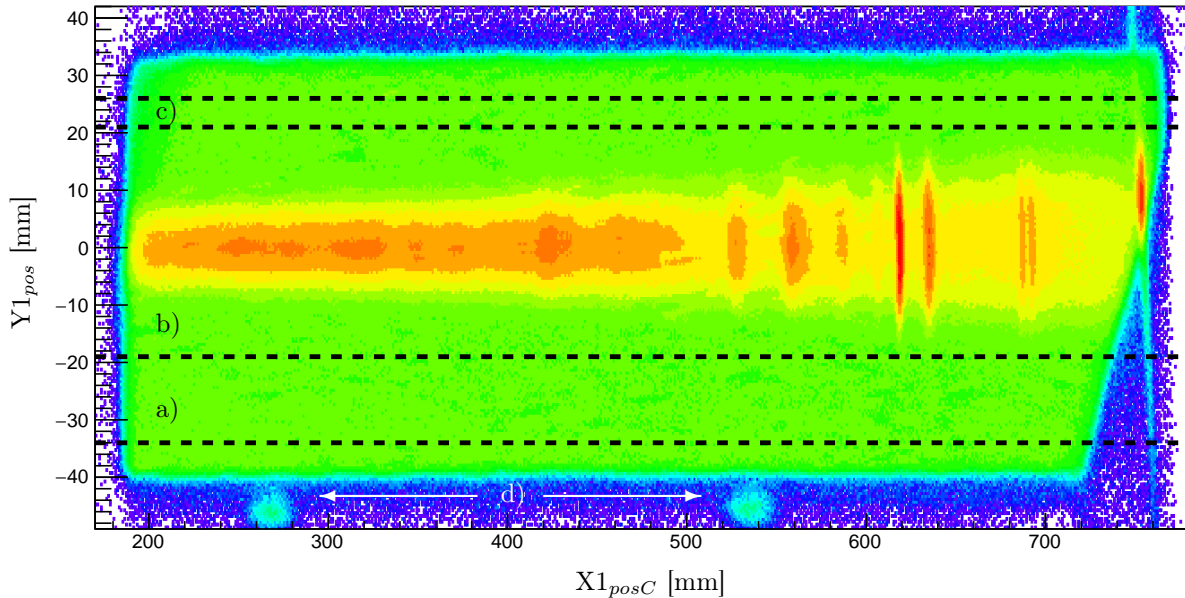


Figure 3.17: Spectrum of $Y1_{pos}$ versus $X1_{posC}$. The green uniform regions justify the assumption that multiple-scatter ejectiles possess a uniform distribution of $Y1_{pos}$ values.

Due to the ion-optics of the spectrometer, the vertical and horizontal focal planes are not aligned. This results in the dependence of vertical focusing upon the horizontal focal plane position. This is evidenced by the decrease in vertical focus with increasing values of $X1_{posC}$. This mode of focus diminishes the vertical angle resolution; the vertical angle being the component of the ejectile scattering angle out of the horizontal plane. This impairs the complete reconstruction of the ejectile trajectory. The benefit of the Y-focused mode is that it enables background subtraction. If an ejectile is correctly transported through the spectrometer, thereby retaining its correlation to the recoil nucleus, it shall traverse the focal plane within the region of vertical focus. Such ejectiles have only scattered off the target and the associated events are defined as single-scatter events, with an associated range of vertical position denoted by $Y1_{pos}^{SS}$. This range of the vertical position also contains background events: ejectiles which have scattered within the spectrometer and consequently possess no usable information pertaining to the recoil nucleus. It is assumed that such ejectiles are uniformly distributed across $Y1_{pos}$ positions and the associated events are defined as multiple-scatter events. The range of vertically focused single-scatter events, denoted $Y1_{pos}^{SS}$, is defined as:

$$Y1_{pos}^{SS} : -19.0 \text{ mm} \leq Y1_{pos} \leq 21.0 \text{ mm}. \quad (3.3.9)$$

The regions of $Y1_{pos}$ that exhibit uniformity, shown in Figure 3.18, correspond purely to multiple-scatter events and are collectively denoted by $Y1_{pos}^{MS}$. The lower and higher ranges of $Y1_{pos}^{MS}$, denoted by $Y1_{pos}^{MSl}$ and $Y1_{pos}^{MSh}$ respectively, are defined as:

$$Y1_{pos}^{MS} = \begin{cases} Y1_{pos}^{MSl} : & -34.0 \text{ mm} < Y1_{pos} < -19.0 \text{ mm} \\ Y1_{pos}^{MSh} : & 21.0 \text{ mm} < Y1_{pos} < 26.0 \text{ mm} \end{cases} \quad (3.3.10)$$

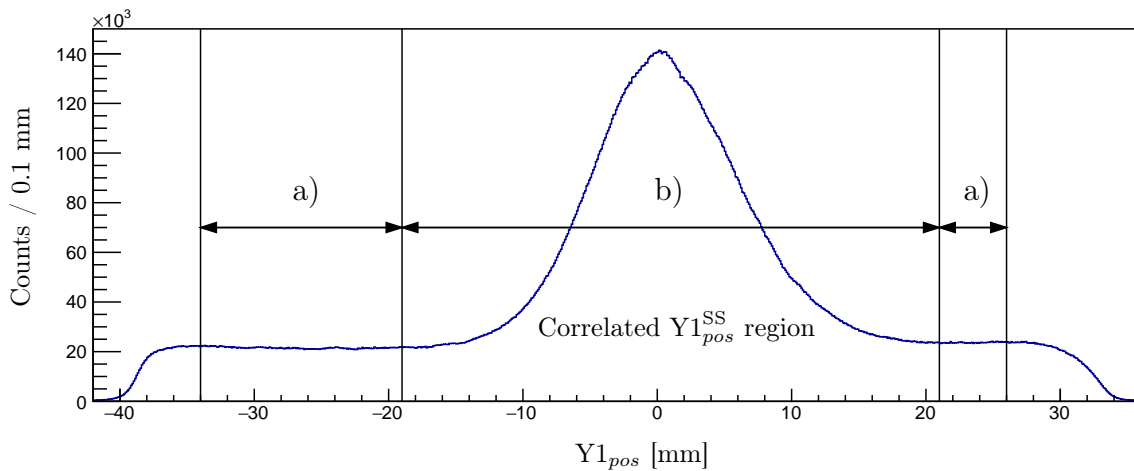


Figure 3.18: Spectrum of $Y1_{pos}$, indicating the a) $Y1_{pos}^{SS}$ single-scatter and b) $Y1_{pos}^{MS}$ multiple-scatter regions.

The focused peak of $Y1_{pos}$ values clearly lie upon a flat background. This justifies the assumption that multiple-scatter ejectiles possess a uniform distribution of $Y1_{pos}$ values. A background spectrum can be extracted by gating upon the $Y1_{pos}^{MS}$ region.

3.3.7 Partial Reconstruction of the Ejectile Kinematics

Another important quantity is θ_{SCAT} , which is defined as the angle between the projection of the ejectile momentum vector onto the horizontal laboratory plane and the beam axis (see Figure 3.19). θ_{SCAT} is calculated from the $X1_{pos}$ and $X2_{pos}$ values from the X1 and X2 wire planes:

$$\theta_{SCAT} = (h_0 X1_{pos} + h_1) \theta_{fp} + h_2 X1_{pos} + h_3, \quad (3.3.11)$$

where $h_0 = 2.28 \times 10^{-4} \text{ mm}^{-1}$, $h_1 = -1.05$, $h_2 = -1.19 \times 10^{-2} \text{ deg/mm}$ and $h_3 = 35.1 \text{ deg}$.

The ejectile scattering angle is necessary to reconstruct the momentum vector of the recoil nucleus. This is not possible for this experiment as the spectrometer was operated in a Y-focused mode, i.e. the vertical position information of the ejectile is not correlated with vertical component of the scattering angle. The vertical information is primarily used for background subtraction purposes. Whilst θ_{SCAT} is insufficient to fully reconstruct the recoil momentum vector, it remains an important observable due to its manifest correlation with the true scattering angle of the ejectile. The spectrum of θ_{SCAT} versus $X1_{posC}$ is displayed in Figure 3.20. The spectrum of θ_{SCAT} is displayed in Figure 3.21.

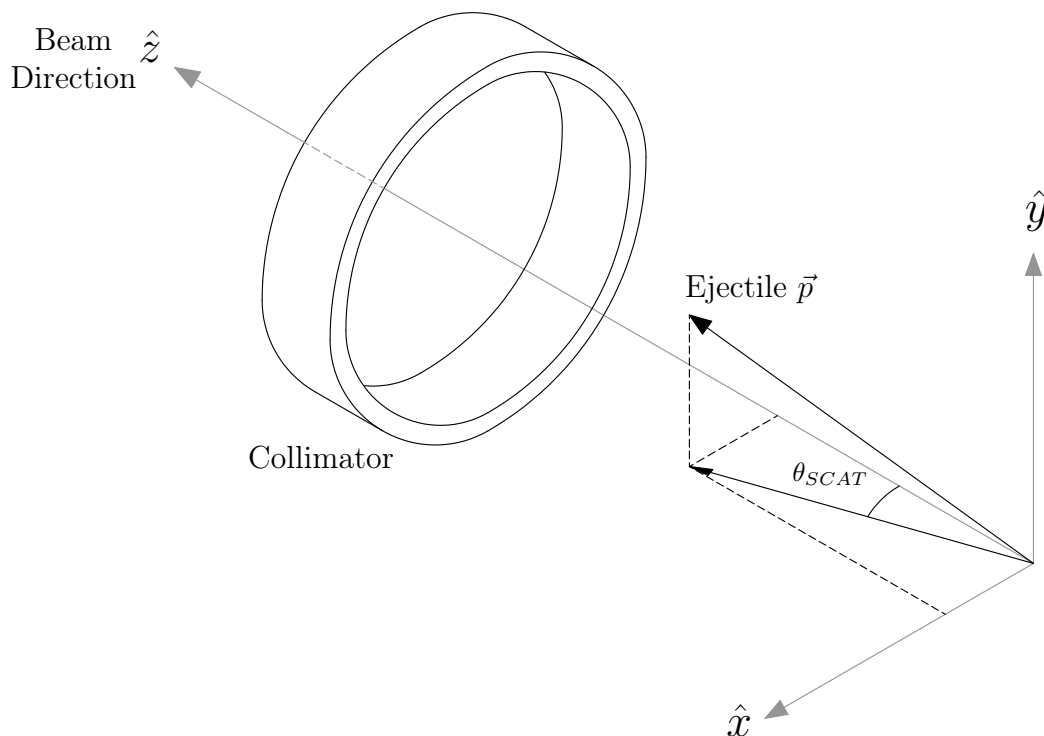


Figure 3.19: Schematic representation of θ_{SCAT} . The collimator imposes a restriction of $\pm 2^\circ$ upon the scattering angle of accepted ejectiles.

The collimator imposes a $\pm 2^\circ$ angular acceptance, centred at 0° . Consequently, valid values of θ_{SCAT} must be constrained to:

$$-2.0^\circ \leq \theta_{SCAT} \leq 2.0^\circ. \quad (3.3.12)$$

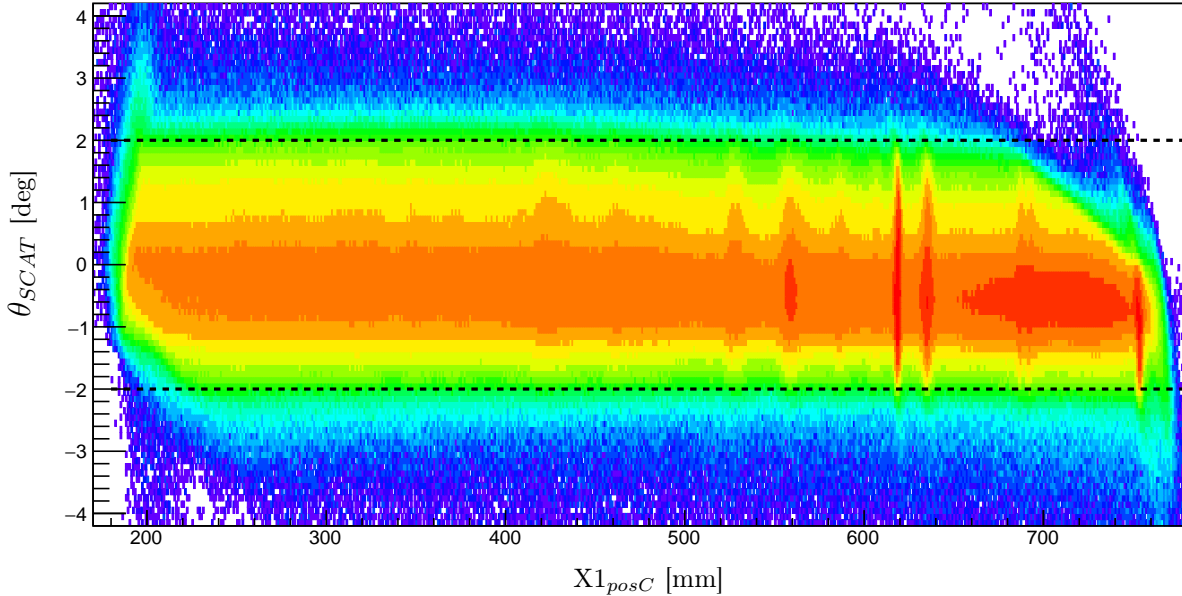


Figure 3.20: Spectrum of θ_{SCAT} versus $X1_{posC}$. The oblique discontinuities in the bottom left and top right regions of the spectrum result from the ejectile acceptance limits of the VDCs. The constraints upon θ_{SCAT} , defined in Equation 3.3.12, are indicated with the dotted lines.

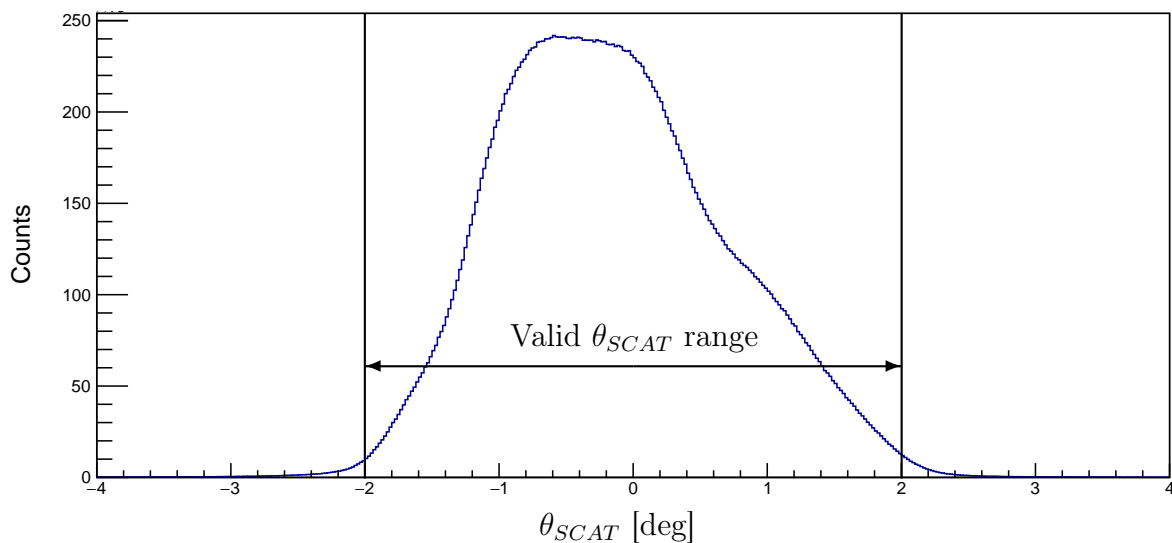


Figure 3.21: Spectrum of θ_{SCAT} . The values of θ_{SCAT} predominantly populate the valid region; the invalid values are gated out of the data analysis. The cause of the asymmetry about 0° is unknown.

3.3.8 Conditions for valid VDC events

By setting conditions upon VDC events, one is able to selectively observe the events that exhibit greater resolution whilst simultaneously discarding events with relatively poor track reconstruction. The analysis of the data is purely conducted with the events that are defined as valid. For a valid event upon a particular wire plane, the following conditions must be satisfied:

- A minimum amount of 3 triggered wires.
- A maximum amount of 8 triggered wires.
- Within a group of triggered wires, no wires can be separated by more than 3 untriggered signal wires.
- Each of the aforementioned triggered wires must yield a drift time within the valid mapping region (see Figure 3.12).

3.3.9 VDC Efficiency

The raw spectra from each wire plane, which are shown in Figure 3.22, are plotted with the valid VDC events superimposed.

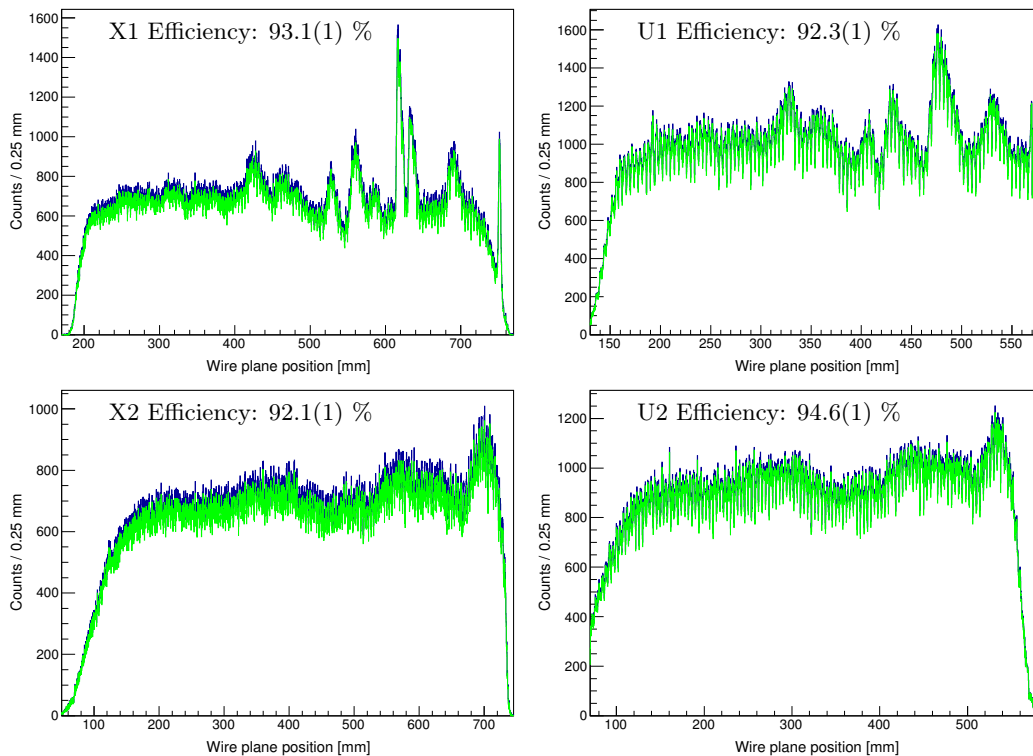


Figure 3.22: The raw and valid spectra are plotted in blue and green respectively. The cause of the fluctuations upon the uncorrected focal plane spectra are currently unknown.

The efficiency per 0.25 mm of each wire plane can also be analysed to ensure that there are no localised inefficiencies (see Figure 3.23). Any prominent deviations in the position dependent efficiency may produce artefacts/false structure in the recoil nucleus's excitation energy spectrum.

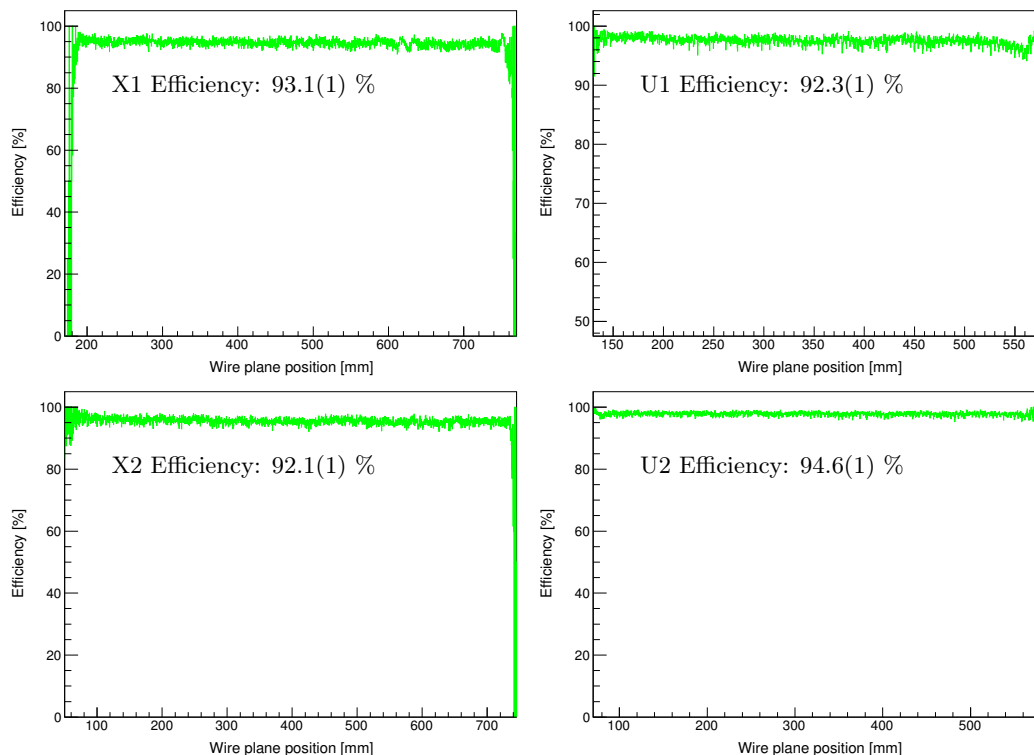


Figure 3.23: Position dependent efficiency for each wire plane.

As mentioned in Section 3.3.4.3, the corrections for the Z and W-type events have a non-negligible impact upon the wire plane efficiencies. Tabulated below are the wire plane efficiencies with and without the newly implemented routine within the raytracing algorithm.

	X1 Efficiency (%)	U1 Efficiency (%)	X2 Efficiency (%)	U2 Efficiency (%)
No Z-/W-type event correction	87.10(9)	90.0(1)	89.26(9)	91.2(1)
With Z-/W-type event correction	93.1(1)	92.3(1)	92.1(1)	94.6(1)

Table 3.2: Tabulated efficiencies of the VDC wire planes. There is a notable increase in efficiency for all wire planes with the newly implemented raytracing subroutines that correct Z- and W-type events. The errors of the efficiencies are purely of Poissonian nature.

3.3.10 Focal Plane Position Correction

The aberrations in the raw and valid wire plane positional spectra (see Figure 3.24) result primarily from θ_{SCAT} and vertical position dependence. The remaining first and second-order ion-optical aberrations that were not fully corrected by the K and H trim coils can be corrected offline with software. Additionally, the dependence of the horizontal focal plane position, $X1_{pos}$, upon the vertical position, $Y1_{pos}$, can also be corrected. It is speculated that this vertical dependence results from the fact that the quadrupole is rotated off axis (see Figure 3.4). Corrections are made to produce X1 wire plane positions which are θ_{SCAT} and $Y1_{pos}$ independent, denoted by $X1_{posC}$:

$$X1_{posC} = X1_{pos} - (i_0\theta_{SCAT}^2 + i_1\theta_{SCAT} + i_2Y1_{pos}), \quad (3.3.13)$$

where $i_0 = 0.5 \text{ mm/deg}^2$, $i_1 = 3.5 \text{ mm/deg}$ and $i_2 = 0.08$.

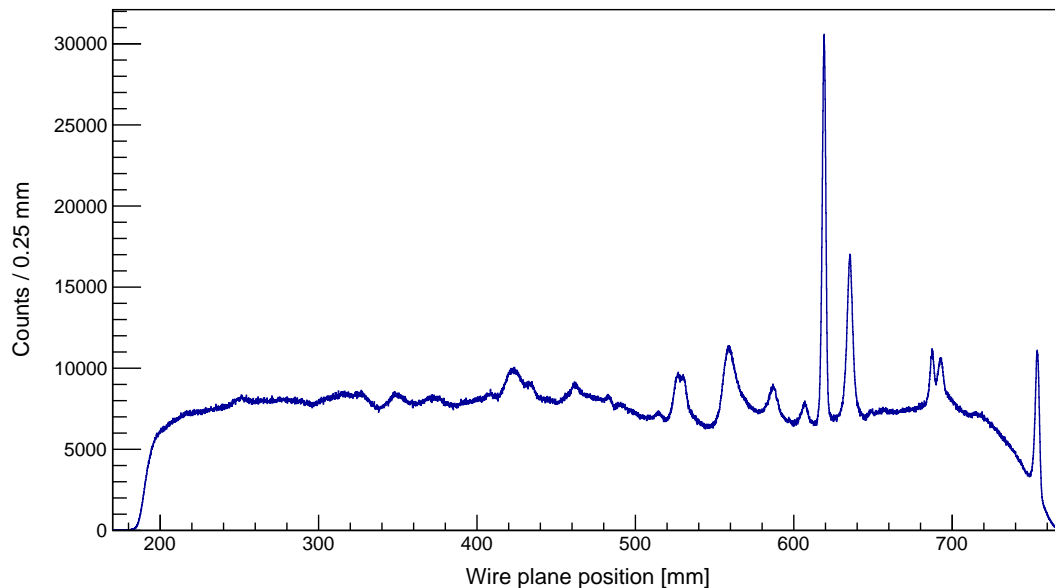


Figure 3.24: The corrected wire plane positional spectrum of the X1 wire plane.

Whilst an analogous correction can be applied upon $X2_{pos}$, this is neglected as $X1_{posC}$ typically exhibits the greatest resolution, thereby rendering $X2_{posC}$ redundant. Unless explicitly stated, all focal plane position spectra from the X1 wire plane henceforth refer to the corrected positions.

3.3.11 Plastic Scintillators (Paddles)

The plastic scintillator detectors, also referred to as paddles, form an integral part of the Focal Plane setup of the K600. The purpose of the paddles is both to trigger events and to provide particle identification capability of the ejectile. There are three available paddles with differing thicknesses of 1/8", 1/4" and 1/2". The focal plane detector system typically employs paddles in pair configurations (upstream and downstream with respect to the flight paths of ejectiles).

The choice of paddle thicknesses is dependent upon the ejectile particle of interest and the incident beam energy. Ideally, the particle of interest should reliably penetrate through the upstream paddle, providing ΔE information.

Whether the particle also penetrates the downstream paddle determines whether $\Delta E-E$ or $\Delta E-\Delta E$ information can be obtained. Due to paddle thickness limitations, it is possible that the particles of interest either do not reliably penetrate through the upstream paddle. For this experiment, the 1/4" and 1/2" thick paddles were employed as the upstream and downstream paddles, referred to paddle 1 and paddle 2 respectively. The current 0° spectrometer configuration, with the detectors mounted in the high dispersion focal plane, is restricted to this choice of paddles as they are the only scintillator detectors with vertically mounted PMTs (see Figure 3.25). The 1/8" paddle possesses horizontally mounted PMTs which cannot be mounted due to spatial limitations.

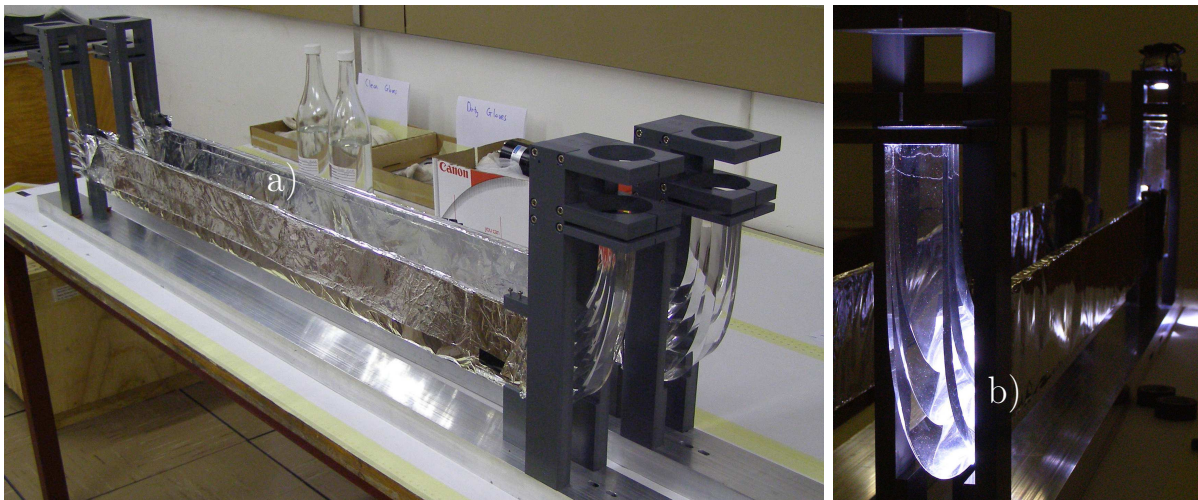


Figure 3.25: Images of the paddles during the construction stages. a) The paddles are wrapped in a layer of Mylar to ensure that the scintillator is insulated from external light sources. The right image highlights the light guides which couple the scintillators to the PMTs (which have yet to be attached). b) The PMTs are vertically mounted onto the light guides - mitigating the horizontal space restrictions of the high dispersion focal plane configuration. The 1/4" and 1/2" thick paddles were employed for this experiment.

When an ejectile traverses a paddle, the interactions that occur cause scintillation of the plastic. This light is then collected by the PMTs on either end of the detector and an electric signal - with a peak area proportional to the amount of light collected - is then sent towards a QDC module. The QDC module, with a range of 0-400 pC, then integrates the signal to provide a digital output towards the DAQ.

The time-of-flight (TOF) of the ejectile can be deduced from the triggered time of the paddle with respect to the Radio Frequency (RF) of the cyclotron. The RF signal is used as a common stop. This TOF, when coupled with the aforementioned energy deposition information, forms a highly selective particle identification (PID) method which can not only discriminate between different types of particles, but between their respective mechanisms of origin (see Figure 4.1). Crucially, the PID gate enables the suppression of background/scattered events, i.e. uncorrelated particles which have not interacted with the target and/or have scattered within the spectrometer.

3.4 The CAKE

The Coincidence Array for K600 Experiments (CAKE), shown in Figure 3.26, is comprised of 4 MMM-type double-sided silicon strip detectors (DSSSDs) manufactured by Micron Semiconductor Ltd. The mounting apparatus for the CAKE was designed with a 3D CAD programme named Solid Edge and is capable of mounting the array at both forward and backward angles with respect to the target.

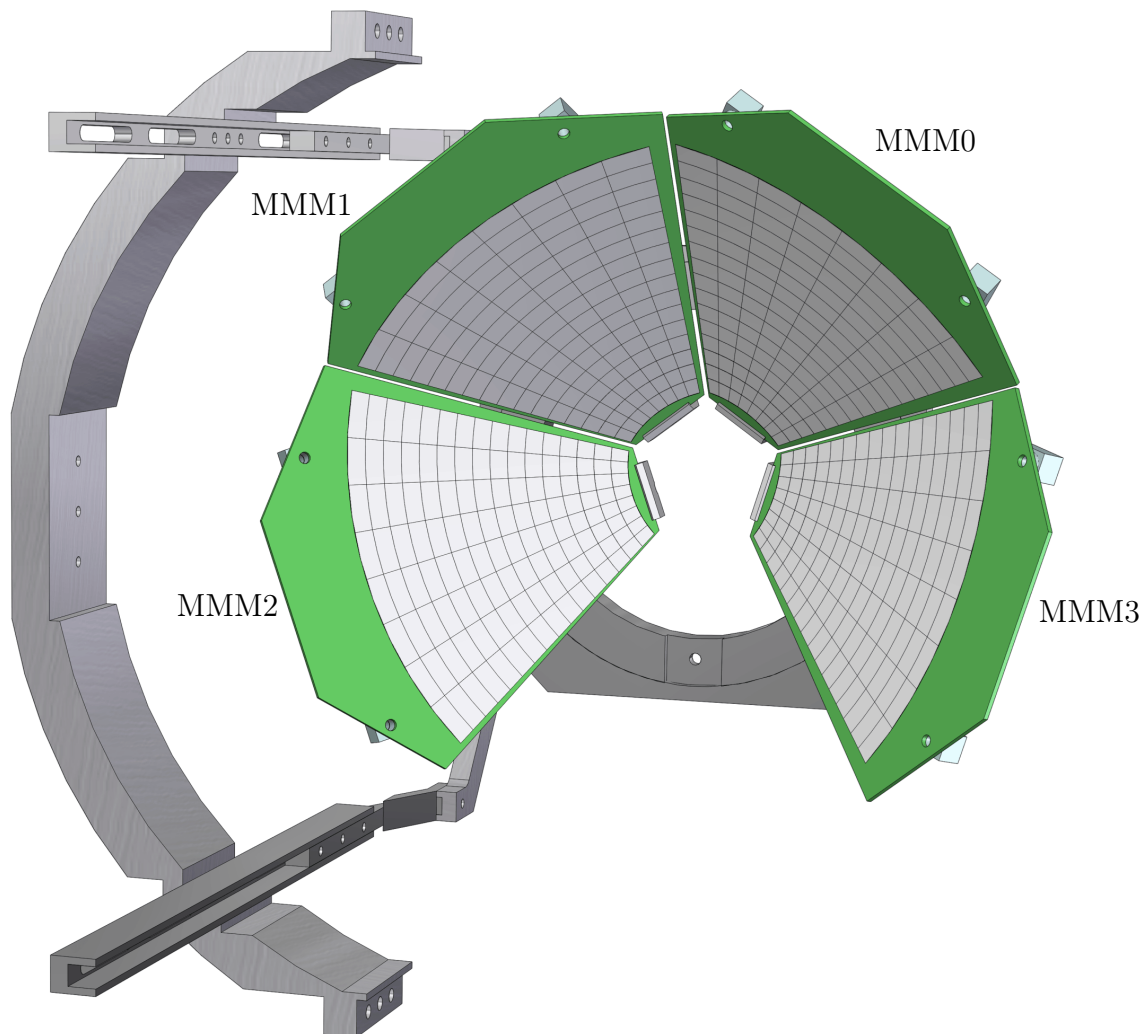


Figure 3.26: The CAKE, comprised of 4 MMM-type DSSSD detectors. The detector numbering is indicated.

3.4.1 Properties of Silicon semiconductor detectors

A semiconductor material is defined to possess an electrical conductivity between a conductor and an insulator. An n-type semiconductor material (see Figure 3.27) exhibits an electron density exceeding that of its hole density, whilst the converse is true for p-type semiconductor materials (see Figure 3.28. Pure silicon is both a poor conductor and a poor insulator. It is doped with the appropriate elements to transform it into either a n-type or p-type semiconductor, e.g. Boron and Phosphorous to create p- and n-doped silicon material respectively [40].

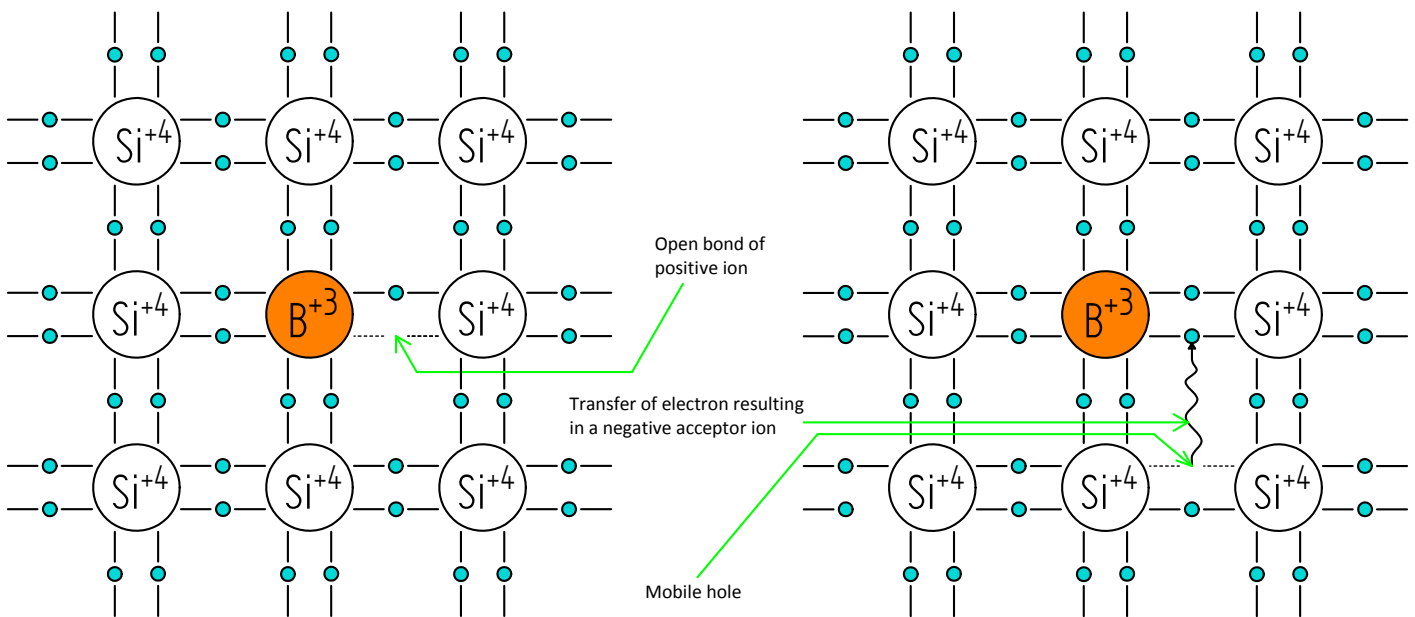


Figure 3.27: Schematic lattice structure of a p-doped silicon material

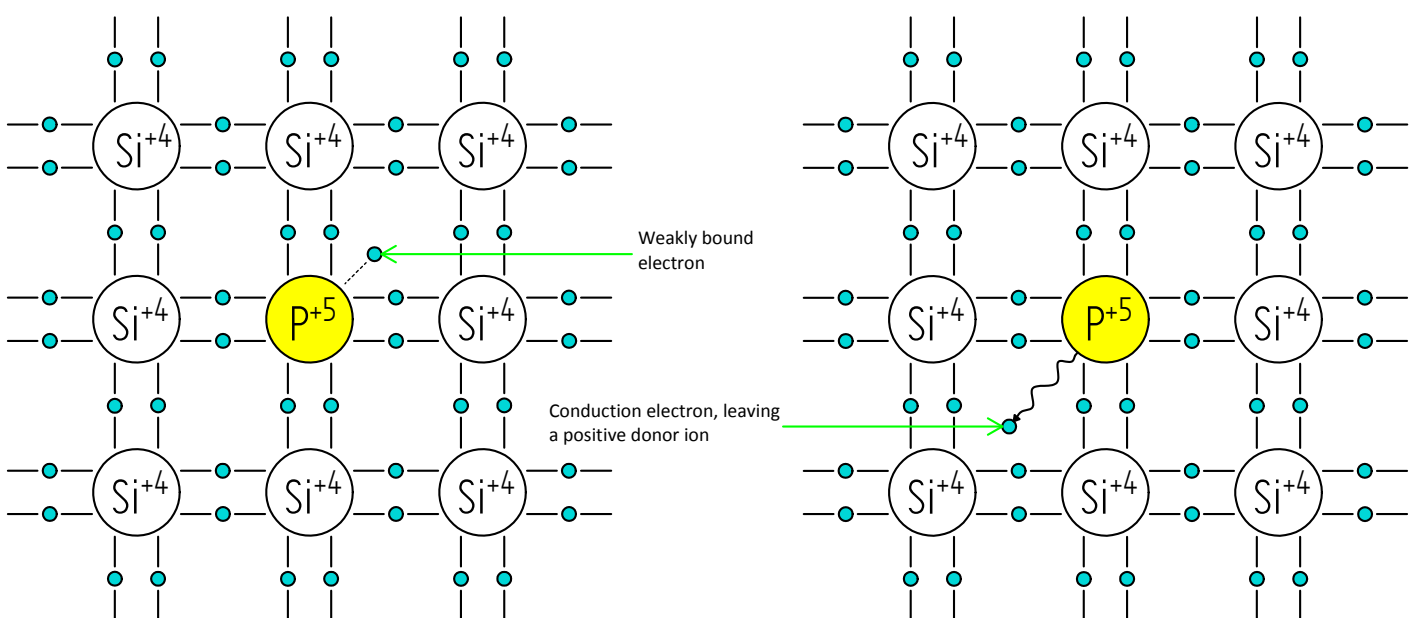


Figure 3.28: Schematic lattice structure of an n-doped silicon material

When a p-type and an n-type semiconductor are brought into contact, they form a p-n junction. The electrons in the n-doped silicon occupy the conduction band of the material, however when these electrons are attracted onto the p-doped silicon material, they occupy the valence band. A depletion zone, the region devoid of all mobile charge carriers, is formed at this junction and acts as an insulator to prevent drift current flowing across this junction. Reverse biasing (see Figure 3.29) is the process through which the p-doped side is supplied with a negative voltage and/or the n-doped side is supplied with a positive voltage. This form of biasing attracts the electrons and the electron holes towards n-doped and p-doped sides respectively, thereby increasing the size of the depletion zone (region with no charge carriers).

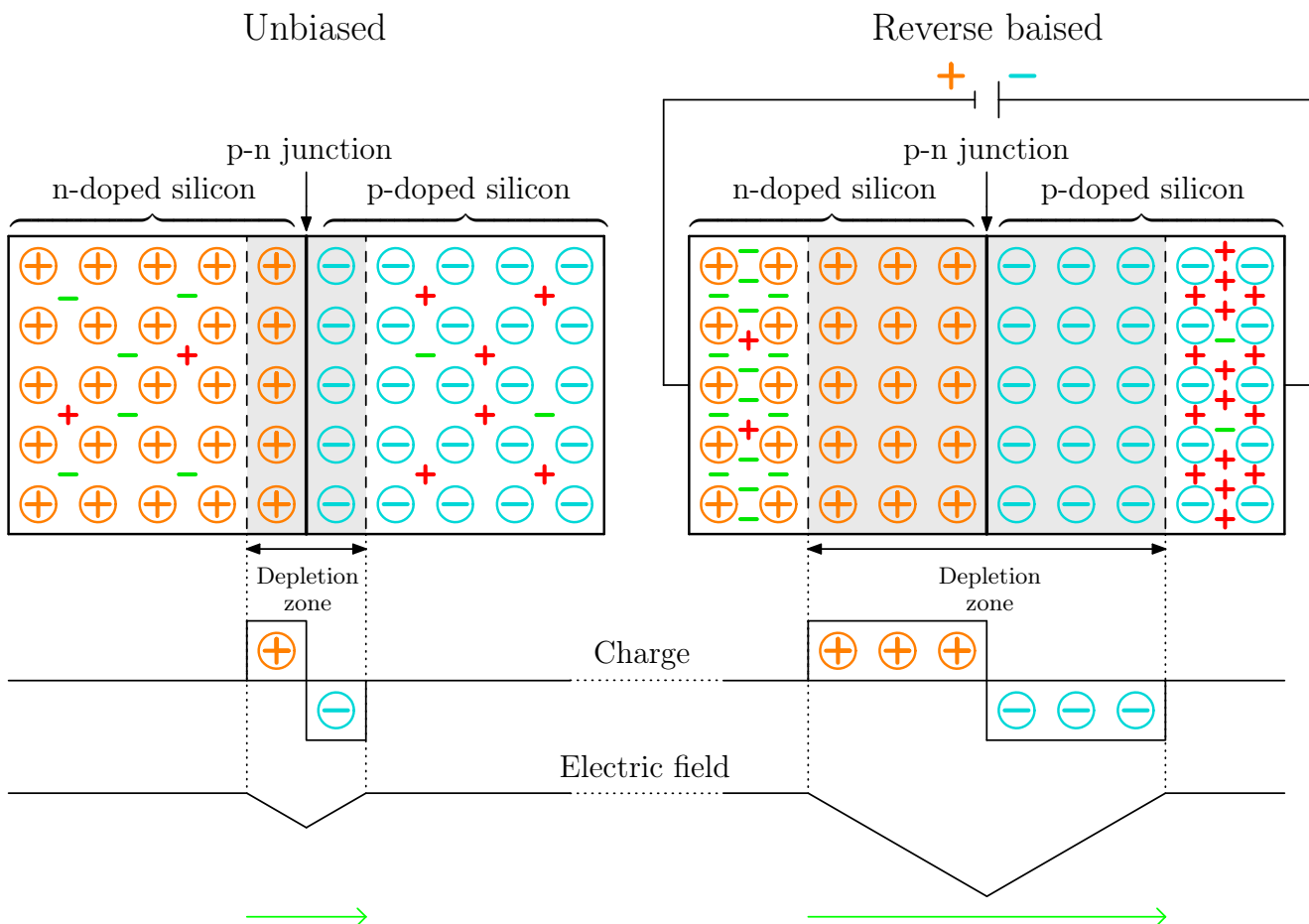


Figure 3.29: Schematic diagram of a p-n junction illustrating the increase of the depletion region with reverse biasing. The encircled orange and blue charges represent the stationary acceptor and donor ions respectively. The green and red charges represent the electron and hole charge carriers respectively. The grey regions in the n- and p-doped silicon represent the depletion zone which is devoid of charge carriers. The green arrow indicates the direction of the electric field.

3.4.2 The MMM-type DSSSDs of the CAKE

The MMM-type DSSSD detectors have 16 ring channels upon the p-side and 8 sector channels upon the n-side, with a channel mapping defined in Figure 3.30. The CAKE was mounted at backward angles within the new scattering chamber in an effort to reduce the background from scattered beam, as shown in Figure 3.31. The silicon of the DSSSDs is predominantly n-doped. The MMM-type detectors were mounted with the p-side (rings) facing the target. Since the electrons move towards the p-side, the energy resolution from the rings is superior. The MMM-type detectors were operated in the aforementioned reverse bias mode using approximately -20 V potential placed the p-side, whilst the n-side was grounded.

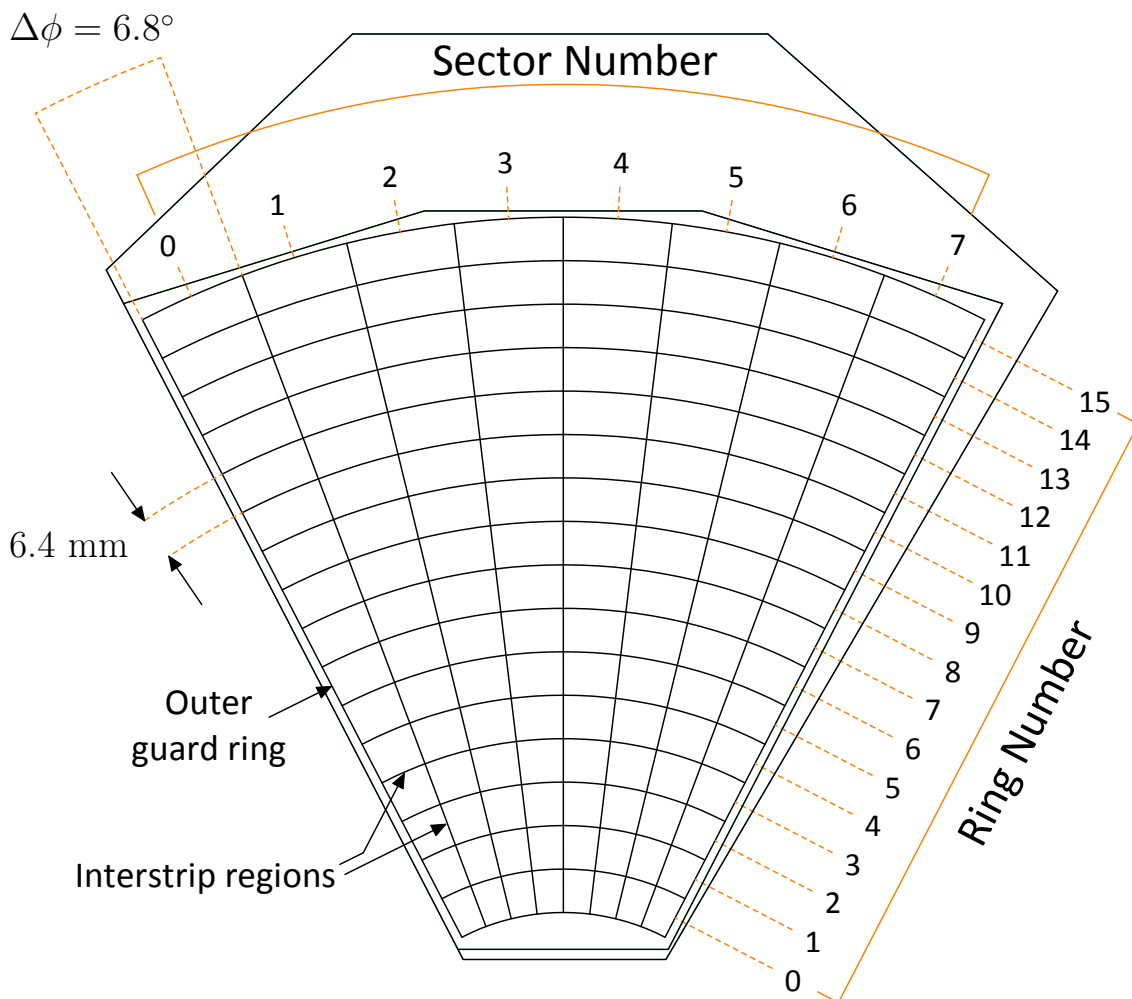


Figure 3.30: Schematic diagram of an MMM-type DSSSD detector manufactured by Micron Semiconductor Ltd.

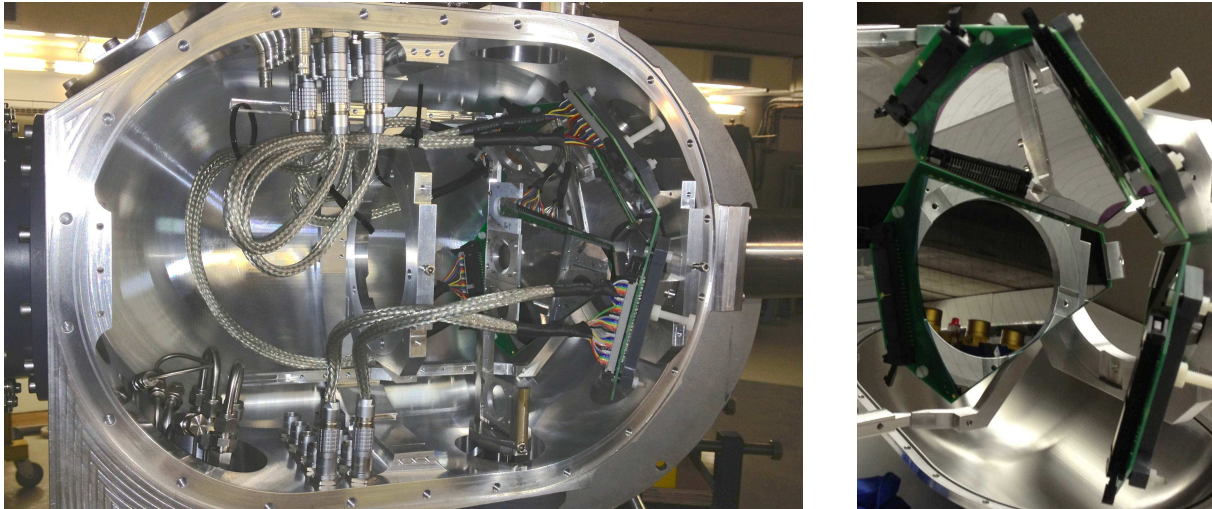


Figure 3.31: Images of the CAKE configuration employed for PR226. The left image displays the fully cabled configuration *in situ*. The right image is of the pre-mounted setup which more clearly displays the ring channels facing the target.

3.4.3 GEANT4 simulation of the CAKE

A simulation of CAKE was written in C++ with the GEANT4 simulation toolkit. The geometry of the MMM-type DSSSDs, shown in Figure 3.32, were precisely modelled from the detector drawings supplied by Micron Semiconductor Ltd. This also allows for a precise simulation of the solid angle subtended by each channel of the CAKE.

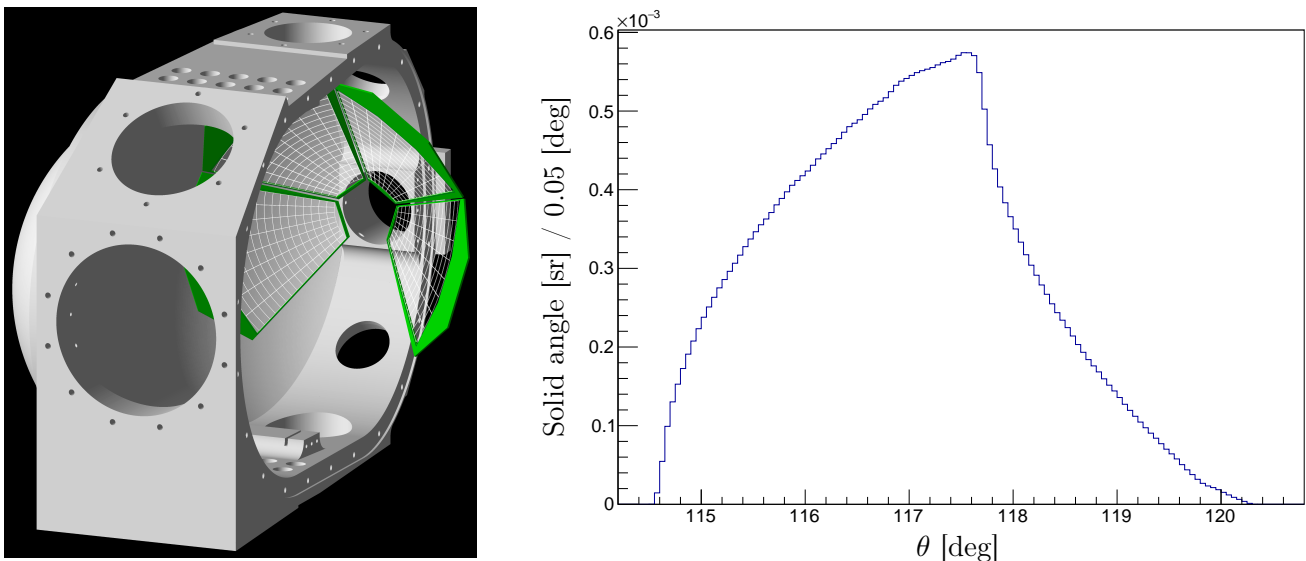


Figure 3.32: The CAKE model within the GEANT4 simulation of the K600. The left image depicts the model within the scattering chamber. The right spectrum is the simulated solid angle subtended by ring 14 of the CAKE. The total solid angle subtended by ring 14 of the CAKE is approximately 0.215 sr.

A plot of the simulated solid angles subtended by the rings of the CAKE, versus the average θ of each ring, is shown in Figure 3.33.

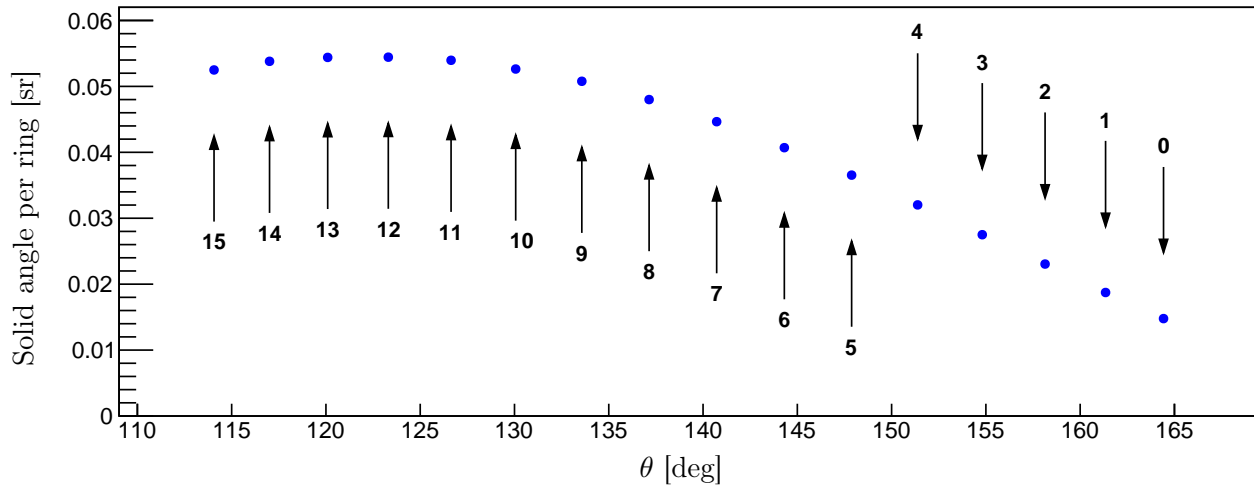


Figure 3.33: The GEANT4 simulated solid angle versus average angle of each ring in the CAKE. The ring numbers are indicated.

3.5 Target setup

The primary target was Lithium Carbonate (Li_2CO_3 with natural Lithium) which was manufactured at the target laboratory department of iThemba Labs. The relevant targets utilised in this experiment are listed below and shown in Figure 3.34.

The targets manufactured at iThemba Labs:

- The primary Li_2CO_3 target (with natural Lithium) of $510 \mu\text{g}/\text{cm}^2$ thickness upon a $50 \mu\text{g}/\text{cm}^2$ ^{12}C backing.
- An enriched $^6\text{Li}_2\text{CO}_3$ target of $460 \mu\text{g}/\text{cm}^2$ thickness upon a $50 \mu\text{g}/\text{cm}^2$ ^{12}C backing. The lithium possessed an isotopic enrichment of greater than 95% of ^6Li .
- A self-supporting Li_2CO_3 target (with natural Lithium) of $\sim 2 \text{mg}/\text{cm}^2$ thickness.

The externally manufactured targets:

- A ^{12}C target of $1 \text{mg}/\text{cm}^2$ thickness.
- A Mylar ($\text{C}_{10}\text{H}_8\text{O}_4$) target of $250 \mu\text{g}/\text{cm}^2$ thickness.

The only stable and naturally occurring isotopes of Lithium are ^6Li and ^7Li , with natural abundances of 7.5% and 92.5% respectively. Whilst the lithium background is not ideal, the associated resonances in the excitation range of interest are fortunately relatively wide, resulting in a smooth background.

An enriched $^6\text{Li}_2\text{CO}_3$ target was also produced in the knowledge that the resonances from ^6Li , in the relevant excitation range, exhibit larger widths than those from ^7Li , thereby resulting in a smoother background. This target was unfortunately destroyed whilst mounted within the scattering chamber.

The purpose of the ^{12}C target is to produce a background spectrum with which one can, in principle, remove the contribution of ^{12}C from the Li_2CO_3 spectra. In reality this process can introduce other complexities as there is a non-negligible contamination from ^{16}O (the principal nucleus of interest) on the ^{12}C target. The data from this target is rather to provide cognisance of the ^{12}C background to some qualitative degree.

The self-supporting Li_2CO_3 target possesses the benefit of a decreased ^{12}C background, however the $\sim 2 \text{mg}/\text{cm}^2$ thickness is not conducive towards coincident measurements of charged decay particles as target energy attenuation becomes non-negligible.

The main advantage of the Lithium Carbonate over the Mylar target is the 750% increase of ^{16}O relative to ^{12}C . An added benefit of Lithium Carbonate is the lack of Nitrogen contamination that is often present in Mylar.

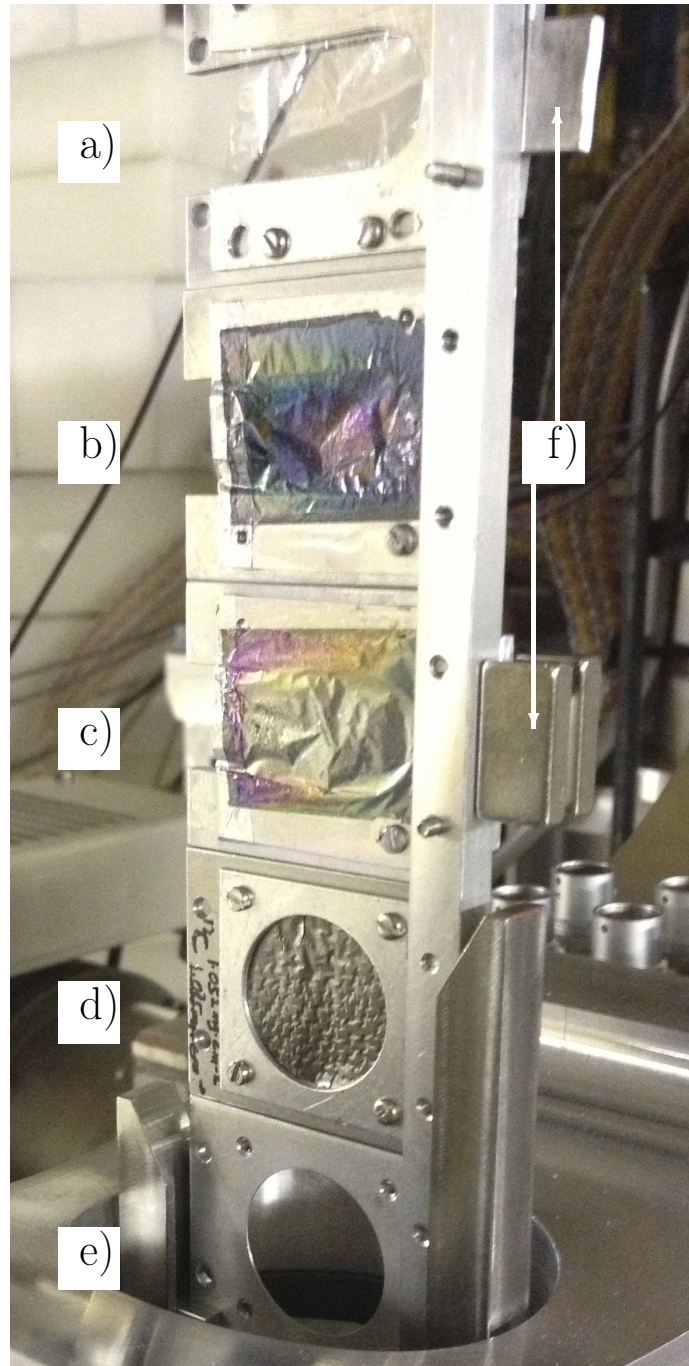


Figure 3.34: The target ladder configuration for the second weekend of PR226 consisted of: a) a $250 \mu\text{g}/\text{cm}^2$ Mylar target, b) a $460 \mu\text{g}/\text{cm}^2$ ${}^6\text{Li}_2\text{CO}_3$ target, c) a $510 \mu\text{g}/\text{cm}^2$ Li_2CO_3 target with natural Lithium and d) a $1\text{mg}/\text{cm}^2$ natural carbon target. Target position e) is the empty frame which is used to gauge background/halo events. Two pairs of magnets f) were attached at target positions a) and c) in an effort to steer electrons away from the CAKE and thereby reduce background noise.

3.6 Electronics and DAQ

3.6.1 The CAKE

When a particle impinges upon the MMM detector, it may ionise electrons in the depletion region of the silicon detector, creating electron hole pairs. Due to the electric field created by the reverse bias, the electrons migrate towards the p-type side of the junction whilst the holes migrate towards the n-type side. This migration causes a temporary net current flow which is typically observed as a signal upon a pair of ring and sector channels (other hit combinations are possible, see Section 4.4). These raw signals upon the ring channels and sector channels are amplified and relayed by the preamplifiers (see Figure 3.35) towards the MSCF-16 modules (manufactured by mesytec) and the CAEN N568B (manufactured by CAEN) modules respectively. The MSCF-16 modules provide both amplitude and timing processing capabilities whilst the CAEN N568B modules possess only amplitude processing capacity.

The 16 input channels of the each MSCF-16 module are internally duplicated: the signals upon one duplicate set of channels are processed through a constant fraction discriminator (CFD) to ultimately produce an emitter coupled logic (ECL) signal. The purpose of the CFD is to provide pulse height-independent timing whilst the ECL gives timing information. The signals upon the complementary set of duplicate channels are then shaped to provide proportionality between the output signal's amplitude and the magnitude of the raw input signal. An equivalent shaping procedure is employed by the CAEN N568B modules upon the sector channels' signals. Due to a limited number of MSCF-16 modules, timing (TDC) information is only acquired from the ring channels.

3.6.2 The HAGAR

The HAGAR is a single cylindrical NaI crystal which is coupled to 7 PMTs at the flat backside of the detector. Energy deposition of particles within the HAGAR induce scintillation of the crystal and this light output is captured by the PMTs. This induces a signal from the PMTs which is relayed through a set of preamps (one preamp per PMT output) towards a CAEN N568B module. This amplifier then produces a shaped signal with a pulse height that is proportional to the area of the input signal which is relayed to the ADC modules of the DAQ. The CAEN N568B module also outputs a duplicate set of the original unshaped input channels. These channels are then sent through a CFD, which then relays timing information to a TDC module of the DAQ.

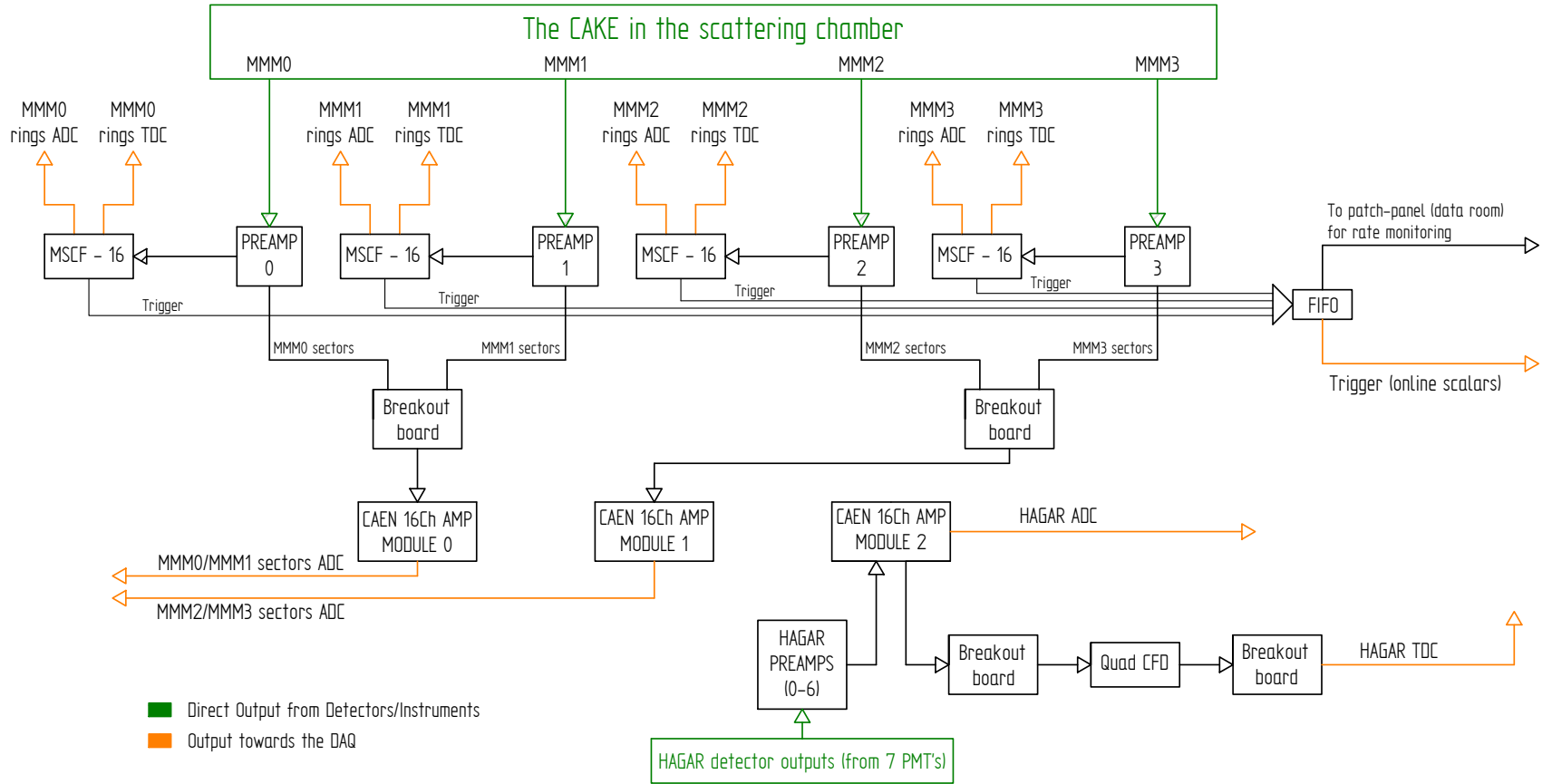


Figure 3.35: Schematic diagram of the CAKE and HAGAR electronics for PR226.

3.6.3 The focal plane detector system

Inelastically scattered protons, with an incident beam energy of 200 MeV, readily penetrate through both paddles. The inelastically scattered α particles of interest for this experiment possess approximately 180 MeV kinetic energy (for the selected excitation energy range of the spectrometer). These α particles, which possess twice the charge and four times the mass of protons, experience a relatively higher stopping power within the paddles. As a consequence, none of the available paddle thicknesses are thin enough to allow reliable penetration of the α particles. Due to this detector limitation, the triggering condition for the Focal Plane Detector System was selected to be a singular trigger upon paddle 1 as opposed to a more selective coincidence trigger between the pair of paddles. In actuality, the unabridged data collected with the singular triggering condition is preferable as any coincident triggering condition upon paddle 2 can be applied post-experiment through software gates. The DAQ is therefore triggered solely by the paddle 1 whilst the ancillary CAKE and HAGAR are slaves.

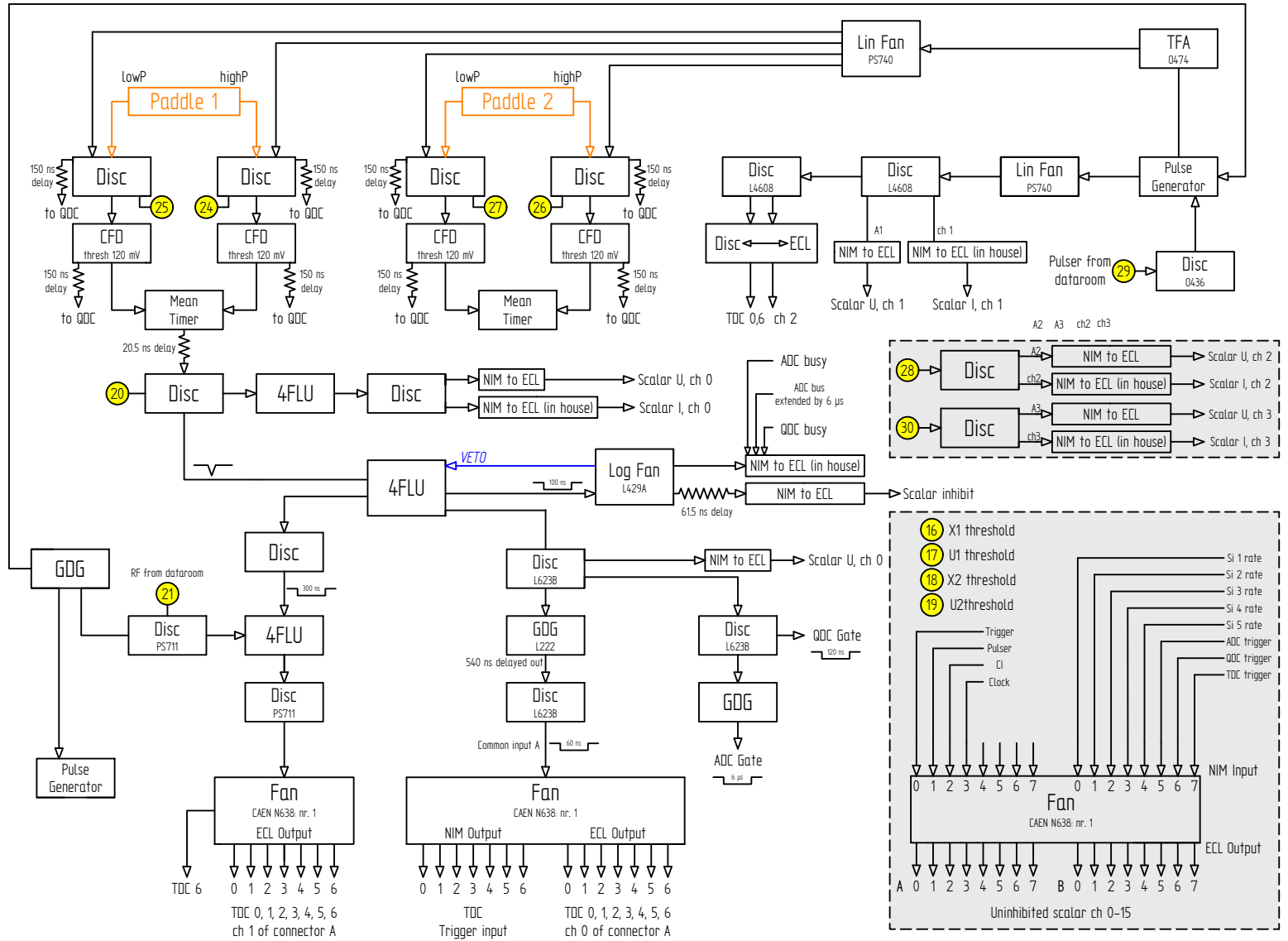


Figure 3.36: Schematic diagram of the focal plane detector system electronics for PR226.

Chapter 4

Data Analysis

Better that we should die on
our feet rather than live on our
knees

François-Noël *Gracchus* Babeuf

The data was analysed with `simsortk600`, which is a combination of two separate sort codes: `fplane` (to process the spectrometer data) and `simsort` (to process data from the ancillary detectors).

4.1 Particle Identification (PID)

A myriad of possible reactions may occur when the 200 MeV ^4He beam impinges upon the Li_2CO_3 target. In order to selectively observe the inelastically scattered α -particles from the $^{16}\text{O}(\alpha, \alpha')$ reaction, a particle-identification gate can be applied upon the data from the paddles. As discussed in Section 3.3.11, the energy deposition in the paddles is observed as the integrated charge from the PMTs. This integrated charge, which is not calibrated to energy, can be used in conjunction with the TOF of the ejectile to define PID regions of interest. Since the TOF is calculated with respect to a common stop signal provided by the RF, larger and smaller TOF values correspond to ejectiles that arrived earlier and later in time respectively.

By plotting the integrated charge from paddle 1 (denoted pad_1) against the TOF, various PID loci become apparent. Spectra for the Li_2CO_3 target and empty frame are displayed in Figures 4.1 and 4.2 respectively. The empty frame enables the estimation of background from target-unrelated beam scattering. Ideally, an empty frame should produce no events as the beam would be steered towards the 0° beam dump (see Figure 3.7). In reality, scattering of the α -particle beam still occurs from target-unrelated sources such as the internal vacuum chamber of the spectrometer; this gives rise to the events within

PID gate (a) from the empty frame, as shown in Figure 4.2. The cause of this background is primarily from a dirty beam: where a non-negligible amount of particles, within each beam packet, possess disparate momenta and/or trajectories with respect to the general distributions of the beam packet. For the Li_2CO_3 target, PID gate (a) is the predominantly populated region - confirming that this gate selects for inelastically target-scattered α -particles.

In principle, an analogous gate with the integrated PMT charge from paddle 2 (denoted pad_2) can be placed, however is not implemented since all the ejectiles do not reliably exit paddle 1 and penetrate paddle 2. By plotting the integrated charge of events within paddle 1 and paddle 2 against each other, one observes that the dominant locus extends towards 0 pC for pad_2 whilst retaining greater than 60 pC for pad_1 . This confirms the hypothesis that not all α -particles reach paddle 2. Such a gate may bias the data in an undetermined manner.

In summary, since paddle 2 is ineffective, PID gate (a) with paddle 1 (see Figure 4.1) is the only viable PID gate that provides selectivity towards observing the (α, α') reaction and is henceforth used for the entirety of the analysis.

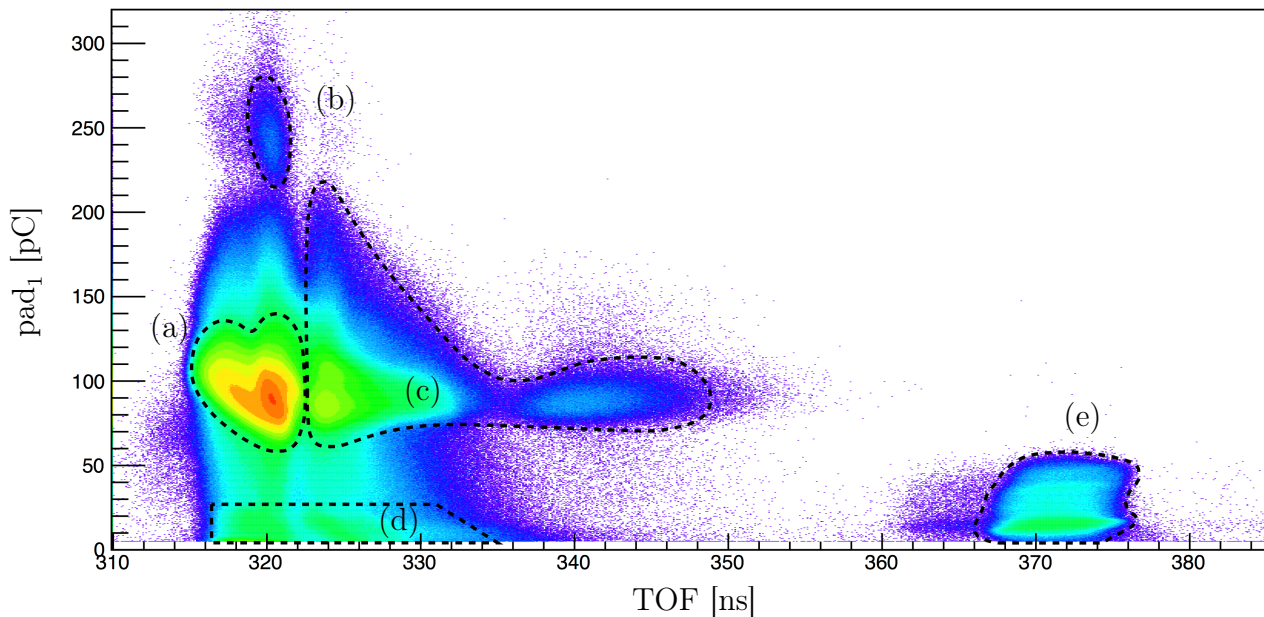


Figure 4.1: Li_2CO_3 PID spectrum: the integrated PMT charge of paddle 1 versus the TOF. Locus (a) contains inelastically scattered α -particles; the momentum of which can be used to infer the excitation energy of the recoil nucleus. Loci (b), (c) and (d) represent structures in the PID spectrum that arise from dirty beam. Locus (e) represents proton ejectiles from the (α, p) reaction

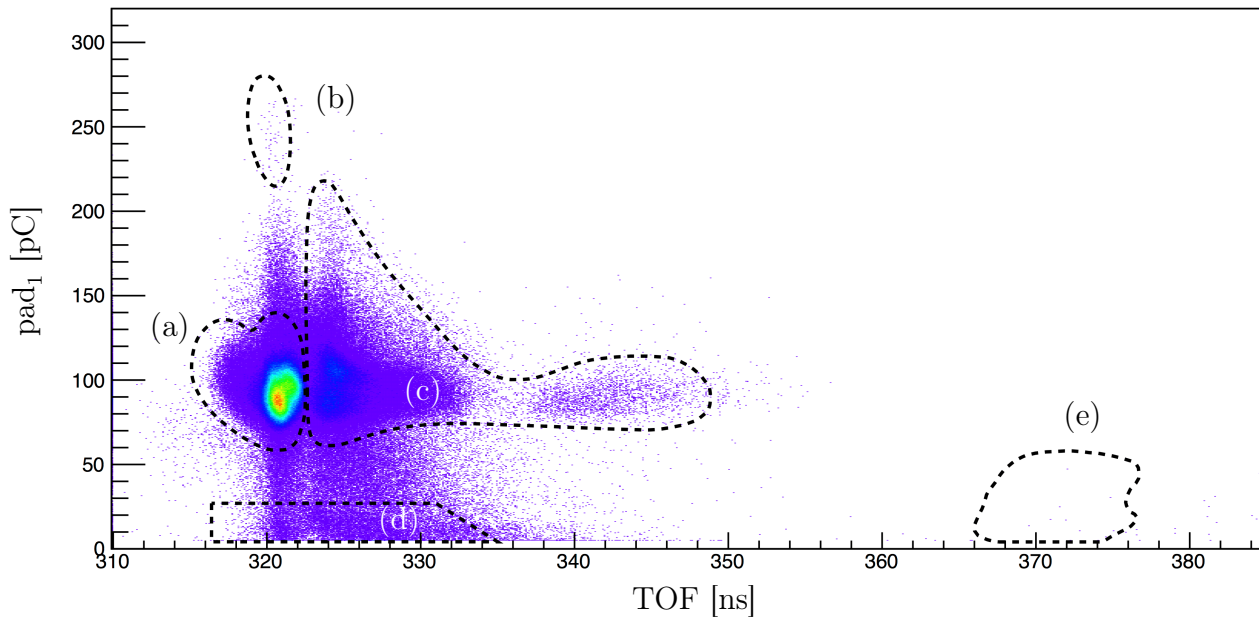


Figure 4.2: The empty frame PID spectrum: the integrated PMT charge upon paddle 1 versus the TOF. Locus (a) contains inelastically scattered α -particles which contributes to the background in the data analysis. Loci (b), (c) and (d) represent structures in the PID spectrum that arise from dirty beam. Locus (e) highlights the absence of proton ejectiles, confirming that the corresponding protons in Figure 4.1 originate from the target.

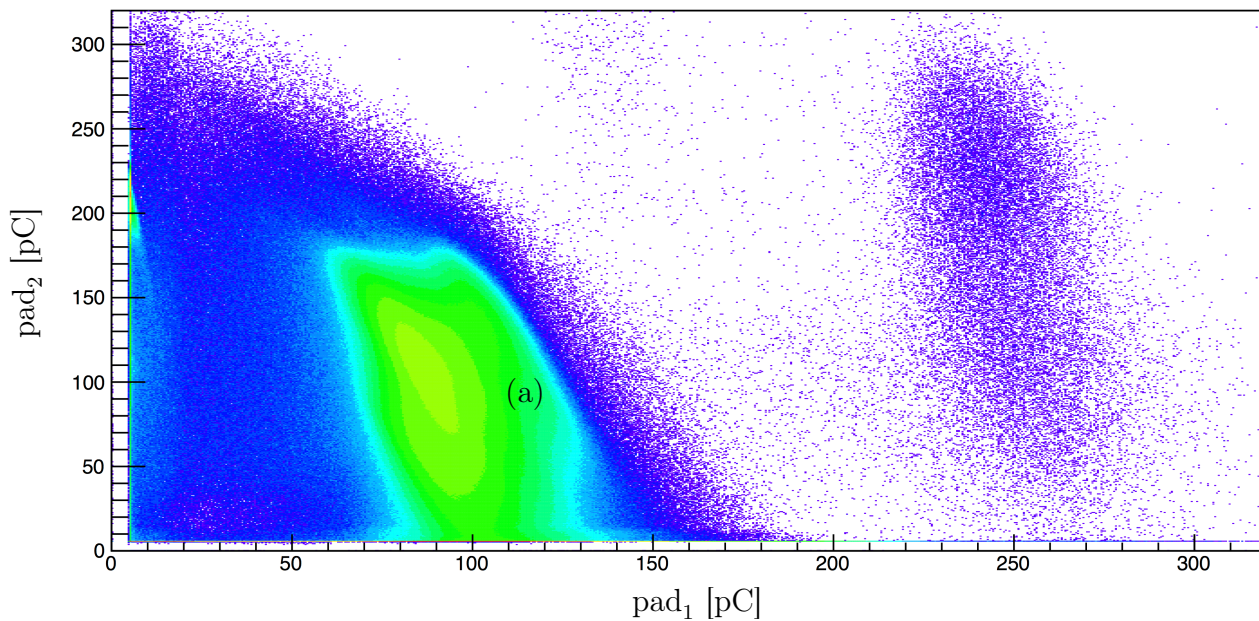


Figure 4.3: Spectrum of the integrated PMT charges from paddle 1 against those from paddle 2. The locus labelled (a) correspond to α -particle ejectiles

4.2 Focal Plane Calibration

The ion-optics of the spectrometer separates ejectiles on the basis of their rigidity, $B\rho$, defined as

$$B\rho = \frac{p}{q} \quad (4.2.1)$$

where p and q are the linear momentum and the charge of the particle respectively and ρ is the gyroradius of the charged particle's circular motion under a uniform magnetic field B .

The corrected X1 wire plane position, $X1_{posC}$ (see Section 3.3.10), reflects the rigidity of the ejectile. Since only inelastically scattered α -particles are selected, the charge dependency is irrelevant and the wire plane position is directly interpreted in terms of momentum. By calibrating the wire plane position to momentum, the excitation energies of recoil nuclei can be inferred.

A relativistic binary kinematics code was written to calculate the associated ejectile energies (at 0°) of known and relatively well-resolved resonances in the $X1_{posC}$ spectrum. An uncertainty in the energy of a resonance directly translates to an uncertainty on the momentum of the scattered ejectile. The resonance energy uncertainties and spin-parities are summarised in Table 4.1 [41]. A fit is employed which takes into account both the energy uncertainty and the positional uncertainty (from the $X1_{posC}$ fit) of each selected resonance. The ion-optics of the spectrometer, coupled with the planar geometry of the focal plane, produce a second order dependence of momentum with focal plane position [42]. The calculated momentum of the ejectile, p_{ejec} , is accordingly fitted with a function of the form:

$$p_{ejec} = d_2 X1_{posC}^2 + d_1 X1_{posC} + d_0. \quad (4.2.2)$$

The fit converges with a reduced $\chi_{reduced}^2$ value of 1.61 (see Figure 4.4) and the parameters are determined to be: $d_2 = -1.30(2) \times 10^{-5}$ MeV/c/mm², $d_1 = 1.230(2) \times 10^{-1}$ MeV/c/mm and $d_0 = 1.12720(7) \times 10^3$ MeV/c. The fit is displayed in Figure 4.4 whilst the associated residual energies are displayed in Figure 4.5.

Resonance label	Energy [MeV]	J^π
(a)	20.945(20)	1^-
(b)	17.197(17)	2^+
(c)	14.926(2)	2^+
(d)	12.440(2)	1^-
(e)	12.049(2)	0^+
(f)	11.520(4)	2^+
(g)	9.8845(5)	2^+

Table 4.1: The energies and spin-parities of the resonances used for momentum calibration of the focal plane [41].

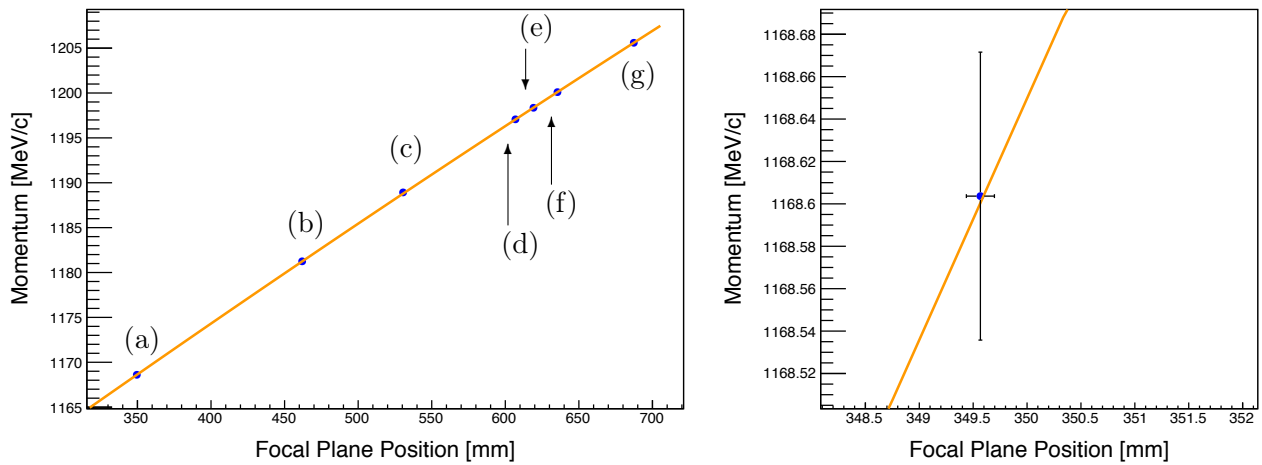


Figure 4.4: The second-order polynomial fit that maps the corrected focal plane position ($X1_{posC}$) to ejectile momentum. The right spectrum emphasises the errors upon both axes for each calibration point, which are present but indiscernible in the left spectrum. The labelled states are summarised in Table 4.1. The displayed errors for the momentum and focal plane position correspond to the standard deviation of Gaussian distribution.

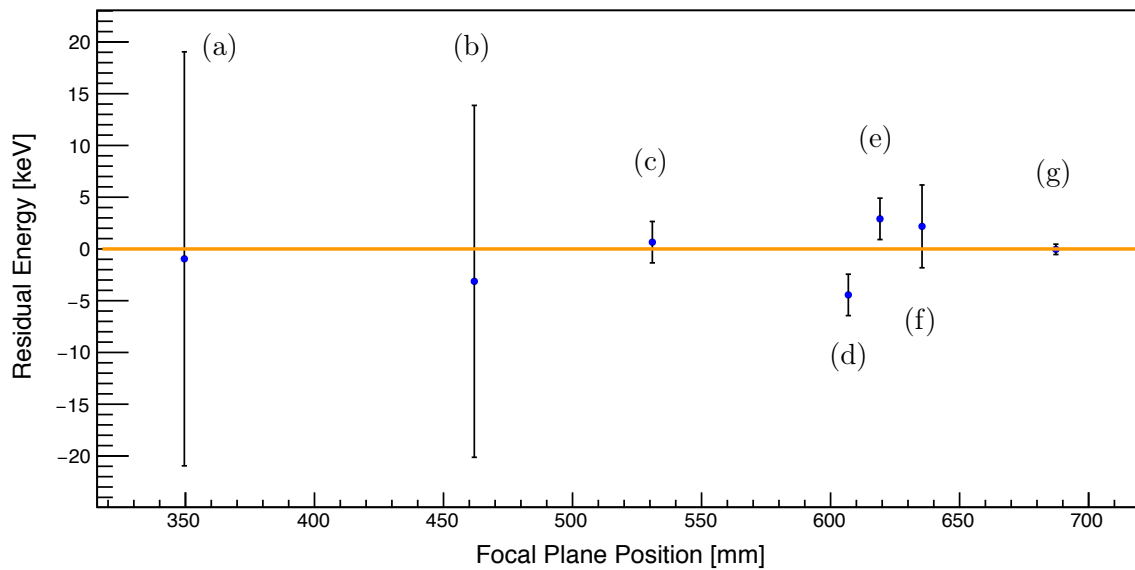


Figure 4.5: The residual energies of the focal plane momentum calibration. The labelled states are summarised in Table 4.1. The displayed errors correspond to the uncertainties (standard deviation) of resonance energies within literature [41] and are of Gaussian distribution.

The resonances selected for momentum calibration of the focal plane are highlighted in Figure 4.6 and summarised in Table 4.1.

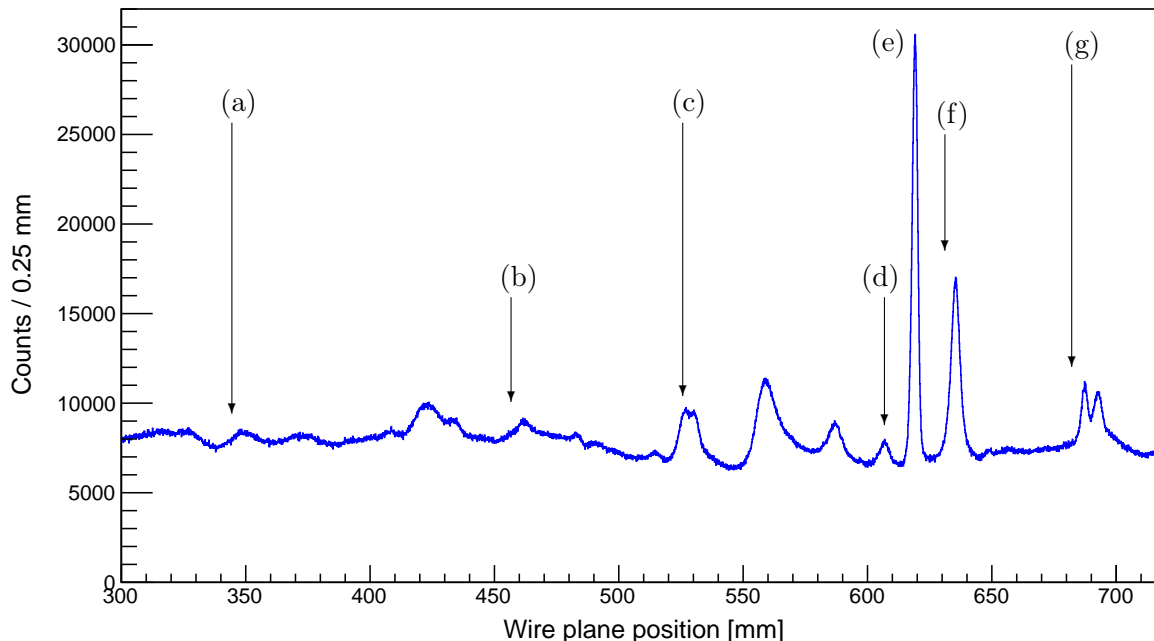


Figure 4.6: The corrected wire plane positional spectrum of the X1 wire plane from the Li_2CO_3 target, indicating the resonances selected for calibration.

Relativistic binary kinematics dictates that if the masses and energies of the projectile, target nucleus and ejectile are known, the excitation energy of the recoil can be directly determined [43]. In the following formalism, the projectile, target, ejectile and recoil nuclei are denoted as particles 0, 1, 2 and 3 respectively. Given a stationary target and a beam energy of T_0 , the initial energy of the system is given by $E_{init.}$:

$$E_{init.} = E_0 + m_1c^2 = T_0 + (m_0 + m_1)c^2. \quad (4.2.3)$$

The energy conservation of the reaction can be expressed as

$$E_{init.} + Q = E_2 + E_3 + E_x = E_{tot.} + E_x, \quad (4.2.4)$$

where $Q = (m_0 + m_1 - m_2 - m_3)c^2$, E_x is the excitation energy of the reaction products and $E_{tot.}$ is the sum of the kinetic and mass energies of the reaction products. E_x can be directly interpreted as the excitation energy of the recoil nucleus as an α -particle ejectile is highly unlikely to be excited from $^{16}\text{O}(\alpha, \alpha')$ at 200 MeV. Moreover, the excited states of the α -particle have lifetimes which are of the order of picoseconds, which prevent any such excited α -particles from reaching the focal plane before decaying.

Momentum conservation yields the following constraints:

$$p_0 = p_2 \cos \theta_2 + p_3 \cos \theta_3 \quad (4.2.5)$$

and

$$0 = p_2 \sin \theta_2 - p_3 \sin \theta_3, \quad (4.2.6)$$

where θ_2 and θ_3 are the polar scattering angles of the ejectile and the recoil nucleus respectively. Algebraic manipulation provides a second order equation in E_2 :

$$\begin{aligned} E_2^2 (4p_0^2 c^2 \cos^2 \theta_2 - 4E_{tot.}^2) + E_2 (4E_{tot.}^3 - p_0^2 c^2 E_{tot.} + 4m_2^2 c^4 E_{tot.} - 4m_3^2 c^4 E_{tot.}) \\ + (2p_0^2 c^2 E_{tot.}^2 - 2m_2^2 c^4 E_{tot.}^2 + 2m_2^2 c^4 p_0^2 c^2 + 2m_3^2 c^4 E_{tot.}^2 - 2m_3^2 c^4 p_0^2 c^2 \\ + 2m_3^2 c^4 m_2^2 c^4 - E_{tot.}^4 - p_0^4 c^4 - m_2^4 c^8 - m_3^4 c^8 - 4m_2^2 c^4 p_0^2 c^2 \cos^2 \theta_2) = 0. \end{aligned} \quad (4.2.7)$$

which is simply solved with the general solution of a quadratic equation. The energy of the recoil, E_3 , can now be calculated in terms of E_2 :

$$E_3 = E_{tot.} - E_2, \quad (4.2.8)$$

which ultimately allows the calculation of the excitation energy of the recoil nucleus, E_x :

$$E_x = E_0 + E_1 + Q - E_2 - E_3. \quad (4.2.9)$$

This calculation of E_x was implemented in the data sorting code to produce excitation energy spectra of the recoil nucleus (see Figure 4.7).

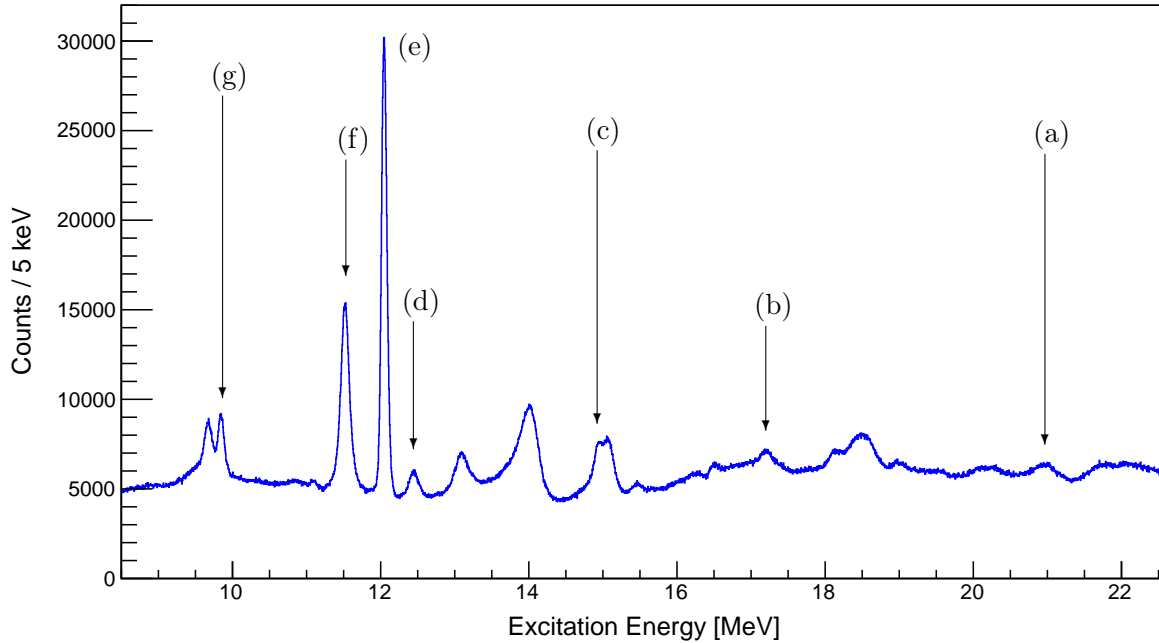


Figure 4.7: Excitation energy of the recoil nucleus for the Li_2CO_3 target. The labelled states are summarised in Table 4.1.

4.3 The Singles Focal Plane Spectra

A spectrum exclusively composed of valid focal plane events is referred to as a singles spectrum. A raw singles spectrum, which has no background subtraction, can be generated by gating upon the single-scatter regions of vertical position in the focal plane (as discussed in Section 3.3.6). There are three primary sources of background for the singles spectra: the multiple-scatter events, the dirty beam and nuclei within the target which are not of interest (i.e. ${}^6\text{Li}$, ${}^7\text{Li}$ and ${}^{12}\text{C}$).

A total background singles spectrum for each target can be generated by gating on the multiple-scatter regions of the vertical position, denoted $Y1_{pos}^{MS}$. As defined in Equation 3.3.10, $Y1_{pos}^{MS}$ is composed of two regions: $Y1_{pos}^{MSl}$ and $Y1_{pos}^{MSh}$, each providing two separate spectra, the combination of which is used for background extraction. A linear fit is then employed upon such a spectrum to extract a background function, which is then subtracted from the raw singles spectrum. This eliminates the need for direct histogram subtraction, mitigating the introduction of noise and artefacts into the background-subtracted spectrum. The Poissonian errors of the raw spectrum, together with the Poissonian and fitting errors from the background function, are propagated to the background-subtracted spectrum.

To qualitatively estimate the background from the dirty beam, the singles spectrum of the empty target is studied. The primary target of interest is Li_2CO_3 . Whilst the target offers a relatively high content of ${}^{16}\text{O}$, the background from ${}^6\text{Li}$, ${}^7\text{Li}$ and ${}^{12}\text{C}$ is non-negligible. To gauge the background from these various nuclei, the data from the ${}^{12}\text{C}$ and Mylar targets were also analysed.

4.3.1 The Li_2CO_3 Target

The background spectra for the Li_2CO_3 target, generated by gating upon different regions of vertical position upon the focal plane, are displayed in Figure 4.8. The background-subtracted singles spectrum from the Li_2CO_3 is displayed in Figure 4.9. The total background spectrum indicates that the uncorrelated scattered ejectiles form a smooth linear background beneath the raw singles spectrum. The state labelled (a) upon the background-subtracted spectrum, with an intrinsic width of 1.5(5) keV, lies upon a significant amount of underlying events in the focal plane spectrum. Since these underlying events remain after background subtraction, it is postulated that they are valid and physical, i.e. not originating from a systematic background. This can be confirmed with analysis of the empty frame singles spectra. The primary source of these underlying events is deduced with the analysis of the Mylar target singles spectra.

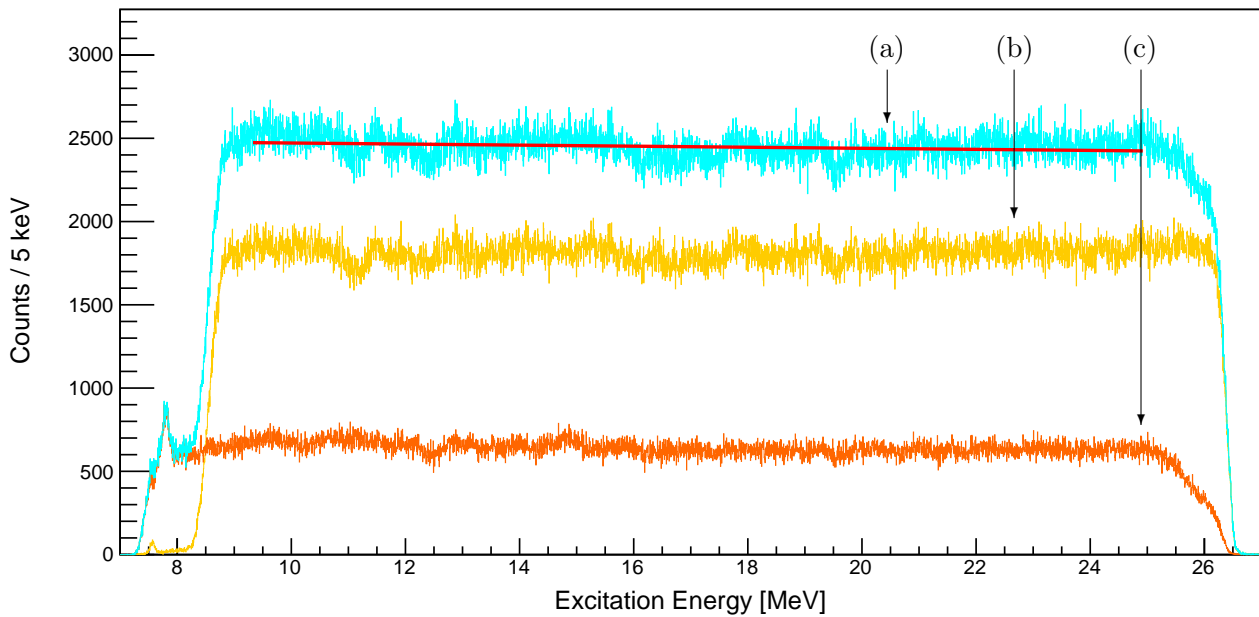


Figure 4.8: Singles background spectra of the Li_2CO_3 target. Label (a) indicates the total background spectrum: the summation of the spectra labelled (b) and (c), which correspond to gates upon $Y1_{pos}^{MSl}$ and $Y1_{pos}^{MSh}$ respectively. The linear background fit, with a reduced $\chi^2_{reduced}$ value of 1.41, is displayed in red.

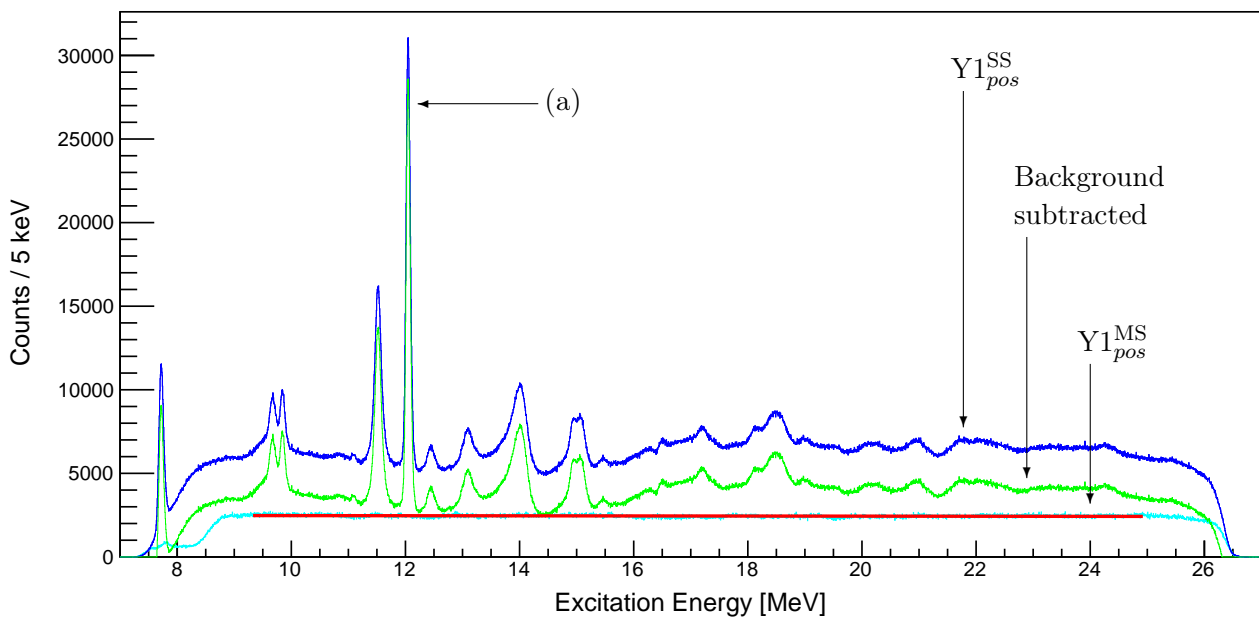


Figure 4.9: The raw (dark blue), total background (light blue) and background-subtracted (green) singles spectra for the Li_2CO_3 target. Label (a) indicates the 12.049 MeV state in ^{16}O , with an intrinsic width of 1.5(5) keV. The linear background fit, with a reduced $\chi^2_{reduced}$ value of 1.41, is displayed in red.

4.3.2 The Empty Frame

The background subtraction method employed for the focal plane singles spectra can be evaluated by analysing the empty frame data. The background spectra for the empty frame are displayed in Figure 4.10. The empty frame provides no target nuclei for the projectile to scatter off. Ideally, the empty frame data should therefore yield no counts in the focal plane, however due to the aforementioned dirty beam, scattering off target-unrelated sources (e.g. the target ladder) does populate the focal plane with events.

In principle, the background subtraction should eliminate the events, producing an empty spectrum. As shown in Figure 4.11, the background-subtracted spectrum of the empty frame is uniform across the focal plane and has a mean value of ~ 0 . This confirms that the background subtraction method with the $Y1_{pos}^{SS}$ and $Y1_{pos}^{MS}$ gates, defined in Section 3.3.6, is effective in removing the background events corresponding to ejectiles which have scattered from non target-related sources (multiple scatter ejectiles). It is concluded that the substantial amount of underlying events, in the background-subtracted spectrum of the Li_2CO_3 target (see Figure 4.9), are valid and physical in nature.

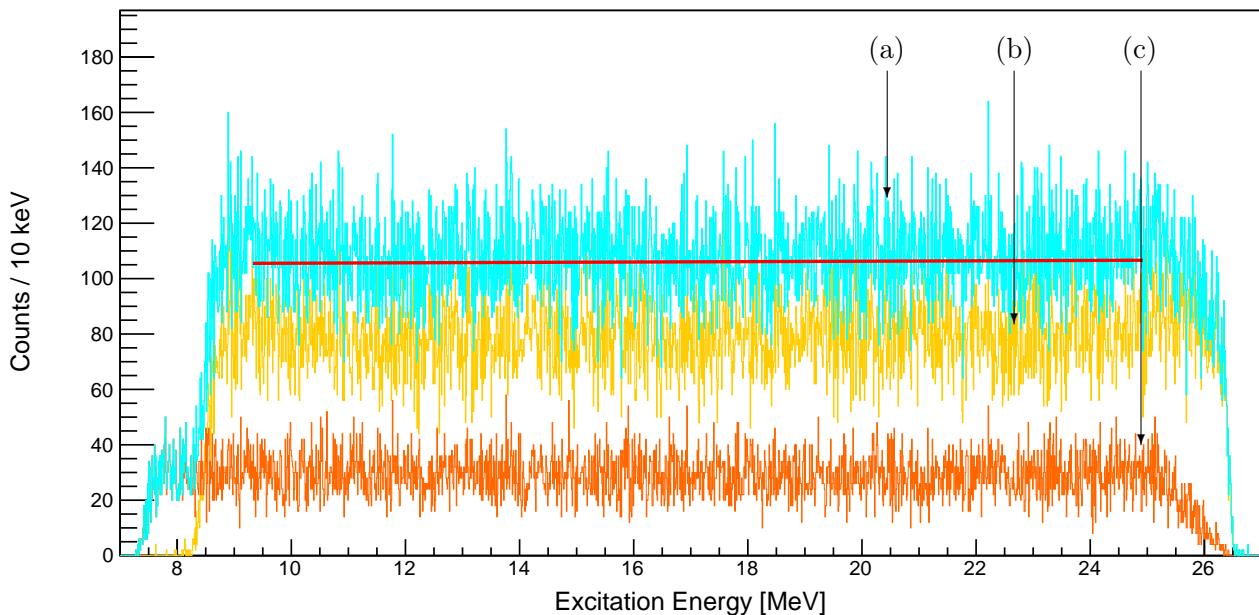


Figure 4.10: Singles background spectra of the empty frame. Label (a) indicates the total background spectrum: the summation of the spectra labelled (b) and (c), which correspond to gates upon $Y1_{pos}^{MS}$ and $Y1_{pos}^{SS}$ respectively. The linear background fit, with a reduced $\chi_{reduced}^2$ value of 1.03, is displayed in red.

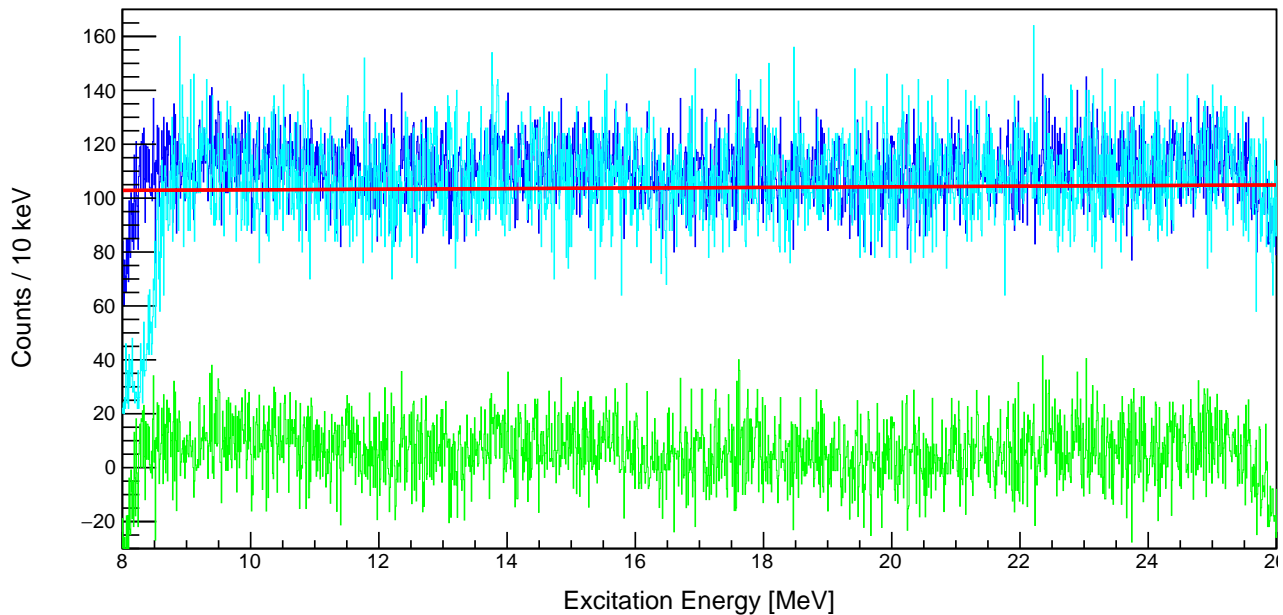


Figure 4.11: The raw (dark blue), total background (light blue) and background-subtracted (green) singles spectra for the empty frame. The linear background fit, with a reduced $\chi^2_{reduced}$ value of 1.03, is displayed in red.

4.3.3 The Mylar Target

The singles focal plane spectra of Mylar provide insight into the ${}^6\text{Li}$ and ${}^7\text{Li}$ background within the Li_2CO_3 spectra. The background spectra for the Mylar target are displayed in Figure 4.12.

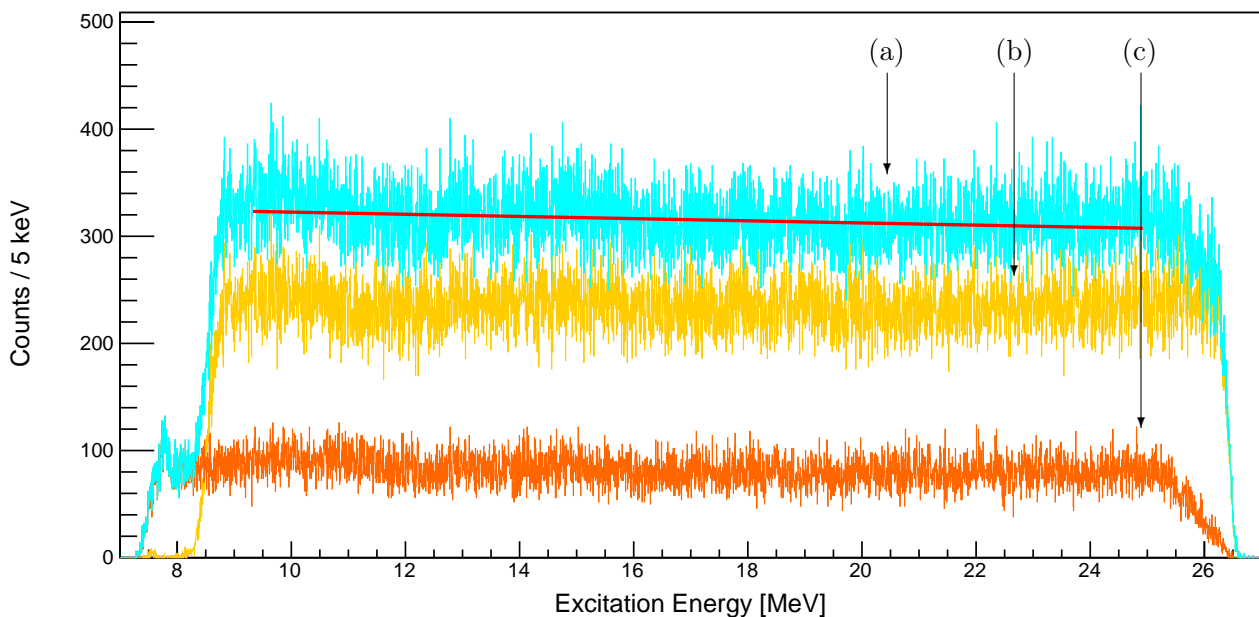


Figure 4.12: Singles background spectra of the Mylar target. Label (a) indicates the total background spectrum: the summation of the spectra labelled (b) and (c), which correspond to gates upon $Y1_{pos}^{MSl}$ and $Y1_{pos}^{MSh}$ respectively. The linear background fit, with a reduced $\chi^2_{reduced}$ value of 1.06, is displayed in red.

The state labelled (a) in the background-subtracted spectrum of Mylar (see Figure 4.13) appears to be relatively well-resolved from all other focal plane events in comparison to the equivalent state in the Li_2CO_3 spectrum (see Figure 4.9). The substantial decrease of underlying events in this excitation region is due to the lack of ${}^6\text{Li}$ and ${}^7\text{Li}$ in Mylar. It is therefore necessary to account for the resonances of ${}^6\text{Li}$ and ${}^7\text{Li}$ when fitting the focal plane spectra of Li_2CO_3 .

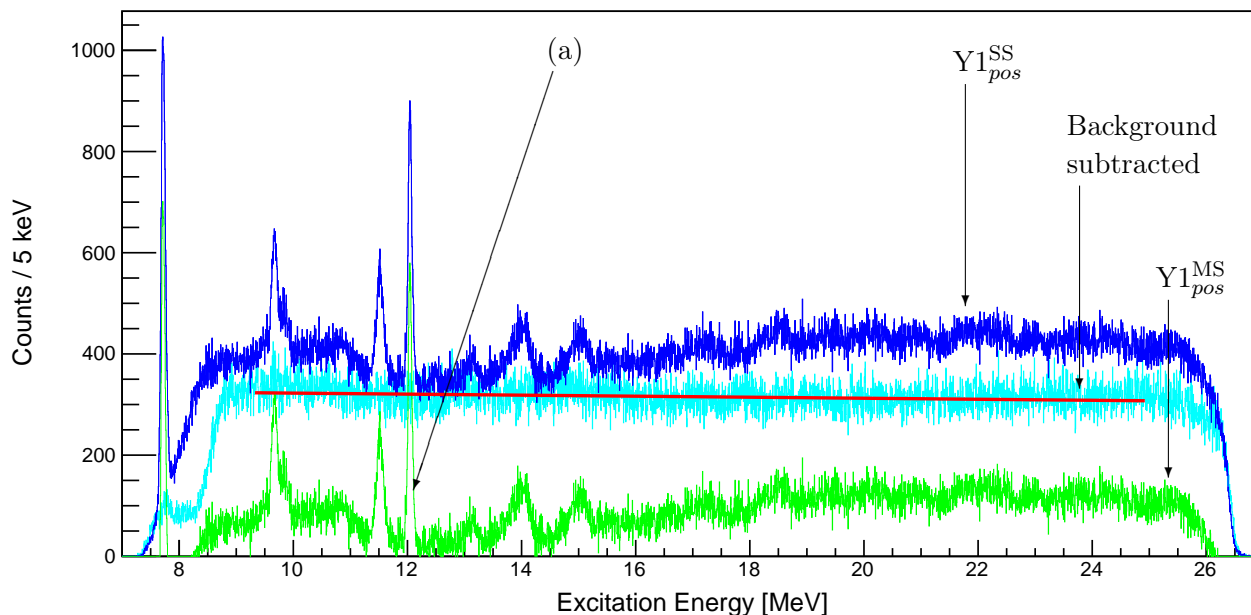


Figure 4.13: The raw (dark blue), total background (light blue) and background-subtracted (green) singles spectra for the Mylar target. Label (a) indicates the 12.049 MeV state in ${}^{16}\text{O}$, with an intrinsic width of 1.5(5) keV. The linear background fit, with a reduced $\chi^2_{reduced}$ value of 1.06, is displayed in red.

4.3.4 The ${}^{12}\text{C}$ Target

The singles focal plane spectra of the ${}^{12}\text{C}$ target provides insight into the ${}^{12}\text{C}$ background within the Li_2CO_3 spectra. The Li_2CO_3 target was created upon a $50 \mu\text{g}/\text{cm}^2$ ${}^{12}\text{C}$ backing. The background spectra for the ${}^{12}\text{C}$ target are displayed in Figure 4.14. The ${}^{16}\text{O}$ resonance that is observed upon the background-subtracted spectrum of ${}^{12}\text{C}$ target, 4.15, indicates ${}^{16}\text{O}$ contamination. Direct subtraction of the ${}^{12}\text{C}$ target spectra for the Li_2CO_3 is therefore problematic since ${}^{16}\text{O}$ is the target nucleus of interest. The data from this target is a measurement of the ${}^{12}\text{C}$ background to some qualitative degree.

The background-subtracted spectrum of the ${}^{12}\text{C}$ target is superimposed on the equivalent spectrum from Li_2CO_3 in Figure 4.16. It is observed that ${}^{12}\text{C}$ forms a relatively smooth background within the Li_2CO_3 focal plane spectra,

especially in the region of interest around 15 MeV. A direct histogram subtraction of the normalised ^{12}C target spectrum can be employed, shown in Figure 4.17.

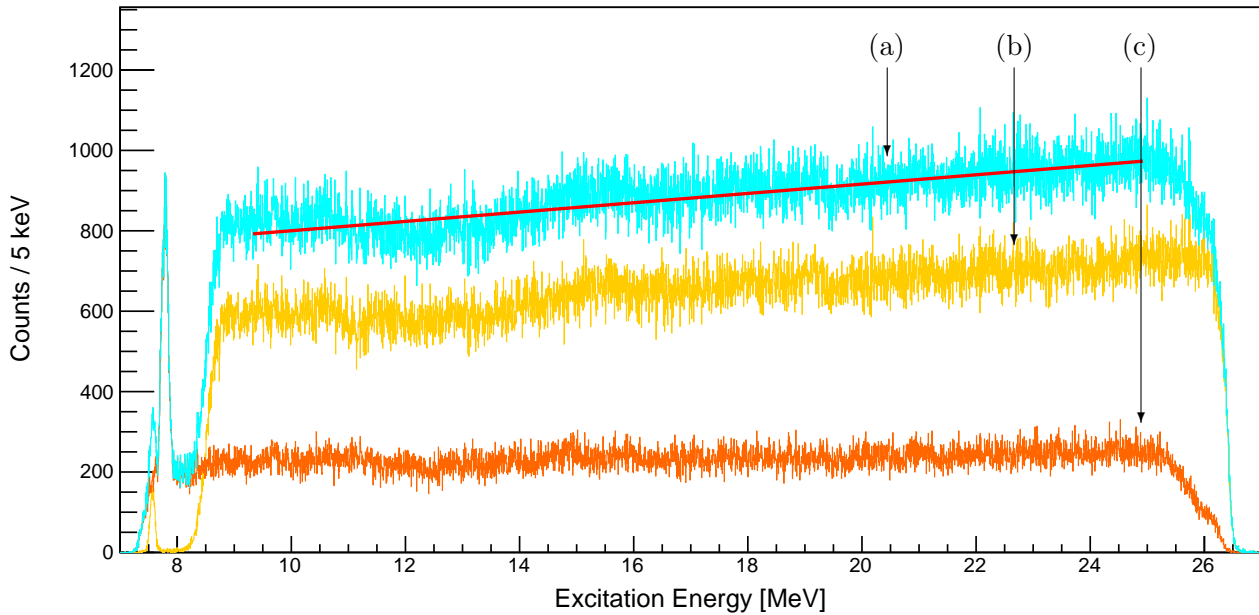


Figure 4.14: Singles background spectra of the ^{12}C target. Label (a) indicates the total background spectrum: the summation of the spectra labelled (b) and (c), which correspond to gates upon $Y1_{pos}^{MSl}$ and $Y1_{pos}^{MSh}$ respectively. The linear background fit, with a reduced $\chi^2_{reduced}$ value of 1.30, is displayed in red.

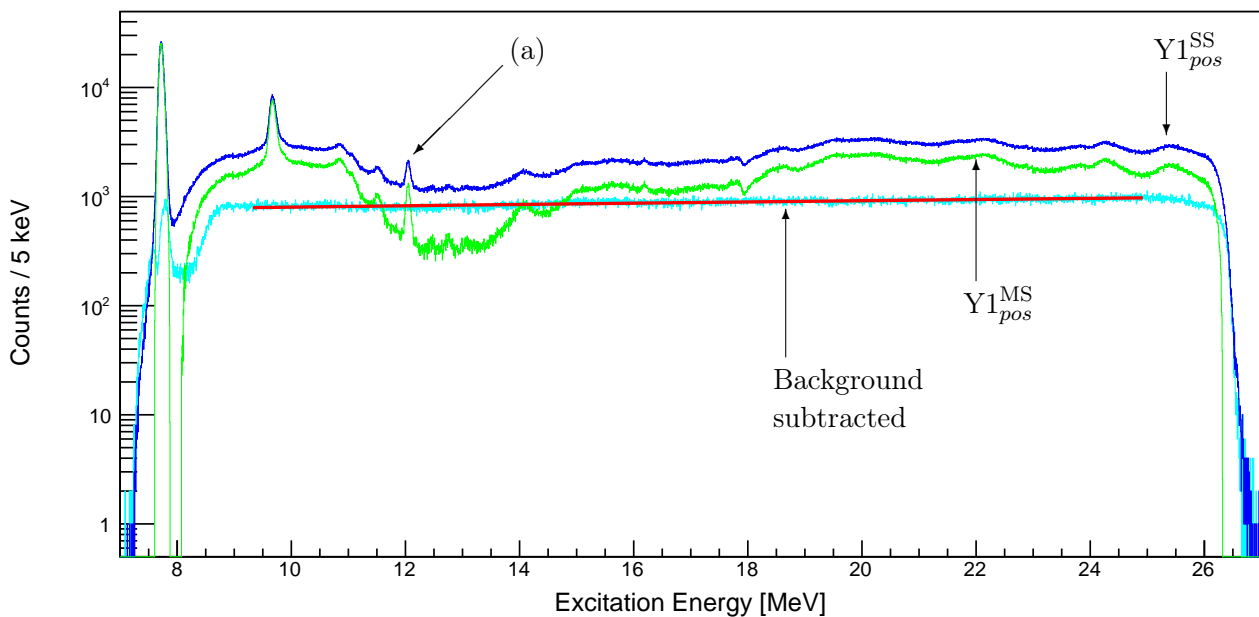


Figure 4.15: The raw (dark blue), total background (light blue) and background-subtracted (green) singles spectra for the ^{12}C target. Label (a) highlights the 12.049 MeV state in ^{16}O , indicating that the ^{12}C target is contaminated with ^{16}O . The linear background fit, with a reduced $\chi^2_{reduced}$ value of 1.30, is displayed in red.

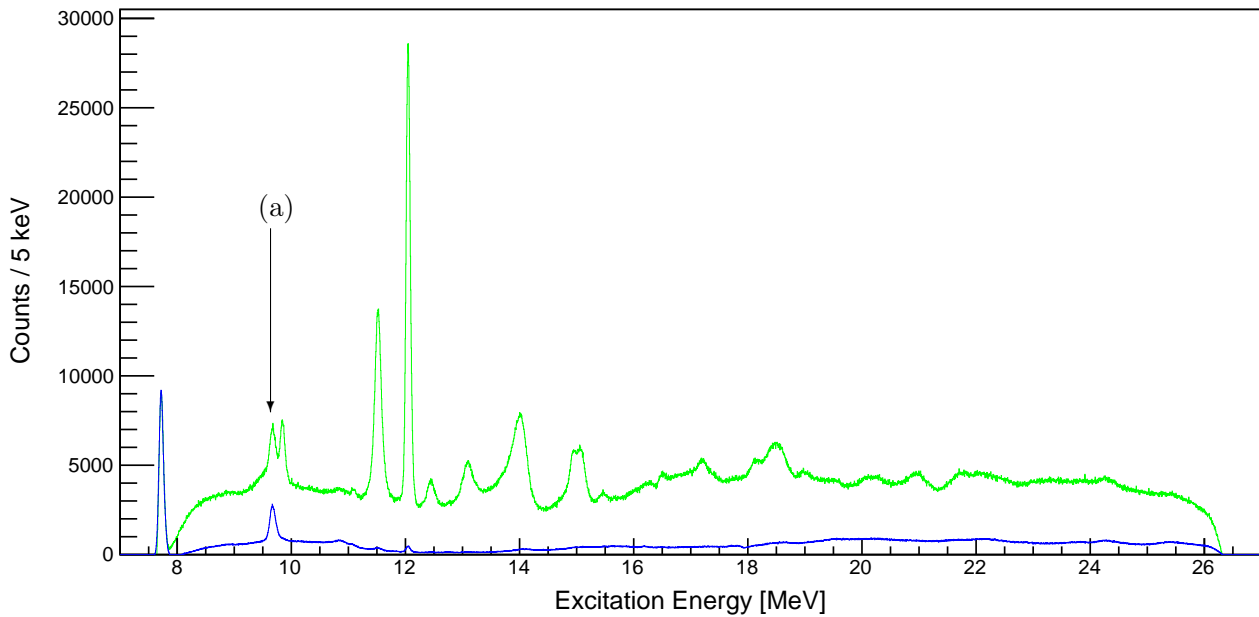


Figure 4.16: The background-subtracted spectra for the Li_2CO_3 and ^{12}C targets are displayed in green and dark blue respectively. The spectrum from the ^{12}C target is normalised to the strength of the 9.641(5) MeV ^{12}C resonance, labelled (a), in the Li_2CO_3 spectrum.

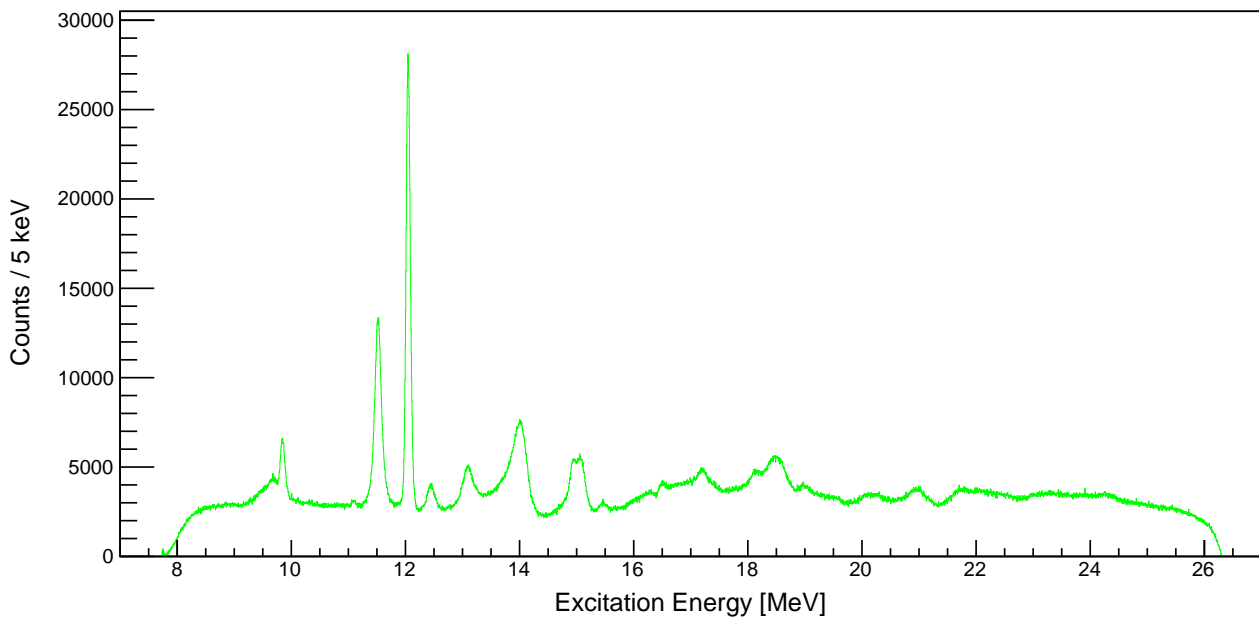


Figure 4.17: The background-subtracted Li_2CO_3 target spectrum with the normalised ^{12}C target spectrum removed. This spectrum is not intended for yield extraction, but rather to provide insight into the effect of ^{12}C background within the Li_2CO_3 target spectrum.

4.4 Data Sorting of the CAKE

When an α -particle inelastically scatters off a target nucleus, the excited recoil may decay through the emission of a charged particle. The focal plane detector system tracks the ejectile to trigger events whilst the CAKE, mounted at backward angles, detects coincident charged particle decays.

4.4.1 Energy Calibration of the CAKE

The CAKE was calibrated with a ^{228}Th source (see Figures 4.18 and 4.19) *in situ* within the new scattering chamber. To quantify the resolution of the CAKE, the 6.28808(10) MeV α -particle from ^{220}Rn is analysed: rings 0 and 1 collectively observe a peak width of 61(3) keV (FWHM) whilst rings 14 and 15 collectively observe a peak width of 90(4) keV (FWHM). The ring dependency of the resolution is due to the geometry of the ^{228}Th source, which provides more attenuation at lower θ angles (relative to the beam axis). An analogous target attenuation occurs within the in-beam data, necessitating ring dependent energy gates for data analysis.

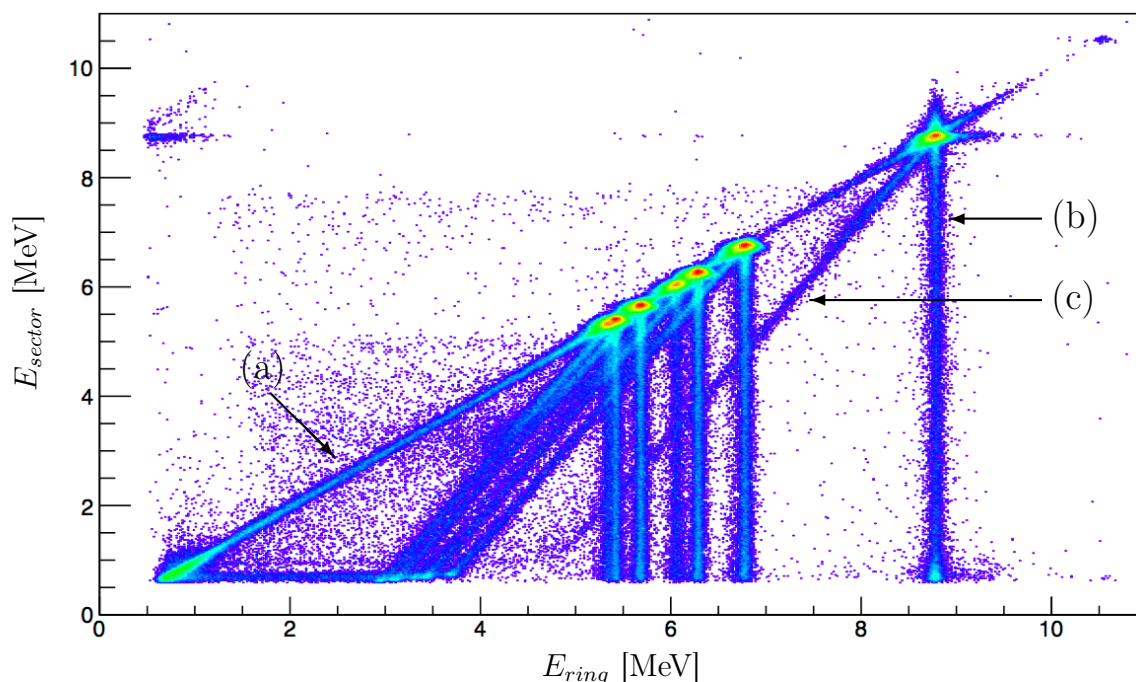


Figure 4.18: ^{228}Th source calibration data for all ring and sector channels: the calibrated energies of sector channels (E_{sector}) versus that of the ring channels (E_{ring}). Label (a) highlights the locus of hits with energy agreement between the ring and sector channels. The vertical structure, labelled (b), indicates hits with reduced detected energies from the sector channels. This can be attributed to inter-strip hits, resulting from charge spreading across channels (see Figure 4.26). The oblique structure, labelled (c), indicates hits which have reduced detected energies in both the ring and sector channels. The correlated decrease of energies between the ring and sector channels implies that this artefact does not arise purely from the segmentation of the detector - as is the case for structure (b). These hits correspond to energy deposition, from the detected particle, within the inter-strip regions. The charge separation that occurs in these regions is inefficiently collected across the p-n junction, thereby resulting in missing energy for both ring and sector channels.

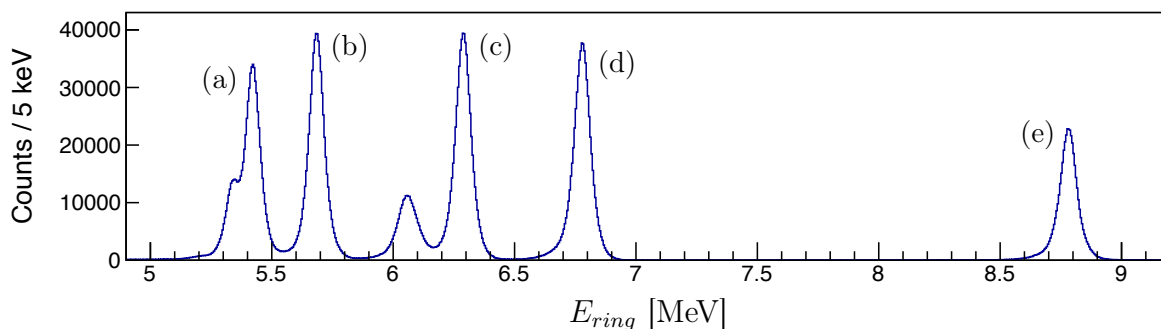


Figure 4.19: Energy spectrum of the ring channels displaying the α decays from a ^{228}Th source. The energies of the selected α decays are: (a) 5.42315(22) MeV from ^{228}Th , (b) 5.68537(15) MeV from ^{224}Ra , (c) 6.28808(10) MeV from ^{220}Rn , (d) 6.7783(5) MeV from ^{212}Pb and (e) 8.78486(12) MeV from ^{212}Po .

4.4.2 Energy Agreement of Valid Hits

Whilst a host of reactions may occur when the beam impinges upon the target, the observation of an ejectile at the focal plane effectively distinguishes a particular set of reaction products to be studied. When a particle hits the active area of the CAKE and deposits sufficient energy to pass the electronic threshold of a particular channel in the amplifier, the channel information is transmitted to the DAQ. If this occurs within a time window of $6 \mu\text{s}$ that is initiated by the paddle trigger, the channel pulse height information is recorded. Within this time window, it is possible for multiple ring and sector channels to be triggered in a single MMM detector - a subset of which may be correlated to the aforementioned reaction products of interest. For a combination of ring and sector channels to be identified as a valid hit in the CAKE, a restriction is placed upon the detected energies:

$$\left| \sum E_{ring} - \sum E_{sector} \right| < 0.2 \text{ MeV}, \quad (4.4.1)$$

where $\sum E_{ring}$ and $\sum E_{sector}$ are the summed energies detected from ring and sector channels respectively. Considering the experimental resolution of 90(4) keV (FWHM) for rings 14 and 15, the energy agreement restriction amounts to a $\sim 5\sigma$ difference between the ring and sector energies of a hit. The energy agreement restriction is implemented in the data sorting code during the search for valid channel combinations, the effect of which is shown in Figures 4.20 and 4.21. The restriction cannot be applied as a gate once a combination of channels has been assigned as a hit. If the restriction were to rather be placed as a gate (post data sorting), then two uncorrelated triggered channels may be incorrectly identified as a hit. If the detected energies of these channels do not satisfy the energy agreement restriction, the event is discarded. This artificially reduces the number of coincident particles detected by the CAKE, thereby biasing the data.

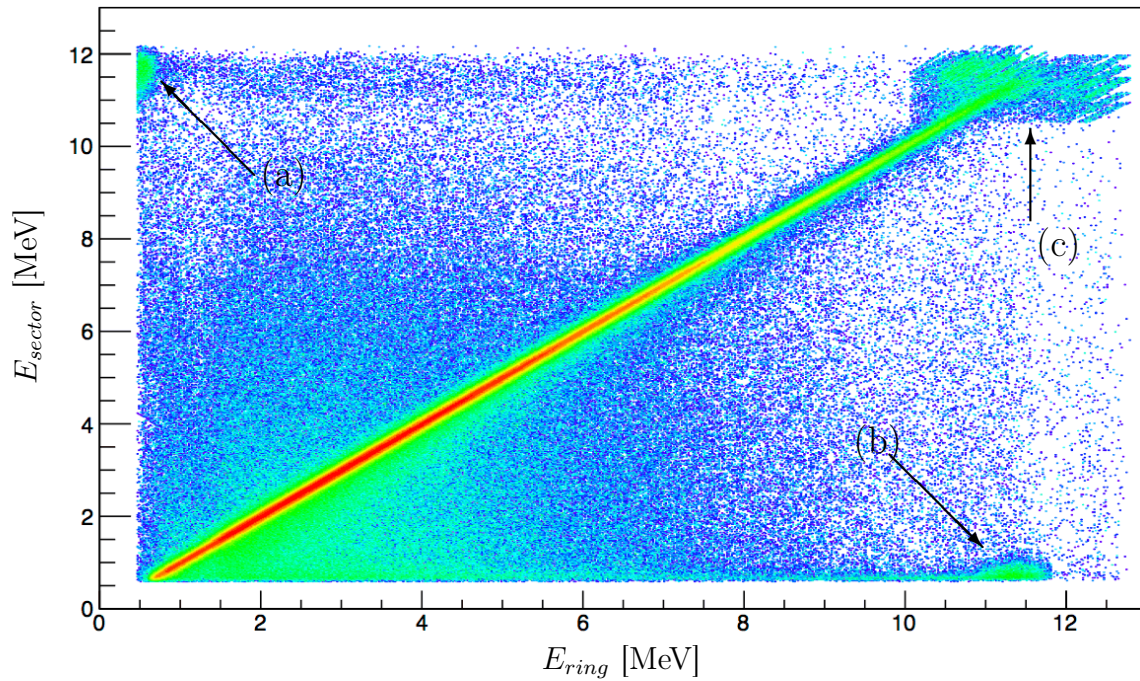


Figure 4.20: All possible RS hits in the CAKE without energy agreement between the detected energies of sector channels (E_{sector}) and ring channels (E_{ring}). Labels (a) and (b) denoted hits with saturated ring and sector channels respectively, i.e. the pulse height is too large for the amplifier to correctly process. Events in locus (c) have both the sector and ring channels saturated, indicating a real hit with an energy beyond the range of the amplifier.

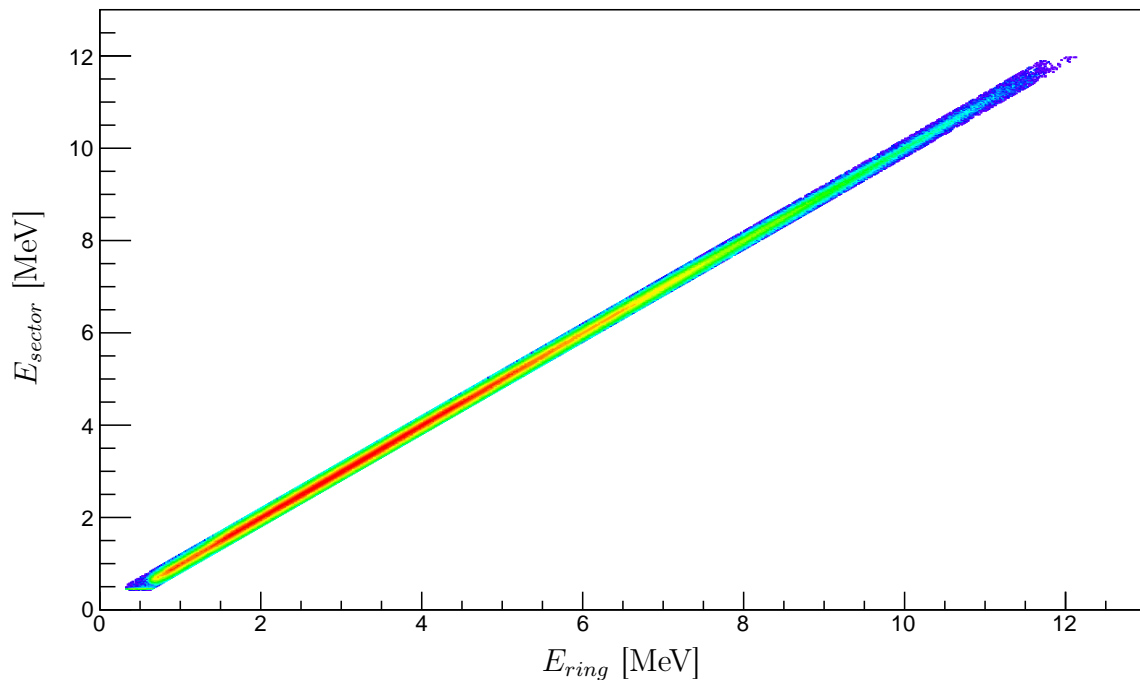


Figure 4.21: Valid hits in the CAKE with energy agreement between the detected energies of sector channels (E_{sector}) and ring channels (E_{ring}). The energy agreement restriction is defined in Equation 4.4.1.

4.4.3 TDC Timing of Valid Hits

The TDC times of valid hits in CAKE were acquired from all ring channels and were measured relative to the trigger signal from the paddle (see Figure 4.22). Due to the size of the ADC time window initiated by the triggered paddle, it is possible that the CAKE detects particles which originate from preceding/subsequent beam pulses. Such particles are uncorrelated in time with the event triggering ejectile, giving rise to random background hits in the CAKE.

4.4.3.1 Classification of Correlated and Uncorrelated TDC times

The peaks in Figure 4.22 represent different beam pulses. The largest peak in the TDC spectrum, labelled (a) in Figure 4.22, predominantly contains hits in the CAKE that are correlated in time with respect to the paddle trigger. A time gate for the correlated times, TDC^{cor} , is defined as:

$$TDC^{cor} : 10000 \text{ ns} < TDC < 12000 \text{ ns}. \quad (4.4.2)$$

To quantify the random background in this peak, the smaller peaks that lie outside the TDC gate of correlation are analysed. The events within these peaks are assumed to correspond purely to uncorrelated hits. The periodicity and height uniformity of the uncorrelated peaks justify this assumption.

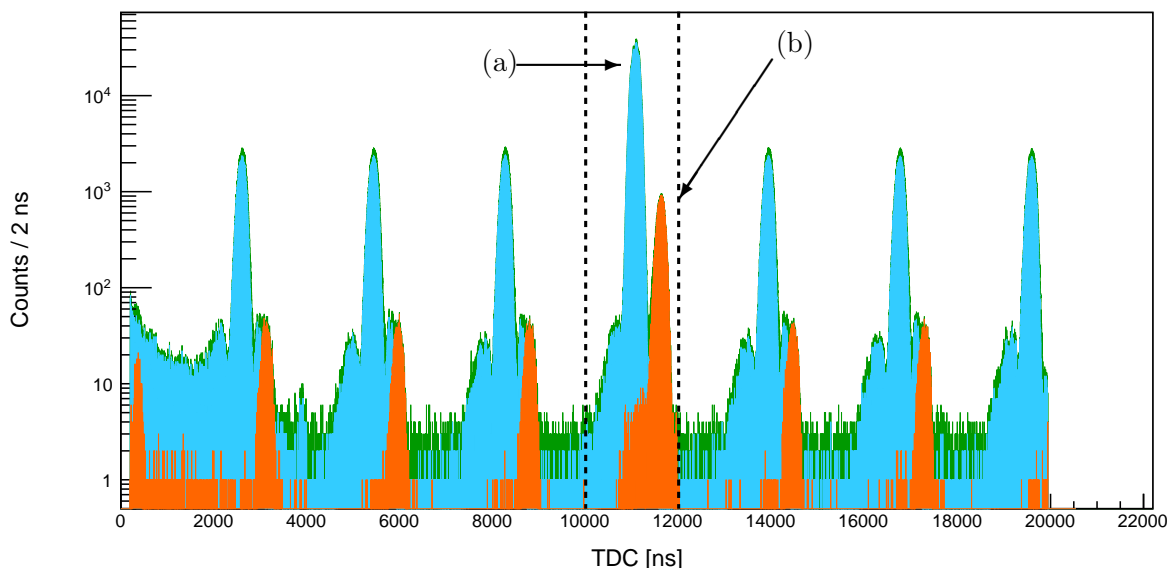


Figure 4.22: The TDC spectrum of hits in the CAKE. The dotted lines indicate the bounds of the TDC gate which contains the correlated CAKE hits. The green spectrum contains the TDC times of all hits in the CAKE which have passed the aforementioned energy agreement condition. The blue and orange spectra displayed in Figure 4.1 correspond to events which pass the PID gates for inelastically scattered α -particles and protons respectively. Label (a) and (b) denote the events triggered by inelastically scattered α -particles and protons respectively, where the coincident decay particle is correlated in time to the paddle trigger.

The uncorrelated peaks enable the quantification of the random background, i.e. for any spectrum generated with a gate upon the correlated TDC region, a corresponding random background spectrum can be generated by gating upon the satellite peak events. The assumption of random background uniformity between peaks allows for subtraction of the random background with a simple normalisation factor.

Gating upon the inelastically scattered α -particles and protons in the PID spectrum, produces the blue and orange spectra in Figure 4.22 respectively. It is observed that the peak labelled (b) in Figure 4.22, which has an approximate separation of 550 ns with respect to the largest peak (a), corresponds entirely to protons in the PID gate. This further confirms that these events are associated with proton ejectiles from the (α, p) reaction.

4.4.4 Multi-Hit TDC mode

The TDC modules that relay information towards the DAQ were operated in "Multi-Hit TDC" mode. In this mode, the DAQ can record multiple signals from a single TDC channel, per event. There is no *a priori* method to distinguish between multiple TDC times of a single channel and determine which one is valid. It is therefore postulated that if any TDC time of a channel falls within the time window of correlation (defined in Equation 4.4.2), the triggering of the channel is correlated in time with the ejectile.

4.4.5 Channel Combinations of Valid Hits

The ring and sector hit patterns of the CAKE from the calibration source and in-beam data are displayed in Figures 4.23 and 4.24 respectively.

Since the detected α -particles from the calibration source are isotropic, the hit pattern of the ring channels should be approximately proportional to the solid angles subtended by the rings (see Figure 3.32). The yield for ring 0 from the in-beam data, labelled (a) in Figure 4.24, exhibits an abnormally high yield with respect to the hit pattern trend. This behaviour is not observed upon the equivalent hit pattern from the calibration source data. It is postulated that these events correspond to beam halo particles. By observing the ring energies of coincident hits in the CAKE versus the excitation energy of the recoil nucleus, the scattered beam events can be identified as a horizontal locus labelled (a) in Figure 4.25. The in-beam data from ring 0 is consequently excluded from the analysis (unless explicitly stated otherwise).

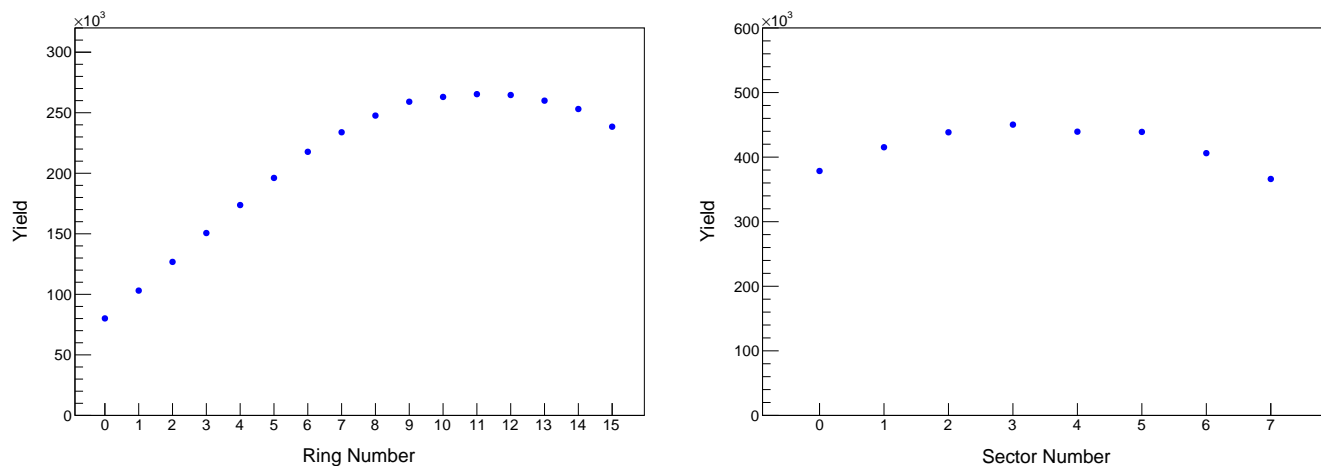


Figure 4.23: Hit patterns for ring and sector channels of the CAKE, from the ^{228}Th source calibration data.

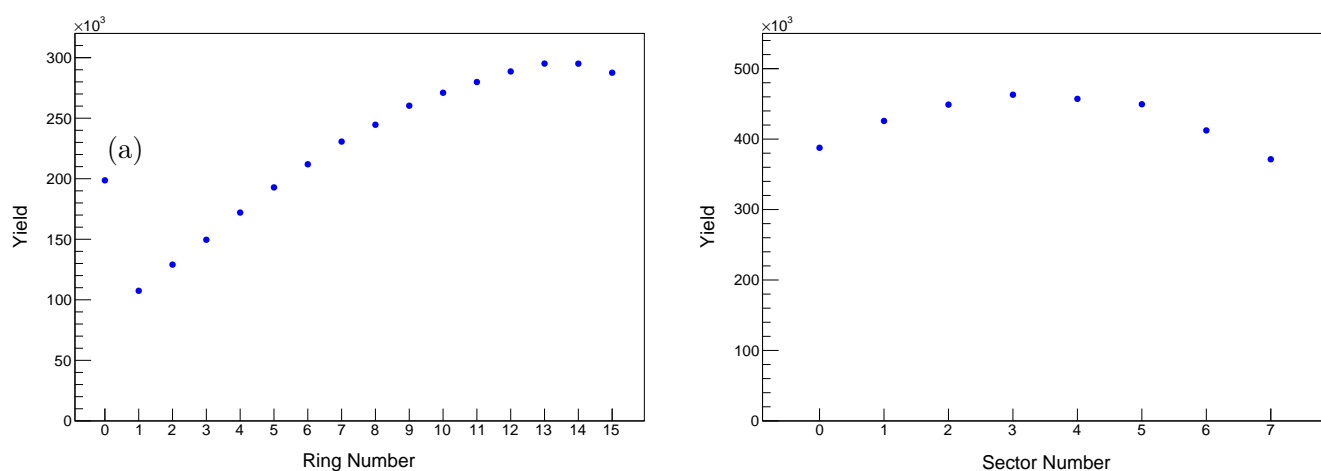


Figure 4.24: Hit patterns for ring and sector channels of the CAKE, from the Li_2CO_3 target data. Label (a) highlights the anomalously high yield in ring 0.

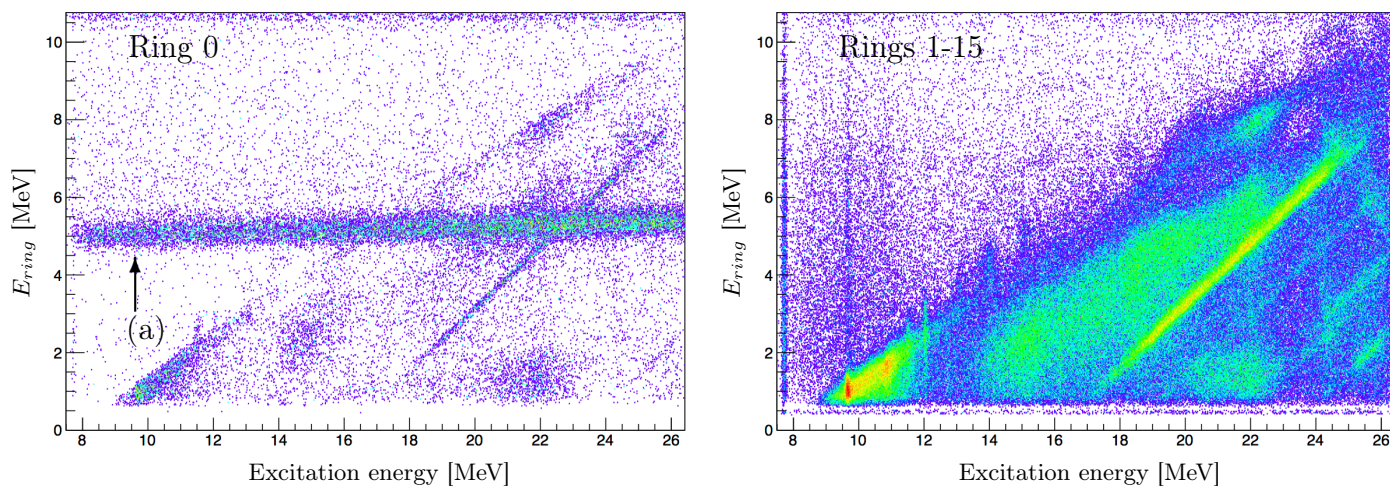


Figure 4.25: ^{12}C spectra of the CAKE ring energy versus recoil nucleus excitation energy, where the locus labelled (a) corresponds to the beam halo events. A display threshold of >1 is imposed.

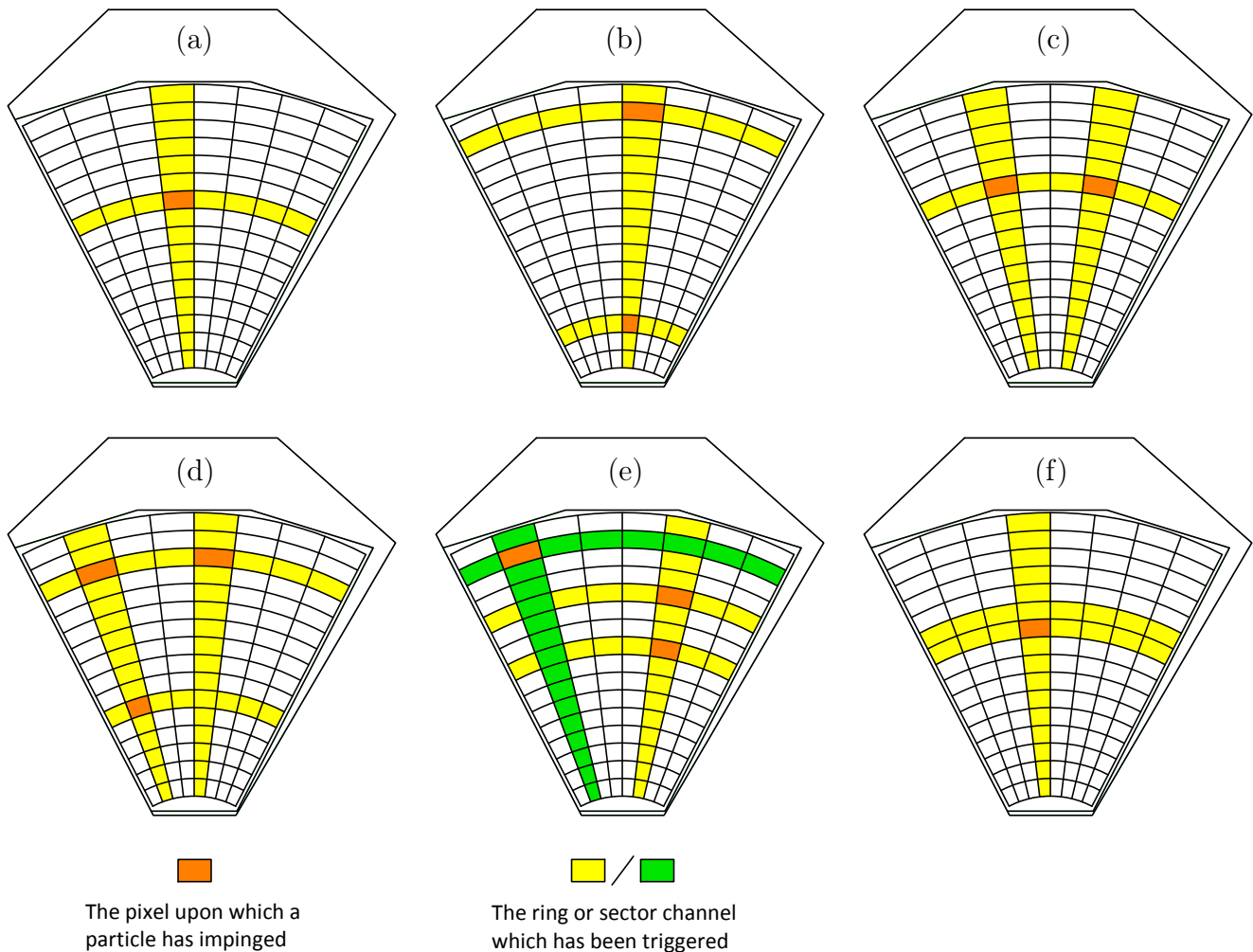


Figure 4.26: Typical ring and sector triggering permutations for the CAKE: (a) 1 particle triggering a pair of ring and sector channels \equiv an RS hit, (b) 2 particles which have triggered 2 ring channels and 1 sector channel \equiv an RRS hit, (c) 2 particles which have triggered 1 ring channel and 2 sector channels \equiv an RSS hit, (d) 3 particles which have triggered 2 ring and 2 sector channels, resulting in a combined hit which cannot be logically decomposed to correctly assign either the impinged pixels or the original particle energies, (e) 3 particles triggering 3 ring channels and 2 sector channels, a hit which can be decomposed into a combination of previously defined RS and RRS hits (f) 1 particle triggering two ring channels and one sector channel due to charge spreading across an inter-strip region \equiv an inter-strip hit.

The permutations for ring-sector hits are analysed by a newly implemented data sorting code are shown in Figure 4.26. The hit multiplicities, of the different ring and sector permutations analysed, are shown in Figure 4.27.

It is possible that a single particle may trigger more than a single ring and sector channel pair through a inter-strip hit, where the charge spreading across the silicon can trigger a neighbouring channel. This only occurs when particles impinge sufficiently close to - or directly upon - an inter-strip region (see Figure 3.30). Should this occur, the ionised charge is not efficiently collected across the inter-strip region, resulting in a mismatch between the energy depositions detected by associated ring and sector channels. The summed energy detected by the energy-sharing (neighbouring) channels will generally be lower than the energy detected by the corresponding individual channel on the converse side of the detector, resulting in rejection of the event by the energy agreement condition (defined in 4.4.1).

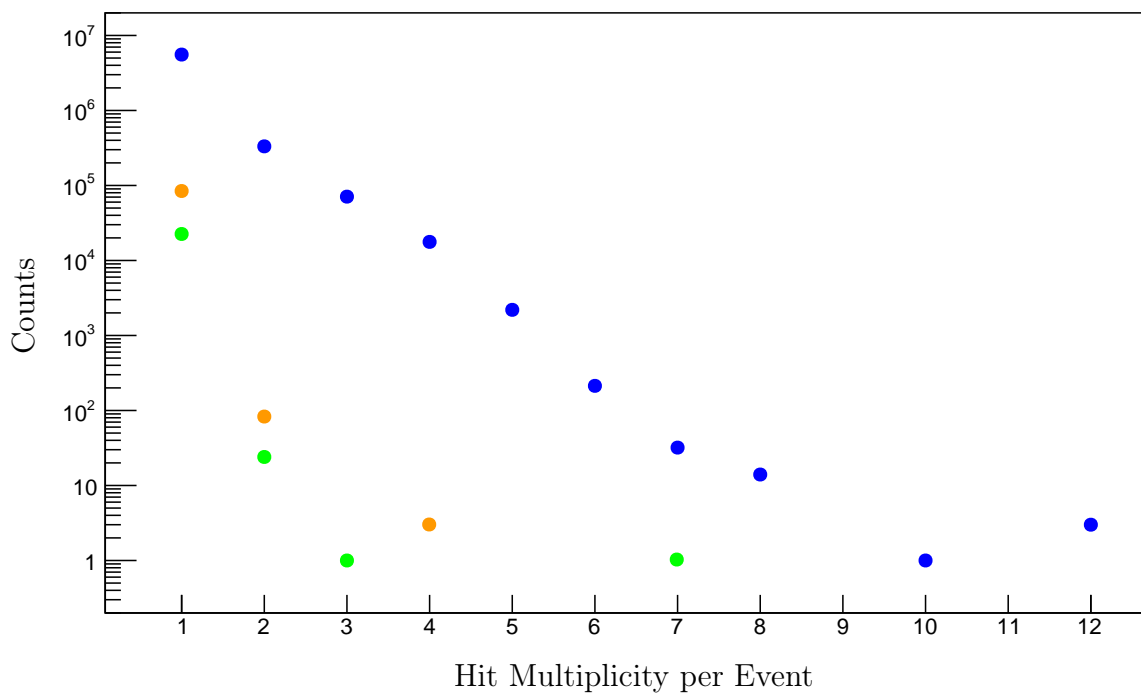


Figure 4.27: Channel combination multiplicities of the CAKE. The blue, green and orange data points correspond to RS, RRS and RSS hits.

4.5 Coincident Decay Particles in the CAKE

Charged decay particles are detected by the CAKE in coincidence with the event triggering ejectile in the K600 magnetic spectrometer. The decay modes and decay channels of these particles provide insight into the structure of the recoil nucleus.

4.5.1 Kinematics of Binary Decay

For binary decay of a recoil nucleus, the energy a single decay product is sufficient to determine the excitation energy of the parent recoil nucleus. For a parent nucleus, denoted particle 0, which decays into particles 1 and 2, energy conservation requires that

$$E_{x0} + T_0 - E_{sep} = E_{x1} + T_1 + E_{x2} + T_2, \quad (4.5.1)$$

whilst momentum conservation gives

$$\vec{p}_0 = \vec{p}_1 + \vec{p}_2. \quad (4.5.2)$$

For a 15.0 MeV excitation of the recoil nucleus (E_{x0}), the angular acceptance of $\pm 2^\circ$ upon the associated ejectile restricts the maximum kinetic energy of the recoil (T_0) to approximately 140 keV. The kinetic energy of the recoil is therefore negligible when target attenuation effects and energy resolution of the CAKE array (see Section 4.4.1) is taken into account. The recoil nucleus can therefore be approximated to be stationary in the laboratory reference frame, yielding a trivial momentum conservation

$$m_1 v_1 = m_2 v_2. \quad (4.5.3)$$

The centre of mass energy available for a given decay channel, denoted E_C , is can be expressed as

$$E_C = T_1 + T_2, \quad (4.5.4)$$

where

$$E_C = E_{x0} - E_{sep} - E_{x1} - E_{x2}. \quad (4.5.5)$$

Solving for v_1^2 gives

$$v_1^2 = 2E_C \left(m_1 + \frac{m_1^2}{m_2} \right)^{-1}, \quad (4.5.6)$$

which is substituted into Equation 4.5.3 to solve for v_2^2 , yielding

$$v_2^2 = 2E_C \left(\frac{m_1}{m_2} \right)^2 \left(m_1 + \frac{m_1^2}{m_2} \right)^{-1}. \quad (4.5.7)$$

It is concluded that with a stationary recoil nucleus approximation, the kinetic energies of the binary decay products (in the laboratory frame) are purely determined by the ratio of their masses

$$T_1 = \left(\frac{m_2}{m_1} \right) T_2. \quad (4.5.8)$$

In particular, the kinetic energy of a decay product is inversely proportional to its mass.

4.5.2 Decay Modes and Decay Channels

A decay mode of a nucleus is classified by the masses and excitation energies of the decay products. Since protons are fundamental particles of nuclear matter and α -particles are unlikely to be excited, the excitation energy of decay products from an α or proton decay mode is possessed by the complementary decay particle, referred to as the residual nucleus. An example of the notation used is " α_0 ". The α denotes the lightest decay product of the binary decay, e.g. $^{16}\text{O}(2_1^+) \rightarrow ^{12}\text{C}(\text{g.s.}) + \alpha$. The 0 is indicative of the excitation energy level of the residual nucleus, i.e. 0 corresponds to the ground state and 1 corresponds to the first excited state, etc.

A decay channel further specifies the initial state, parameters and quantum numbers of the decay. For a particular decay mode of a state/resonance, multiple decay channels may exist. An example is the α_1 decay mode of the 11.520(4) MeV 2^+ resonance in ^{16}O . Through the α_1 decay mode, the α -particle decay product may take $0\hbar$, $1\hbar$ or $2\hbar$ of angular momenta. Each possible outcome specifies a particular decay channel. Data shows that the decay channel - through which the minimum possible angular momentum is imparted - typically dominates a decay mode, however exceptional cases do occur. This can be interpreted to be as a result of the centrifugal potential, of the residual nucleus, that the decay particle has to penetrate through (and *vice versa*).

From section 4.5.1, the kinematics of binary decay determines a linear relationship between the kinetic energies of the decay particles (T_1 and T_2) and the excitation energy of the recoil nucleus (E_{x0}).

$$T_1 = \left(1 + \frac{m_1}{m_2} \right)^{-1} (E_{x0} - E_{sep} - E_{x1} - E_{x2}) \quad (4.5.9)$$

$$T_2 = \left(1 + \frac{m_2}{m_1} \right)^{-1} (E_{x0} - E_{sep} - E_{x1} - E_{x2}) \quad (4.5.10)$$

By plotting the energies of coincident hits in the CAKE against the excitation energies of the recoil nucleus, various decay modes and channels can be identified. These spectra for the Li_2CO_3 and ^{12}C targets are displayed in Figures

4.28 and 4.29 respectively. The linear structures correspond to the different decay modes of the various target nuclei; the gradients of which reflect the aforementioned mass ratios of the decay particles.

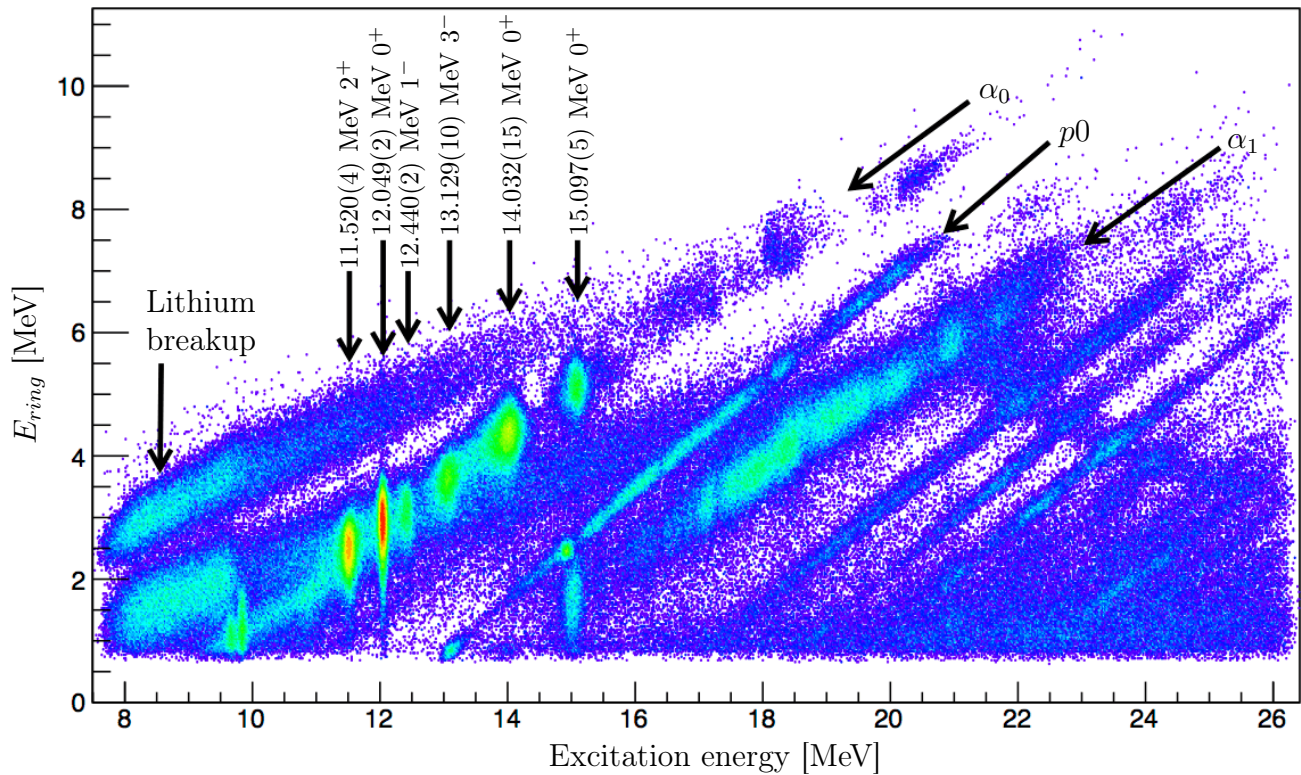


Figure 4.28: The ring energies of coincident hits in the CAKE, from the Li_2CO_3 target, versus the excitation energy of the recoil nucleus. Prominent decay models and decay channels observed from ^{16}O are indicated. A display threshold of >5 is imposed.

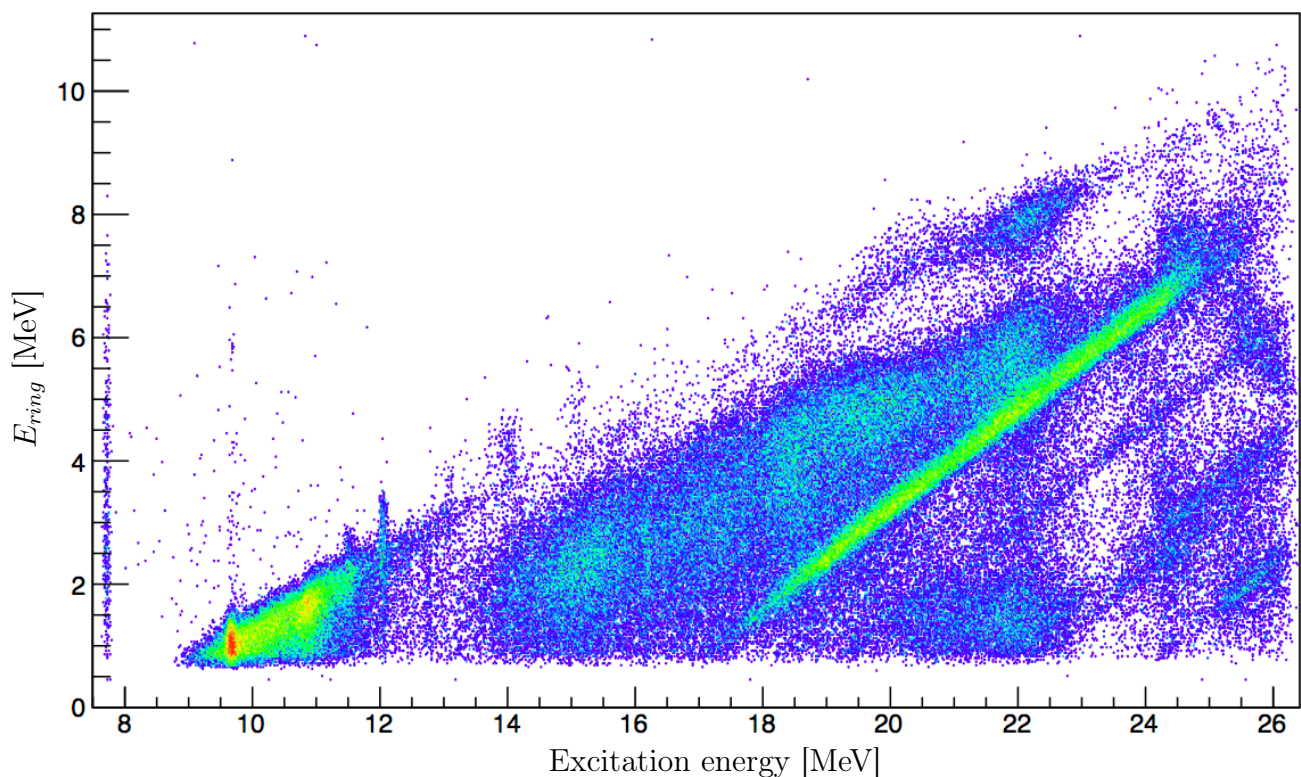


Figure 4.29: The ring energies of coincident hits in the CAKE, from the ^{12}C target, versus the excitation energy of the recoil nucleus. A display threshold of >3 is imposed.

4.5.3 Electronic Threshold Limitation of the CAKE

The electronic thresholds in the MSCF-16 amplifiers, for the channels of the MMM detectors, were not identically set. MMMs 0 and 1 were configured with the same threshold and similarly for MMMs 2 and 3 (see Figure 4.30). The higher thresholds of MMMs 2 and 3 do not allow the full detection of certain decay channels, e.g. an α_1 decay channel from a $E_x \sim 15.1$ MeV resonance of ^{16}O (see Figure 4.31). The extraction of yields from these affected decay channels are therefore performed upon data exclusively from MMMs 0 and 1. For decay channels which lie above the electronic thresholds, the data from the entire CAKE can be analysed.

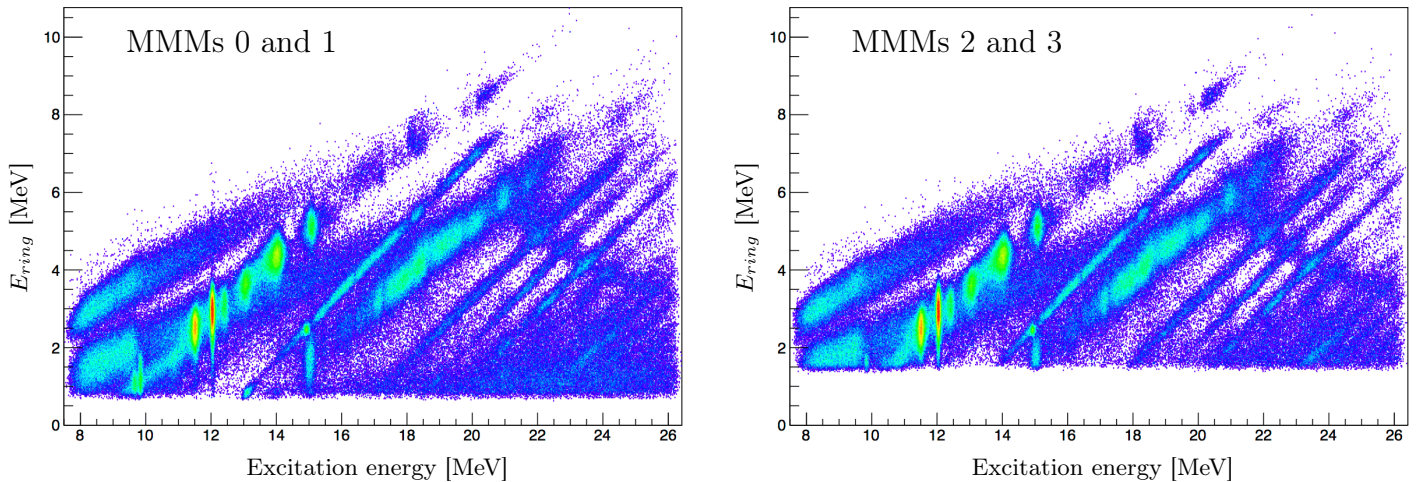


Figure 4.30: Li_2CO_3 spectra of the CAKE ring energy versus recoil nucleus excitation energy, illustrating the different electronic thresholds between the MMM detectors. A display threshold of >5 is imposed.

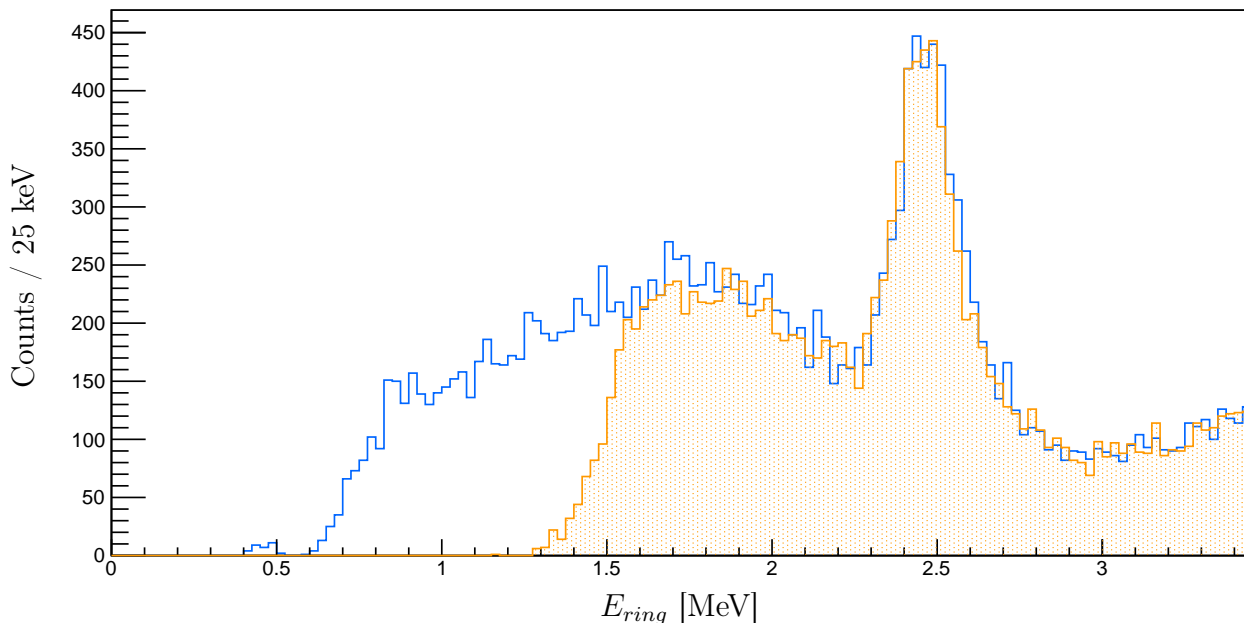


Figure 4.31: The ring energies of CAKE hits, from the Li_2CO_3 target, with a gate upon the recoil excitation energy: $14.8 \text{ MeV} < E_{x0} < 15.2 \text{ MeV}$. The blue spectrum corresponds to hits in MMMs 0 and 1. The orange spectrum, which corresponds to hits in MMMs 2 and 3, clearly shows the effect of the electronic threshold for $E_{ring} < 1.6 \text{ MeV}$.

4.5.4 Target Attenuation Effects

In general, the average distance travelled by decay products through the target is dependent upon the initial angle of emission. Since the ring channels of the CAKE subtend different polar angles with respect to the beam axis, the average target attenuation is dependent upon the ring number of the hit. Since α -particles have twice the charge and approximately four times the mass of protons, the target attenuation of α decay modes is more severe relative to proton decay modes. The influence on the energy resolution upon the decay particle measurement is shown clearly in Figures 4.32 and 4.33.

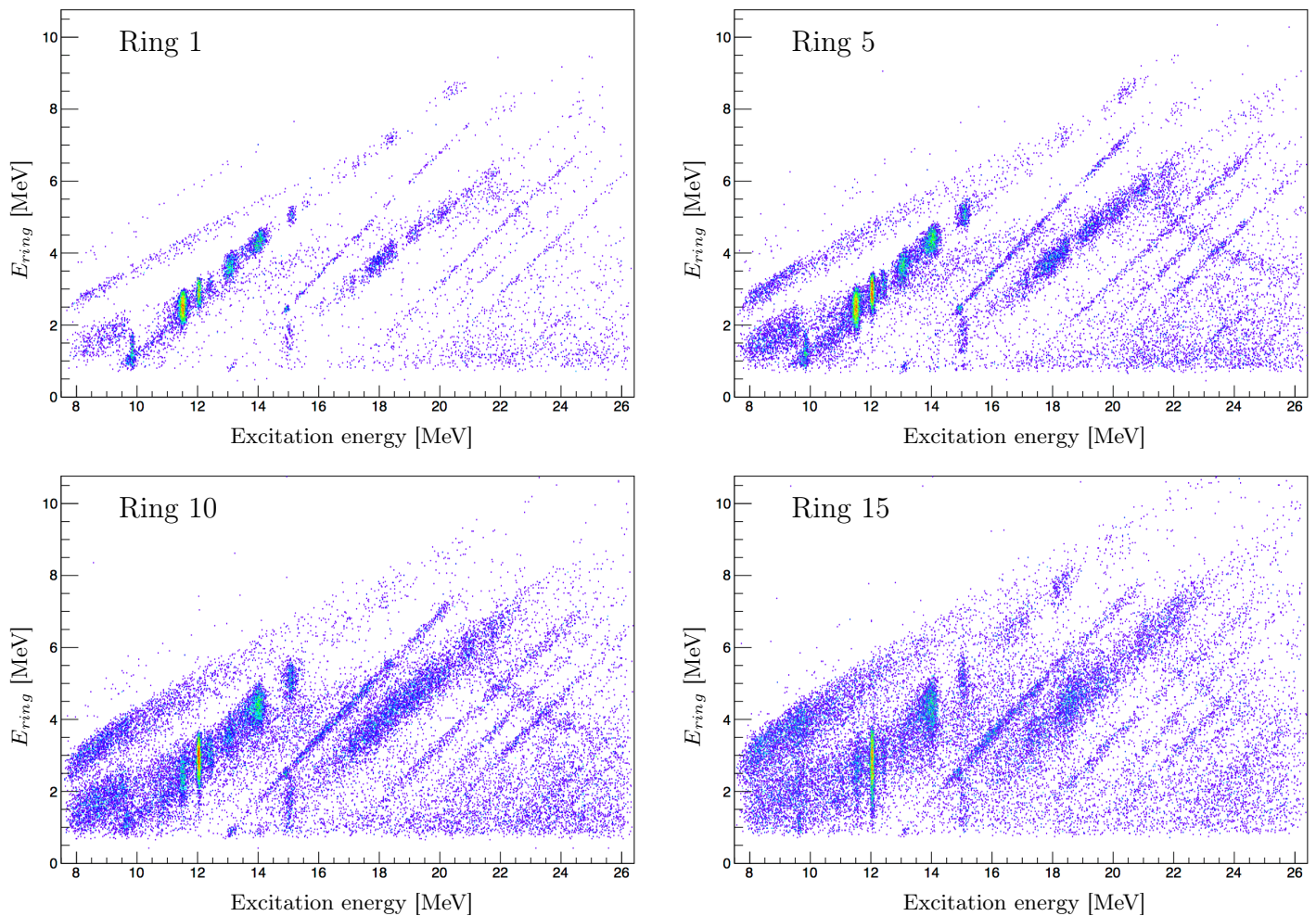


Figure 4.32: Li_2CO_3 spectra of the CAKE ring energy versus recoil nucleus excitation energy, illustrating the dependency of target attenuation upon the associated ring channel. A display threshold of >2 is imposed.

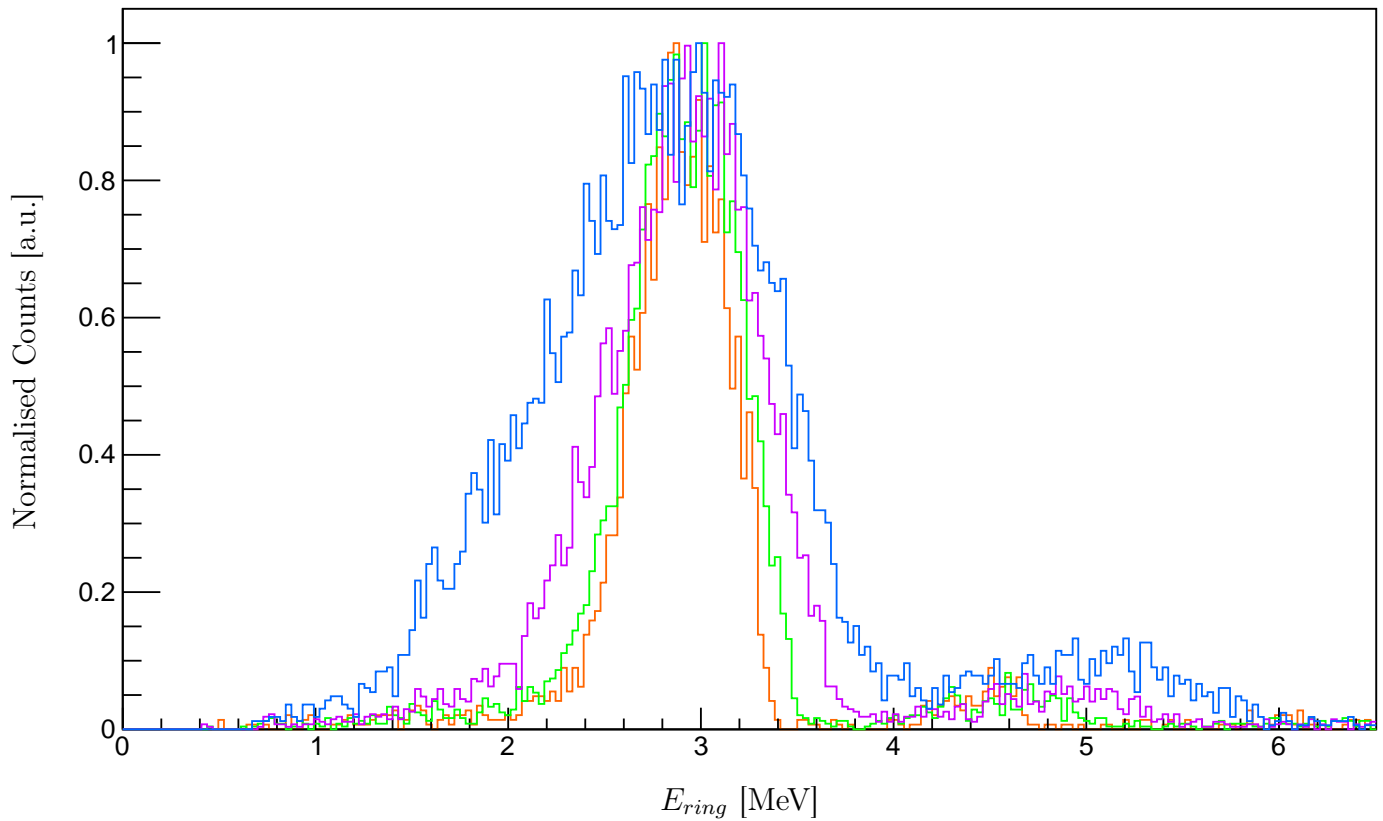


Figure 4.33: The ring energies of CAKE hits, from the Li_2CO_3 target, with a gate upon the recoil excitation energy: $14.8 \text{ MeV} < E_{x0} < 15.2 \text{ MeV}$. The orange, green, violet and blue spectra correspond to hits within rings 1, 5, 10 and 15 respectively. The maximum of each spectrum is normalised to 1.

4.6 Background Subtraction of Coincidence Focal Plane Spectra

There are two primary sources for the background events in coincidence focal plane spectra. One such source is the "random" events: it is possible for multiple recoil nuclei to be excited when a beam packet impinges the target. It is possible that the parent recoil nucleus of a decay product is uncorrelated with regards to the event triggering ejectile. It is not possible to directly exclude such random events and hence an associated random background spectrum is generated by gating upon events where the TDC times from the cake do not pass the TDC^{cor} gate (see Section 4.4.3). The second source of background corresponds to events with ejectiles which have undergone multiple scatters before reaching the focal plane. A corresponding background spectrum can be generated by gating on the $Y1_{pos}^{MS}$ gate, as defined in Section 3.3.6. The two sources of background, which are normalised, are displayed in Figure 4.34.

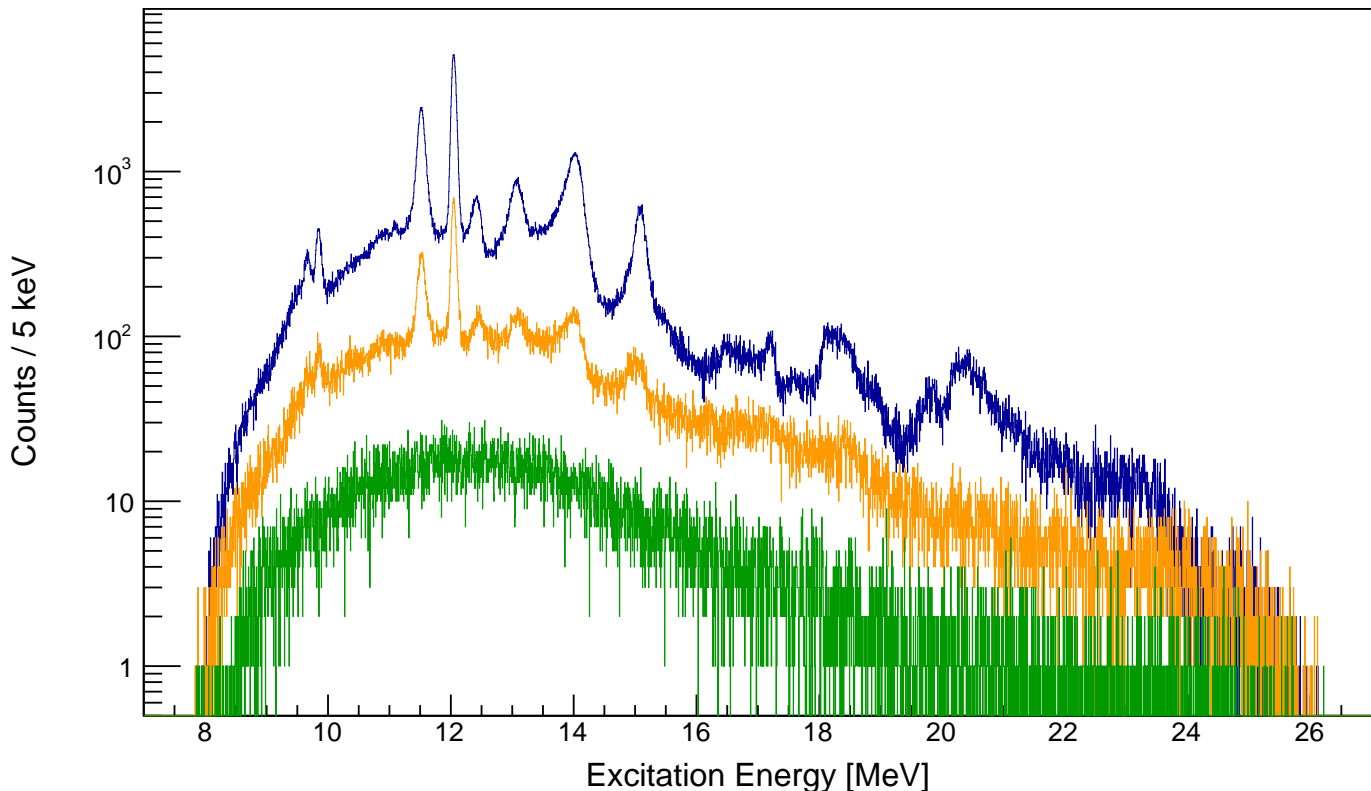


Figure 4.34: The background sources of the coincidence focal plane spectra. The blue spectrum is the raw spectrum without background subtraction. The orange background spectrum corresponds to events which do not pass the TDC^{cor} gate. The green background spectrum corresponds to events which pass the $Y1_{pos}^{MS}$ gate.

4.7 Selectivity of Magnetic Substates

As mentioned in Section 3.3.7, the full scattering angle of the ejectile cannot be reconstructed as the K600 spectrometer was operated in the Y-focused mode. It is however possible to determine θ_{SCAT} : the ejectile scattering angle in the horizontal plane with respect to the beam axis.

The magnetic substate population ratios of a resonance, which are polar scattering angle dependent, are characteristic of the spin and parity of the resonance. These ratios directly influence the angular distributions of recoil nuclei decay - both in the lab frame and the centre of mass frame of the recoil nucleus. Since θ_{SCAT} is correlated with the true scattering angle of the ejectile, a gate upon θ_{SCAT} consequently selects for different magnetic substate distributions. In principle, such a gate can augment the differences between angular distributions from unresolved states/resonances, allowing not only for their differentiation, but also the assignment of spin-parities. These gates shall prove particularly illuminating in the analysis of the 15.097(5) MeV 0_6^+ state in ^{16}O .

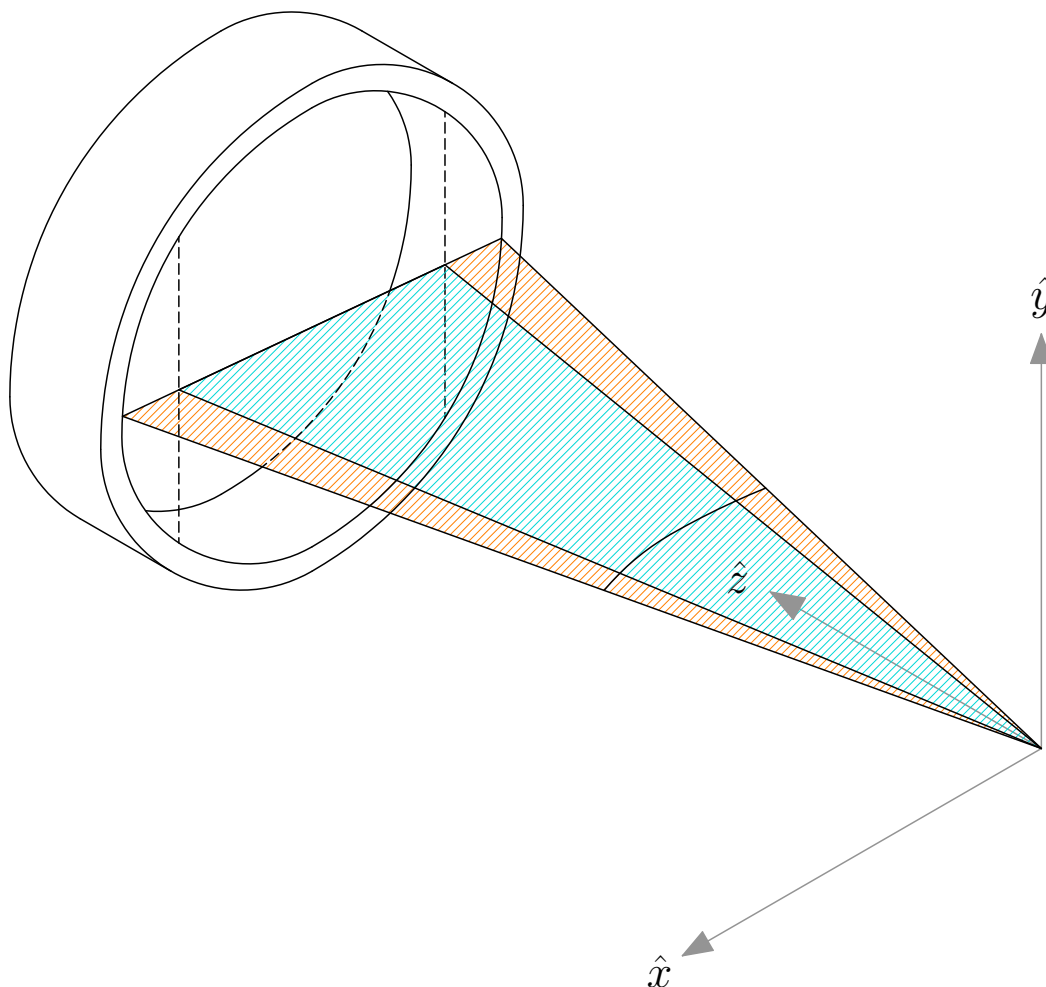


Figure 4.35: Schematic representation of the θ_{SCAT} cuts which allow for selection over different distributions of ejectile scattering angles. The blue shaded region corresponds to $(|\theta_{\text{SCAT}}| < 1.4)$, which selects for lower values of θ_{SCAT} . The orange shaded region corresponds to $(1.4 < |\theta_{\text{SCAT}}| < 2.0)$, which selects for higher values of θ_{SCAT} .

Figure 4.35 schematically shows two gates of θ_{SCAT} : a lower range (displayed in blue), which is defined as

$$\theta_{\text{SCAT}}^l : |\theta_{\text{SCAT}}| < 1.4 \text{ deg}, \quad (4.7.1)$$

and a higher range (displayed in orange) defined as:

$$\theta_{\text{SCAT}}^h : 1.4 \text{ deg} < |\theta_{\text{SCAT}}| < 2.0 \text{ deg}. \quad (4.7.2)$$

The ideal ranges of ejectile scattering angles (θ_{lab} and ϕ_{lab}), which correspond to the θ_{SCAT}^l and θ_{SCAT}^h gates, are displayed in Figures 4.36 and 4.37 respectively. These distributions were calculated with a Monte Carlo simulation.

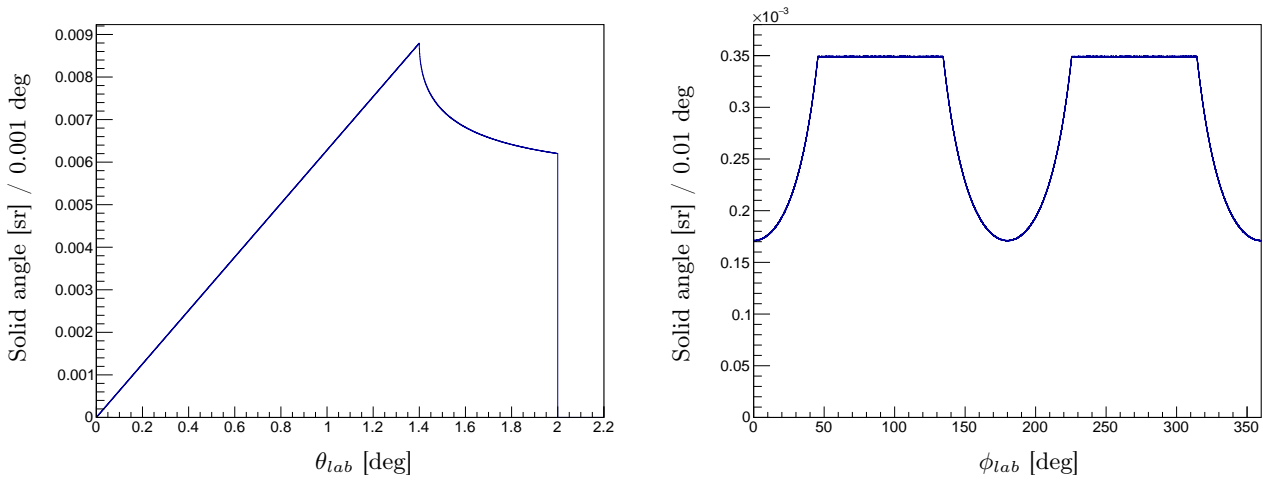


Figure 4.36: The ideal ranges of ejectile scattering angle (θ_{lab} and ϕ_{lab}) covered by the θ_{SCAT}^l gate.

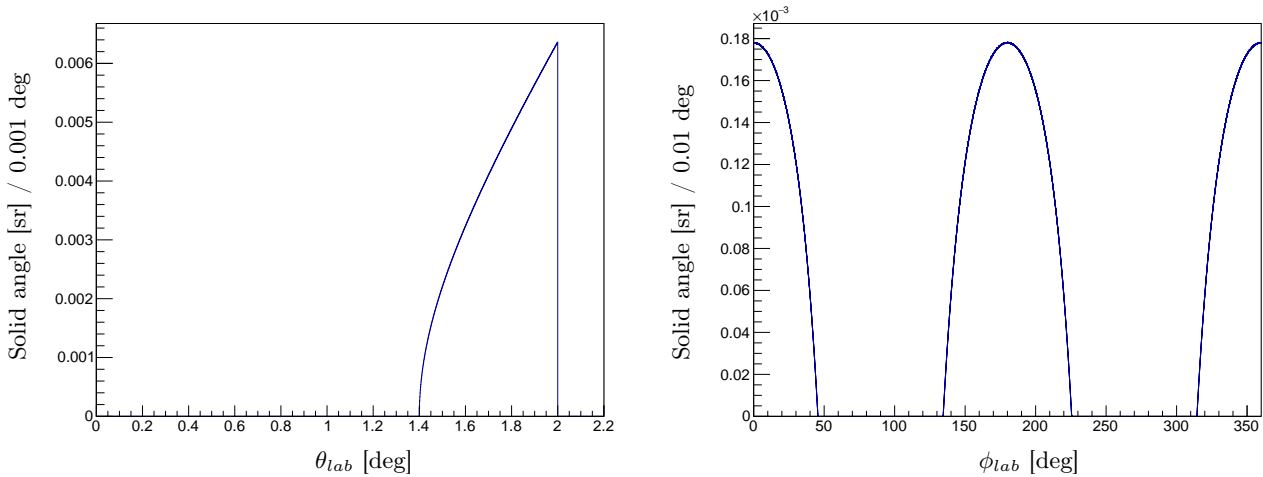


Figure 4.37: The ideal ranges of ejectile scattering angle (θ_{lab} and ϕ_{lab}) covered by the θ_{SCAT}^h gate.

Quantifying the experimental error of θ_{SCAT} is non-trivial as there is no observable from the data, *a priori*, with which to compare. To provide insight into how the error may affect the ejectile scattering angle distributions, and consequently the relative magnetic substate population ratios, a Gaussian smearing, with a standard deviation of $\sigma = 0.4$ deg (10% with respect to the $\pm 2^\circ$), was applied upon the simulated θ_{SCAT} quantity. The Gaussian smeared ranges of ejectile scattering angles (θ_{lab} and ϕ_{lab}), which correspond to the θ_{SCAT}^l and θ_{SCAT}^h gates, are displayed in Figures 4.38 and 4.39 respectively. It is observed that under such an experimental error, the θ_{SCAT}^l and θ_{SCAT}^h gates still effectively bias the ejectile scattering angle distributions.

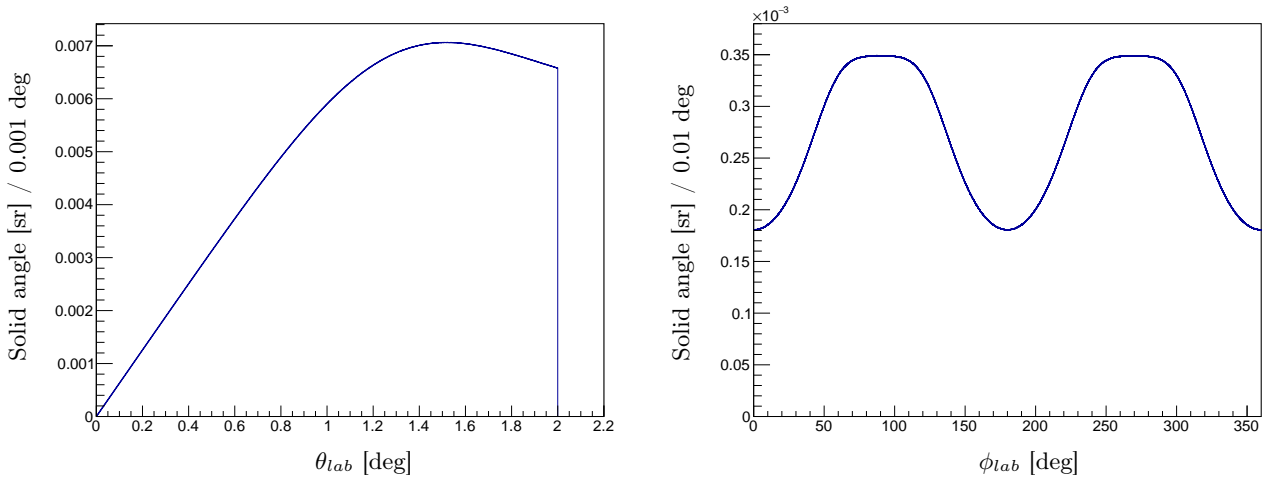


Figure 4.38: The Gaussian smeared ranges of ejectile scattering angle (θ_{lab} and ϕ_{lab}) covered by the θ_{SCAT}^l gate.

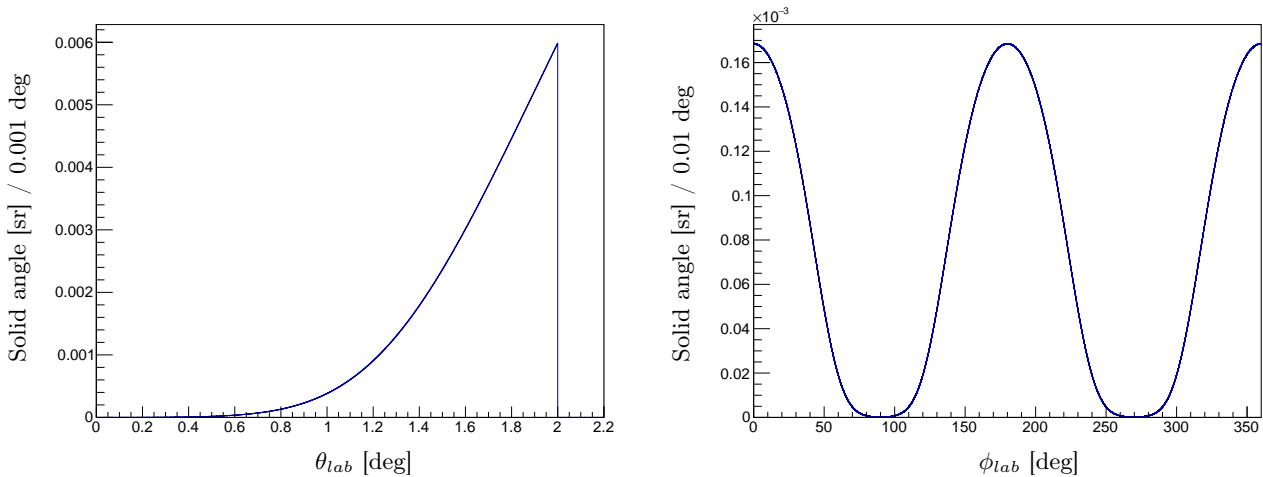


Figure 4.39: The Gaussian smeared ranges of ejectile scattering angle (θ_{lab} and ϕ_{lab}) covered by the θ_{SCAT}^h gate.

4.8 R-matrix Analysis

The lineshape of resonances is given in Equation 2.2.13. The Lorentzian function, with an energy dependent width (see Equation ??), is appropriate to fit resonances. The intrinsic experimental resolution of the focal plane detection system is assumed to be Gaussian in nature and therefore to fit the focal plane spectra, a Voigt profile must be employed. The Voigt profile is defined as the convolution of a Gaussian $G(x, \sigma)$ and a Lorentzian $L(x, \Gamma)$ distribution. The Gaussian distribution is defined as

$$G(x, \mu_G, \sigma) = \frac{e^{-(x-\mu_G)^2/(2\sigma^2)}}{\sigma\sqrt{2\pi}}. \quad (4.8.1)$$

where σ is the standard deviation and μ_G is the mean of the resonance. The Lorentzian distribution is defined as

$$L(x, \mu_L, \Gamma) = \frac{\Gamma/2}{\pi [(x - \mu_L)^2 + (\Gamma/2)^2]} \quad (4.8.2)$$

where Γ is the full width half maximum and μ_L is the location parameter (the mean of the Lorentzian is undefined). The Voigt profile is given by

$$V(x, \mu_V, \sigma, \Gamma) = \int_{-\infty}^{\infty} G(x, \mu_G, \sigma)L(x - x', \mu_L, \Gamma)dx', \quad (4.8.3)$$

where σ and Γ are the aforementioned Gaussian standard deviation and Lorentzian FWHM respectively. The mean of the Voigt is undefined and its location parameter μ_V is given by

$$\mu_V = \mu_G + \mu_L \quad (4.8.4)$$

The Voigt Profile can also be expressed in terms of the Faddeev function w :

$$V(x, \sigma, \Gamma) = \frac{\text{Re} \left[w \left(\frac{x+i(\Gamma/2)}{\sigma\sqrt{2}} \right) \right]}{\sigma\sqrt{2\pi}} \quad (4.8.5)$$

Since the Gaussian distribution is assumed to be centred, the location parameters of the Voigt and the associated Lorentzian are always equal. The location parameter of the Voigt is therefore directly interpreted as the observed resonance energy E_R .

For a particular decay channel, where the decay products have mass numbers A_1 and A_2 , the chosen external radius r is given by

$$r = r_0(A_1^{1/3} + A_2^{1/3}), \quad (4.8.6)$$

where $r_0 = 1.2$.

Standard Gaussian, Lorentzian and Voigt lineshape are displayed in Figure 4.40 to qualitatively illustrate the effect of the Gaussian convolution. The

spectra in Figure 4.41 shows the dependence of the lineshape on the l -value (of the reaction products relative to one another) of decay. A multi-channel R-matrix fitting code was written to analyse the data and ultimately extract the yield, Γ and μ_V for each resonance observed in the focal plane spectra.

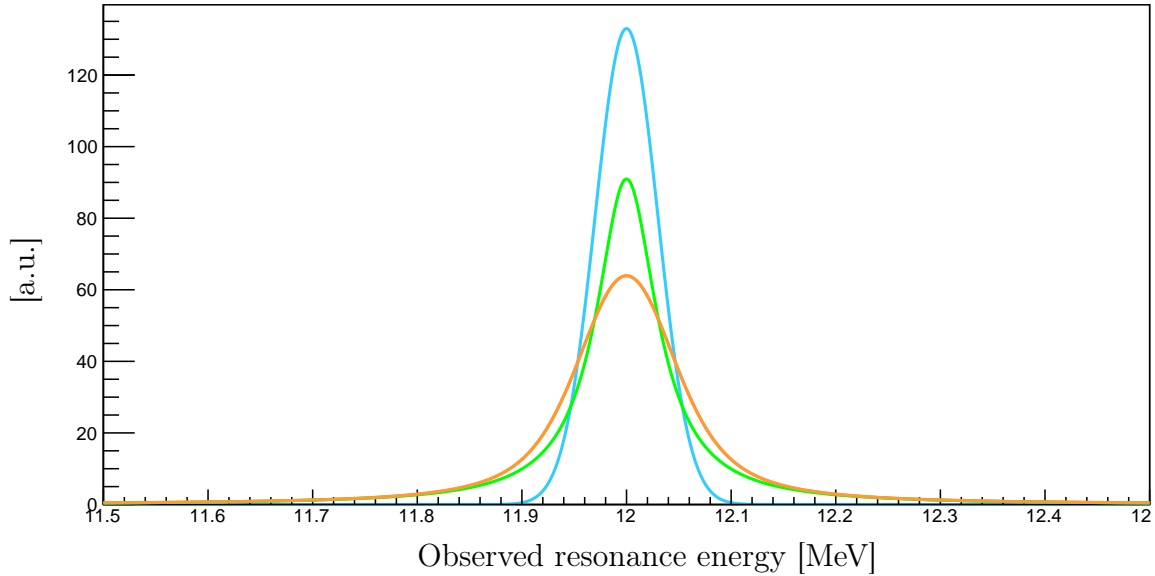


Figure 4.40: Examples of Gaussian, Lorentzian and Voigt lineshapes. The blue, orange and green functions correspond to the Gaussian, Lorentzian and Voigt lineshapes respectively.

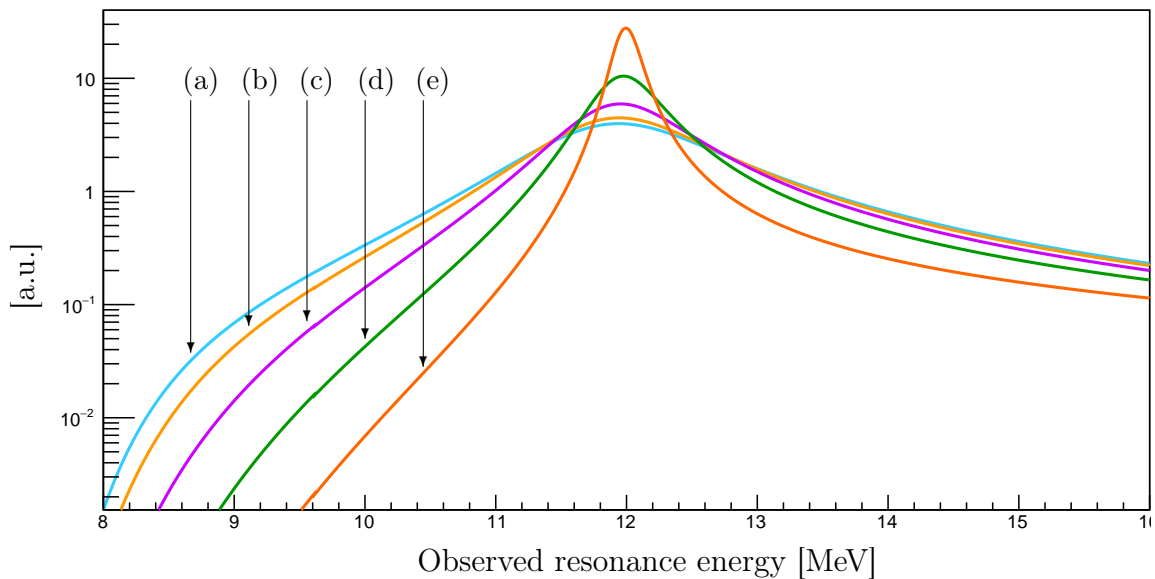


Figure 4.41: Voigt profiles with R-matrix lineshapes, showing the dependence of the width Γ on the l -value (of decay) dependent penetrability. The constant parameters are: $\sigma = 0.03$ and $\Gamma = 0.07$ and the L-values for the lineshapes are: (a) $L = 0$, (b) $L = 1$, (c) $L = 2$, (d) $L = 3$ and (e) $L = 4$.

4.8.1 Error Propagation

The error of the extracted yield, denoted σ_Y , is given by

$$\sigma_Y = \sqrt{\sigma_P^2 + \sigma_{fit}^2}, \quad (4.8.7)$$

where σ_P^2 and σ_{fit}^2 are the Poissonian and fit errors respectively. The covariance matrix of the fit, which provides the correlations between the parameters of the fit, is used to evaluate the fit error σ_{fit} of the extracted Yield.

For an R-matrix lineshape, the extracted observed width $\Gamma(E)$ is given by

$$\Gamma(E) = \sum_i^n 2P_{l,i}(E)\gamma_i, \quad (4.8.8)$$

where n is the amount of open channels. $P_{l,i}(E)$ is the penetrability, evaluated at energy E , of the i 'th channel with angular momentum l and γ_i is the associated reduced width.

The propagated error for the observed width, denoted σ_Γ , is consequently given by

$$\sigma_{\Gamma(E)} = \sqrt{\sum_i^n (2P_{l,i}(E)\sigma_{\gamma_i})^2}. \quad (4.8.9)$$

For a standard Voigt fit of a resonance, the error on the extracted observed width Γ is given by

$$\sigma_\Gamma = \sqrt{\sum_i^n (\sigma_{\Gamma_i})^2}. \quad (4.8.10)$$

4.8.2 Angular Momentum Conservation for (α, α')

The angular momentum conservation that governs inelastic scattering yields

$$\vec{j}_{proj} + \vec{j}_{targ} + \vec{l}_{proj} = \vec{j}_{ejec} + \vec{j}_{rec}, \quad (4.8.11)$$

where \vec{j} and \vec{l} denote total and orbital angular momenta respectively. The subscripts: proj, targ, ejec and rec correspond to the projectile, target, ejectile and recoil respectively. For (α, α') inelastic scattering, the angular momentum conservation is greatly simplified since the α -particle projectile is assumed to invariably remain in its ground state with spin and parity $j_{proj}^\pi = 0^+$:

$$j_{recoil} = |j_{targ} - l_{proj}|, |j_{targ} - l_{proj}| + 1, \dots, j_{targ} + l_{proj} \quad (4.8.12)$$

The primary target used for this experiment was Li_2CO_3 (with natural lithium) and therefore the angular momentum selection rules pertaining to

the (α, α') reaction for the following target nuclei are of interest: ^{16}O , ^{12}C , ^7Li and ^6Li , as shown below in Table 4.2.

α	+	^{16}O		\rightarrow	α	+	^{16}O
j_α		$j^{16}\text{O}$	l_α	\rightarrow	j_α		$j^{16}\text{O}$
0^+		0^+	0		0^+		0^+
			1				1^-
			2				2^+
			3				3^-
			\vdots				\vdots
α	+	^{12}C		\rightarrow	α	+	^{12}C
j_α		$j^{12}\text{C}$	l_α	\rightarrow	j_α		$j^{12}\text{C}$
0^+		0^+	0		0^+		0^+
			1				1^-
			2				2^+
			3				3^-
			\vdots				\vdots
α	+	^7Li		\rightarrow	α	+	^7Li
j_α		$j^7\text{Li}$	l_α	\rightarrow	j_α		$j^7\text{Li}$
0^+		$3/2^-$	0		0^+		$3/2^-$
			1				$1/2^+, 3/2^-, 5/2^+$
			2				$1/2^+, 3/2^-, 5/2^+, 7/2^-$
			3				$3/2^-, 5/2^+, 7/2^-, 9/2^+$
			\vdots				\vdots
α	+	^6Li		\rightarrow	α	+	^6Li
j_α		$j^6\text{Li}$	l_α	\rightarrow	j_α		$j^6\text{Li}$
0^+		1^+	0		0^+		1^+
			1				$0^-, 2^-$
			2				$1^+, 2^-, 3^+$
			3				$2^-, 3^+, 4^-$
			\vdots				\vdots

Table 4.2: The angular momentum selection rules for $^{16}\text{O}(\alpha, \alpha')$, $^{12}\text{C}(\alpha, \alpha')$, $^7\text{Li}(\alpha, \alpha')$ and $^6\text{Li}(\alpha, \alpha')$. The α -particle projectile is assumed to remain in its ground state.

4.8.3 Angular Momentum Conservation for Decay

Since one of the fundamental assumptions of R-matrix theory is the absence or unimportance of all processes in which more than two product nuclei are formed, the angular momentum selection rules of interest solely pertain to binary decay. The angular momentum conservation that governs the binary decay of particles yields

$$\vec{j}_R = \vec{j}_1 + \vec{j}_2 + \vec{l}, \quad (4.8.13)$$

where \vec{j}_1 and \vec{j}_2 are the angular momenta of the decay products respectively. The angular momentum of the resonance in the parent particle is denoted \vec{j}_R and \vec{l} is the relative angular momentum between the reaction products.

The channel spin s , which is defined as the coupled intrinsic angular momenta of the reaction products, is given by

$$s = |j_1 - j_2|, |j_1 - j_2| + 1, \dots, j_1 + j_2. \quad (4.8.14)$$

Under the angular momentum selection rules, the possible l -values of decay are restricted to

$$l = |s - j_R|, |s - j_R| + 1, \dots, s + j_R. \quad (4.8.15)$$

The parity relation describing the decay is given by

$$\pi_R = \pi_1 \pi_2 (-1)^l, \quad (4.8.16)$$

where π_1 and π_2 are the parities of the decay products and π_R denotes the parity of the resonance of the parent particle.

The primary target for this experiment was lithium carbonate (Li_2CO_3 , with natural lithium) and therefore the angular selection rules for various decay modes of ^{16}O , ^{12}C , ^7Li and ^6Li are considered, as summarised in the following Tables 4.3 to 4.6. If either of the decay products are assumed to invariably remain in a $J^\pi = 0^+$ state, as is the case for the α decay modes of ^{16}O , ^{12}C , the selection rules are greatly simplified.

In general, it is possible for a particular decay mode from a resonance to be comprised of multiple decay channels: each corresponding to a different l -value of decay. For this work, it is assumed that decay channels with the lowest l -value dominate a decay mode and the corresponding l -value is exclusively used in evaluating the penetrability. The dominance of low l -values is experimentally observed and verified [*citation]. Loosely speaking, this dominance can be partially attributed to the centrifugal barrier which favours lower l -value particles to penetrate through the potential barrier.

4.8.3.1 Decay Modes of ^{16}O

Only natural parity states/resonances are excited in $^{16}\text{O}(\alpha, \alpha')$, as shown in Table 4.2. For α_0 decay from ^{16}O , the selection rules are trivial as both the decay products have $j_1^\pi = j_2^\pi = 0^+$ spin and parity.

^{16}O	\rightarrow	α	$+$	^{12}C (g.s.)
$j_{^{16}\text{O}}$		j_α		$j_{^{12}\text{C}}$
0^+		0^+		0^+
1^-				0
2^+				1
3^-				2
\vdots				3
				\vdots

^{16}O	\rightarrow	α	$+$	^{12}C (2_1^+)
$j_{^{16}\text{O}}$		j_α		$j_{^{12}\text{C}}$
0^+		0^+		2^+
1^-				2
2^+				$1, 3$
3^-				$0, 2, 4$
\vdots				$1, 3, 5$
				\vdots

^{16}O	\rightarrow	p	$+$	^{15}N (g.s.)
$j_{^{16}\text{O}}$		j_p		$j_{^{15}\text{N}}$
0^+		$1/2^+$		$1/2^-$
1^-				$1 (s = 1)$
2^+				$0, 2 (s = 1)$
3^-				$1, 3 (s = 1)$
\vdots				$2, 4 (s = 1)$
				\vdots

Table 4.3: The angular momentum selection rules for the α_0 , α_1 and $p0$ decay modes of ^{16}O . For the α decay modes, the α -particle is assumed to remain in its ground state.

4.8.3.2 Decay Modes of ^{12}C

Only natural parity states/resonances are excited in $^{12}\text{C}(\alpha, \alpha')$, as shown in Table 4.2. For α_0 decay from ^{12}C , the selection rules are trivial as both the decay products have $j_1^\pi = j_2^\pi = 0^+$ spin and parity.

^{12}C	\rightarrow	α	$+$	^8Be (g.s.)
$j_{^{12}\text{C}}$		j_α		$j_{^8\text{Be}}$
0^+		0^+		0^+
1^-				0
2^+				1
3^-				2
\vdots				3
\vdots				\vdots
^{12}C	\rightarrow	α	$+$	^8Be (2_1^+)
$j_{^{12}\text{C}}$		j_α		$j_{^8\text{Be}}$
0^+		0^+		2^+
1^-				2
2^+				$1, 3$
3^-				$0, 2, 4$
\vdots				$1, 3, 5$
\vdots				\vdots
^{12}C	\rightarrow	p	$+$	^{11}B (g.s.)
$j_{^{12}\text{C}}$		j_p		$j_{^{11}\text{B}}$
0^+		$1/2^+$		$3/2^-$
1^-				$1 (s = 1)$
				$0, 2 (s = 1)$
				$2 (s = 2)$
2^+				$1, 3 (s = 1)$
				$1, 3 (s = 2)$
3^-				$2, 4 (s = 1)$
				$2, 4 (s = 2)$
\vdots				\vdots
\vdots				\vdots

Table 4.4: The angular momentum selection rules for the α_0 , α_1 and p_0 decay modes of ^{12}C . For the α decay modes, the α -particle is assumed to remain in its ground state.

4.8.3.3 Decay Modes of ${}^7\text{Li}$

${}^7\text{Li}$	\rightarrow	α	$+$	${}^3\text{H}$ (g.s.)	
$j_{7\text{Li}}$		j_α		$j_{3\text{H}}$	l
$1/2^+$		0^+		$1/2^+$	0
$3/2^-$					1
$5/2^+$					2
$7/2^-$					3
\vdots					\vdots

Table 4.5: The angular momentum selection rules for the α_0 decay mode of ${}^7\text{Li}$. The α -particle is assumed to remain in its ground state.

4.8.3.4 Decay Modes of ${}^6\text{Li}$

${}^6\text{Li}$	\rightarrow	α	$+$	${}^2\text{H}$ (g.s.)	
$j_{6\text{Li}}$		j_α		$j_{2\text{H}}$	l
0^-		0^+		1^+	1
1^+					0, 2
2^-					1, 3
3^+					2, 4
\vdots					\vdots

Table 4.6: The angular momentum selection rules for the α_0 decay mode of ${}^6\text{Li}$. The α -particle is assumed to remain in its ground state.

4.8.4 R-matrix Fitting

The R-matrix fitting code [44], which utilises both ROOT [45] and GSL [46] libraries, is capable of multi-channel lineshapes.

The assumptions made for the fitting:

- Only the resonances of target nuclei which can be validly excited, considering the angular momentum selection rules for (α, α') , are considered.
- In literature, there are resonances with multiple spin and parity possibilities. In accordance with the aforementioned angular momentum selection rules, only the valid spin-parities are considered. In the case that multiple valid spin-parities are proposed for a resonance, the spin and parity that corresponds to the smallest angular momentum transfer ΔL in the (α, α') reaction is considered. This is based on the fact that with a 0° measurement, the inelastic scattering favours lower ΔL .
- For each decay mode, multiple decay channels corresponding to different l -values of decay may exist. As previously mentioned, it is generally observed that the channel with the lowest l -value dominates the decay mode of a resonance. In such cases, the penetrability, and hence the R-matrix resonance lineshape, is calculated with the parameters and quantum numbers of the decay channel with the lowest l -value.
- As evidenced in Section 4.3, the background subtraction methods used effectively eliminate the systematic background of the focal plane spectra and hence no polynomial background functions are used.
- For the primary Li_2CO_3 target, the contributions from the contaminating nuclei, ^6Li , ^7Li and ^{12}C , are non-negligible and must be included in the fit.

The conventions and procedures for the fitting:

- The location parameter of each resonance must be within 2σ with respect to the error upon the observed resonance energy listed in literature. In the case that the error is not listed in literature, the initial value of the location parameter is set to the listed value and no limits are placed on the range of the location parameter.
- The Wigner limit given in Equation 2.2.9, whose derivation invokes the principle of causality, is imposed as an upper limit on the reduced width parameter of each decay channel. Decay channels from resonances in ^6Li and ^7Li are exempt from this limit as their lineshapes have been artificially altered. This is a purely kinematic effect: the magnets of

the K600 spectrometer have to be set to minimise dependence between the horizontal and vertical wireplane positions. This optimisation is dependent upon the mass of the target nucleus and was implemented for ^{16}O . Whilst this kinematic broadening is negligible for ^{12}C , it is significant for ^6Li and ^7Li due to the relatively larger mass difference. The R-matrix lineshapes for resonances in ^6Li and ^7Li purely serve as a background parameterisation and no accurate structural information from these nuclei can be extracted.

- The R-matrix fitting code, minimises the $\chi^2_{reduced}$ and is iteratively performed. If a fitted resonance is statistically insignificant, it is discarded from the following iteration of the fit.
- To obtain errors for the extracted parameters, the fit must converge to provide a valid covariance matrix.
- The experimental error of the wireplane position is assumed to be Gaussian and uniform across the range of the focal plane. The experimental error is determined to be 84.6(2) keV (FWHM) by fitting the well-resolved 12.049(2) MeV 0_4^+ state in ^{16}O , which has an experimentally observed width of 1.5(5) keV. This Gaussian error is fixed for all focal plane spectra.
- Whilst the R-matrix code is capable of multi-channel lineshapes, for this thesis, the singles spectrum fit is single channel as an initial approximation. The single channel parameterisation is sufficient to extract yields and widths, however the internal structural information of the nucleus cannot be reliably obtained. The exceptional cases are resonances which, for all intents and purposes, decay through a single-channel.
- To obtain the angular distributions of a decay mode from a particular resonance, an R-matrix fit is first applied on the focal plane spectrum of the decay mode from data corresponding to the entire CAKE. Focal plane spectra of the decay mode, each requiring coincidence with a particular ring of the CAKE, are then generated. To fit these focal plane spectra and extract the yields of each resonance per ring, the reduced widths and resonance energies are then fixed, leaving the amplitude as the sole free parameter of the Voigt profile for a resonance. This is implemented to ensure self-consistency within a particular decay mode.

Chapter 5

Results

A man should hear a little
music, read a little poetry, and
see a fine picture everyday of his
life, in order that worldly cares
may not obliterate the sense of
beautiful which God has
implanted in the human soul

Johann Wolfgang van Goethe

This chapter contains analysis results pertaining to the Li_2CO_3 target and in particular, focusing on the ^{16}O nucleus:

- R-matrix fit results of the singles and coincidence focal plane spectra.
- Angular distributions extracted from R-matrix fits of focal spectra with coincidence requirements with particular rings.
- Differential cross sections, calculated with CHUCK, for $^{16}\text{O}(\alpha, \alpha')$ and spin parties: $J^\pi = 0^+, 1^-, 2^+, 3^-, 4^+$ and 5^- .
- Angular distributions of particle decay, calculated with ANGCOR, for α_0 decay modes from resonances with spin parties: $J^\pi = 0^+, 1^-, 2^+, 3^-, 4^+, 5^-$.
- An in-depth analysis of the 11.520(4) MeV 2^+ , 12.049(2) MeV 0^+ , 14.926(2) MeV 2^+ and 15.097(5) MeV 0^+ resonances in ^{16}O .

Evidence which refutes the 0^+ nature of the 15.097(5) MeV resonance in ^{16}O is highlighted throughout this chapter.

5.1 R-matrix Fits of the Focal Plane Spectra

The fitted focal plane spectra correspond solely to the primary Li_2CO_3 target. The resonances are fitted with R-matrix Voigt lineshapes which assume a uniform Gaussian error of 84.6(2) keV (FWHM) across the excitation energy range of the focal plane. This error is fixed for all fits of focal plane spectra to provide self-consistency. Given the relatively large range of excitation energy, the focus of the fit results are limited to resonances of interest that are within the scope of this thesis. The coincident focal plane spectra correspond to the entire CAKE unless otherwise specified.

5.1.1 R-matrix Fit: Singles Spectrum

The R-matrix fit of the singles spectrum from the Li_2CO_3 target converges with $\chi^2_{\text{reduced}} = 0.90$, as displayed on Figures 5.1 - 5.12. The extracted parameters from the fit are summarised in Table 5.1. The Voigt R-matrix lineshapes, which are used to fit resonances, can be deconvolved to produce the pure Lorentzian R-matrix lineshapes of resonances. This provides a unique perspective of the excitation energy range which can be particularly illuminating for unresolved resonances. The 11.520(4) MeV 2^+ , 12.049(2) MeV 0^+ and 15.097(5) MeV 0^+ resonances in ^{16}O are highlighted in green, orange and blue respectively. The resonance displayed in purple denotes a resonance in ^{16}O which was independently suggested by Wakasa *et al.* [47] as necessary to fit this excitation energy region and our analysis concurs with this suggestion.

The observed 162(4) keV total width of the 15.097(5) MeV 0^+ state in ^{16}O , from this experiment, agrees well with the 166(30) keV value listed in literature.

Singles spectrum fit of $^{16}\text{O}(\alpha, \alpha')$						
E_R [MeV] (literature)	Width [keV] (literature)	E_R [MeV] (this work)	J^π	l	Yield	Width $\Gamma(E_R)$
11.520(4)	71(3)	11.520(9)	2^+	2	394336(1983)	80.2967(9)
12.049(2)	1.5(5)	12.049(9)	0^+	0	482624(726)	5(1)
12.440(2)	91(6)	12.446(8)	1^-	1	61154(1811)	98(5)
13.020(10)	150(10)	13.00(8)*	2^+	2	270819(10502)	98(5)
-	-	13.588(28)	0^+	0	18274(1999)	502(44)
13.090(8)	130(5)	13.074(8)	1^-	1	117180(4909)	160(6)
14.032(15)	185(35)	14.003(8)	0^+	0	272827(4943)	178(4)
14.926(2)	54(5)	14.930(8)	2^+	2	80437(320)	101(1)
15.097(5)	166(30)	15.076(7)	0^+	0	197336(2939)	162(4)

Table 5.1: Extracted fit parameters from the singles spectrum fit of $^{16}\text{O}(\alpha, \alpha')$. *Extracted resonance energy parameter which has converged at their respective 2σ limits.

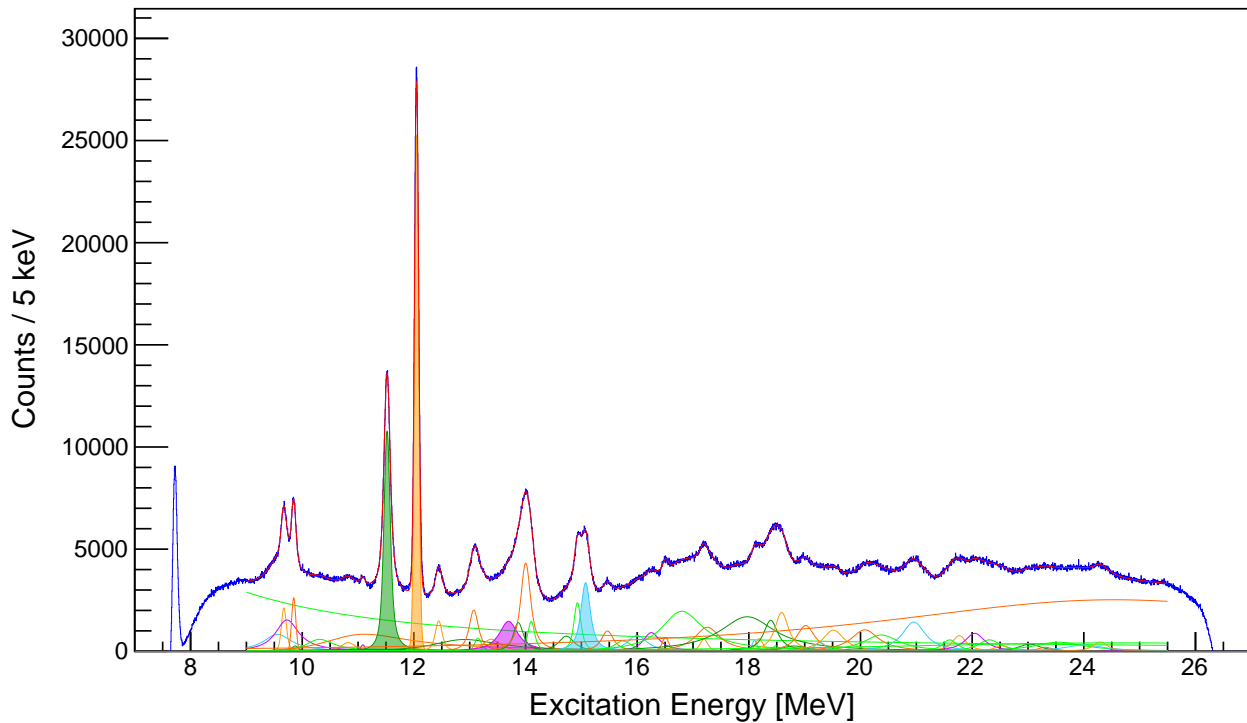


Figure 5.1: Complete singles spectrum from the Li_2CO_3 target with an R-matrix fit for resonances in ${}^6,7\text{Li}$, ${}^{12}\text{C}$ and ${}^{16}\text{O}$. The 11.520(4) MeV 2^+ , 12.049(2) MeV 0^+ and 15.097(5) MeV 0^+ resonances in ${}^{16}\text{O}$ are highlighted in green, orange and blue respectively. The resonance displayed in purple denotes a resonance in ${}^{16}\text{O}$ suggested by Wakasa *et al.* [47].

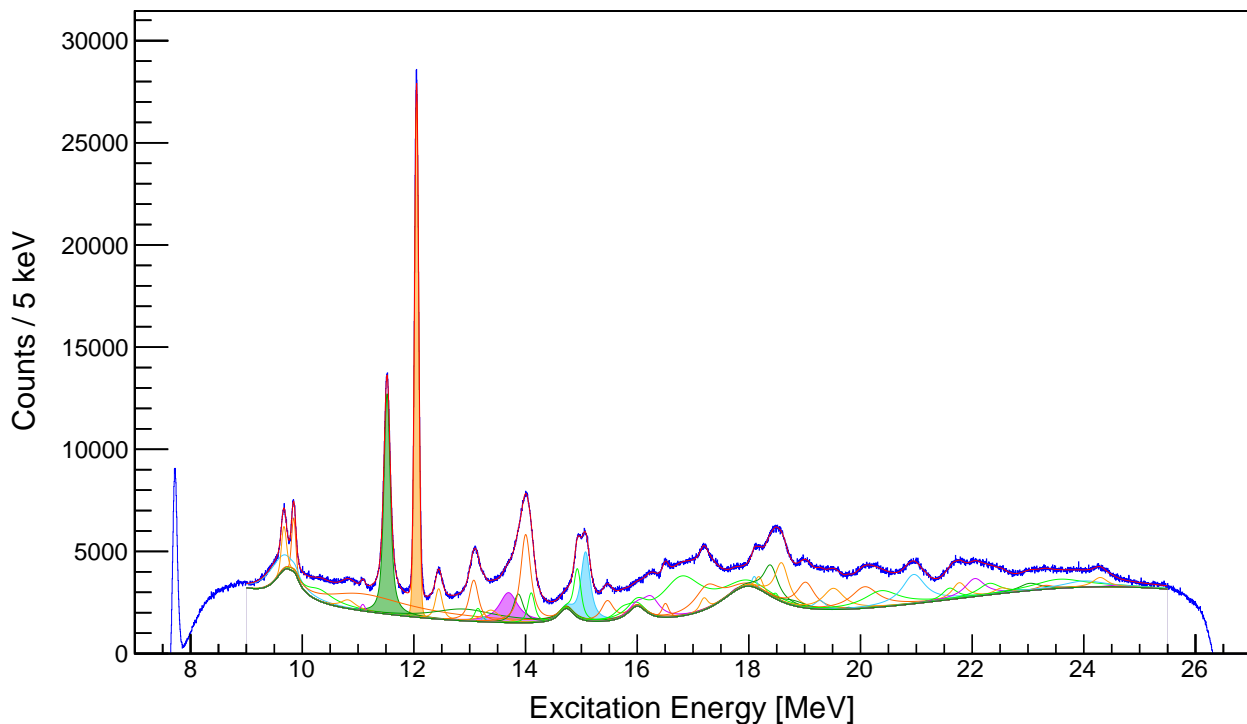


Figure 5.2: Complete singles spectrum from the Li_2CO_3 target with the ${}^{16}\text{O}$ and ${}^{12}\text{C}$ resonances superimposed upon the lithium resonances.

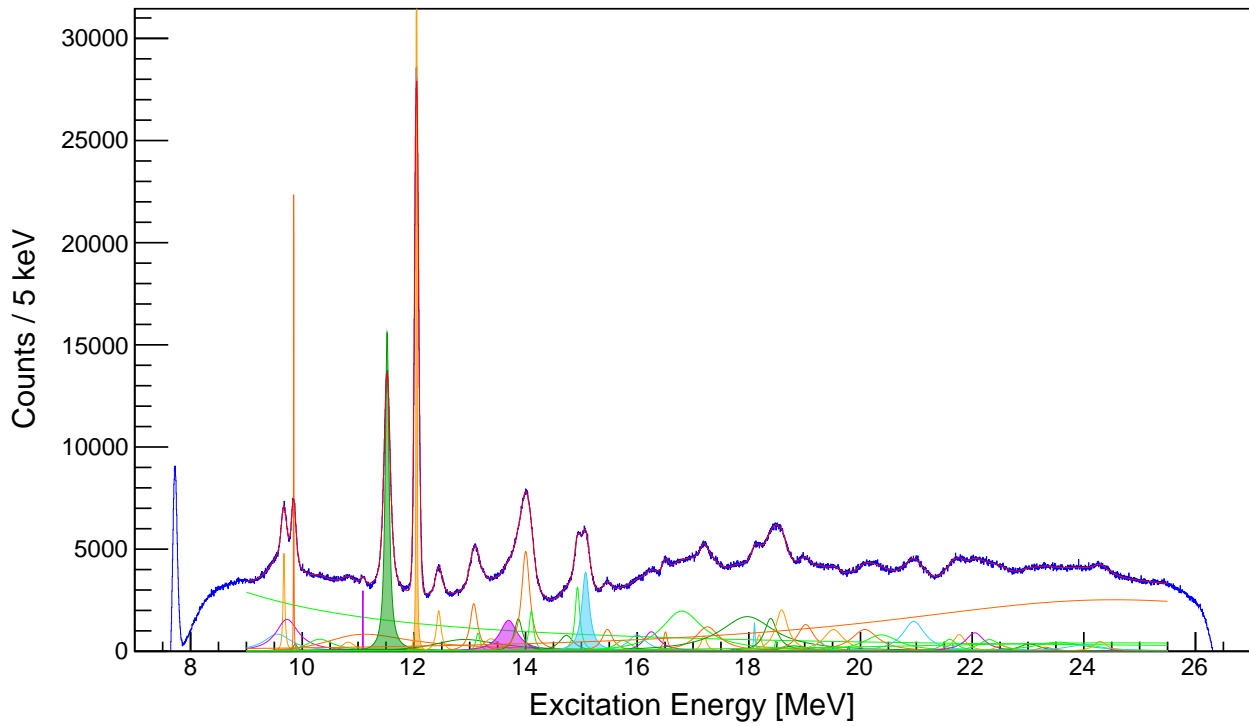


Figure 5.3: Complete singles spectrum from the Li_2CO_3 target with Lorentzian resonance line-shapes which are deconvolved from the fitted Voigt lineshapes.

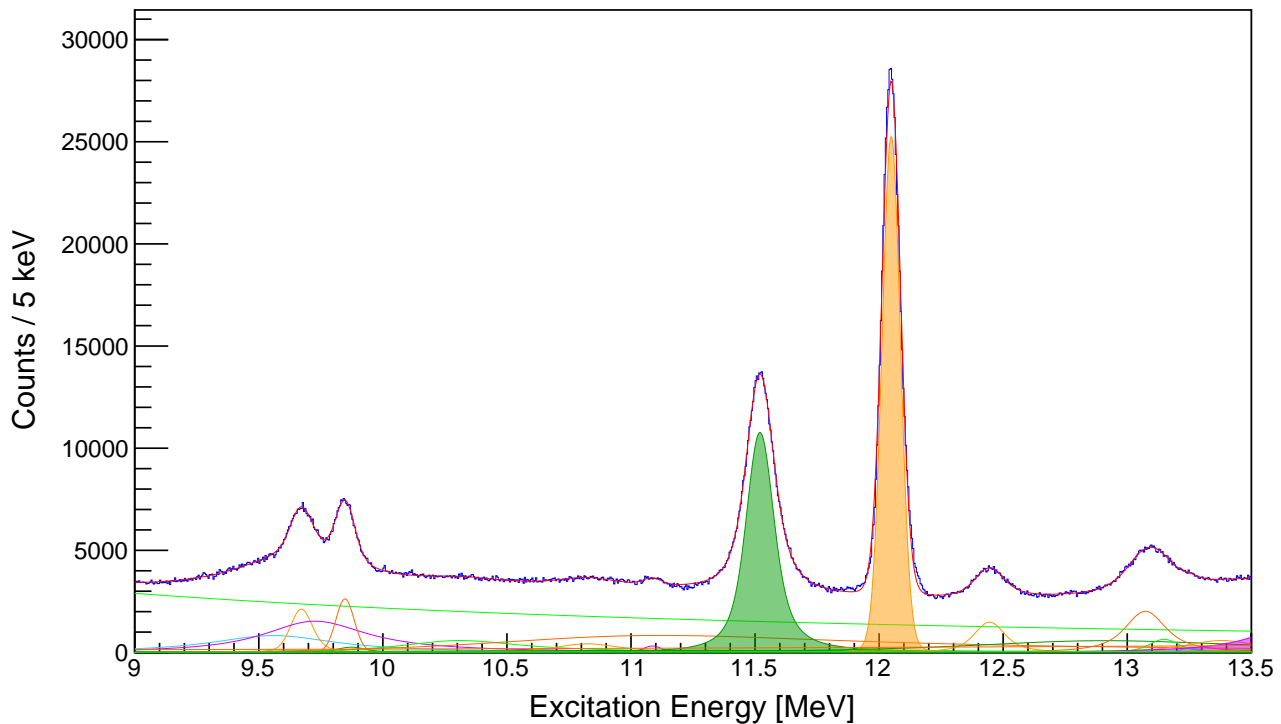


Figure 5.4: Singles spectrum from the Li_2CO_3 target with an R-matrix fit, displayed over an excitation energy range: $9.0 \text{ MeV} < E_x < 13.5 \text{ MeV}$.

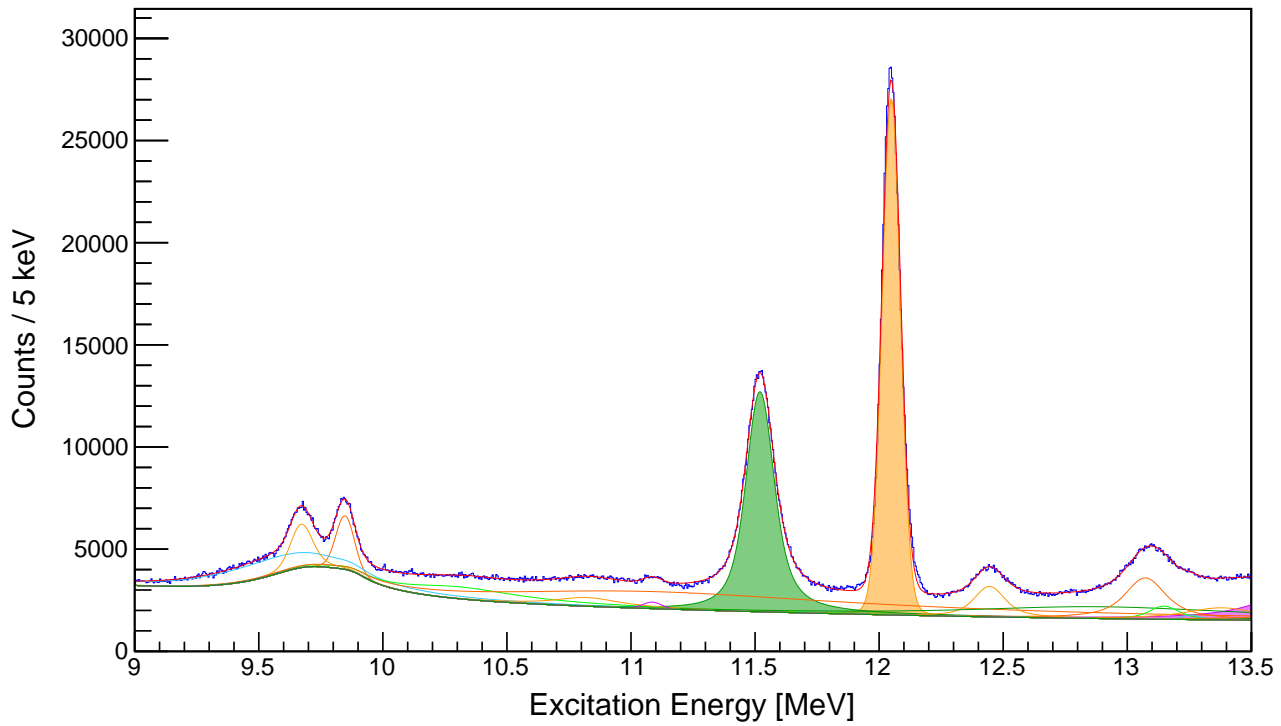


Figure 5.5: Singles spectrum from the Li_2CO_3 target with the ^{16}O and ^{12}C resonances superimposed upon the lithium resonances, displayed over an excitation energy range: $9.0 \text{ MeV} < E_x < 13.5 \text{ MeV}$.

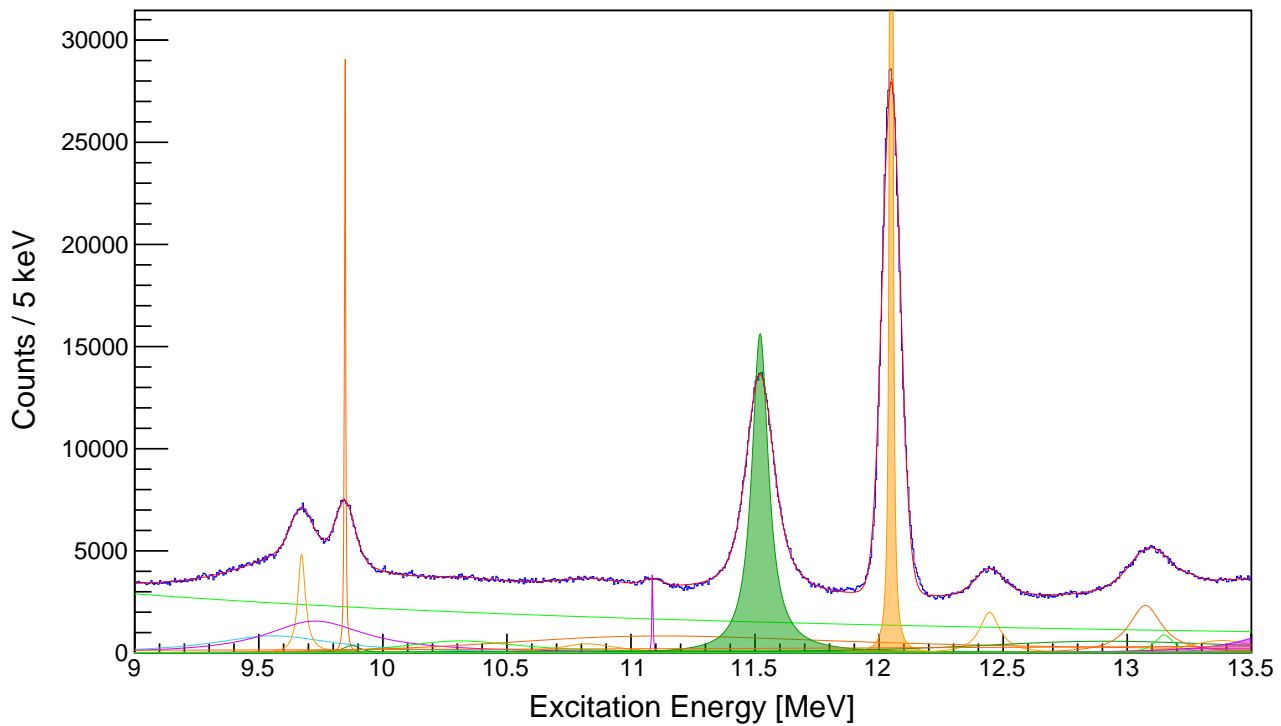


Figure 5.6: Singles spectrum from the Li_2CO_3 target with Lorentzian resonance line-shapes which are deconvolved from the fitted Voigt lineshapes, displayed over an excitation energy range: $9.0 \text{ MeV} < E_x < 13.5 \text{ MeV}$.

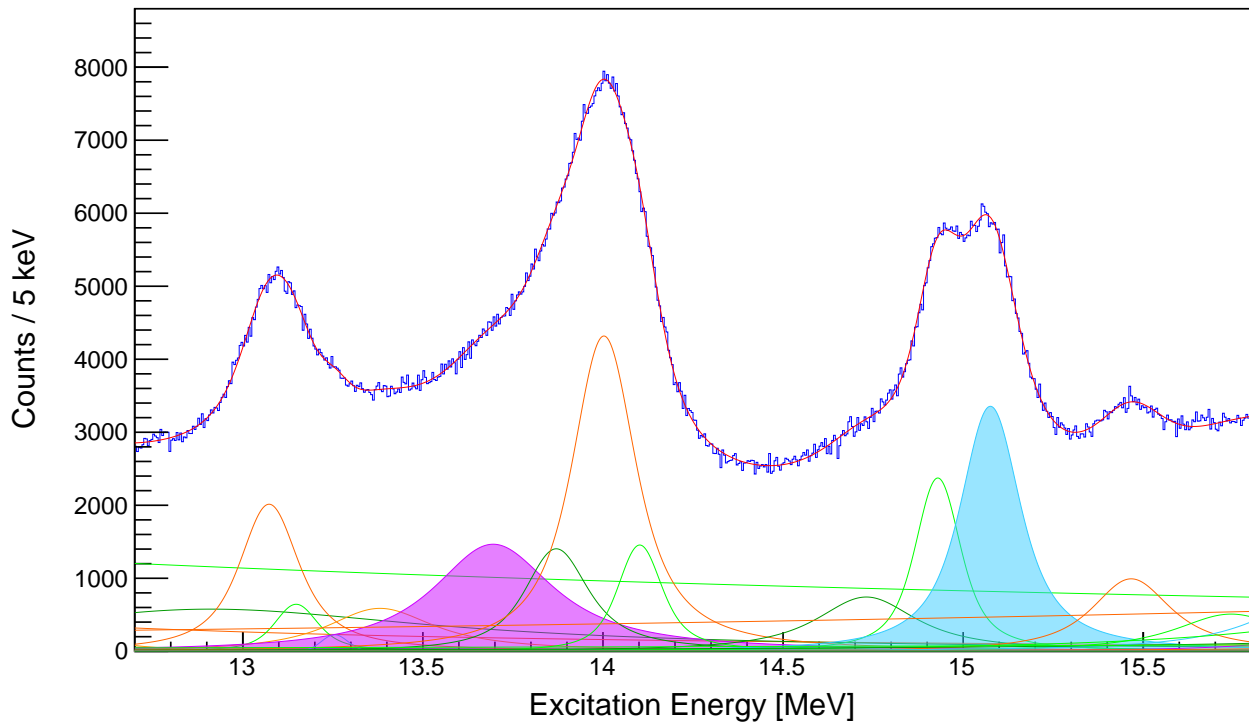


Figure 5.7: Singles spectrum from the Li_2CO_3 target with an R-matrix fit, displayed over an excitation energy range: $12.7 \text{ MeV} < E_x < 15.8 \text{ MeV}$.

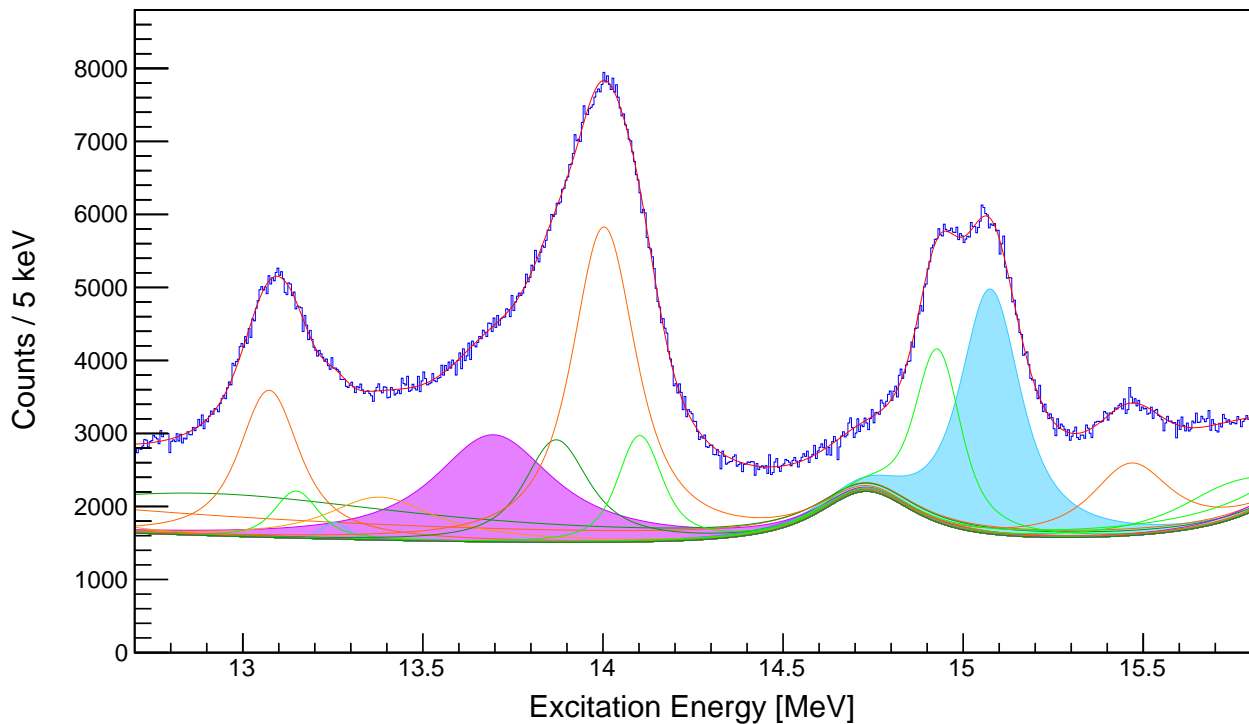


Figure 5.8: Singles spectrum from the Li_2CO_3 target with the ^{16}O and ^{12}C resonances superimposed upon the lithium resonances, displayed over an excitation energy range: $12.7 \text{ MeV} < E_x < 15.8 \text{ MeV}$.

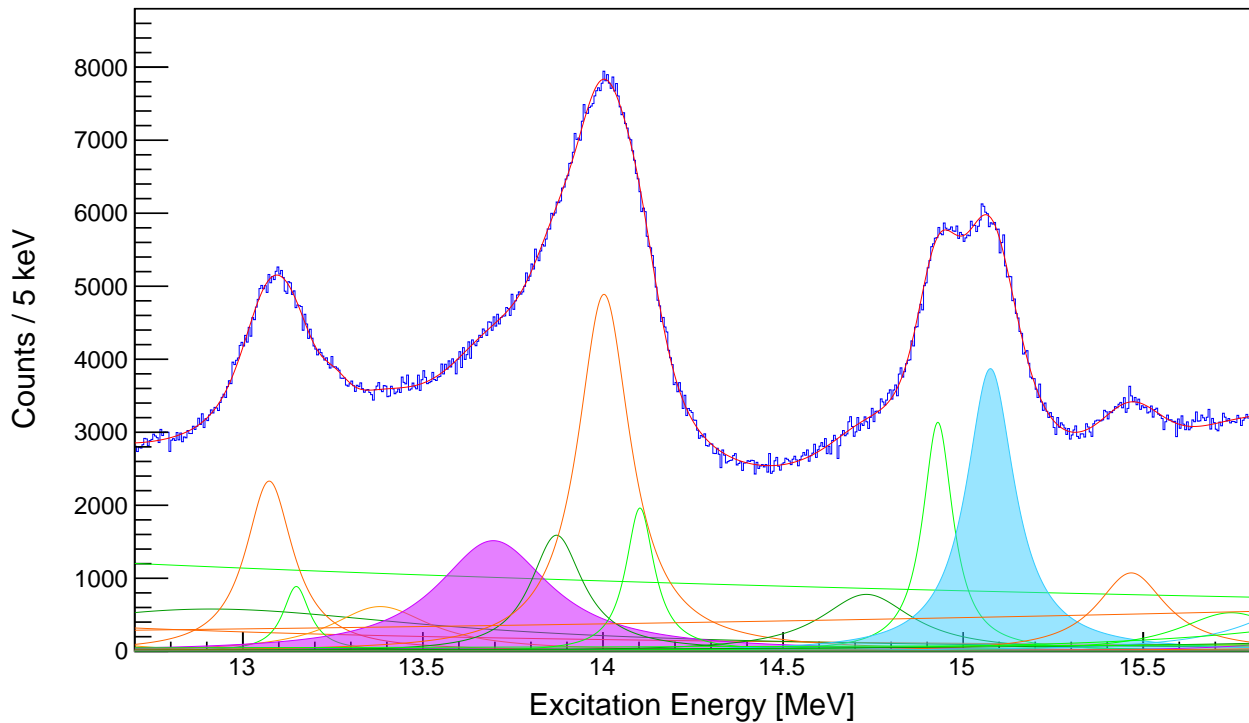


Figure 5.9: Singles spectrum from the Li_2CO_3 target with Lorentzian resonance line-shapes which are deconvolved from the fitted Voigt lineshapes, displayed over an excitation energy range: $12.7 \text{ MeV} < E_x < 15.8 \text{ MeV}$.

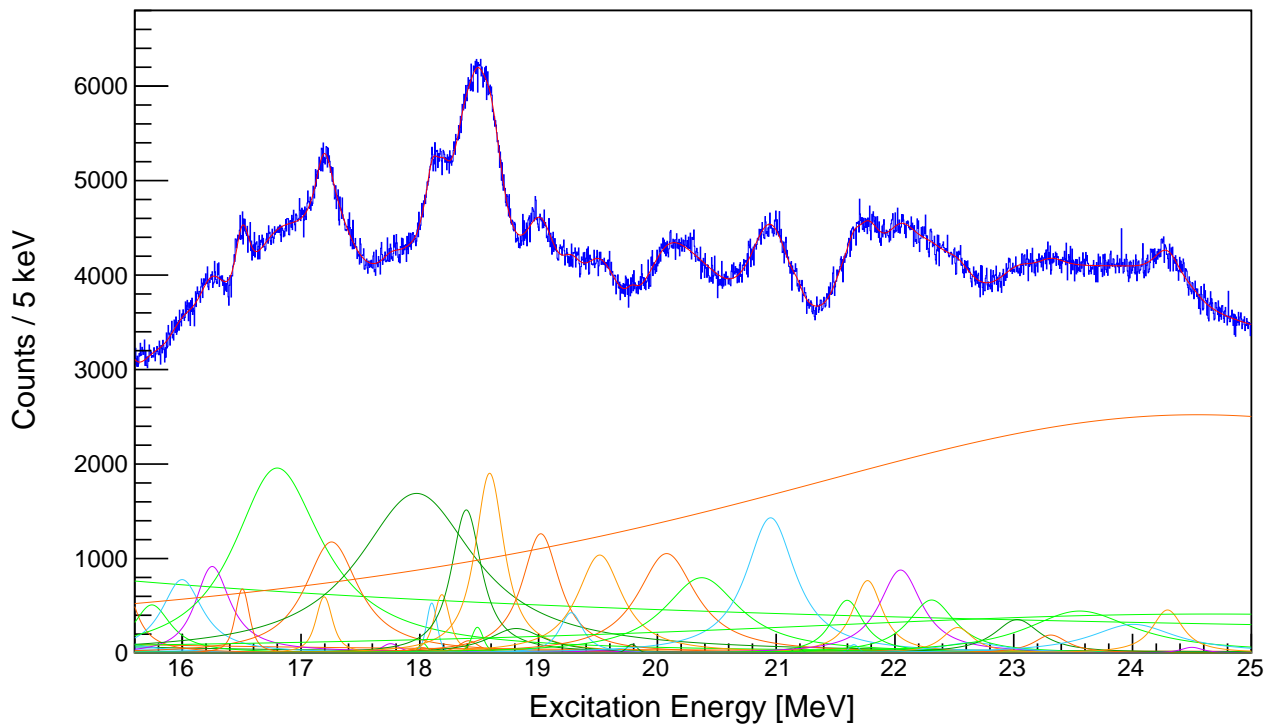


Figure 5.10: Singles spectrum from the Li_2CO_3 target with an R-matrix fit, displayed over an excitation energy range: $15.6 \text{ MeV} < E_x < 25.0 \text{ MeV}$.

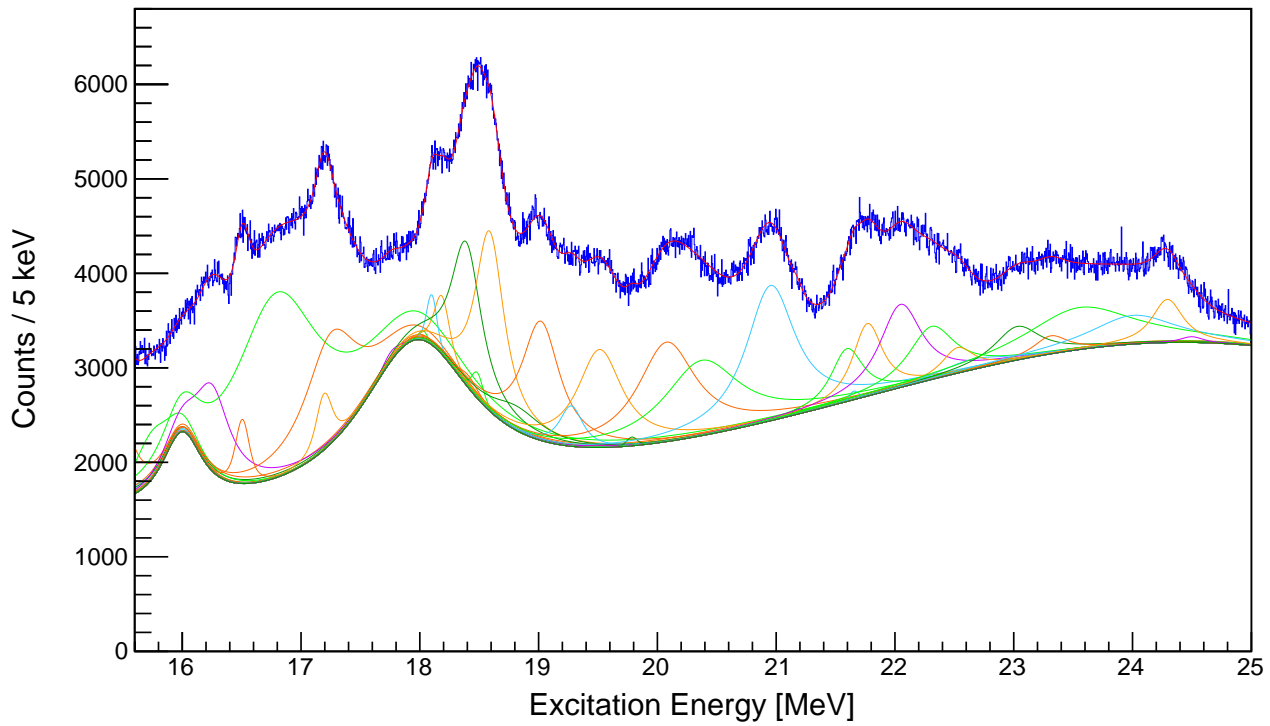


Figure 5.11: Singles spectrum from the Li_2CO_3 target with the ^{16}O and ^{12}C resonances superimposed upon the lithium resonances, displayed over an excitation energy range: $15.6 \text{ MeV} < E_x < 25.0 \text{ MeV}$.

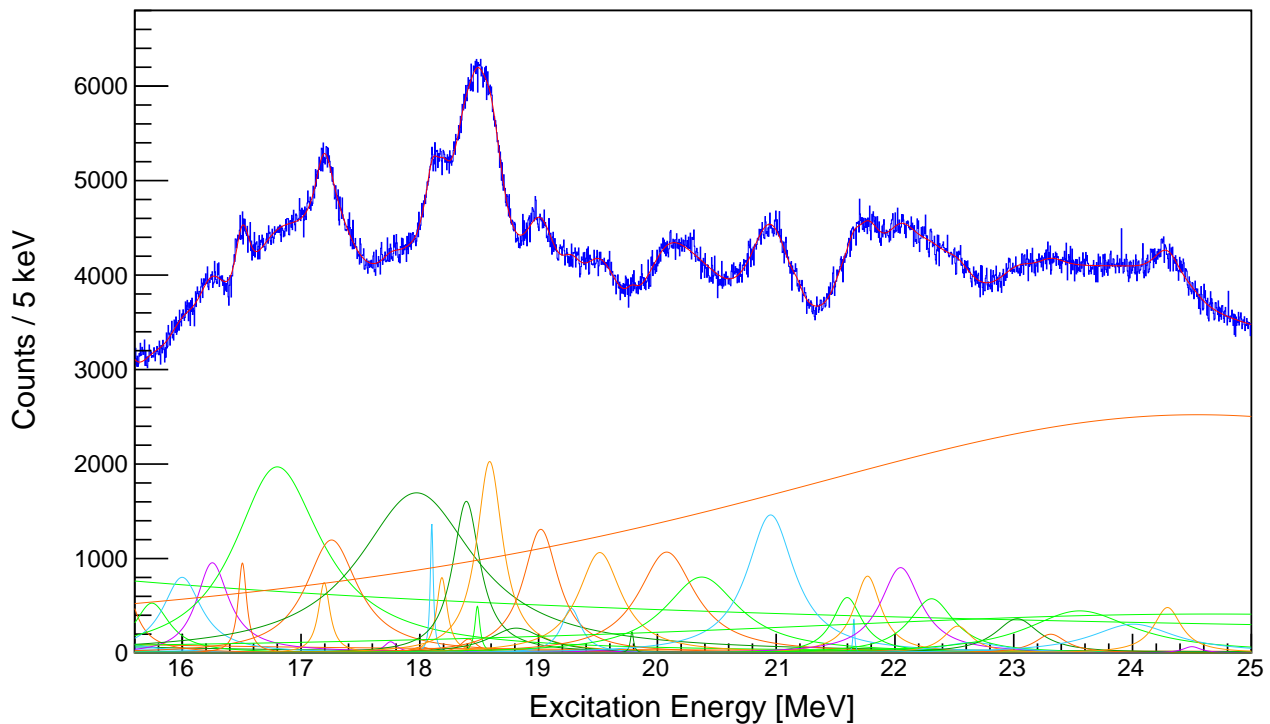


Figure 5.12: Singles spectrum from the Li_2CO_3 target with Lorentzian resonance line-shapes which are deconvolved from the fitted Voigt lineshapes, displayed over an excitation energy range: $15.6 \text{ MeV} < E_x < 25.0 \text{ MeV}$.

5.1.2 R-matrix Fit: α_0 decay mode of ^{16}O

The focal spectra from the Li_2CO_3 target, with ring-dependent energy gates upon the α_0 decay line, are fitted with R-matrix Voigt lineshapes. These spectra are displayed over various excitation energy ranges on Figures 5.13 - 5.16. The extracted parameters from the fit are summarised in Table 5.2.

From the α_0 decay mode spectrum, the total width of the 15.097(5) MeV 0^+ state is observed to be 164(5) keV (assuming the α_0 decay mode dominates the resonance). This agrees well with the 166(30) keV value listed in literature. The 162(4) keV total width of this state (obtained from the singles spectrum), suggests that the α_0 decay mode should completely dominate the decay of this resonance. There appears to be, however, a strong α_1 decay mode from this resonance with respect to the α_0 decay mode (see Section 5.1.3).

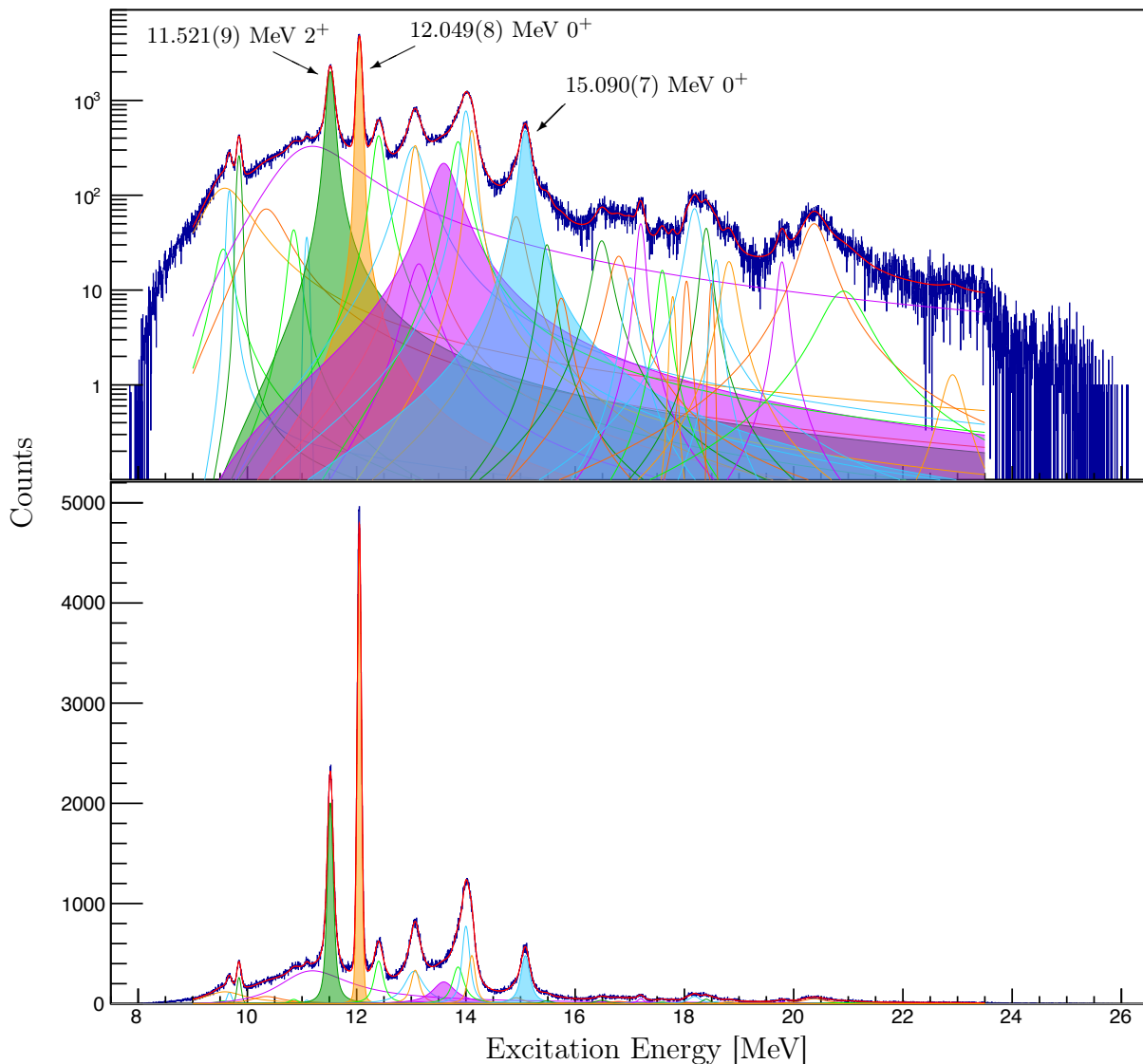


Figure 5.13: The complete α_0 decay mode spectrum of ^{16}O from the Li_2CO_3 target. The resonance highlighted in purple is a resonance proposed to fit the excitation energy region, which was initially suggested by Wakasa *et al.* [47]. The fit converged with $\chi^2_{reduced} = 1.37$

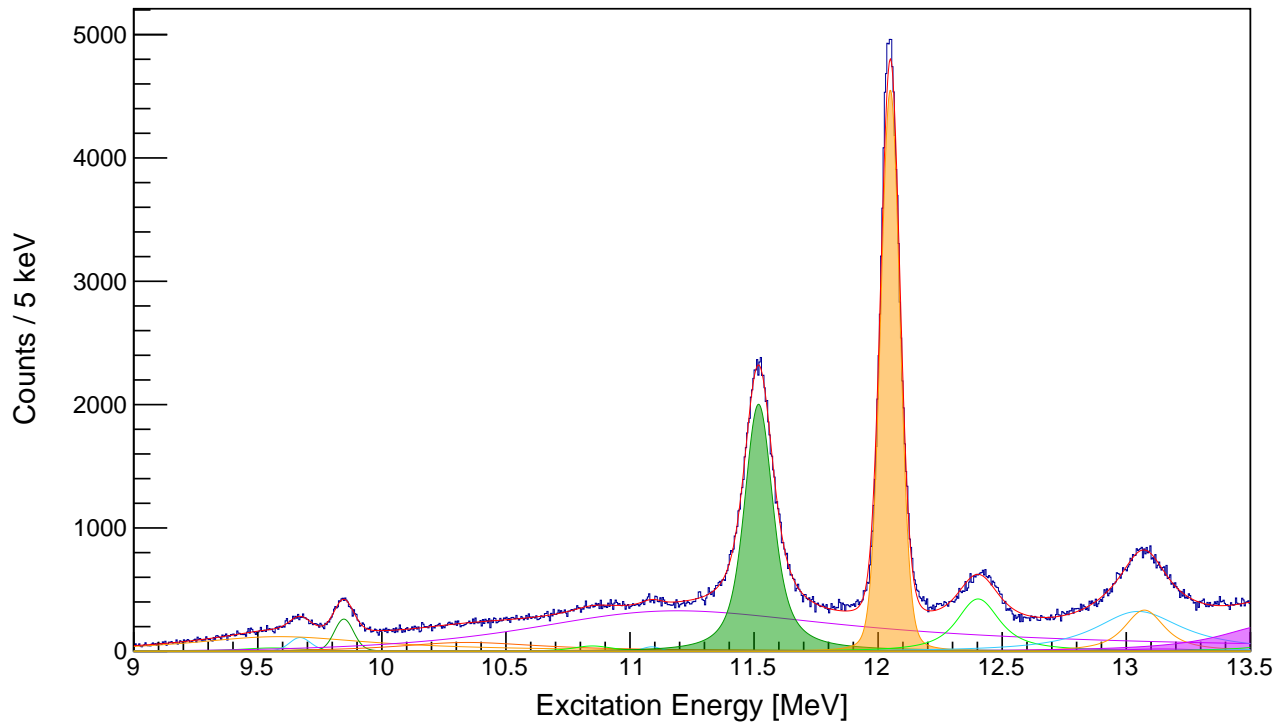


Figure 5.14: The α_0 decay mode spectrum of ^{16}O from the Li_2CO_3 target, displayed over an excitation energy range: $9.0 \text{ MeV} < E_x < 13.5 \text{ MeV}$.

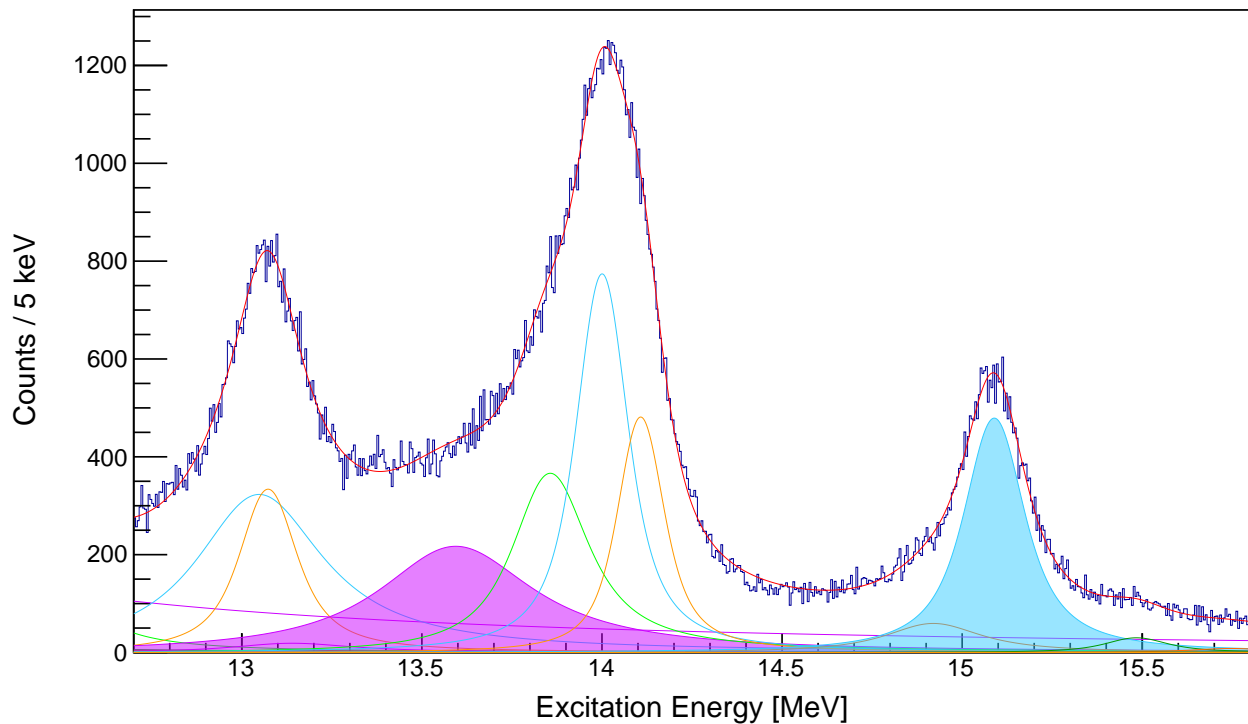


Figure 5.15: The α_0 decay mode spectrum of ^{16}O from the Li_2CO_3 target, displayed over an excitation energy range: $12.7 \text{ MeV} < E_x < 15.8 \text{ MeV}$.

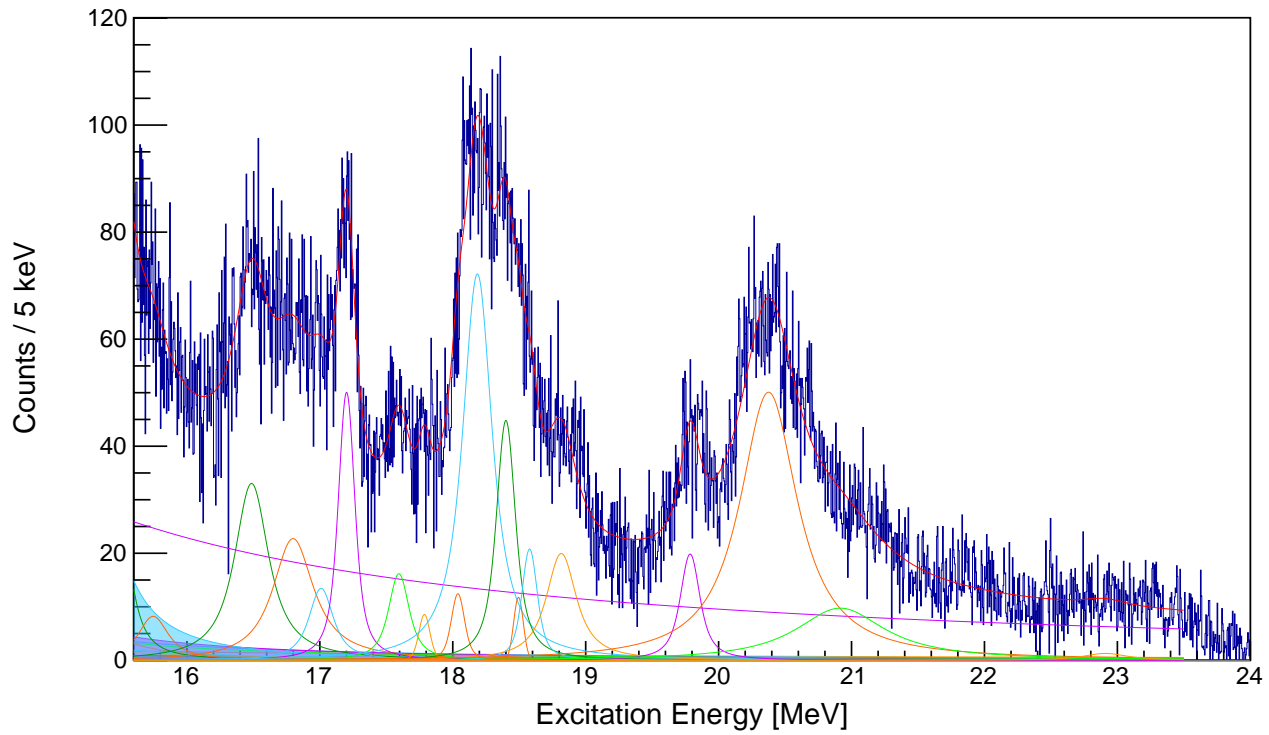


Figure 5.16: The α_0 decay mode spectrum of ^{16}O from the Li_2CO_3 target, displayed over an excitation energy range: $15.6 \text{ MeV} < E_x < 24.0 \text{ MeV}$.

α_0 decay mode of ^{16}O									
E_R [MeV] (literature)	Width [keV] (literature)	E_R [MeV] (this work)	J^π	l	Yield	Reduced width γ	Penetrability $P_l(E_R)$	Width [keV] $\Gamma(E_R)$	Wigner ratio θ_W^2
11.260	2500	11.340(9)	0^+	0	177904(6252)	0.52(1)	1.72908	$1.58(6) \times 10^3$	0.59(3)
11.520(4)	71(3)	11.521(9)	2^+	2	74614(842)	0.0405(6)	1.00279	81(1)	0.00401(8)
12.049(2)	1.5(5)	12.049(8)	0^+	0	94287(341)	0.0027(1)	2.18583	12(1)	$1.75(9) \times 10^{-5}$
12.440(2)	91(6)	12.404(8)	1^-	1	25590(564)	0.040(1)	2.10291	167(6)	0.0039(2)
13.020(8)	150(10)	12.995(15)	2^+	2	42606(4575)	0.11(1)	1.92005	41(3)	0.0023(7)
13.090(8)	130(5)	13.074(24)	1^-	1	18751(6751)	0.031(7)	2.48193	153(35)	0.0023(6)
14.032(15)	185(35)	14.001(9)	0^+	0	38538(3653)	0.020(2)	3.2111	129(11)	0.0010(1)
15.097(5)	166(30)	15.090(7)	0^+	0	28483(584)	0.0223(7)	3.68231	164(5)	0.00122(5)

Table 5.2: Extracted fit parameters from the α_0 decay mode of ^{16}O .

5.1.3 R-matrix Fit: α_1 decay mode of ^{16}O

The focal spectra from the Li_2CO_3 target, with ring-dependent energy gates upon the α_1 decay line, are fitted with R-matrix Voigt lineshapes. These spectra are displayed over various excitation energy ranges on Figures 5.17 - 5.20. The extracted parameters from the fit are summarised in Table 5.3.

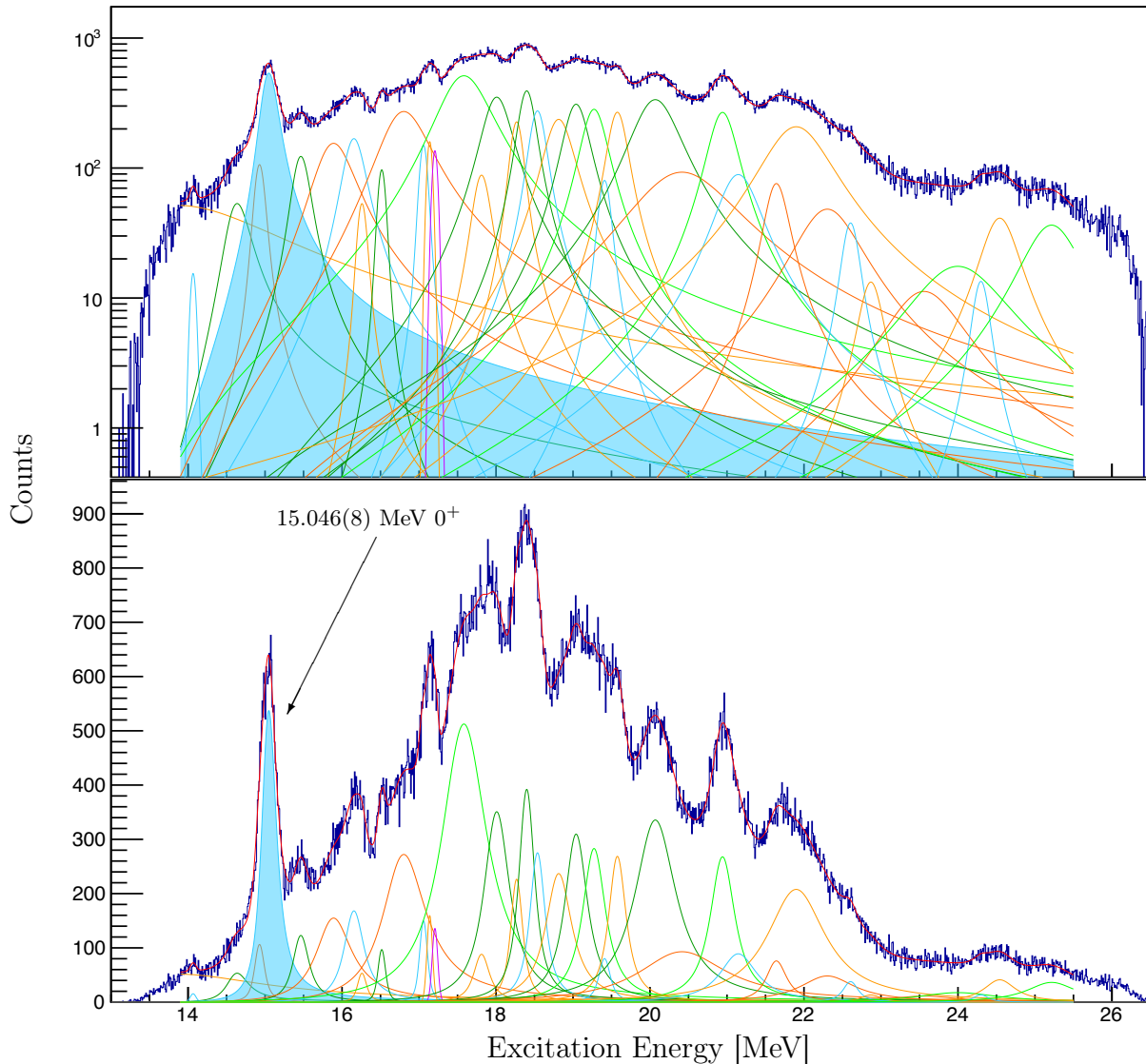


Figure 5.17: The complete α_1 decay mode spectrum of ^{16}O from the Li_2CO_3 target. The fit converged with $\chi_{reduced}^2 = 1.10$.

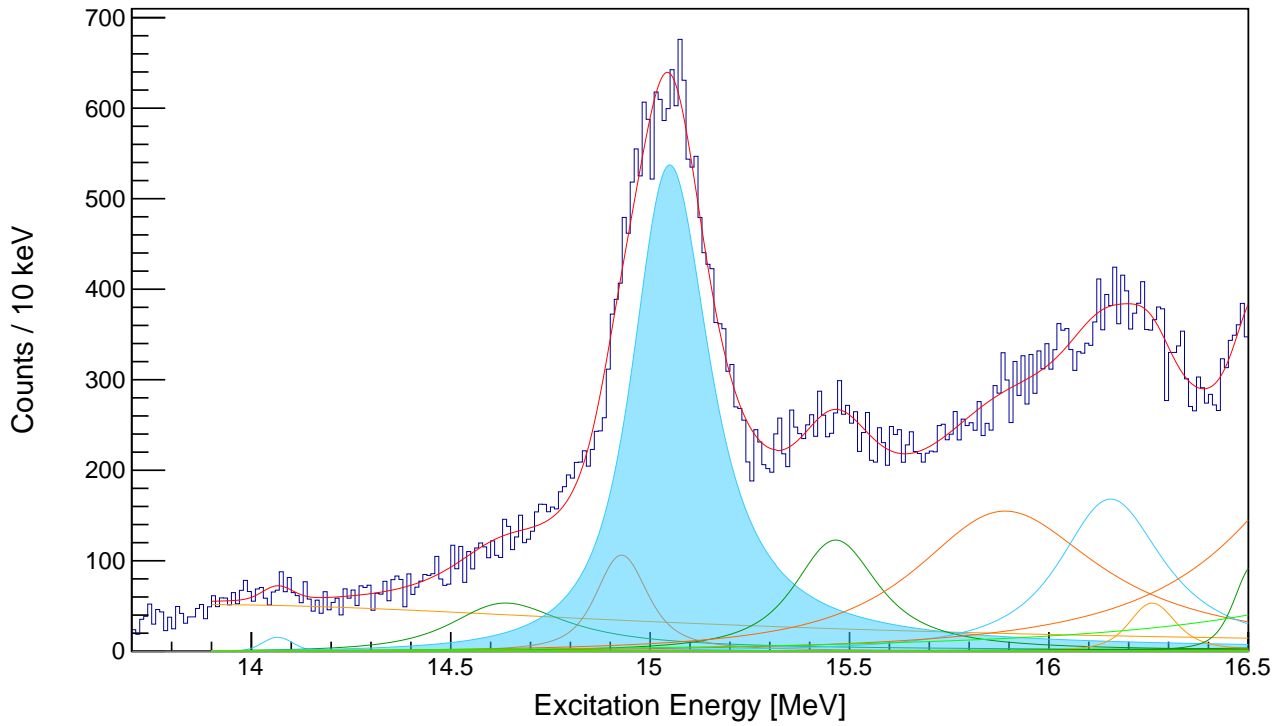


Figure 5.18: The α_1 decay mode spectrum of ^{16}O from the Li_2CO_3 target, displayed over an excitation energy range: $13.7 \text{ MeV} < E_x < 16.5 \text{ MeV}$.

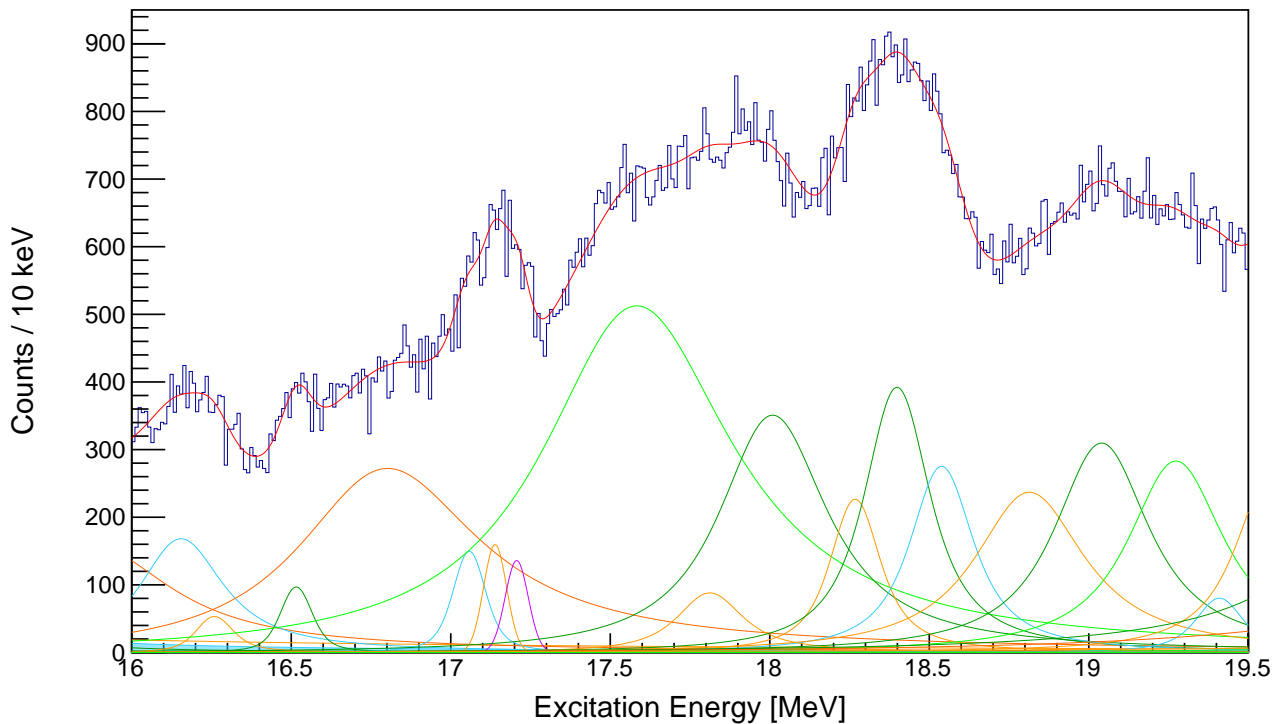


Figure 5.19: The α_1 decay mode spectrum of ^{16}O from the Li_2CO_3 target, displayed over an excitation energy range: $16.0 \text{ MeV} < E_x < 21.0 \text{ MeV}$.

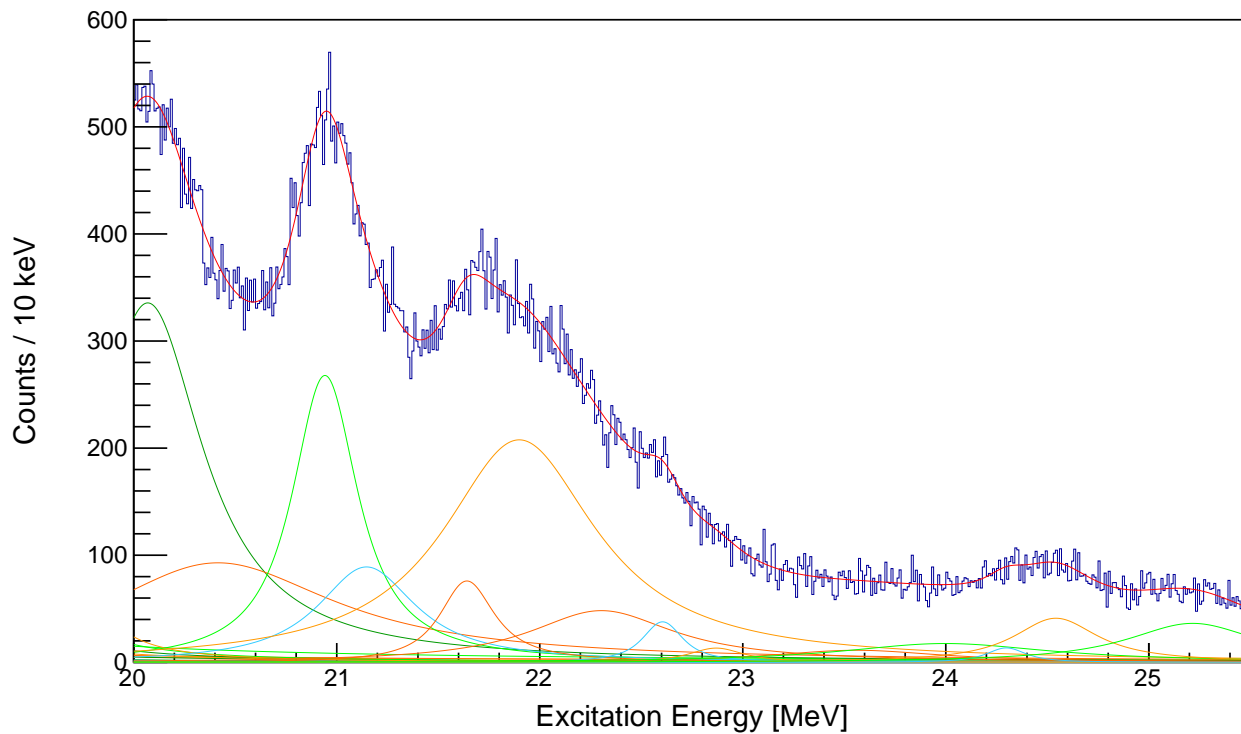


Figure 5.20: The α_1 decay mode spectrum of ^{16}O from the Li_2CO_3 target, displayed over an excitation energy range: $20.0 \text{ MeV} < E_x < 25.5 \text{ MeV}$.

α_1 decay mode of ^{16}O									
E_R [MeV] (literature)	Width [keV] (literature)	E_R [MeV] (this work)	J^π	l	Yield	Reduced width γ	Penetrability $P_l(E_R)$	Width [keV] $\Gamma(E_R)$	Wigner ratio θ_W^2
14.926(2)	54(5)	14.930(10)	2^+	1	2294(827)	0.05(2)	1.11077	106(45)	0.006(3)
15.097(5)	166(30)	15.046(8)	0^+	2	25810(836)	0.22(1)	0.485618	216(10)	0.121(7)

p_0 decay mode of ^{16}O									
E_R [MeV] (literature)	Width [keV] (literature)	E_R [MeV] (this work)	J^π	l	Yield	Reduced width γ	Penetrability $P_l(E_R)$	Width [keV] $\Gamma(E_R)$	Wigner ratio θ_W^2
14.926(2)	54(5)	14.929(8)	2^+	1	5203	0.041(5)	0.483927	40(5)	0.00026(17)

Table 5.3: Extracted fit parameters from the α_0 and p_0 decay modes of ^{16}O .

5.1.4 R-matrix Fit: p_0 decay mode of ^{16}O

The focal spectra from the Li_2CO_3 target, with ring-dependent energy gates upon the p_0 decay line, are fitted with R-matrix Voigt lineshapes, as displayed in Figure 5.21. The p_0 decay mode is not of particular interest for the scope of this thesis, however a significant result is that the 15.097(5) MeV 0^+ resonance in ^{16}O possesses a negligible p_0 branching ratio. The extracted parameters from the fitted 14.926(2) MeV 2^+ resonance in ^{16}O (see Table 5.3) are insightful as the resonance is relatively well resolved in this experiment. The well known characteristics of this resonance provide us with a good opportunity to assess the results of the R-matrix fitting code. From the p_0 decay mode spectrum, the total width of this resonance is observed to be 40(5) keV (assuming the p_0 decay mode dominates the resonance). This agrees well with the 54(5) keV value listed in literature.

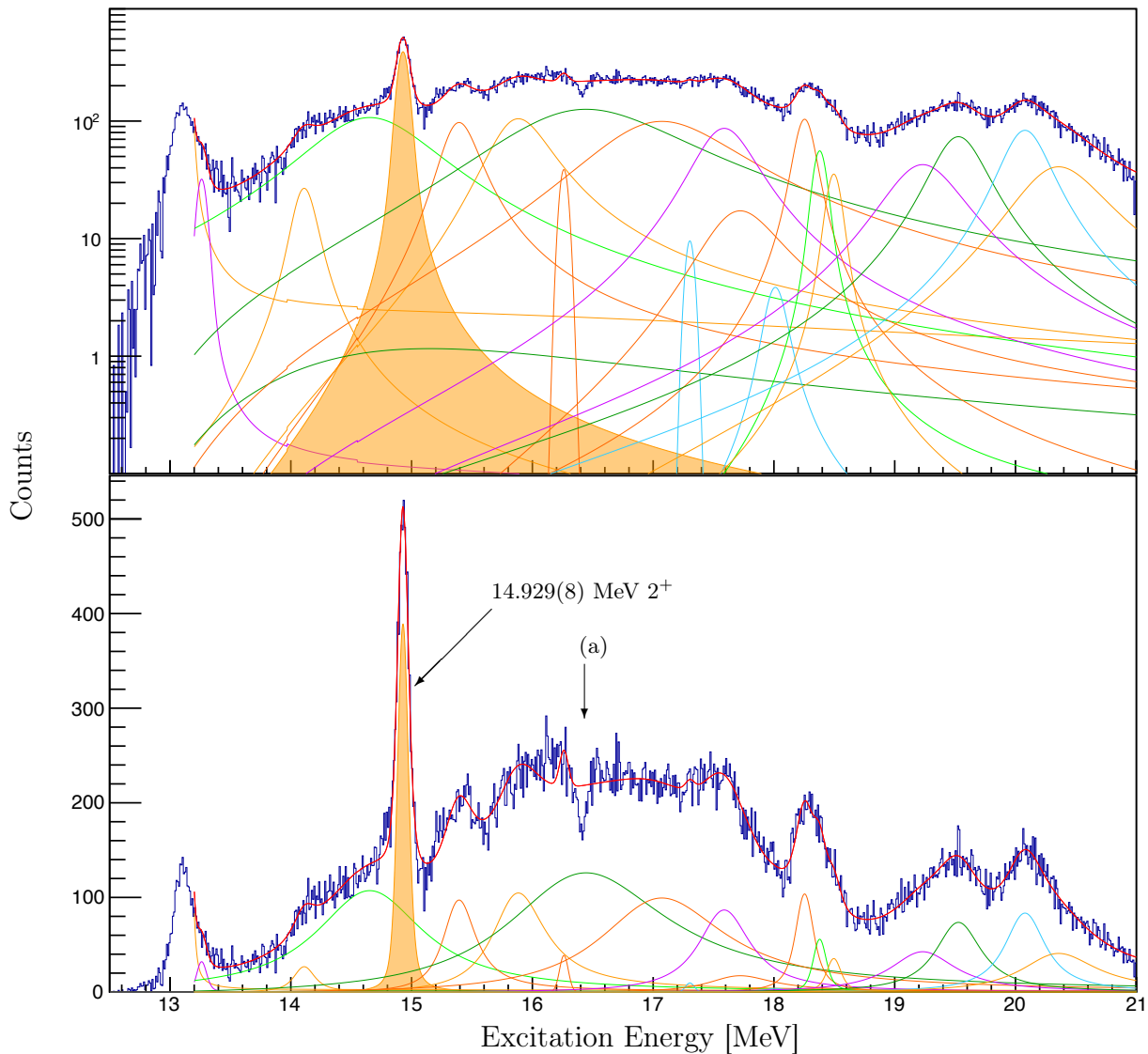


Figure 5.21: The complete α_1 decay mode spectrum of ^{16}O from the Li_2CO_3 target. The sharp dip in the spectrum, denoted (a), is verified to not possess systemic origins. The fit converged with $\chi^2_{reduced} = 1.29$

The sharp dip in the spectrum, denoted (a) in spectrum 5.21, has been verified to not possess systemic origins such as the wireplane detection efficiencies (see Section 3.3.3). It has also been verified to not stem from the ^{12}C background by analysing the data from the ^{12}C target. The analysis of this feature is beyond the scope of this thesis.

5.2 Branching Ratios of Charged Particle Decay

The 0^+ nature of the 12.049(2) MeV state in ^{16}O enables a trivial calculation of the branching ratios of the decay modes. Since there is no momentum vector with which to polarise the recoil nucleus, all subsequent decay channels exhibit isotropy. The branching ratios (B_i 's) can therefore be directly calculated through:

$$B_i = \frac{Y_i}{f_\Omega \times Y_{inc}} \quad (5.2.1)$$

where the B_i is the branching ratio of the i 'th decay channel and Y_{inc} is the inclusive yield of the resonance, i.e. without coincidence conditions. The yield of the i 'th decay channel is denoted Y_i and f_Ω is the fraction of the 4π solid angle subtended by the apparatus used for the coincidence measurement. The GEANT4 simulation of the CAKE, as discussed in Section 3.4.3, was used to calculate the total solid angle Ω of the CAKE to be approximately $\Omega = 2.57$ sr, giving $f_\Omega = 0.205$.

The spin and parity of the 12.049(2) MeV resonance in ^{16}O is well known to be 0^+ . Given the 7.16192 MeV α separation energy for ^{16}O , the α_1 decay mode is energetically possible for this resonance. In this experiment, this decay mode is not observed as electronic thresholds of the CAKE impose a lower limit in the observable energy of decay products. This electronics limitation, when coupled with the target attenuation of charged particles, make the α_1 decay mode from this state difficult to observe. Whilst the α_0 branching ratio of 95.3(5) % agrees relatively well with respect to the 100 % literature value, the lack of an error in literature prevents a more meaningful comparison.

Branching Ratios of the α_0 , α_1 and $p0$ Decay Modes								
E_R [MeV] (literature)	J^π	Literature			This work			
		B_{α_0} [%]	B_{α_1} [%]	B_{p0} [%]	B_{α_0} [%]	B_{α_1} [%]	B_{p0} [%]	B_{total} [%]
12.049(2)	0^+	100*	0.0	0.0	95.3(5)	0.0	0.0	95.3(5)
15.097(5)	0^+	-	-	-	70(2)	64(1)	0.0	134(2)

Table 5.4: The decay branching ratios of the 12.049(2) MeV 0^+ and 15.097(5) MeV resonances in ^{16}O . *The error of the branching ratio is not listed in literature

Assuming that the 15.097(5) MeV resonance in ^{16}O has 0^+ spin and parity, the sum of the α_0 and α_1 branching ratios exceeds 100 % in a statistically significant manner. This is a strong indication that either the resonance is not 0^+ in nature, or there is another unresolved and previously unidentified resonance of ^{16}O in the $E_x \sim 15.1$ MeV excitation energy region.

5.3 R-matrix Fits with θ_{SCAT} gates

The ability to use gates upon θ_{SCAT} , the ejectile scattering angle in the horizontal plane, to select different magnetic substate population ratios of a resonance is investigated in Section 4.7. The two gates used to select lower and higher ejectile scattering angles, defined as θ_{SCAT}^l and θ_{SCAT}^h , are used to analyse the α_0 and α_1 decay modes from ^{16}O . The analysis methodology is identical to that of Section 5.1. Whilst the ability to bias the m-state population ratios can, in principle, be used to elucidate the spin and parity of any resonance, the focus of this section is limited to the 11.520(4) MeV 2^+ , 12.049(2) MeV 0^+ and 15.097(5) MeV 0^+ resonances in ^{16}O .

R-matrix fits of the spectra, generated with the θ_{SCAT}^l and θ_{SCAT}^h gates, are shown in Figures 5.22 - 5.25. The extracted yields, which are the quantities of interest in the observation of m-state biasing, are summarised in Table 5.5.

α_0 decay mode of ^{16}O with the θ_{SCAT}^l gate

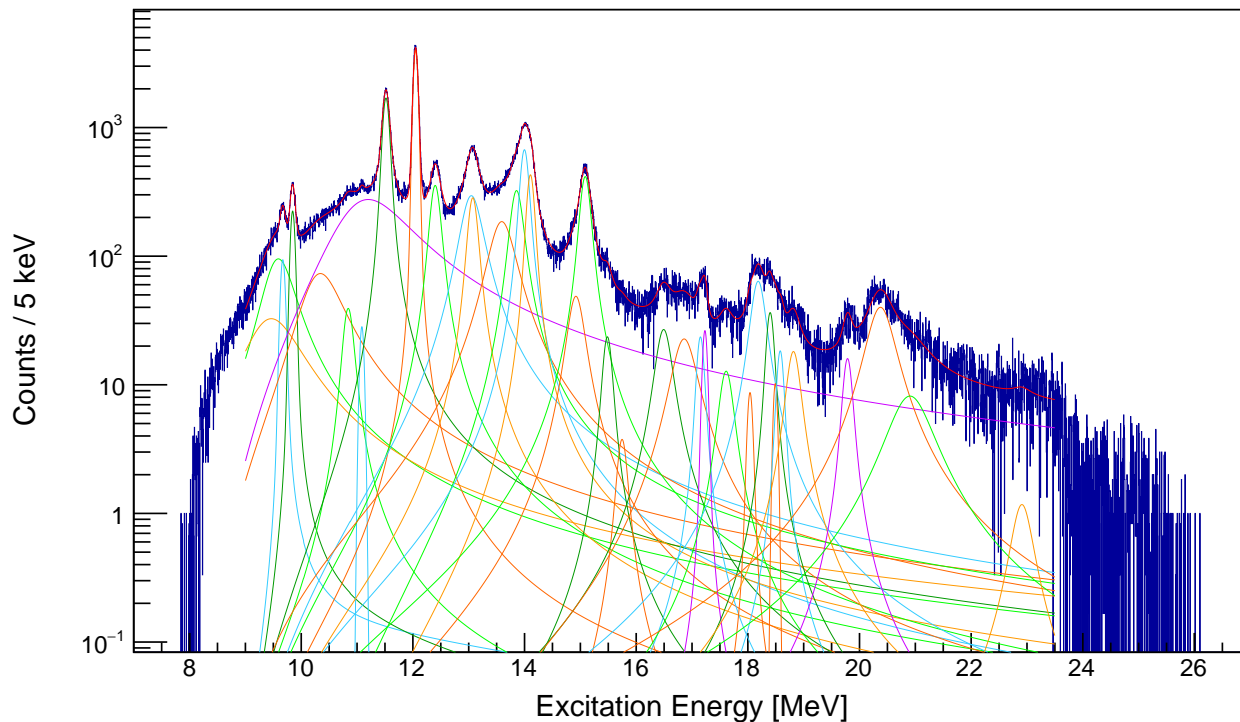


Figure 5.22: The α_0 decay mode spectrum of ^{16}O , from the Li_2CO_3 target, with the θ_{SCAT}^l gate.

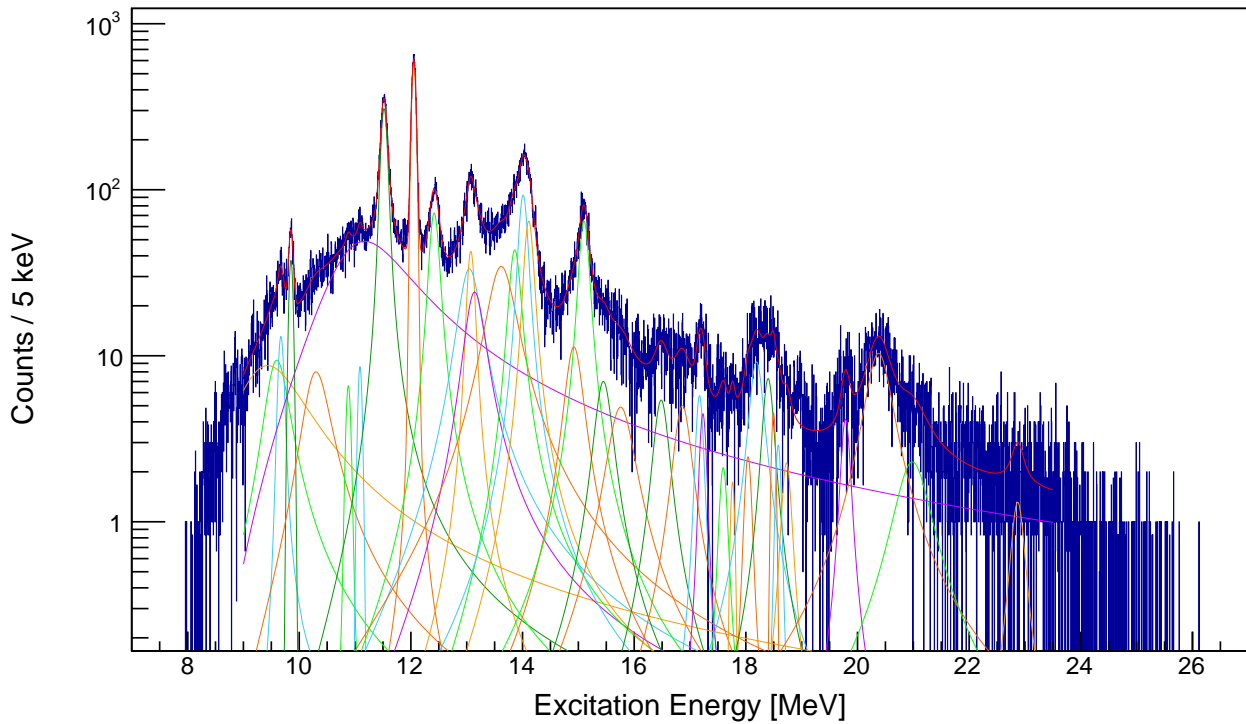
α_0 decay mode of ^{16}O with the θ_{SCAT}^h gate

Figure 5.23: The α_0 decay mode spectrum of ^{16}O , from the Li_2CO_3 target, with the θ_{SCAT}^l gate.

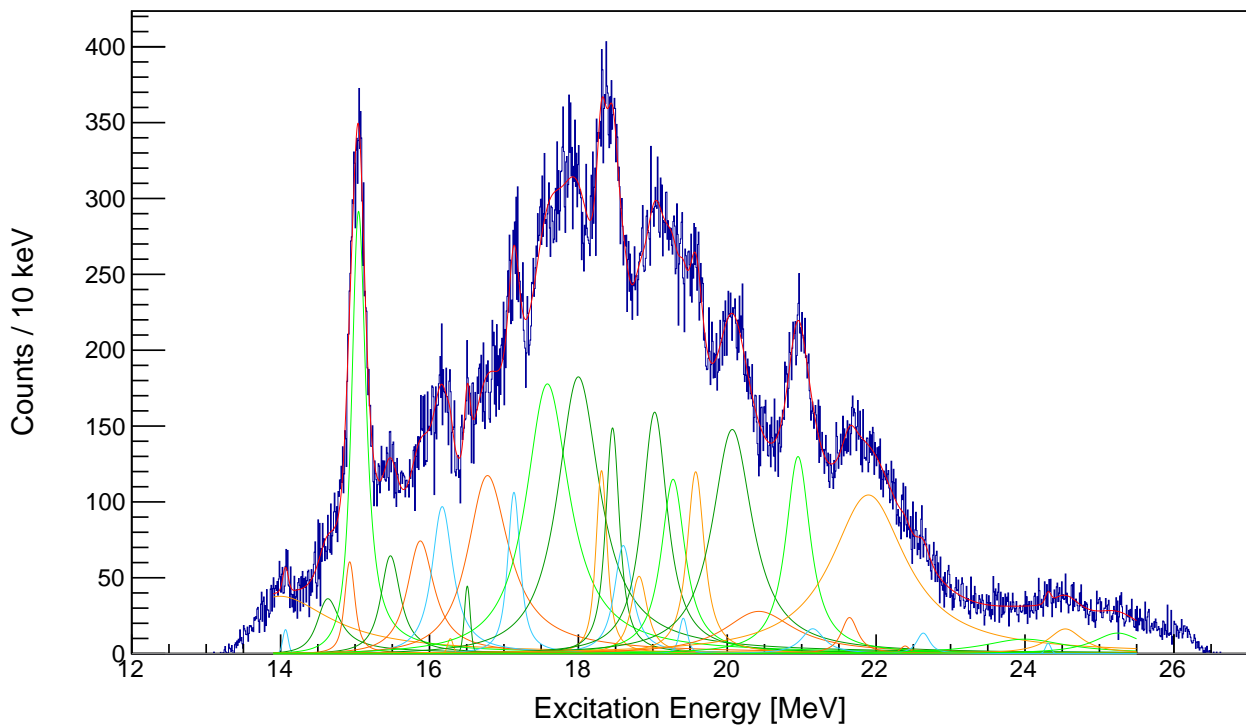
 α_1 decay mode of ^{16}O with the θ_{SCAT}^l gate

Figure 5.24: The α_1 decay mode spectrum of ^{16}O , from the Li_2CO_3 target, with the θ_{SCAT}^l gate. The events are in coincidence with MMMs 0 or 1.

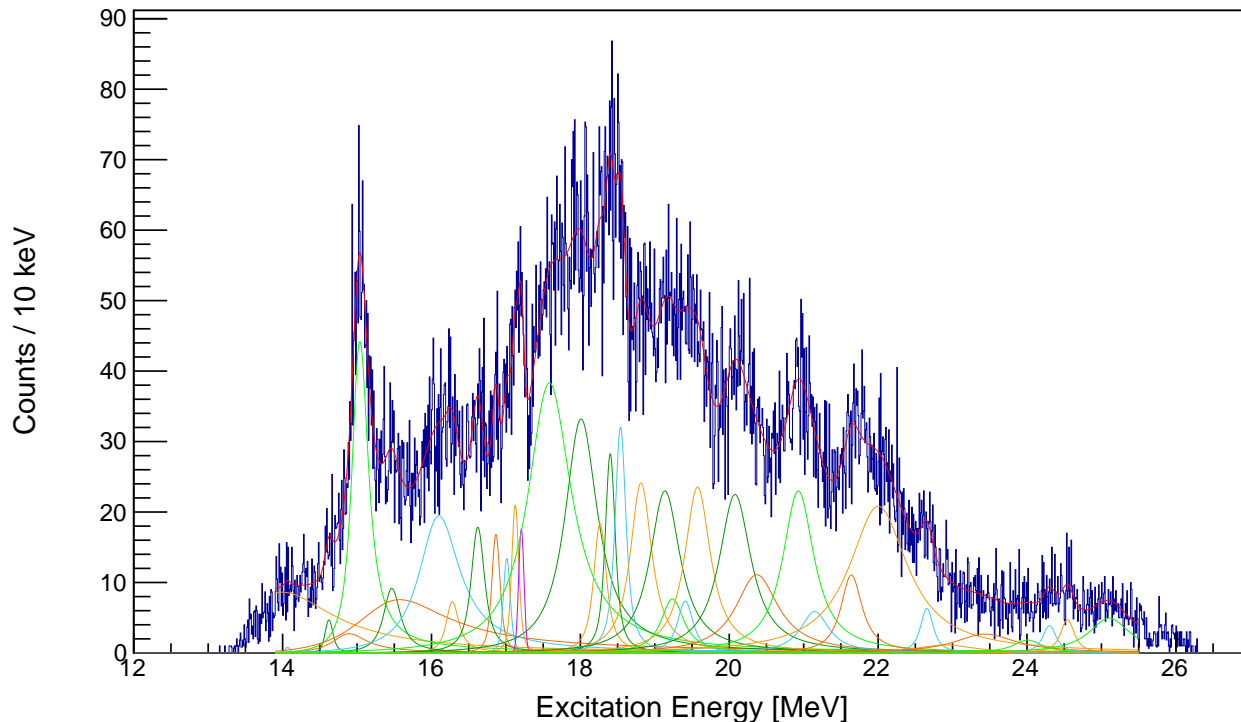
α_1 decay mode of ^{16}O with the θ_{SCAT}^h gate

Figure 5.25: The α_1 decay mode spectrum of ^{16}O , from the Li_2CO_3 target, with the θ_{SCAT}^l gate. The events are in coincidence with MMMs 0 or 1.

The kinematics of the reaction allow for the recoil nucleus to be well approximated as stationary and decaying at the origin of the lab frame. Given the purported 0^+ nature of the 15.097(5) MeV state in ^{16}O , the θ_{SCAT}^l and θ_{SCAT}^h gates can have no effect upon the angular distributions of any decay channels. The relative branching ratios of any decay channels from resonances with $J = 0^+$ spin and parity must be independent of the θ_{SCAT}^l and θ_{SCAT}^h gates. For the 15.097(5) MeV state, the relative branching ratios between the α_0 and α_1 decay modes for the θ_{SCAT}^l and θ_{SCAT}^h gates: determined to be 1.2(1) and 1.1(1) respectively, agree well with each other. This result is suggestive that the prominent α_0 and α_1 decay modes in the $E_x \sim 15.1$ MeV region correspond to a single 0^+ resonance. It is shown later in Section 5.7.2 that this result cannot be trusted as it appears that there appears to be a lack of correlation between θ_{SCAT} and the full scattering angle of the ejectile. Whilst the simulations of such gates, discussed in Section 4.7, suggests that such correlations should still exist, it may be possible that at 0° , the beam optics of the spectrometer may sufficiently worsen the horizontal scattering angle resolution such that the correlation is negligible. The exact cause of this is still under investigation. This hypothesis explains why the α_0 decay mode spectra with

the θ'_{SCAT} and θ^h_{SCAT} gates, shown in Figures 5.22 and 5.23 respectively, appear to be scaled versions of one another (and similarly for α_1 decay mode).

α_0 and α_1 decay modes of ^{16}O with θ_{SCAT}^l and θ_{SCAT}^h gates

E_R [MeV] (literature)	J^π	Yield $_l(\alpha_0)$	Yield $_h(\alpha_0)$	Yield $_l(\alpha_1)$	Yield $_h(\alpha_1)$	$\frac{\text{Yield}_l(\alpha_0)}{\text{Yield}_h(\alpha_0)}$	$\frac{\text{Yield}_l(\alpha_1)}{\text{Yield}_h(\alpha_1)}$	$\frac{\text{Yield}_l(\alpha_0)}{\text{Yield}_l(\alpha_1)}$	$\frac{\text{Yield}_h(\alpha_0)}{\text{Yield}_h(\alpha_1)}$
11.520(4)	2 ⁺	63553(845)	11428(277)	-	-	5.6(2)	-	-	-
12.049(2)	0 ⁺	83505(773)	10979(154)	-	-	7.6(1)	-	-	-
14.926(2)	2 ⁺	4744(627)	1134(149)	-	247(362)	-	4.2(8)		
15.097(5)	0 ⁺	24770(613)	3995(111)	19956(1872)	3616(232)	6.2(2)	5.5(6)	1.2(1)	1.1(1)

Table 5.5: Extracted yields from the α_0 and α_1 decay modes of ^{16}O with the θ_{SCAT}^l and θ_{SCAT}^h gates. The Yield $_l$ and Yield $_h$ refer to yields extracted from data with the θ_{SCAT}^l and θ_{SCAT}^h gates respectively.

5.4 The difference in resonance energies of the α_0 and α_1 decay modes from ^{16}O

Assuming that the 15.097(5) MeV resonance in ^{16}O has spin and parity $J^\pi = 0^+$, the l -values of decay for the α_0 and α_1 decay modes are $l = 0$ and $l = 2$ respectively. For a nucleus with $J^\pi = 0^+$ spin and parity, there is only one solution for the l -value of α decay (assuming the α -particle invariably remains in its ground state). The relative energy of decay, in the centre of mass reference frame of the recoil nucleus, is larger for the α_0 decay mode in comparison to the α_1 . The penetrability of the α_0 decay mode is therefore, in general for some excitation energy, higher than that of the α_1 decay mode. This indicates that the resonance energy (location parameter) of the R-matrix Lorentzian lineshape should be lower for the α_0 decay mode in comparison to the α_1 , however the converse is observed.

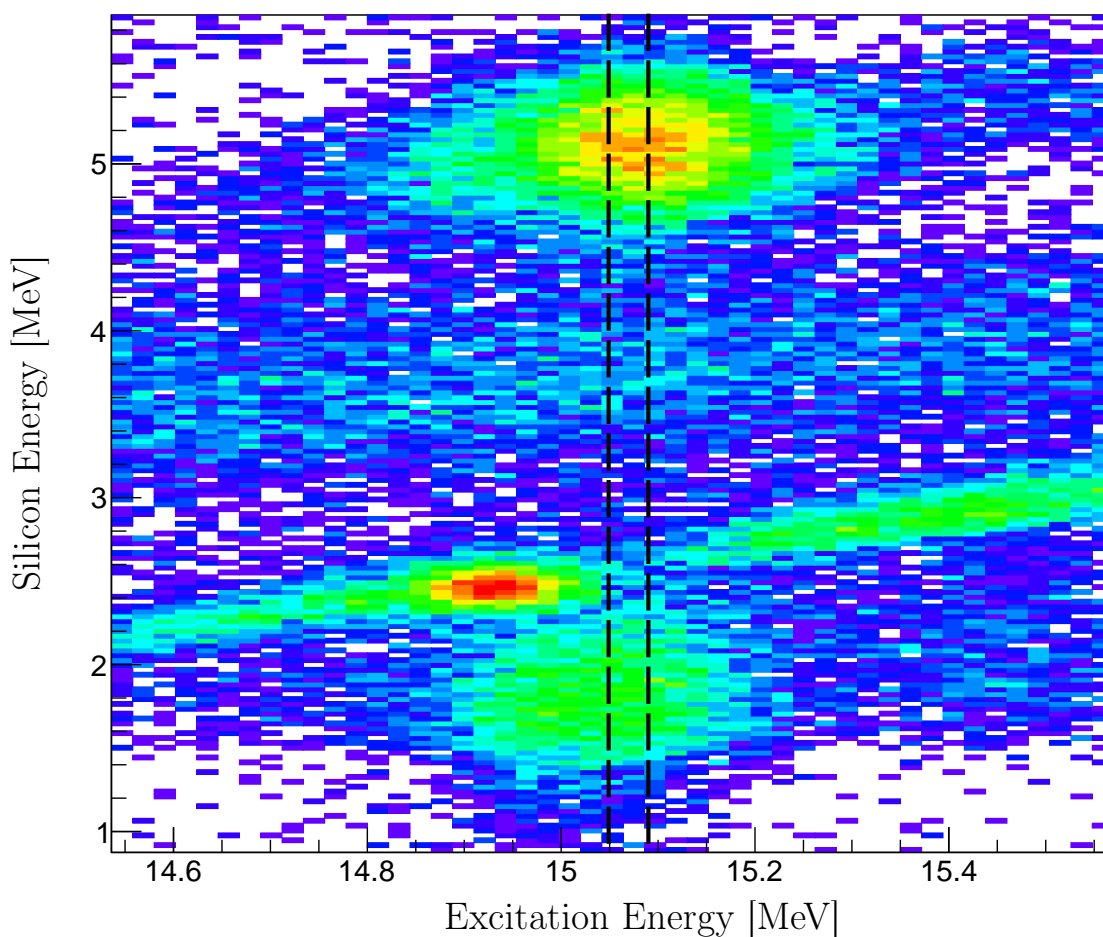


Figure 5.26: The excitation energy of the of coincident particles in the CAKE versus the excitation energy of the recoil nucleus, focusing on the difference in resonances energies between the α_0 and α_1 decay modes from the 15.097(5) MeV resonance in ^{16}O . The resonance energies (location parameters) of the α_0 and α_1 decay modes are indicated.

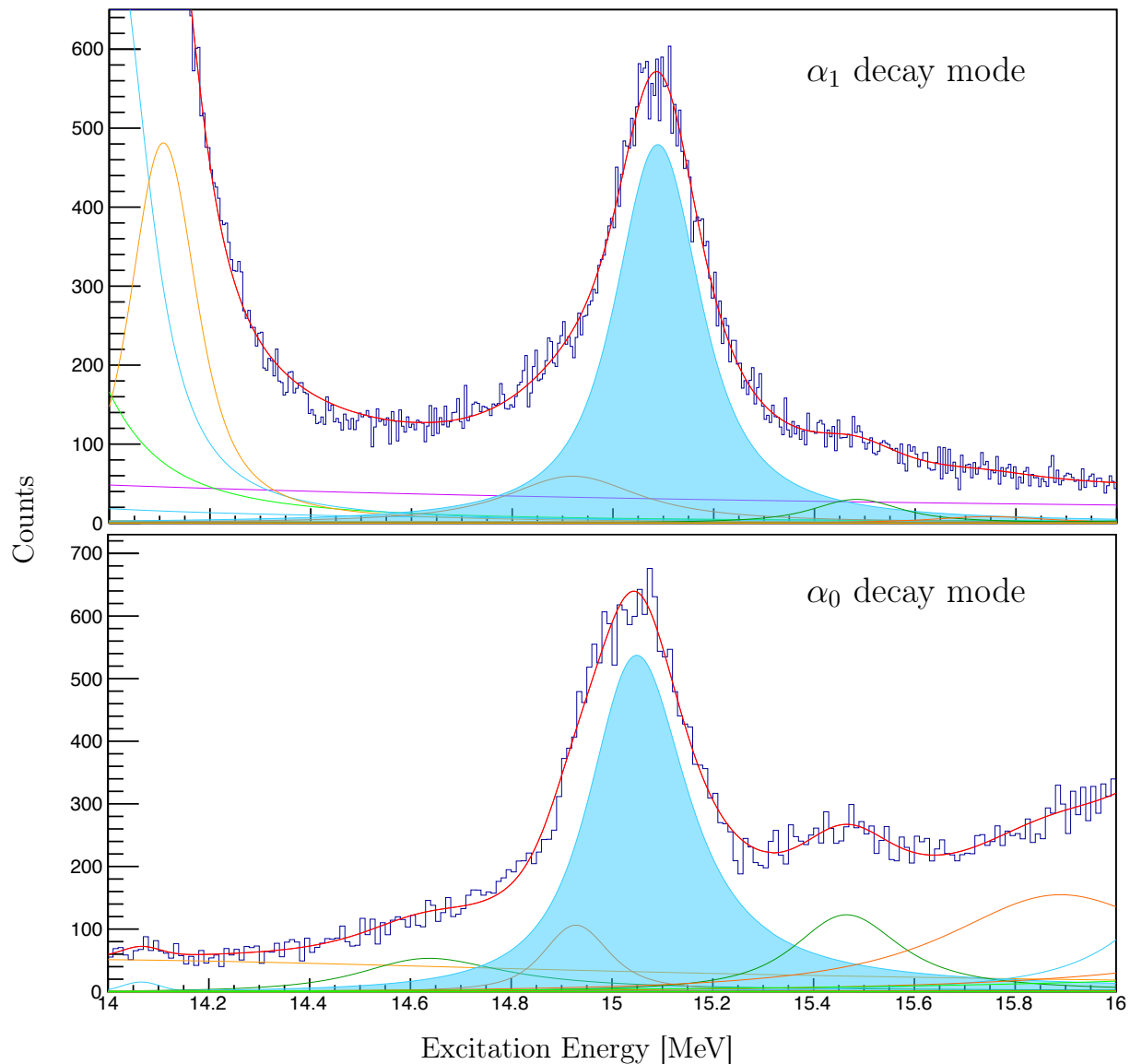


Figure 5.27: The excitation energy spectra highlight the different resonance energies of the α_0 and α_1 decay modes from the 15.097(5) MeV resonance in ^{16}O .

Resonance energies of the 15.097(5) MeV resonance in ^{16}O

	Singles spectrum	α_1 decay mode	α_0 decay mode
Resonance Energy	15.076(7)	15.046(8)	15.090(7)

Table 5.6: Tabulated resonance energies, equivalent to the location parameters for the Voigt R-matrix lineshapes, of the 15.097(5) MeV resonance in ^{16}O .

If it is assumed that the α_0 and α_1 decay modes from ^{16}O , in the $E_x \sim 15.1$ MeV region, originate from two distinct states, it is only possible for the l -value of decay for the α_0 decay mode to exceed that of the α_1 if the excited nucleus has $J^\pi = 3^-$ spin and parity (see Table 5.7). The penetrabilities for the α_0 and α_1 decay modes of the 15.097(5) MeV resonance in ^{16}O are calculated for two cases: the spin and parity of the resonance being $J^\pi = 0^+$ and $J^\pi = 3^-$, as displayed in Figure 5.28. Further investigation into these two hypothetical cases and their associated penetrabilities and lineshapes is ongoing.

Display Colour	^{16}O	\rightarrow	α	+	^{12}C (g.s.)	
	$j^{16}\text{O}$		j_α		$j^{12}\text{C}$	l
Green	0^+		0^+		0^+	0
Orange	3^-		0^+		0^+	3

Display Colour	^{16}O	\rightarrow	α	+	^{12}C (2_1^+)	
	$j^{16}\text{O}$		j_α		$j^{12}\text{C}$	l
Blue	0^+		0^+		2^+	2
Violet	3^-		0^+		2^+	1

Table 5.7: The display colours for the α_0 and α_1 decay modes for a 15.097 MeV resonance in ^{16}O for $J^\pi = 0^+$ and $J^\pi = 3^-$. The lowest l -value allowed by the angular momentum selection rules is chosen as the l -value of decay.

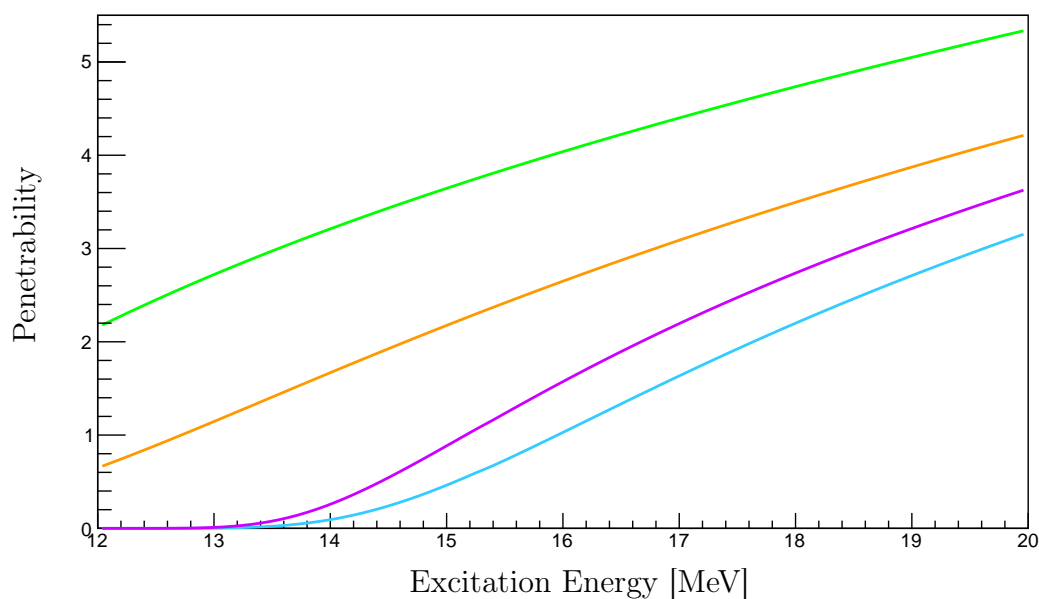


Figure 5.28: Penetrabilities of various distinct decay channels which only in the l -value of decay and the final state of the residual nucleus, as defined in Table 5.7.

5.5 Angular Correlations

The angular correlations exhibited by the decay products of recoil nuclei reveal the rotational dynamics of the associated decay channels. If the angular momentum quantum numbers of the decay products are known (i.e. α -particles are assumed to remain in their ground states with $J^\pi = 0^+$ spin and parity), the spin parities for states/resonances of excited recoil nuclei can be inferred. Angular correlations, in the reference frame defined by the momentum vector of the recoil nucleus, can be expressed as a linear combination of Legendre polynomials [48]:

$$W(\theta_{cm}) = \sum_{l=0,2,\dots} A_l P_l(\cos \theta_{cm}), \quad (5.5.1)$$

where θ_{cm} is the polar angle in the centre of mass reference frame of the recoil nucleus and P_l are the Legendre polynomials.

As previously mentioned, the K600 spectrometer was operated in its Y-focused mode for this experiment, thereby disabling the accurate reconstruction of the vertical angle of the inelastically scattered α' ejectile. Without the complete trajectory of the ejectile, it is not possible to fully reconstruct the recoil nucleus's momentum vector and transform the angular distributions of particle decay from the laboratory reference frame, to the centre of mass reference frame of the recoil nucleus. Consequently for this experiment, the experimental and theoretical angular distributions of particle decay must be compared in the laboratory reference frame.

For nuclear states/resonances with $I = 0$, there is no momentum vector with which to polarise the nucleus, resulting in the nucleus being intrinsically unpolarised relative to the beam direction. As a consequence, all decay channels from such states/resonances exhibit isotropy. For a binary decay mode from a state/resonance with angular momentum I_{init} , forming decay products with angular momenta I_1 and I_2 , the yield Y observed at the polar angle θ_{lab} is given by

$$Y(\theta_{lab}|I_{init}, I_1, I_2) = N Y_{tot} W_{tot}(\theta_{lab}|I_{init}, I_1, I_2) \Omega(\theta_{lab}) \quad (5.5.2)$$

where Y_{tot} is the total yield of the relevant decay channel, $\Omega(\theta_{lab})$ is the solid angle subtended at θ_{lab} and N is a normalisation factor:

$$N = \left(\int_0^\pi d\theta_{lab} W_{tot}(\theta_{lab}|I_{init}, I_1, I_2) \right)^{-1}. \quad (5.5.3)$$

$W_{tot}(\theta_{lab}|I_{init}, I_1, I_2)$ is the total angular correlation function of the decay. For this experiment, we are primarily interested in the decay modes producing α -particles, which exhibit a ground state with $J^\pi = 0^+$ spin and parity. For

α decay modes the total angular correlation function can therefore be simplified to solely depend on the angular momenta of the initial resonance parent particle and the the residual nucleus:

$$W_{tot}(\theta_{lab}|I_{init}, I_{res}, I_{\alpha}) = W_{tot}(\theta_{lab}|I_{init}, I_{res}), \quad (5.5.4)$$

as the α -particle decay product is assumed to invariably remain in its ground state. Since the α -particle decay product is assumed to invariably remain in its ground state, the angular correlation function can therefore be simplified to $W_{tot}(\theta_{lab}|I_{init}, I_{res}, I_{\alpha}) = W_{tot}(\theta_{lab}|I_{init}, I_{res})$, where I_{res} represents the angular momentum of the complementary residual nucleus of an α decay mode.

The total angular correlation function, sums the various contributions to the angular distribution from each magnetic substate by weighting each substate with its associated differential cross section:

$$W_{tot}(\theta_{lab}|I_{init}, I_{res}) = \int_0^{2\pi} d\phi'_{lab} \int_0^{2.0^\circ} d\theta'_{lab} \sin(\theta'_{lab}) \times \left(\sum_{m_I=-I}^{+I} \frac{d\sigma_{m_I}}{d\Omega}(\theta'_{lab}) W_{I,m_I}(\theta_{lab}|I_{init}, I_{res}, m_I, \theta'_{lab}) \right) \quad (5.5.5)$$

where m_I denotes the magnetic substate, θ'_{lab} is the polar angle of the ejectile in the laboratory reference frame and $\frac{d\sigma_{m_I}}{d\Omega}(\theta'_{lab})$ is the m-state dependent differential cross section. $W_{I,m_I}(\theta_{lab}|I_{init}, I_{res}, m_I, \theta'_{lab})$ is the angular correlation function, at θ_{lab} , of decay products given the ejectile's polar angle of scattering, θ'_{lab} .

Under the assumption of a single step mechanism for two body scattering, the scattering angle of the ejectile fully determines the momentum vector of the recoil nucleus. Furthermore, the kinematics of the reaction may allow for nucleus to be approximated as stationary and decaying at the origin in the laboratory frame. Given the 200 MeV α -particle beam in this experiment, the projectile energy is approximately ~ 50 MeV/u, which is an energy range where the single step mechanism is dominant. For the $\pm 2^\circ$ acceptance for the ejectile, centred at 0° , the minimum and maximum kinetic energies imparted to the recoil nucleus are 81 keV and 141 keV for a 15.097 MeV resonance in ^{16}O . The associated minimum and maximum angles of the recoil nucleus are 0° and $\approx 40^\circ$ respectively. Given the short lifetimes of states/resonances of interest, which have intrinsic widths ranging from ≈ 10 to ≈ 500 keV, the decays of the recoil nuclei are therefore approximated to occur at the origin in the laboratory inertial reference frame.

An experimental limitation is the target attenuation of the decay products; this is particularly pronounced for low energy decay products. Since the mean path through the target material is greater for decay products directed at

lower polar angles in the laboratory frame, the data from the higher rings of the CAKE may be selectively omitted to more accurately observe the angular distributions of low energy decay products.

5.6 Theoretical Calculations: Differential Cross Sections of $^{16}\text{O}(\alpha, \alpha')$ and the Angular Distributions of the Subsequent α_0 Decay Modes.

In order to calculate the theoretical angular distributions of particle decay from resonances in $^{16}\text{O}(\alpha, \alpha')$, the differential cross sections are first calculated with CHUCK [49], which utilises an optical potential to model the inelastic scattering. Since the nature of the 15.097(5) MeV resonance in ^{16}O is to be investigated, differential cross sections have been calculated for a 15.097(5) MeV resonance with various hypothetical spin parities: $J^\pi = 0^+, 1^-, 2^+, 3^-, 4^+$ and 5^- , as shown in Figures 5.29. CHUCK3 also provides an output describing the reaction in the form of partial waves. This out is interpreted by ANGCOR [50] to calculate the magnetic substate population ratios of a populated resonance (which are dependent upon the polar scattering angle of the ejectile). These population ratios are then used by ANGCOR to calculate the angular distributions of decay in the inertial reference frame of the recoil nucleus, where the polar axis is the axis of quantisation (z -axis).

Given the kinematics of the $^{16}\text{O}(\alpha, \alpha')$ reaction, the difference in the inertial reference frames of the laboratory and the recoil nucleus must be accounted for. Each calculated distribution of particle decay takes into account the solid angle acceptance of the spectrometer by sampling a large number of ejectile angles. The m-state population ratios and angular distributions of decay are then calculated for the each sampled angle. Each separate distribution is then Lorentz boosted into the laboratory frame, after which they are all summed, with weights determined by the associated cross sections, to produce the final angular distribution of decay in the laboratory inertial reference frame.

5.6.1 15.097 MeV state in ^{16}O with $J^\pi = 0^+$ spin and parity

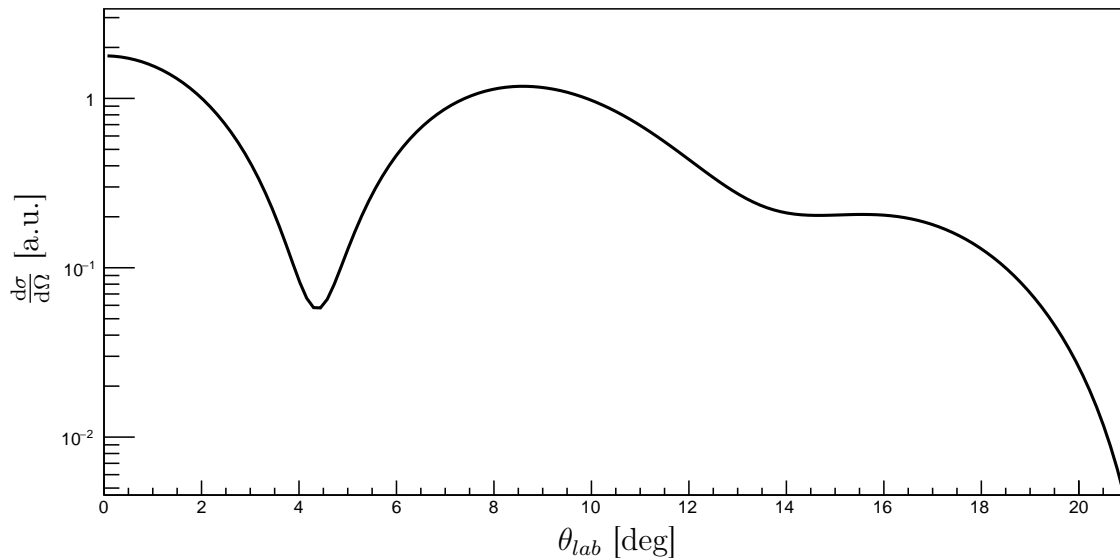


Figure 5.29: The differential cross section, of the ejectile from the $^{16}\text{O}(\alpha, \alpha')$ reaction, for a 15.097 MeV state in ^{16}O with $J^\pi = 0^+$ spin and parity.

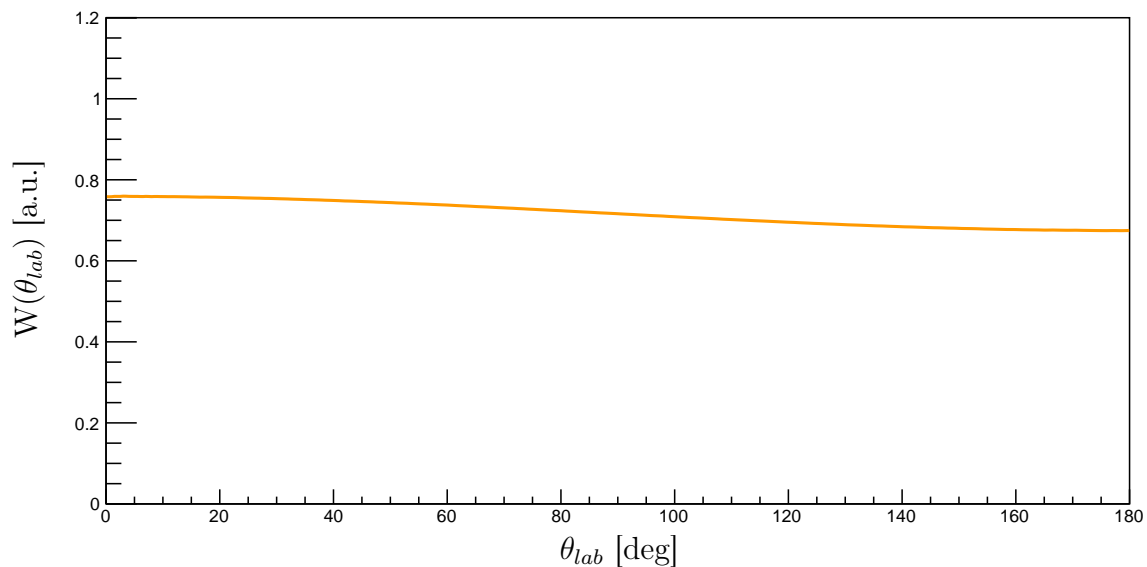


Figure 5.30: The angular distribution of the α -particle decay product from the α_0 decay mode of a 15.097(5) MeV state in ^{16}O with $J^\pi = 0^+$ spin and parity.

5.6.2 15.097 MeV state in ^{16}O with $J^\pi = 1^-$ spin and parity

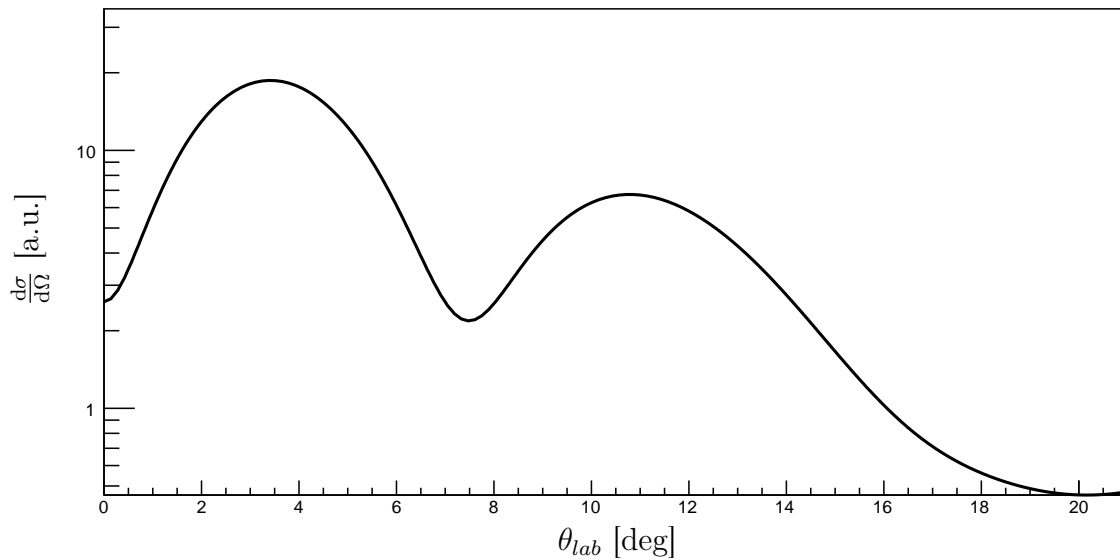


Figure 5.31: The differential cross section, of the ejectile from the $^{16}\text{O}(\alpha, \alpha')$ reaction, for a 15.097 MeV state in ^{16}O with $J^\pi = 1^-$ spin and parity.

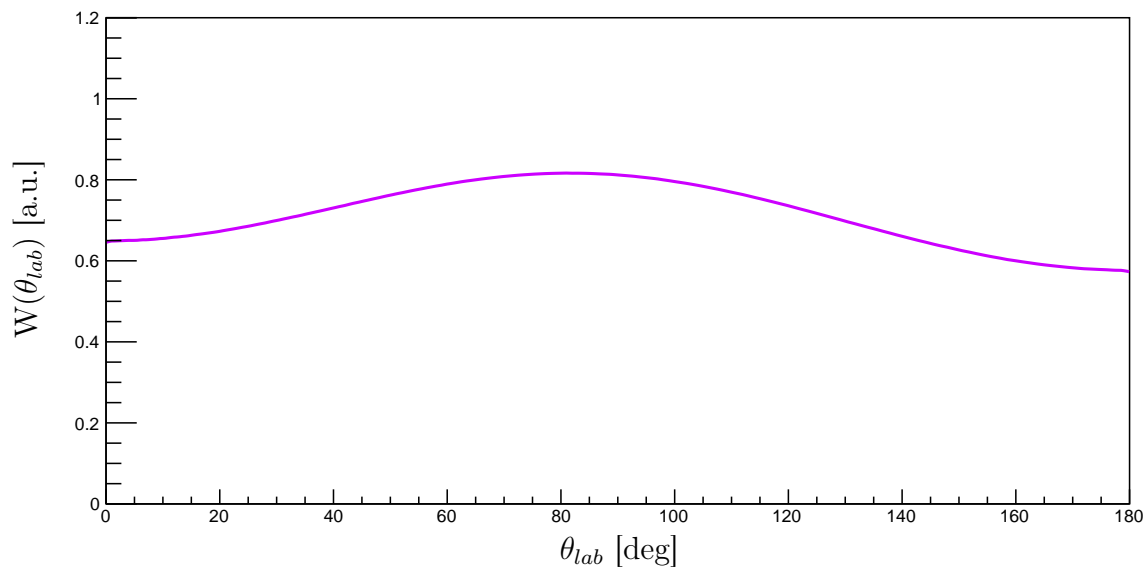


Figure 5.32: The angular distribution of the α -particle decay product from the α_0 decay mode of a 15.097(5) MeV state in ^{16}O with $J^\pi = 1^-$ spin and parity.

5.6.3 15.097 MeV state in ^{16}O with $J^\pi = 2^+$ spin and parity

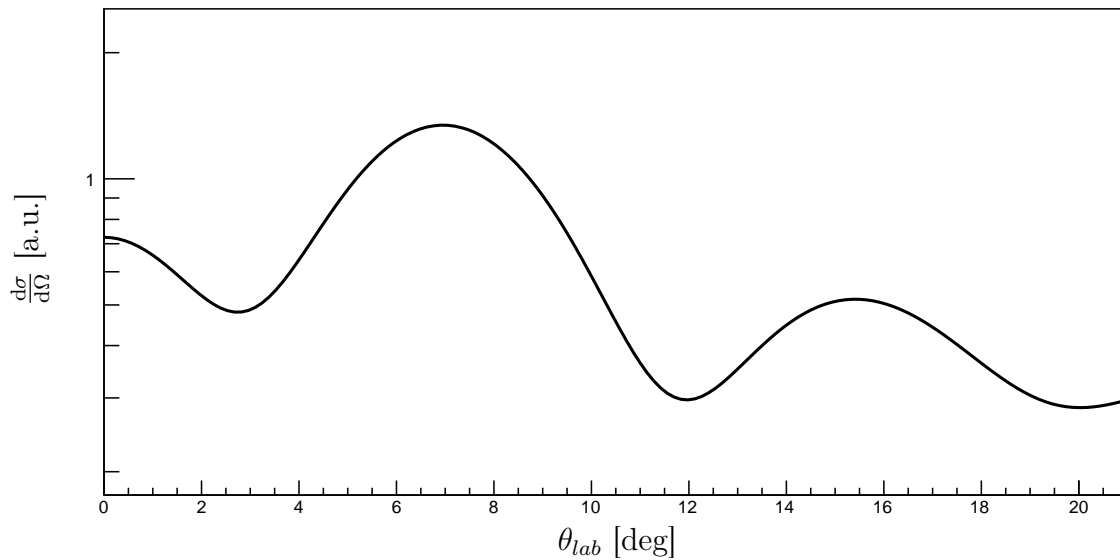


Figure 5.33: The differential cross section, of the ejectile from the $^{16}\text{O}(\alpha, \alpha')$ reaction, for a 15.097 MeV state in ^{16}O with $J^\pi = 2^+$ spin and parity.

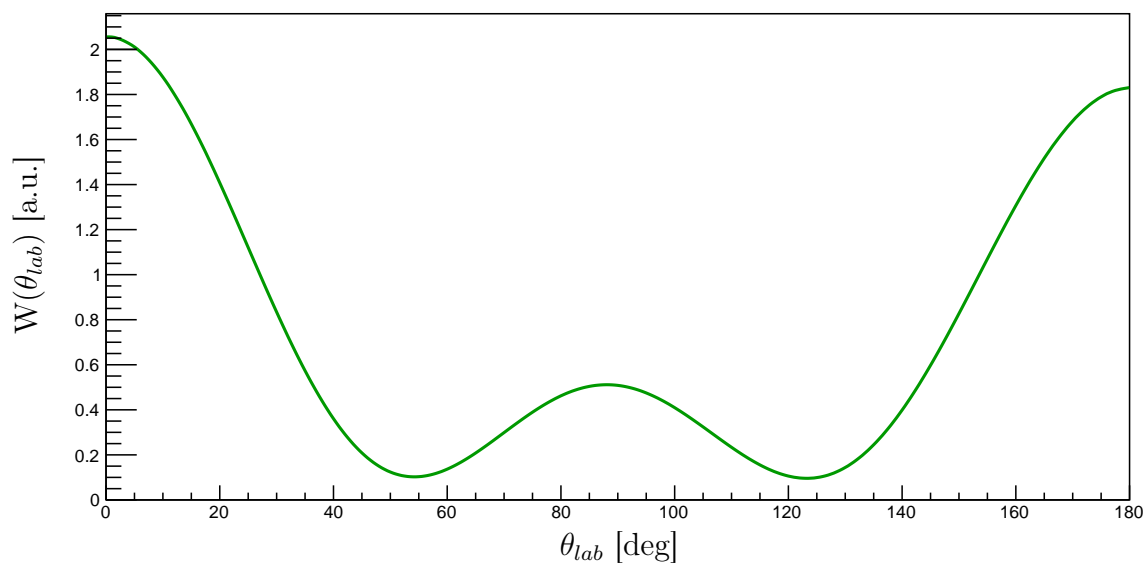


Figure 5.34: The angular distribution of the α -particle decay product from the α_0 decay mode of a 15.097(5) MeV state in ^{16}O with $J^\pi = 2^+$ spin and parity.

5.6.4 15.097 MeV state in ^{16}O with $J^\pi = 3^-$ spin and parity

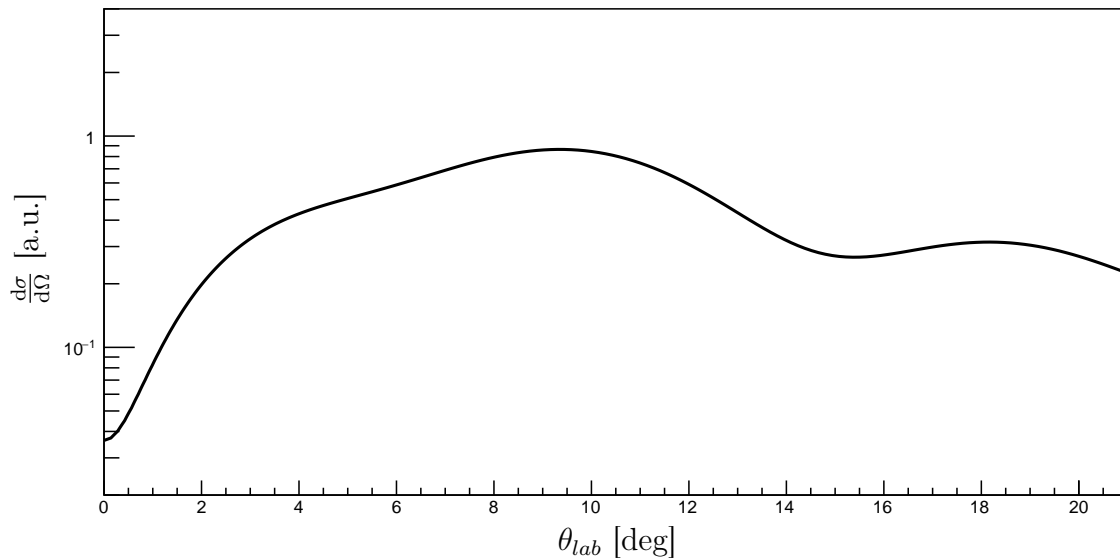


Figure 5.35: The differential cross section, of the ejectile from the $^{16}\text{O}(\alpha, \alpha')$ reaction, for a 15.097 MeV state in ^{16}O with $J^\pi = 3^-$ spin and parity.

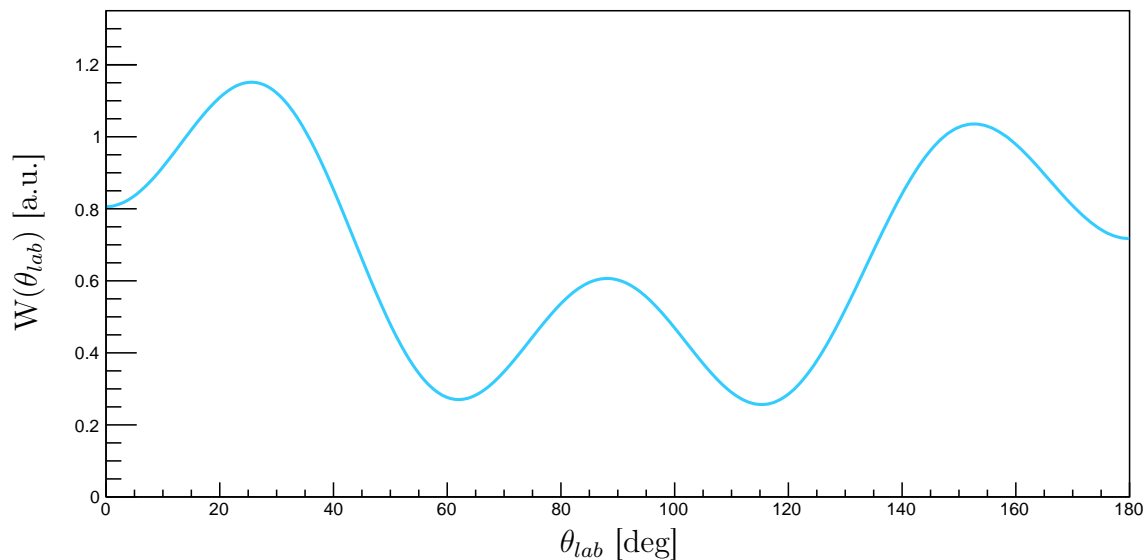


Figure 5.36: The angular distribution of the α -particle decay product from the α_0 decay mode of a 15.097(5) MeV state in ^{16}O with $J^\pi = 3^-$ spin and parity.

5.6.5 15.097 MeV state in ^{16}O with $J^\pi = 4^+$ spin and parity

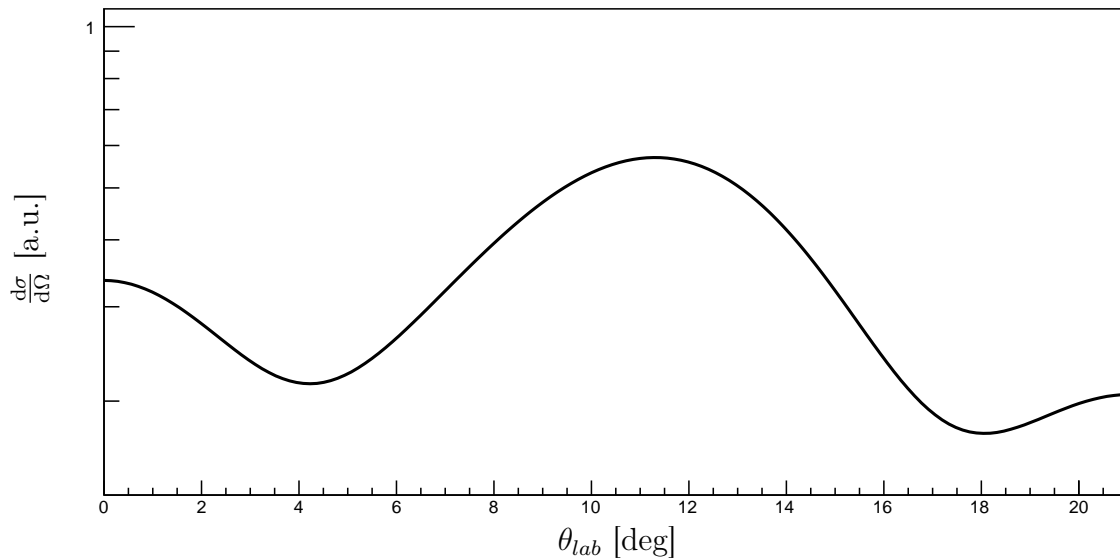


Figure 5.37: The differential cross section, of the ejectile from the $^{16}\text{O}(\alpha, \alpha')$ reaction, for a 15.097 MeV state in ^{16}O with $J^\pi = 4^+$ spin and parity.

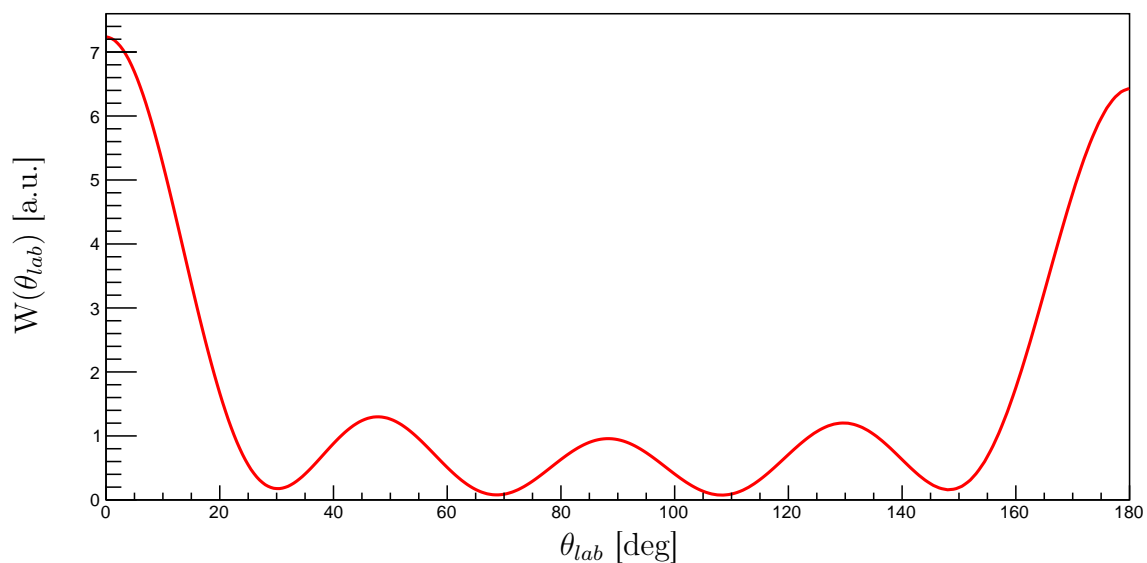


Figure 5.38: The angular distribution of the α -particle decay product from the α_0 decay mode of a 15.097(5) MeV state in ^{16}O with $J^\pi = 4^+$ spin and parity.

5.6.6 15.097 MeV state in ^{16}O with $J^\pi = 5^-$ spin and parity

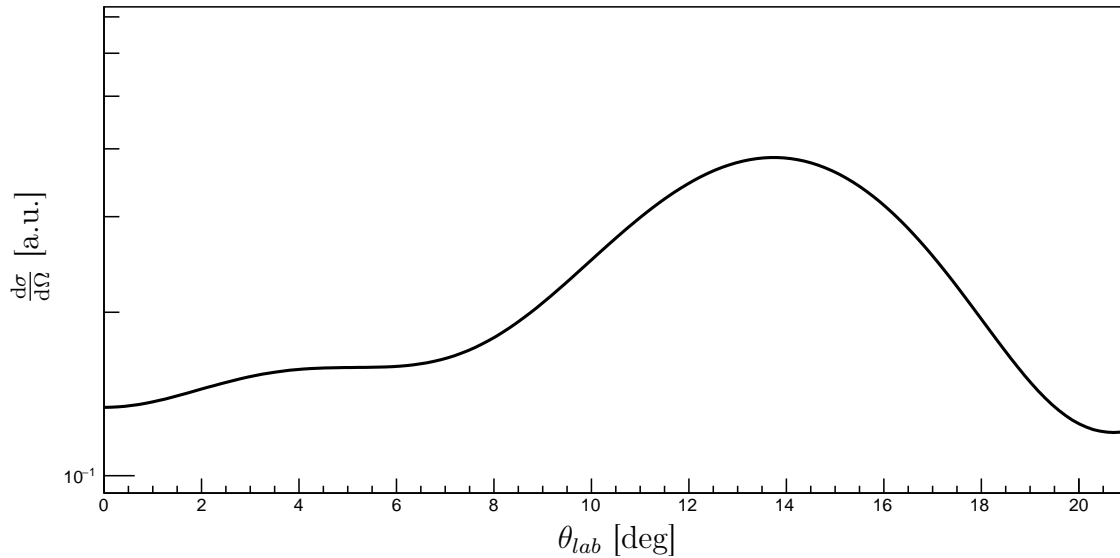


Figure 5.39: The differential cross section, of the ejectile from the $^{16}\text{O}(\alpha, \alpha')$ reaction, for a 15.097 MeV state in ^{16}O with $J^\pi = 5^-$ spin and parity.

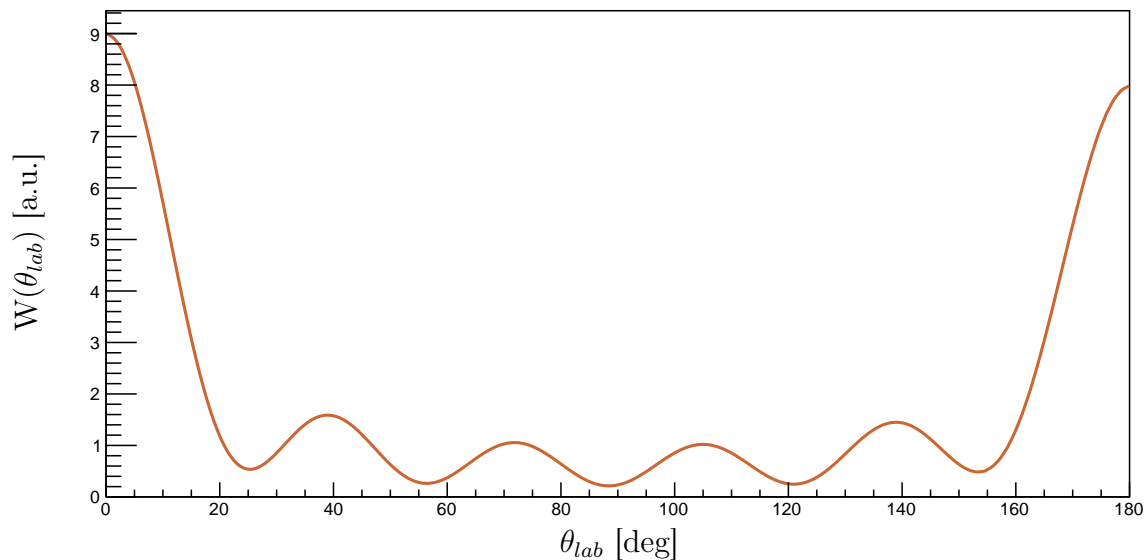


Figure 5.40: The angular distribution of the α -particle decay product from the α_0 decay mode of a 15.097(5) MeV state in ^{16}O with $J^\pi = 5^-$ spin and parity.

5.7 Angular Distributions of Decay Products from Data

By requiring the detection of coincident decay particles in the CAKE for particular rings, angular distributions of a decay mode can be determined. These yields are fitted with the same R-matrix fitting code used to fit all preceding focal plane spectra. Additional conventions/restrictions are placed upon the fitting of these spectra. For each decay mode:

- The focal plane spectrum in coincidence with the entire CAKE is first fitted with the R-matrix code to crucially determine the location parameters and reduced widths of each resonance. These parameters are assumed to be the most accurate and are henceforth referred to as the reference parameters.
- The location parameter of each observed resonance is fixed to the associated reference parameter value to give self-consistency.
- The reduced width parameter of each observed resonance is fixed to the associated reference parameter value to give self-consistency.

The solid angle of each rings 1-15 in the CAKE are displayed in Figure 5.41. These solid angles represent the $\Omega(\theta_{lab})$ in Equation 5.5.2. Equation ?? shows that for isotropic decay, the yield of coincident decay products is directly proportional to the solid angle subtended by the detector.

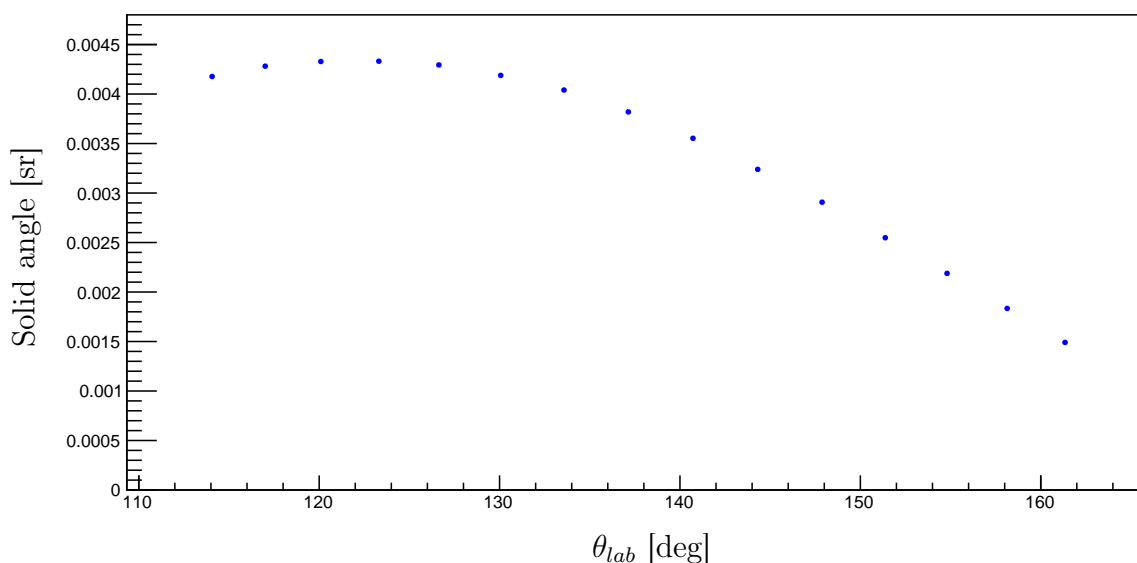


Figure 5.41: The GEANT4 simulated solid angle of the CAKE versus the average angle of each ring.

5.7.1 The α_0 Decay Mode from the 12.049(2) MeV 0^+ resonance in ^{16}O

The yields and angular distributions of the α_0 decay mode, which are observed in coincidence with population of the 12.049(2) MeV 0^+ resonance in ^{16}O , are plotted against the average angle of the associated ring, as shown in Figure 5.42 and 5.43 respectively.

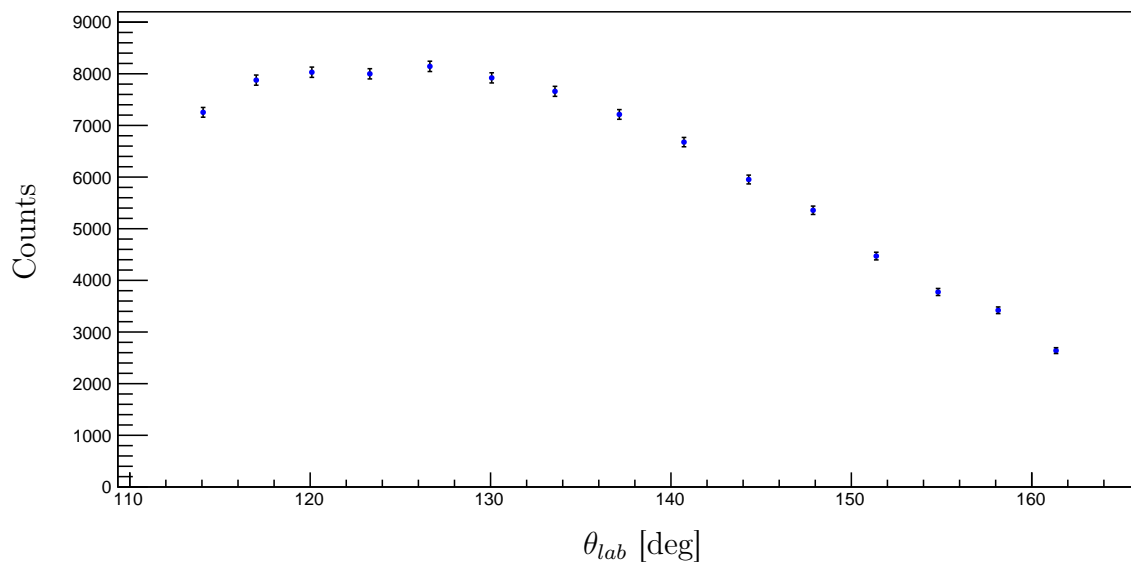


Figure 5.42: The yield of decay particles from the 12.049(2) MeV 0^+ resonance in ^{16}O , versus the average angle of the associated triggered channel in the CAKE.

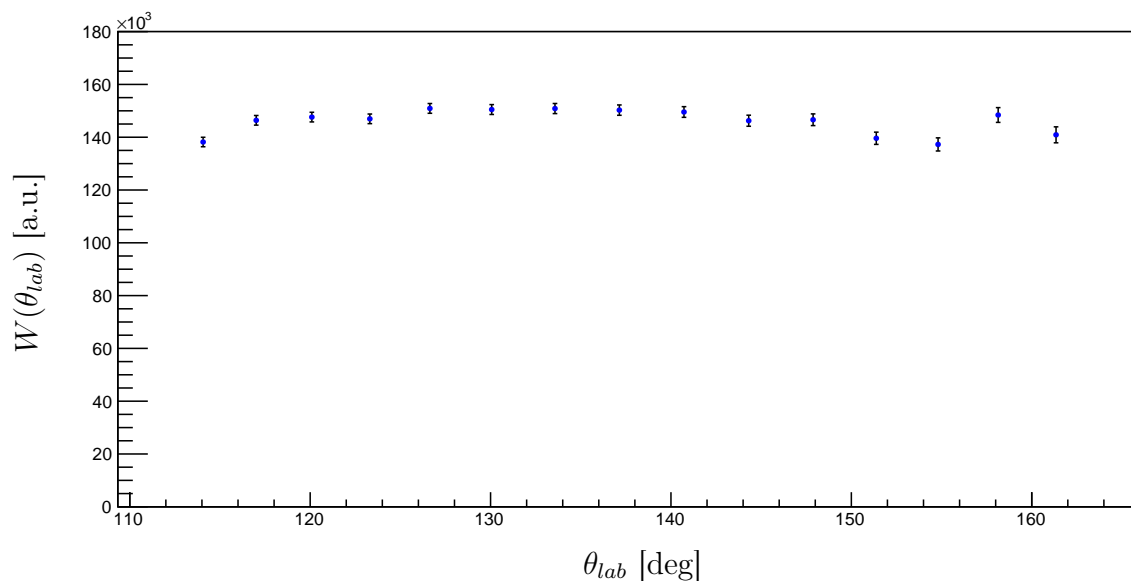


Figure 5.43: The angular distribution of decay particles from the 12.049(2) MeV 0^+ resonance in ^{16}O , versus the average angle of the associated triggered channel in the CAKE.

As expected, the yield for a decay mode from a 0^+ resonance appears to be directly proportional to the solid angle (see Figure 5.41). The uniform angular correlation, which removes the solid angle dependence of the yield, confirms the isotropy.

This resonance not only serves as a validation of the GEANT4 calculated solid angles, but also as the archetypal 0^+ resonance, in this data set, to which other 0^+ resonances may be compared.

5.7.2 The α_0 Decay Mode from the 11.520(4) MeV 2^+ resonance in ^{16}O

The yields and angular distributions of the α_0 decay mode, which are observed in coincidence with population of the 11.520(2) MeV 2^+ resonance in ^{16}O , are plotted against the average angle of the associated ring, as shown in Figure 5.42 and 5.43 respectively. Both the yields and angular correlation differ drastically to the corresponding α_0 decay from the 12.049(2) MeV 0^+ resonance in ^{16}O . The angular correlation indicates that the decay is primarily at backward angles. This is confirmed with the theoretical calculation shown in Figure 5.34. The minimum of the angular correlation, which is at approximately 120° in the laboratory frame, also agrees well with the minimum from theory.

The relatively high population of this resonance and the strong anisotropy of the α_0 decay establishes this resonance as a primary candidate upon which the effects of the θ_{SCAT}^l and θ_{SCAT}^h gates should be observed. The yields and angular distributions of the α_0 decay mode from this resonance, with the θ_{SCAT}^l and θ_{SCAT}^h gates imposed, are shown Figures 5.46 - 5.49. It can be observed that these yields and angular distributions appear to be qualitatively identical to the corresponding results without the θ_{SCAT}^l and θ_{SCAT}^h gates. This confirms the aforementioned hypothesis that for a 0° measurement, the θ_{SCAT} quantity is not strongly correlated with the true scattering angle of the ejectile. The reason for this is not yet fully known and the θ_{SCAT}^l and θ_{SCAT}^h gates are henceforth omitted from the analysis.

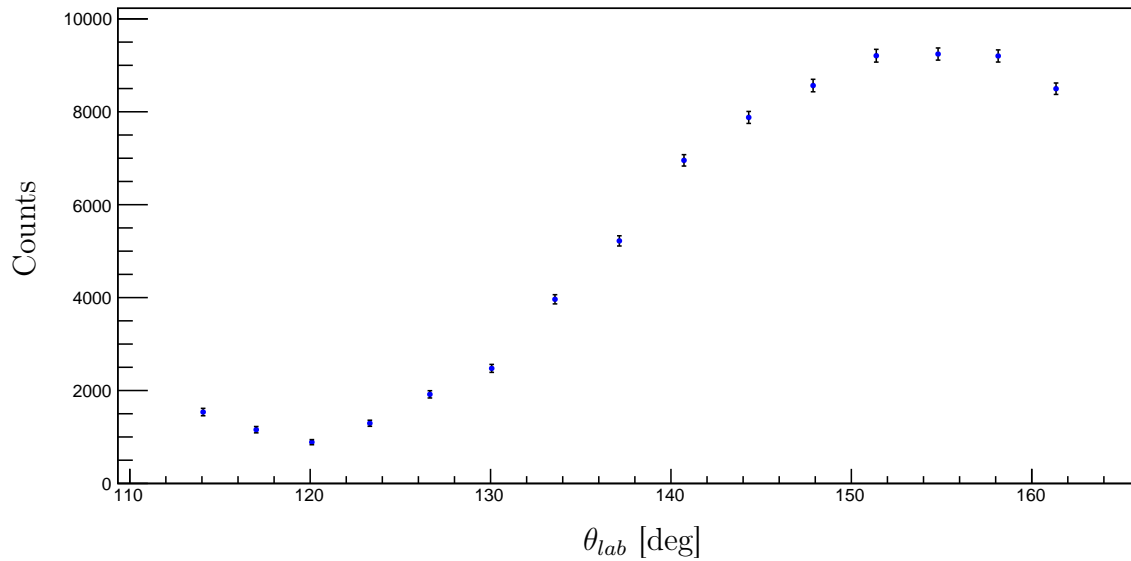


Figure 5.44: The yield of decay particles from the 11.520(4) MeV 2^+ resonance in ^{16}O , versus the average angle of the associated triggered channel in the CAKE.

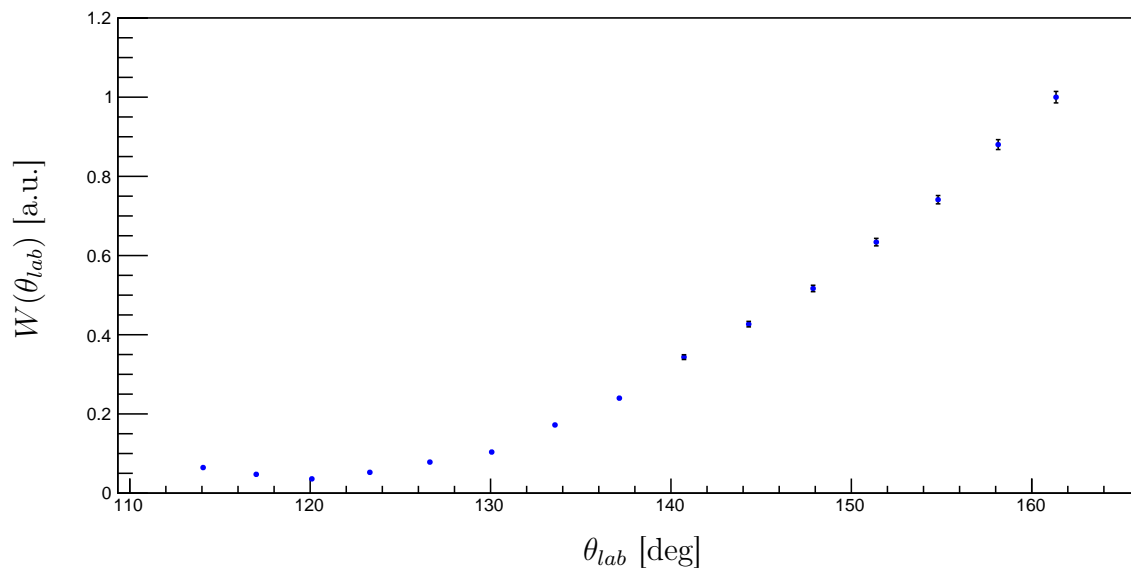


Figure 5.45: The angular distribution of decay particles from the 11.520(4) MeV 2^+ resonance in ^{16}O , versus the average angle of the associated triggered channel in the CAKE.

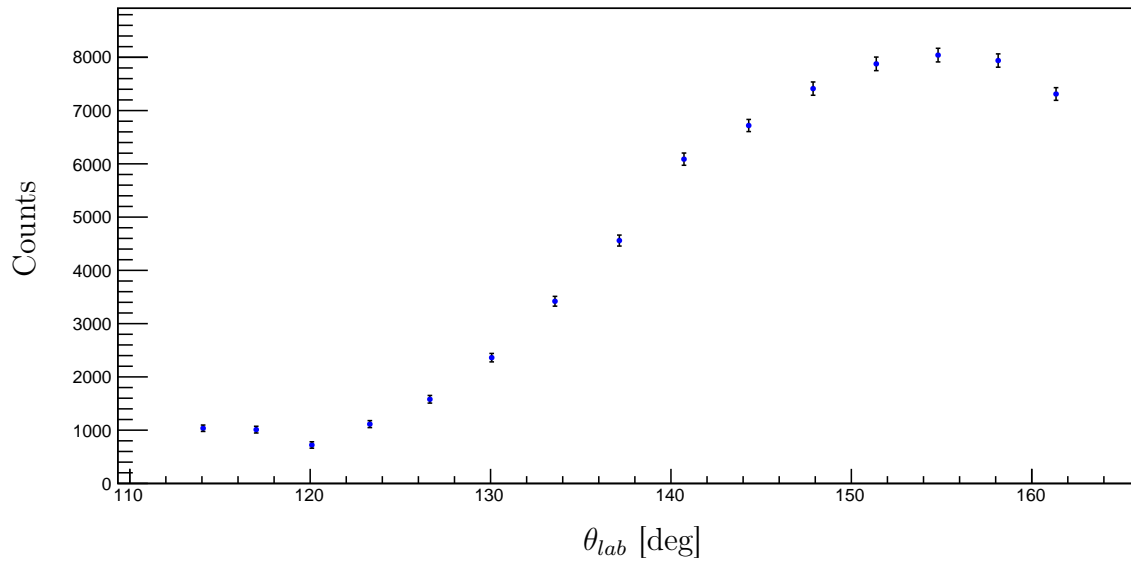


Figure 5.46: The yield of decay particles from the 11.520(4) MeV 2^+ resonance in ^{16}O , with the θ_{SCAT}^l gate imposed, versus the average angle of the associated triggered channel in the CAKE.

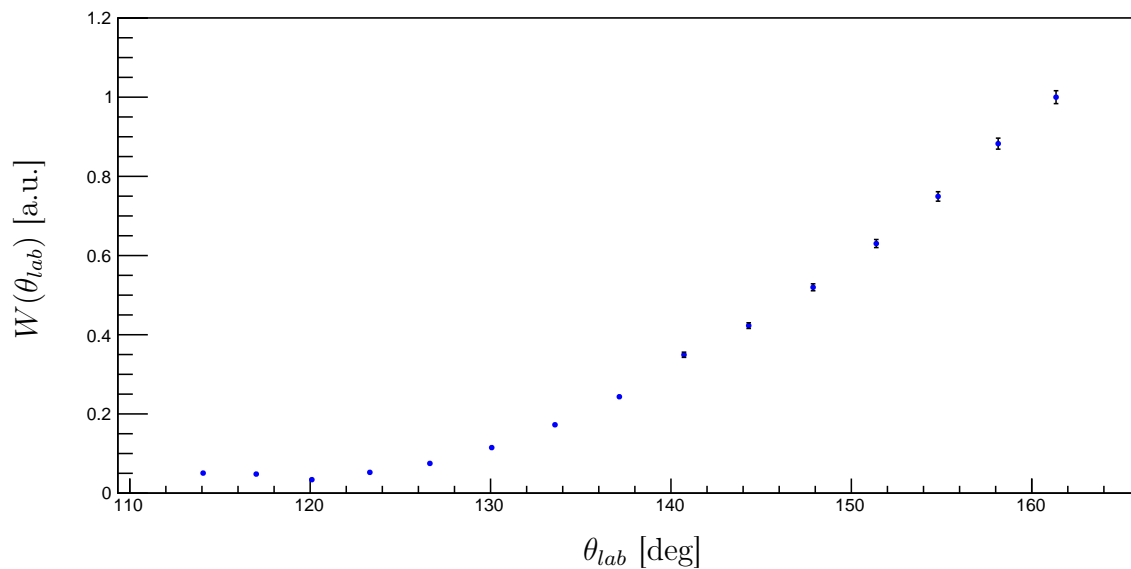


Figure 5.47: The angular distribution of decay particles from the 11.520(4) MeV 2^+ resonance in ^{16}O , with the θ_{SCAT}^l gate imposed, versus the average angle of the associated triggered channel in the CAKE.

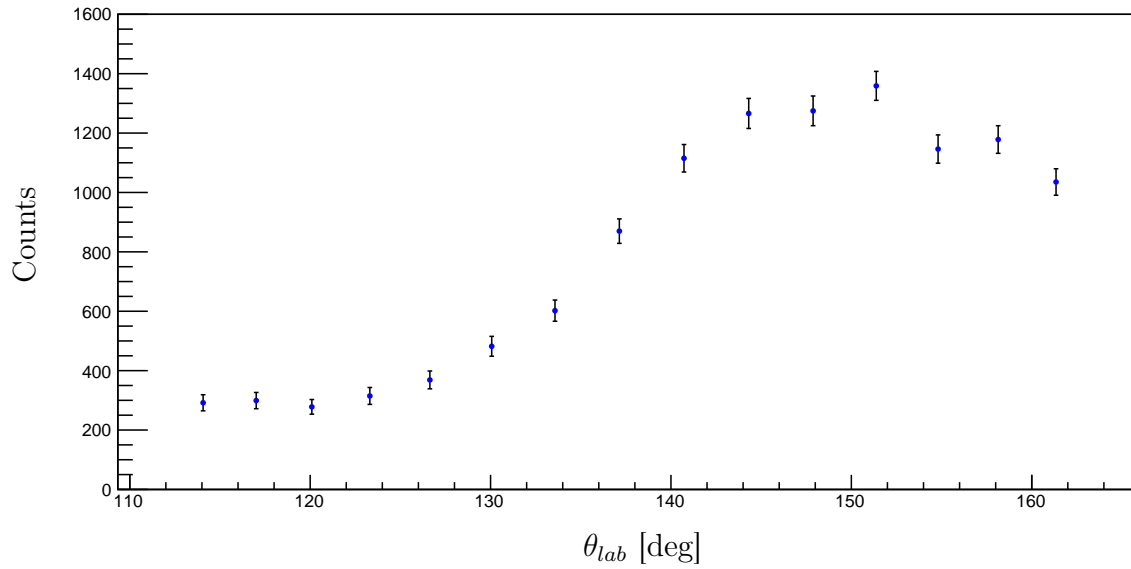


Figure 5.48: The yield of decay particles from the 11.520(4) MeV 2^+ resonance in ^{16}O , with the θ_{SCAT}^h gate imposed, versus the average angle of the associated triggered channel in the CAKE.

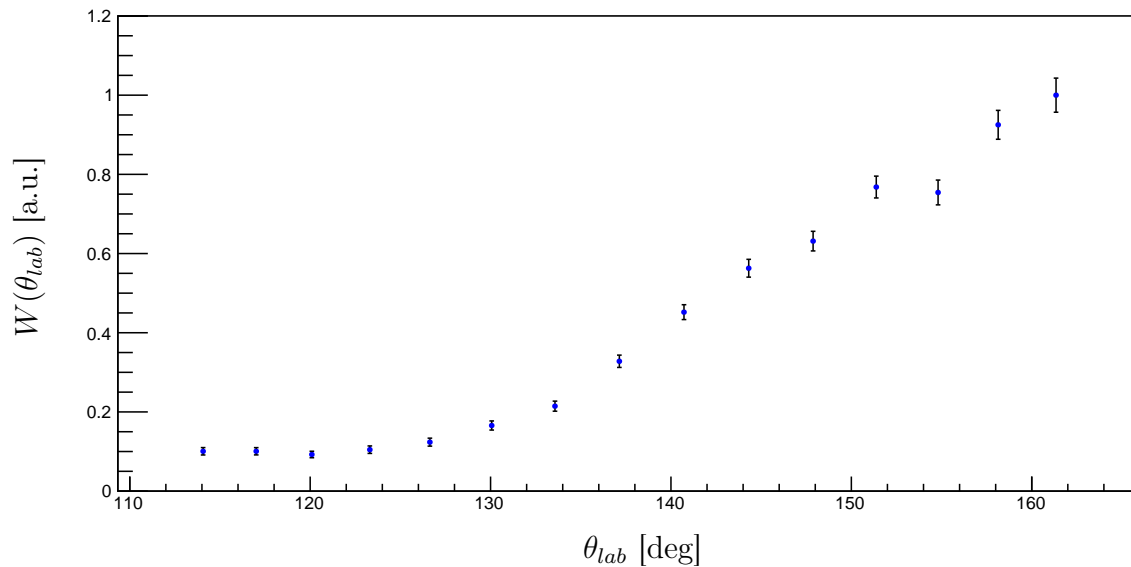


Figure 5.49: The angular distribution of decay particles from the 11.520(4) MeV 2^+ resonance in ^{16}O , with the θ_{SCAT}^h gate imposed, versus the average angle of the associated triggered channel in the CAKE.

5.7.3 The α_0 and α_1 Decay Mode from the 15.097(5) MeV resonance in ^{16}O

The yields and angular distributions of the α_0 and α_1 decay modes, which are observed in coincidence with population of the 15.097(5) MeV 0^+ resonance in ^{16}O , are plotted against the average angle of the associated ring, as shown in Figures 5.50 - 5.53.

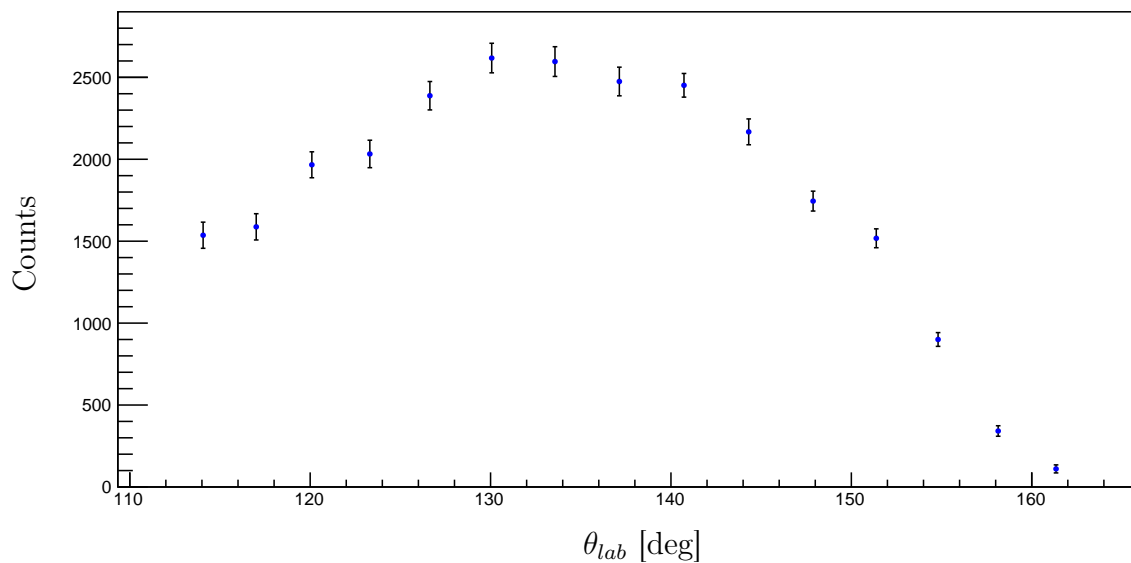


Figure 5.50: The yield of decay particles from the 15.097(5) MeV 0^+ resonance in ^{16}O , versus the average angle of the associated triggered channel in the CAKE.

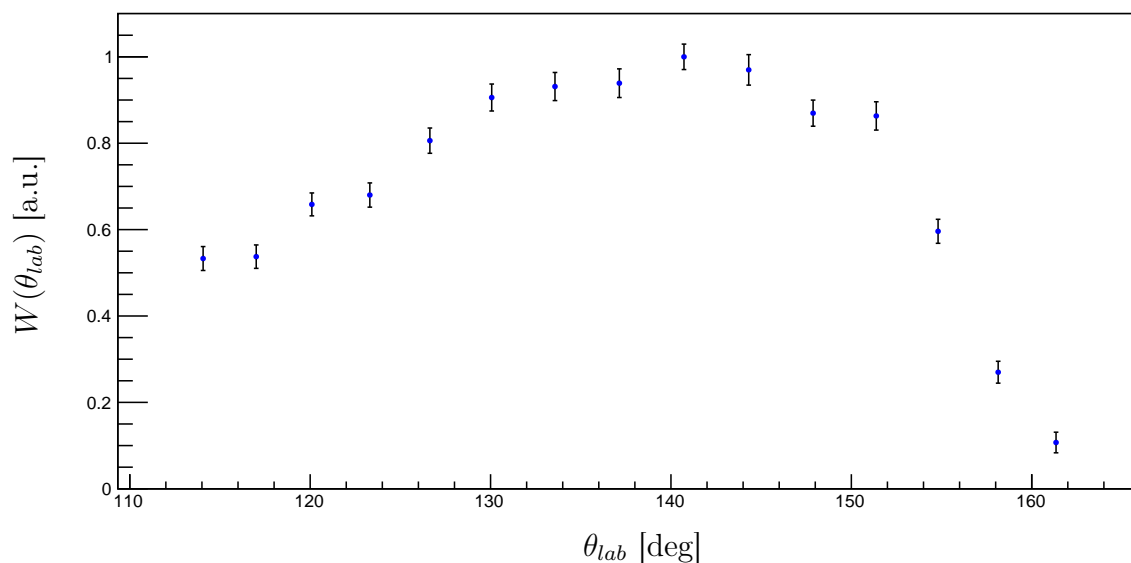


Figure 5.51: The angular distribution of decay particles from the 15.097(5) MeV 0^+ resonance in ^{16}O , versus the average angle of the associated triggered channel in the CAKE.

It is observed that the α_0 angular distribution deviates from isotropy in a statistically significant manner. This deviation cannot be attributed to target attenuation as the corresponding α_0 decay mode from the 12.049(2) MeV 0^+ resonance in ^{16}O , which imparts less kinetic energy to the α -particle and is therefore more prone to target attenuation, still clearly exhibits isotropy.

If there is indeed only a single resonance that contributes to the α_0 decay mode in this excitation region, the theoretical calculations in Section 5.6 suggest that this resonance may be have angular momentum $J \geq 3$ since there appears to be a local maximum in the angular correlation within a range of approximately 40° , which typically only occurs with higher l -values of decay.

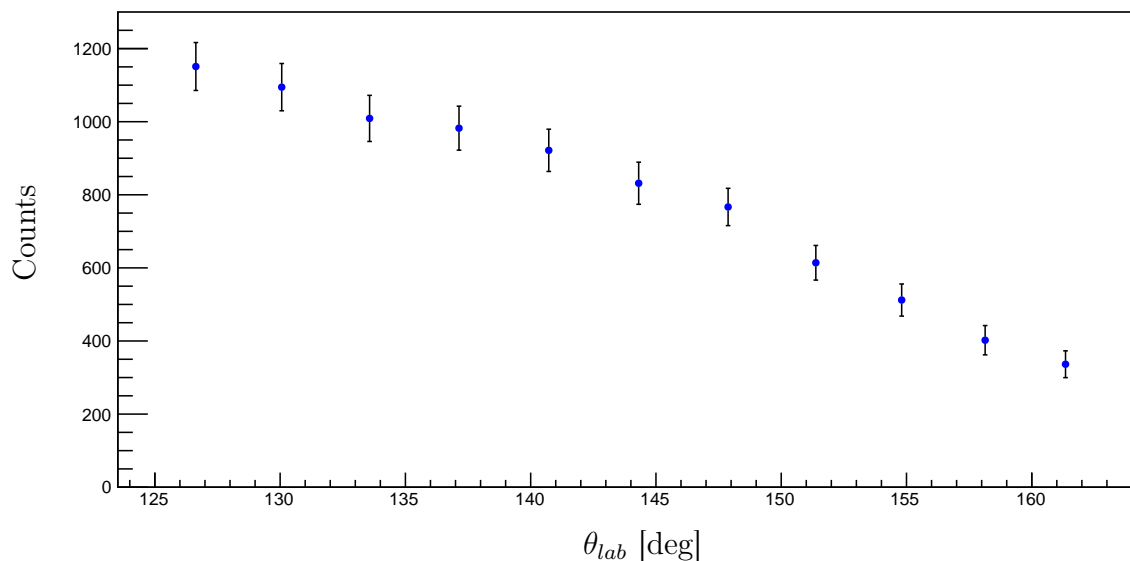


Figure 5.52: The yield of decay particles from the 15.097(5) MeV 0^+ resonance in ^{16}O , versus the average angle of the associated triggered channel in the CAKE.

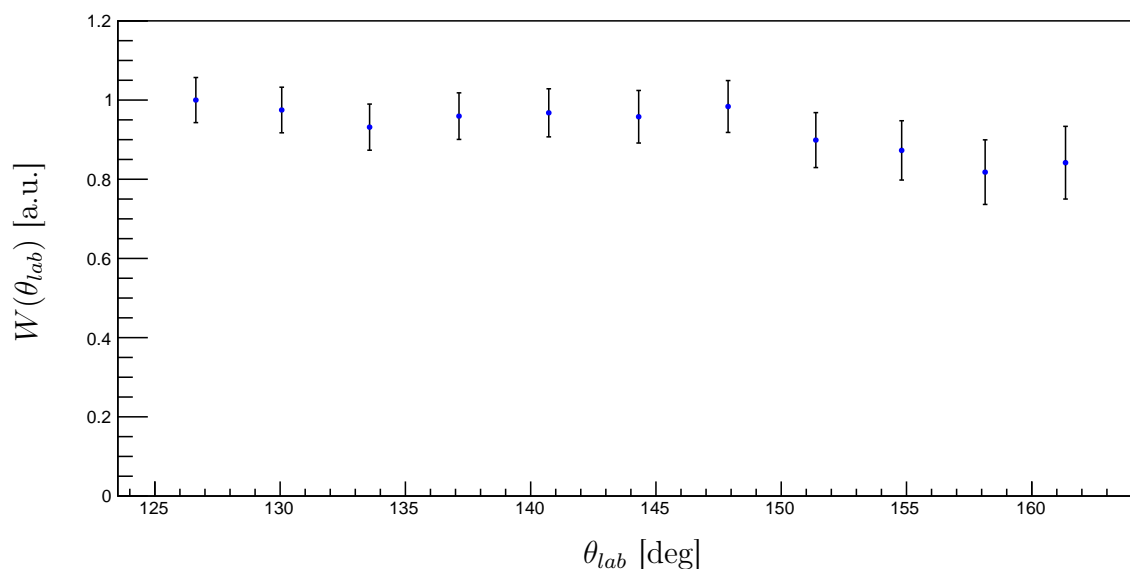


Figure 5.53: The angular distribution of decay particles from the 15.097(5) MeV 0^+ resonance in ^{16}O , versus the average angle of the associated triggered channel in the CAKE.

For the α_1 decay mode, the data corresponding to rings 12-15 are excluded from these results as since they have a lower average θ_{lab} , the effect of target attenuation, on the relatively low energy decay products from the α_1 decay mode, is more pronounced.

It is observed that the α_1 angular distribution appears to be isotropic in nature. This suggests that the resonance in ^{16}O at $E_x \sim 15.1$ MeV, from which this α_1 decay mode originates, may have either 0^+ or 2^+ spin and parity. Whilst a 0^+ resonance would necessitate an isotropic α_1 decay mode, a 2^+ resonance would require the dominance of the decay channel with an l -value of $l = 0$ to exhibit isotropy (the possible l -values are 0,1,2,3 and 4).

Chapter 6

Conclusion and Outlook

As if one could kill time
without injuring eternity

Henry David Therox

Various charged particle decay modes of ^{16}O were successfully observed and investigated by measuring the $^{16}\text{O}(\alpha, \alpha')$ reaction at 0° with a newly constructed ancillary silicon detector array. The relatively large range covered by the focal plane enabled the characterisation of many resonances of the ^{16}O nucleus. Particular focus was placed upon the analysis of the 15.097(5) MeV resonance in ^{16}O which is widely purported to be 0^+ in nature and is currently the pre-eminent candidate for a Hoyle-analogue state.

6.1 Refuting the 0^+ nature of the previously observed 15.097(5) MeV resonance in ^{16}O

The 0^+ nature of the "well known" 15.097(5) MeV resonance in ^{16}O is refuted. It is proposed that either the spin and parity of the resonance is not 0^+ or there is an unidentified resonance at $E_x \sim 15.1$ MeV which has not been previously resolved. Either possibility shall have major implications for investigations into the structure of the ^{16}O nucleus: if the spin and parity of the resonance is determined to not be 0^+ , this results in the rejection of the primary candidate for a Hoyle-analogue α cluster state in ^{16}O . If there is a previously unidentified resonance in the $E_x \sim 15.1$ MeV excitation energy region, this may explain why the theoretically calculated width, for the aforementioned cluster state at 15.097(5) MeV, is consistently exceeded by the observed widths of the resonance in previous measurements.

A result which casts doubt over the established spin and parity of the resonance is the angular distribution of the α_0 mode decay from the 15.097 MeV resonance, as shown in Figure 5.51. The angular distribution of the decay

deviates from isotropy in a statistically significant manner. This deviation is not an artefact of the analysis as the analogous α_0 decay mode from the 12.049(2) MeV 0^+ resonance in ^{16}O , which is lower in energy and therefore more prone to target attenuation effects, clearly exhibits isotropy (see Figure 5.43).

It is suggested that the α_0 and α_1 decay modes from ^{16}O , in the ~ 15 MeV region, do not originate from the same resonance. This is strongly indicated by the difference in resonance energies (location parameters) of the decay modes (summarised in Table 5.6). If the resonance previously observed at 15.097(5) MeV in ^{16}O is indeed a single resonance with $J = 0^+$ spin and parity, it is expected for the α_0 decay mode to exhibit a lower resonance energy with respect to the α_1 decay mode since the angular momentum selection rules would restrict the l -values of decay to be $l = 0$ and $l = 2$ for the α_0 and α_1 decay modes respectively. We have also investigated the case of a single $J = 3^-$ resonance in ^{16}O at 15.097 MeV, for which the α_1 decay mode may exhibit a lower l -value of decay in comparison to the α_0 .

In summary, it is proposed that the α_0 and α_1 decay modes from ^{16}O , at ~ 15 MeV, either originate from two distinct resonances, or from a single $J = 3^-$ resonance. Given the isotropy of the corresponding α_1 decay, shown in Figure 5.53, the resonance from which this decay mode originates can only be of two possible spin parities: $J = 0^+$ or $J = 2^+$. Further investigations to elucidate the nature of the ^{16}O nucleus at ~ 15 MeV is ongoing.

6.2 Future R-matrix Analysis

As stated in Section 4.8.4, the R-matrix fitting code written can account for the lineshapes of multiple decay channels, however the R-matrix fit of the singles spectrum is currently single channel as a first approximation. This is sufficient for the purposes of this thesis as the primary quantities of interest to be extracted from the singles spectrum are the yields and observed widths. In principle, the singles spectrum and the coincidence spectra of each observed decay mode should be simultaneously fitted. This inherently provides self-consistency of all the extracted parameters, which is not true for the current R-matrix fitting method. The simultaneous fitting of all spectra would also mitigate the need to fix the gaussian experimental error (which is currently implemented to enforce self-consistency across all spectra for the experimental resolution).

Whilst the analysis of the 15.097(5) MeV resonance in ^{16}O was the primary motivation for this experiment, the quality of the data allows for the characterisation of a large range of resonances in ^{16}O . The high statistics of coincident charged decay particles detected by the CAKE, combined with a unique 0° measurement of the inelastically scattered α ejectile, provides an

unprecedented opportunity to elucidate the structure of the ^{16}O nucleus in the $E_x \sim 9$ to $E_x \sim 23$ MeV excitation energy range.

6.3 Branching Ratios and Angular Distributions

To obtain the angular distributions of decay from resonances of a particular decay mode, the decay mode is first fitted with all the data. To fit spectra with particular coincidence requirements: the reduced widths and resonance energies are then fixed, leaving the amplitude as the sole free parameter. This is to ensure self-consistency within a particular decay mode.

The branching ratios for the decay channels of a resonance are observables which can be directly compared to theoretical calculations to gain insight into the nucleus. To calculate the branching ratio of a decay channel, the angular distribution of the decay channel must be known in the laboratory frame. This is necessary to correct for the yield of coincident events. Since the very nature of the 15.097(5) MeV resonance is under examination, the branching ratios cannot be reliably calculated. Postulating the spin and parity of the resonance to be $J = 0^+$ results in the sum of all observed branching ratios exceeding 100 % (see Table 5.4). This is further indicative that the α_0 and α_1 decay modes, at $E_x \sim 15.1$ MeV in ^{16}O , do not originate from a single resonance with $J = 0^+$ spin and parity.

Further development into an angular correlation code is necessary to calculate the angular distribution of decay channels in the laboratory reference frame. A Monte Carlo code has already been written to transform angular correlations, from the centre of mass frame of the recoil nucleus to the laboratory frame, whilst accounting for the experimentally imposed restriction of the ejectile scattering angle of $\pm 2^\circ$. These results will be pivotal in spin and parity assignments for the resonances at $E_x \sim 15.1$ MeV in ^{16}O . Preliminary tests for this code, which incorporates the pre-existing ANGOR and CHUCK programmes, is ongoing.

Appendices

Appendix A

R-matrix Fits of the Focal Plane Spectra to Extract Angular Distributions

The focal plane spectra of the α_0 decay mode from ^{16}O , in coincidence with individual rings: 3, 7, 11 and 15, are displayed in Figures A.1 - A.4. The focal plane spectra of the α_1 decay mode from ^{16}O , in coincidence with individual rings: 3, 7, 11 and 15, are displayed in Figures A.5 - A.8.

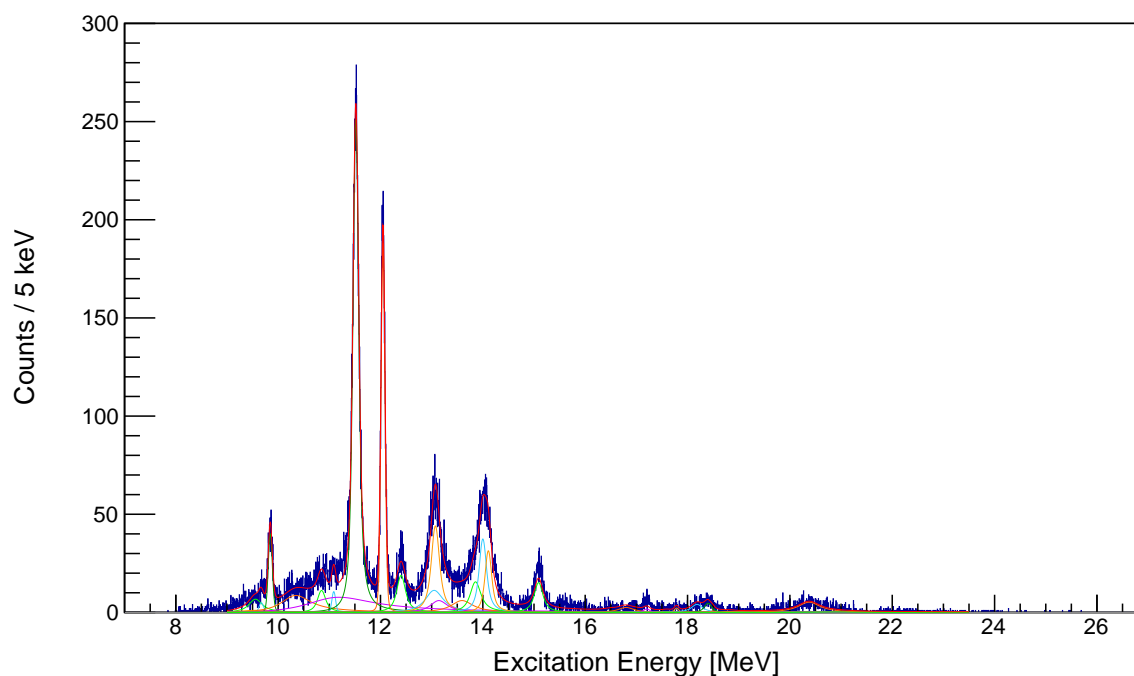


Figure A.1: R-matrix fitted focal plane spectrum of the α_0 decay mode from ^{16}O , with a coincidence condition on ring 3.

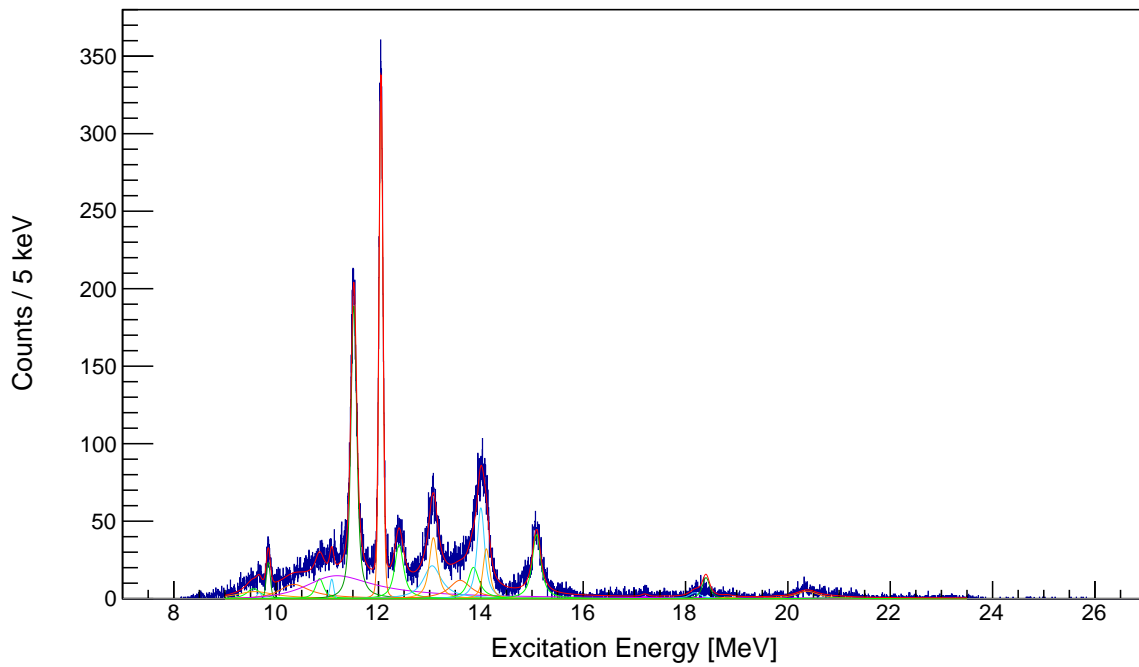


Figure A.2: R-matrix fitted focal plane spectrum of the α_0 decay mode from ^{16}O , with a coincidence condition on ring 7.

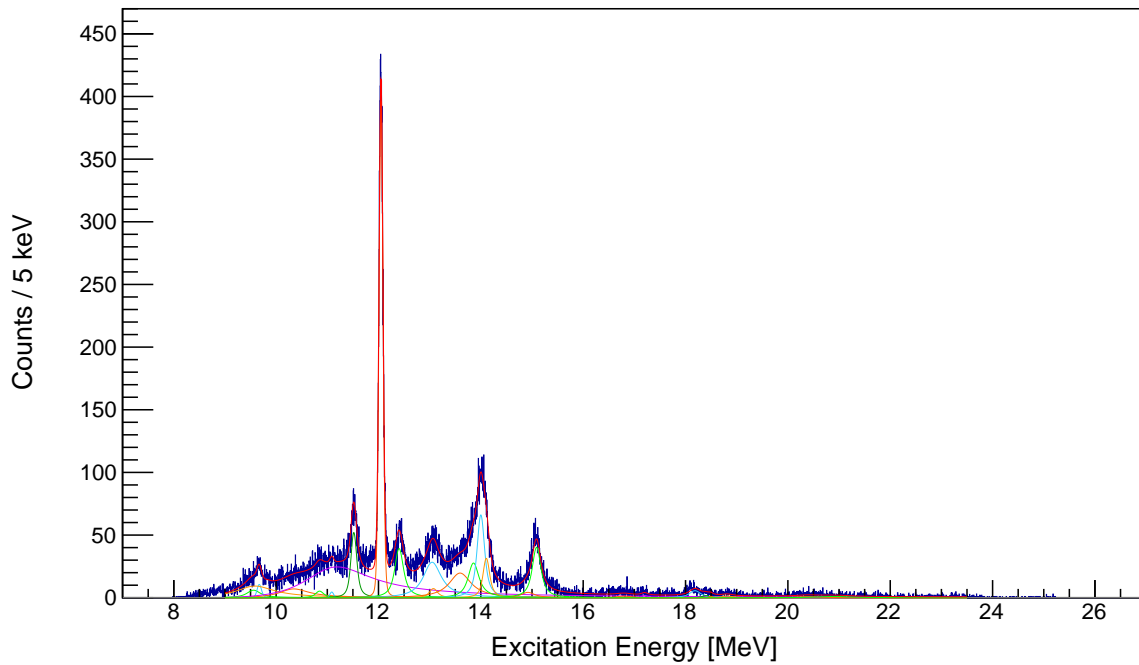


Figure A.3: R-matrix fitted focal plane spectrum of the α_0 decay mode from ^{16}O , with a coincidence condition on ring 11.

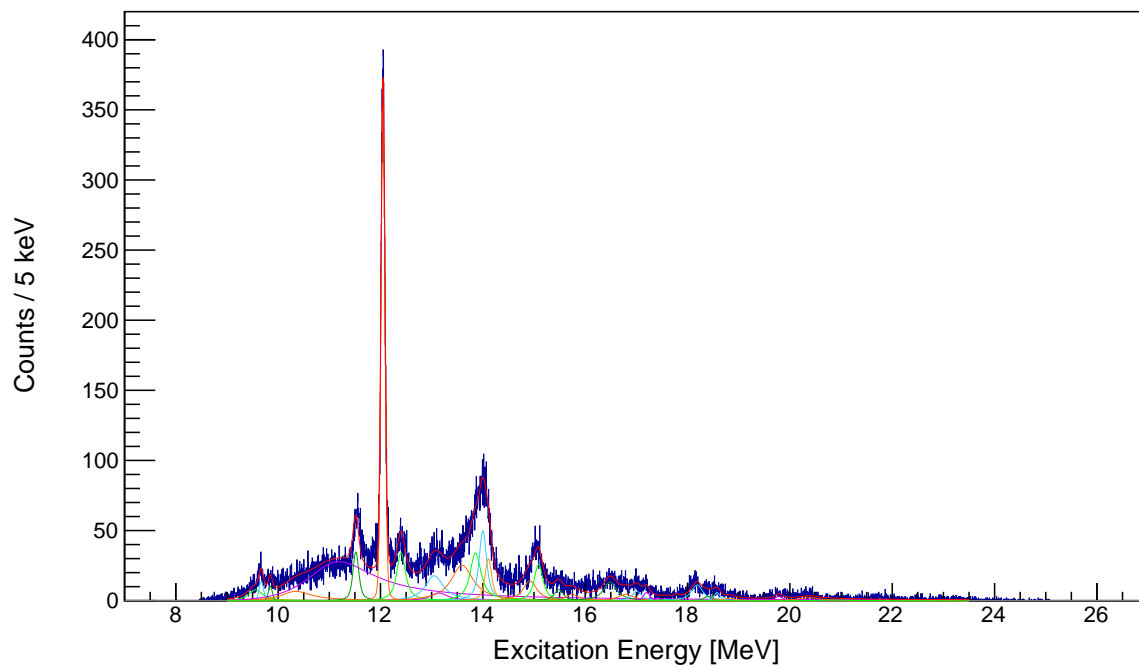


Figure A.4: R-matrix fitted focal plane spectrum of the α_0 decay mode from ^{16}O , with a coincidence condition on ring 15.

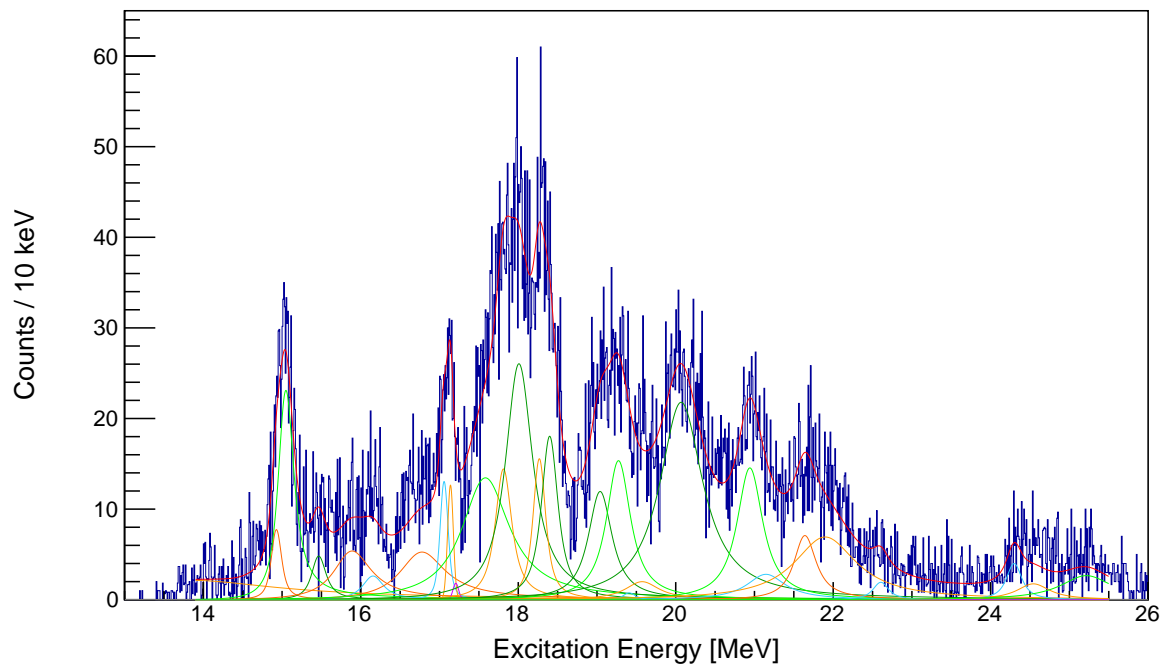


Figure A.5: R-matrix fitted focal plane spectrum of the α_1 decay mode from ^{16}O , with a coincidence condition on ring 3.

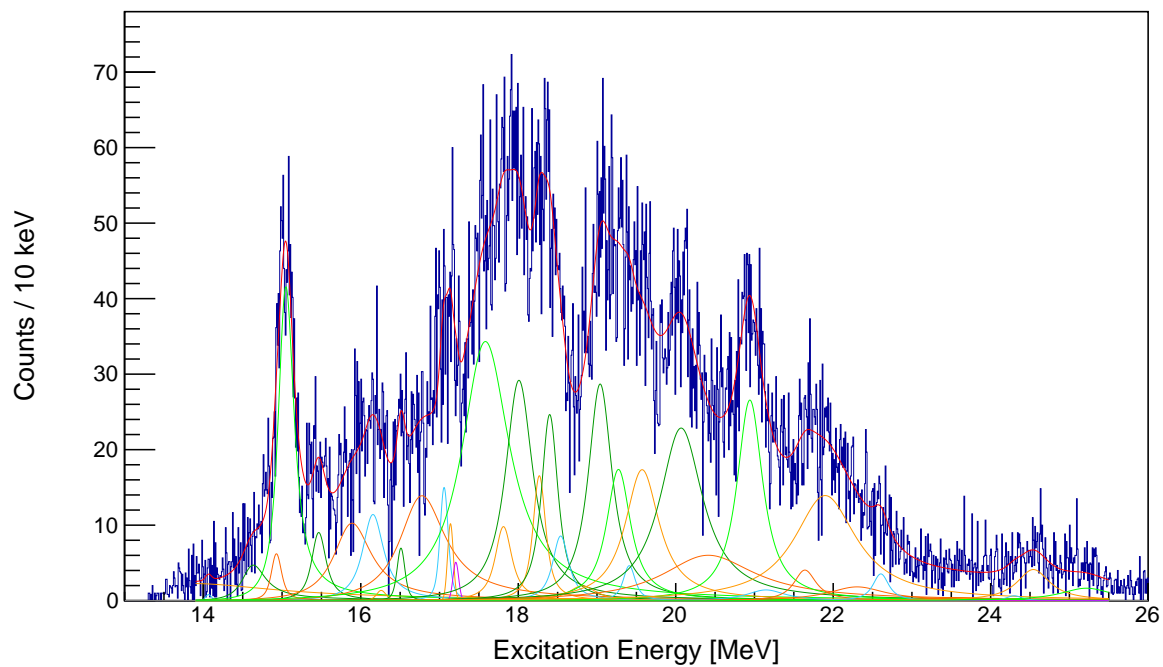


Figure A.6: R-matrix fitted focal plane spectrum of the α_1 decay mode from ^{16}O , with a coincidence condition on ring 7.

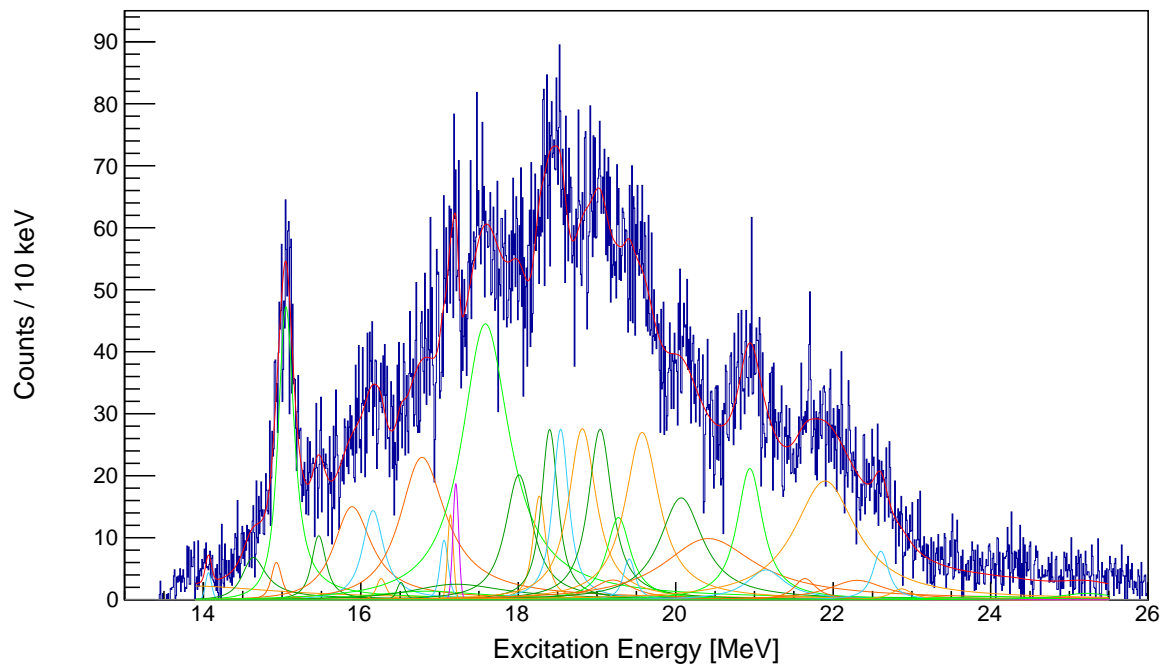


Figure A.7: R-matrix fitted focal plane spectrum of the α_1 decay mode from ^{16}O , with a coincidence condition on ring 11.

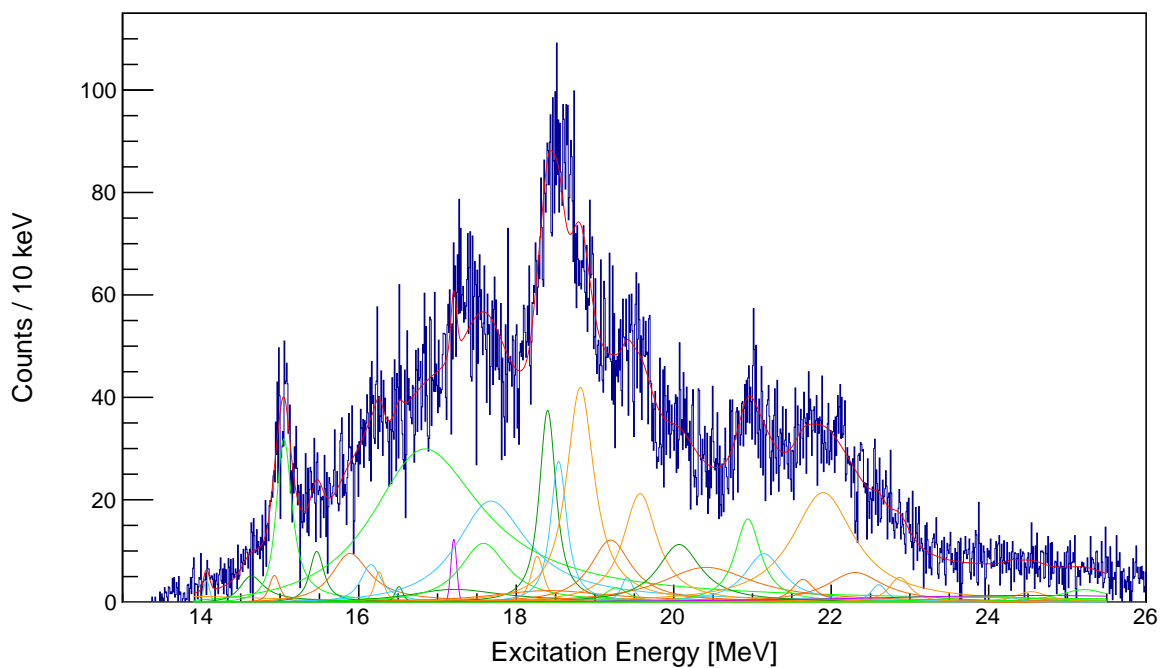


Figure A.8: R-matrix fitted focal plane spectrum of the α_1 decay mode from ^{16}O , with a coincidence condition on ring 15.

List of References

- [1] L.R. Hafstad and E. Teller. The alpha-particle model of the nucleus. *Phys. Rev.*, 54, (1938).
- [2] D.M. Brink and E. Boeker. The alpha-particle model of the nucleus. *Nuclear Physics A*, 91, (1967).
- [3] F. Hoyle. On nuclear reactions occurring in very hot stars. i. the synthesis of elements from carbon to nickel. *Astrophysical Journal Supplement*, 1(1):121–146, (1954).
- [4] M. Chernykh, H. Feldmeier, T. Neff, P. von Neumann-Cosel, and A. Richter. Structure of the hoyle state in ^{12}C . *Phys. Rev. Lett.*, 98:032501, Jan 2007.
- [5] O. S. Kirsebom, M. Alcorta, M. J. G. Borge, M. Cubero, C. Aa. Diget, L. M. Fraile, B. R. Fulton, H. O. U. Fynbo, D. Galaviz, B. Jonson, M. Madurga, T. Nilsson, G. Nyman, K. Riisager, O. Tengblad, and M. Turrión. Improved limit on direct α decay of the hoyle state. *Phys. Rev. Lett.*, 108:202501, May 2012.
- [6] M. Itoh, S. Ando, T. Aoki, H. Arikawa, S. Ezure, K. Harada, T. Hayamizu, T. Inoue, T. Ishikawa, K. Kato, H. Kawamura, Y. Sakemi, and A. Uchiyama. Further improvement of the upper limit on the direct 3α decay from the hoyle state in ^{12}C . *Phys. Rev. Lett.*, 113:102501, Sep 2014.
- [7] Evgeny Epelbaum, Hermann Krebs, Dean Lee, and Ulf-G. Meißner. *Ab Initio* calculation of the hoyle state. *Phys. Rev. Lett.*, 106:192501, May 2011.
- [8] Evgeny Epelbaum, Hermann Krebs, Timo A. Lähde, Dean Lee, and Ulf-G. Meißner. Structure and rotations of the hoyle state. *Phys. Rev. Lett.*, 109:252501, Dec 2012.
- [9] S. Ishikawa. Decay and structure of the hoyle state. *Phys. Rev. C*, 90:061604, Dec 2014.
- [10] Y. Funaki. Hoyle band and α condensation in ^{12}C . *Phys. Rev. C*, 92:021302, Aug 2015.
- [11] Yoshiko Kanada-En'yo. Cluster aspect of nuclear systems. *Physica E: Low-dimensional Systems and Nanostructures*, 43(3):811 – 814, 2011. NanoPHYS 09Proceedings of the International Symposium on Nanoscience and Quantum Physics.

- [12] Sonia Bacca, Hans Feldmeier, and Thomas Neff. Long range tensor correlations in charge and parity projected fermionic molecular dynamics. *Phys. Rev. C*, 78:044306, Oct 2008.
- [13] Evgeny Epelbaum, Hermann Krebs, Dean Lee, and Ulf-G. Meißner. *Ab Initio* calculation of the hoyle state. *Phys. Rev. Lett.*, 106:192501, May 2011.
- [14] J.-P. Ebran, E. Khan, T. Nikšić, and D. Vretenar. Density functional theory studies of cluster states in nuclei. *Phys. Rev. C*, 90:054329, Nov 2014.
- [15] C. Scholl, Y. Fujita, T. Adachi, P. von Brentano, H. Fujita, M. Górska, H. Hashimoto, K. Hatanaka, H. Matsubara, K. Nakanishi, T. Ohta, Y. Sakemi, Y. Shimbara, Y. Shimizu, Y. Tameshige, A. Tamii, M. Yosoi, and R. G. T. Zegers. High-resolution study of the ${}^9\text{Be}({}^3\text{He},t){}^9\text{B}$ reaction up to the ${}^9\text{B}$ triton threshold. *Phys. Rev. C*, 84:014308, Jul 2011.
- [16] Bose S.N. Plancks gesetz und lichtquantenhypothese. *Zeitschrift für Physik*, 26:178, (1924).
- [17] A. Einstein. Quantentheorie des einatomigen idealen gases. *Sitzungsberichte der Preussischen Akademie der Wissenschaften*, 1:3, (1925).
- [18] P Schuck, Y Funaki, H Horiuchi, G Röpke, A Tohsaki, and T Yamada. Alpha-particle condensation in nuclear systems. *Journal of Physics: Conference Series*, 413(1):012009, 2013.
- [19] Y. Funaki, T. Yamada, H. Horiuchi, A. Tohsaki, G. Röpke, and P. Schuck. Gas-like alpha-cluster states and condensates in nuclei. *J. Phys. Conf. Ser. Journal of Physics: Conference Series*, 436, (2013).
- [20] P. Schuck, Y. Funaki, H. Horiuchi, G. Röpke, A. Tohsaki, and T. Yamada. Alpha-particle condensation in nuclear systems. *J. Phys. Conf. Ser. Journal of Physics: Conference Series*, 413(1), (2013).
- [21] Lawrence L. Ames. Natural parity levels in ${}^{16}\text{O}$. *Phys. Rev. C*, 25:729–755, Feb 1982.
- [22] E. P. Wigner and L. Eisenbud. Higher angular momenta and long range interaction in resonance reactions. *Phys. Rev.*, 72:29–41, Jul (1947).
- [23] A. M. Lane and R. G. Thomas. R-matrix theory of nuclear reactions. *Rev. Mod. Phys.*, 30:257–353, Apr (1958).
- [24] Thompson I.J. and Nunes F.M. *Nuclear Reactions for Astrophysics*. Cambridge University Press, New York, (2009).
- [25] Iliadis C. *Nuclear Physics of Stars*. Wiley-VCH, Verlag, (2007).
- [26] Griffiths D.J. *Introduction to Quantum Mechanics*. Pearson Prentice Hall, Upper Saddle River, NJ, (2005).

- [27] G. Breit and M. E. Ebel. Nucleon transfer and virtual coulomb excitation. *Phys. Rev.*, 104:1030–1046, Nov 1956.
- [28] M. Abramowitz and Stegun I.A. *Handbook of mathematical functions, with formulas, graphs, and mathematical tables*. Dover Publications, New York, (1965).
- [29] Merzbacher E. *Quantum Mechanics*. John Wiley & Sons, New York, (1965).
- [30] Eugene P. Wigner. Lower limit for the energy derivative of the scattering phase shift. *Phys. Rev.*, 98:145–147, Apr 1955.
- [31] L. Eisenbud. *Dissertation, Princeton*, (1948).
- [32] Descouvemont P. and Baye D. The r -matrix theory. *Reports on Progress in Physics*, 73(3):036301, (2010).
- [33] R. Neveling *et al.* Characterization of potential cluster states in ^{16}O . *Research Proposal, Physical Sciences Research Program SSC facility, iThemba Laboratory for Accelerator Based Sciences*, (2013).
- [34] R. *et al.* Neveling. High energy-resolution zero-degree facility for light-ion scattering and reactions at ithemba labs. *Nucl. Instrum. Methods Physics Research A*, 654:29–39, (2002).
- [35] Indiana University Cyclotron Facility. *Annual Scientific and Technical Report*, page 221, (1982).
- [36] G. de Villiers. *SPEXCIT*, (2009). iThemba LABS.
- [37] H. *et al.* Fujita. The alpha-particle model of the nucleus. *Nucl. Instrum. Methods Phys. Res. A*, 484:17–26, (2002).
- [38] Y. *et al.* Fujita. The alpha-particle model of the nucleus. *Nucl. Instrum. Methods Phys. Res. B*, 126:274–276, (1997).
- [39] J.A. Swartz. *Master's thesis, Stellenbosch University*, (2010).
- [40] M. Krammer. Silicon detectors. Institute of High Energy Physics, Vienna, Austria, (2010).
- [41] National Nuclear Data Center. *Nuclear Science References*, version of (2015). Information extracted from the NSR database <http://www.nndc.bnl.gov/ensdf>.
- [42] R. Neveling. *PhD dissertation, Stellenbosch University*, (2001). iThemba LABS.
- [43] C. Wheldon. Derivations for two-body kinematics (both relativistic and non-relativistic). (2014).
- [44] K.C.W. Li and P. Adsley. *Multi-channel R-matrix fit code*. Unpublished.
- [45] R. Brun and F. Rademakers. Root - an object oriented data analysis framework. *Nucl. Instrum. Methods in Phys. Res. A.*, 389:81–86, (1997). See also <http://root.cern.ch/>.

- [46] M. Galassi *et al.* *GNU Scientific Library Reference Manual (3rd Ed.)*, ISBN 0954612078. <http://www.gnu.org/software/gsl/>.
- [47] T. Wakasa, E. Ihara, K. Fujita, Y. Funaki, K. Hatanaka, H. Horiuchi, M. Itoh, J. Kamiya, G. Röpke, H. Sakaguchi, N. Sakamoto, Y. Sakemi, P. Schuck, Y. Shimizu, M. Takashina, S. Terashima, A. Tohsaki, M. Uchida, H.P. Yoshida, and M. Yosoi. New candidate for an alpha cluster condensed state in at 400 mev. *Physics Letters B*, 653(2-4):173 – 177, 2007.
- [48] A. J. Ferguson. *Angular Correlation Methods in Gamma-ray Spectroscopy*. Wiley, New York, (1965).
- [49] P.D. Kunz. *CHUCK3, Coupled Channels Programme*. University of Colorado.
- [50] M.N. Harakeh and L.W. Put. *ANGCOR, Angular Correlation Programme*, (1979). KVI-67.